

---

Measurement of  $ZZ$  production and search  
for anomalous neutral triple gauge couplings  
in  $pp$  collisions at  $\sqrt{s} = 13$  TeV with the  
**ATLAS** experiment

---

Dissertation

zur Erlangung des Grades

DOKTOR DER NATURWISSENSCHAFTEN

am Fachbereich Physik, Mathematik und Informatik

der Johannes Gutenberg - Universität

in Mainz



JOHANNES GUTENBERG  
UNIVERSITÄT MAINZ

Maurice Becker

geboren in Frankfurt am Main

Mainz, den 28.12.2017

Erster Berichtstatter:

Zweiter Berichtstatter:

Datum der mündlichen Prüfung: 20.06.2018

# Kurzfassung

Die Untersuchung von Boson Paarproduktion in Proton-Proton-Kollisionen am Large Hadron Collider (LHC) ist prädestiniert für Tests des elektroschwachen Sektors des Standardmodells und die Suche nach neuer Physik bei höchsten Energien. Einer dieser Prozesse ist die Produktion von zwei  $Z$ -Bosonen, welcher unter anderem ein dominanter Untergrund in der Analyse von Higgszerfällen in zwei  $Z$  Bosonen ist.

In dieser Arbeit wird eine Analyse der  $ZZ$  Produktion im leptonischen Zerfallskanal,  $\ell^+\ell^-\ell'^+\ell'^-$  ( $\ell, \ell' = e, \mu$ ), vorgestellt. Die dazu genutzten Daten wurden vom ATLAS Experiment zwischen 2015 und 2016 bei einer Schwerpunktsenergie von  $\sqrt{s} = 13$  TeV aufgezeichnet und entsprechen einer integrierten Luminosität von  $36.1 \text{ fb}^{-1}$ . Dabei werden Daten mit  $Z$ -Boson Kandidaten in einem Massenfenster von 66 GeV bis 116 GeV selektiert, mit Simulationen verglichen und verwendet, um differenzielle und integrierte Wirkungsquerschnitte zu messen. Die auf Detektoreffizienzeffekte korrigierten Wirkungsquerschnitte werden in einem Phasenraum bereitgestellt, welcher der Detektorakzeptanz entspricht. Die differentiellen Wirkungsquerschnitte werden als Funktion von sieben verschiedenen Observablen präsentiert, was unter anderem Variablen einschließt, welche sensitiv auf die Jetaktivität in  $ZZ$  Ereignissen sind. Die Analyse von  $ZZ$  Ereignissen mit weiteren Jets ist von besonderem Interesse, wenn man Eigenschaften höherer störungstheoretischer Korrekturen der Quantenchromodynamik untersuchen möchte. Der integrierte Wirkungsquerschnitt wird außerdem auf den ganzen Phasenraum, einschließlich aller Standardmodell  $Z$  Boson Zerfälle, für  $Z$  Bosonen mit einer invarianten Masse zwischen 66 GeV und 116 GeV extrapoliert. Der resultierende Wert von  $17.3 \pm 0.9[\pm 0.6(\text{stat.}) \pm 0.4(\text{syst.}) \pm 0.6(\text{lumi.})]$  pb stimmt mit Standardmodellvorhersagen überein.

Des Weiteren können  $ZZ$  Ereignisse verwendet werden, um nach Kopplungen von drei neutralen Bosonen zu suchen, welche im Standardmodell nicht erlaubt sind. Die hohe Schwerpunktsenergie des LHC bietet perfekte Bedingungen, um nach solchen Effekten zu suchen, welche hauptsächlich im Bereich hoher Energien erwartet werden. Dabei wird nach Abweichungen zwischen Standardmodellerwartung und Daten im Bereich hoher transversaler Impulse des  $Z$  Bosonkandidaten gesucht, welches den höheren Transversalimpuls besitzt. Es konnten keine signifikanten Unterschiede festgestellt werden, weswegen Ausschlussgrenzen mit 95 % Konfidenzniveau (C.L.) auf vier verschiedene anormale Kopplungsparameter, welche auf zwei Unterschiedliche Arten parametrisiert werden können, gesetzt werden. Die bisher besten, mit ATLAS-Daten bestimmten, Ausschlussgrenzen auf Kopplungsparameter, welche durch einen Ansatz zur Vertexparametrisierung erhalten werden, resultieren in:  $-0.0018 < f_4^\gamma < 0.0018$ ,  $-0.0018 < f_5^\gamma < 0.0018$ ,  $-0.0015 < f_4^Z < 0.0015$ ,  $-0.0015 < f_5^Z < 0.0015$ . Zum ersten Mal werden auch folgende Ausschlussgrenzen auf Dimension 8 Operatoren gesetzt, welche sich aus einem Ansatz der effektiven Feldtheorie ergeben:  $-5.9 \text{ TeV}^{-4} < C_{\tilde{B}W}/\Lambda^4 < 5.9 \text{ TeV}^{-4}$ ,  $-3.0 \text{ TeV}^{-4} < C_{WW}/\Lambda^4 < 3.00 \text{ TeV}^{-4}$ ,  $-3.3 \text{ TeV}^{-4} < C_{BW}/\Lambda^4 < 3.3 \text{ TeV}^{-4}$ ,  $-2.7 \text{ TeV}^{-4} < C_{BB}/\Lambda^4 < 2.8 \text{ TeV}^{-4}$ .





# Abstract

The study of boson pair production in proton-proton ( $pp$ ) interactions at the Large Hadron Collider (LHC) gives the opportunity to test the electroweak sector of the Standard Model and search for new physics at highest available energies. One of these processes is the production of two  $Z$  bosons, which is also a dominating background for analyses studying the decay of the Higgs boson to two  $Z$  bosons.

A measurement of  $ZZ$  production in the  $\ell^+\ell^-\ell'^+\ell'^-$  ( $\ell, \ell' = e, \mu$ ) decay channel is presented in this thesis. Data of  $pp$  collisions at  $\sqrt{s} = 13$  TeV which was collected by the ATLAS experiment is used. The amount of collected data from 2015 and 2016 corresponds to an integrated luminosity of  $36.1 \text{ fb}^{-1}$ . Selected data is compared to simulations for on-shell  $Z \rightarrow \ell^+\ell^-$  candidate masses in the range of 66 GeV to 116 GeV and used to extract differential and integrated cross sections. The cross sections are corrected for detector effects and measured in a fiducial phase space corresponding to the detector acceptance. The differential cross sections are provided as functions of seven observables, including some that describe the jet activity in the event. Analyzing  $ZZ$  events with additional jets is particularly important to study properties of higher order QCD corrections. The integrated cross section is also extrapolated to a total on-shell phase space and all  $Z$  boson decay modes in the Standard Model using simulations. The resulting cross section is  $17.3 \pm 0.9 [\pm 0.6(\text{stat.}) \pm 0.4(\text{syst.}) \pm 0.6(\text{lumi.})]$  pb, which is in good agreement with Standard Model predictions.

The production of two  $Z$  bosons can also be used to search for neutral triple gauge boson couplings which are forbidden in the Standard Model. The high center of mass energy of the LHC is a perfect environment to search for such phenomena which are expected to be located predominantly at high energies. High tails of the transverse momentum distribution of the leading  $Z$  boson candidate are analyzed for deviations between the Standard Model expectation and data. No significant differences are found. Therefore 95% C.L. limits on four different anomalous coupling parameters are set using two different parameterizations. The currently best limits extracted from ATLAS data on anomalous couplings using a vertex parameterization are:  $-0.0018 < f_4^\gamma < 0.0018$ ,  $-0.0018 < f_5^\gamma < 0.0018$ ,  $-0.0015 < f_4^Z < 0.0015$ ,  $-0.0015 < f_5^Z < 0.0015$ . For the first time also following limits are set on dimension 8 operators using an effective field theory parameterization:  $-5.9 \text{ TeV}^{-4} < C_{\tilde{B}W}/\Lambda^4 < 5.9 \text{ TeV}^{-4}$ ,  $-3.0 \text{ TeV}^{-4} < C_{WW}/\Lambda^4 < 3.00 \text{ TeV}^{-4}$ ,  $-3.3 \text{ TeV}^{-4} < C_{BW}/\Lambda^4 < 3.3 \text{ TeV}^{-4}$ ,  $-2.7 \text{ TeV}^{-4} < C_{BB}/\Lambda^4 < 2.8 \text{ TeV}^{-4}$ .



# Contents

Kurzfassung	iii
Abstract	v
Contents	vii
<b>1 Introduction</b>	<b>1</b>
<b>2 Theory foundations</b>	<b>5</b>
2.1 The Standard Model of particle physics	5
2.1.1 Feynman formalism	8
2.1.2 Strong interaction	11
2.1.3 Electroweak interaction and symmetry breaking	13
2.2 $pp$ collisions	15
2.2.1 Phenomenology of $pp$ collisions	15
2.2.2 Structure of the proton	17
2.2.3 LHC kinematics	19
2.2.4 $Z$ boson pair production at the LHC	21
2.3 Physics beyond the Standard Model	23
2.3.1 Limitations of the Standard Model	23
2.3.2 Anomalous triple gauge couplings	24
<b>3 The LHC and the ATLAS experiment</b>	<b>27</b>
3.1 The LHC	27
3.1.1 Design of the LHC	27
3.1.2 Performance of the LHC	28
3.1.3 LHC experiments	29
3.2 The ATLAS experiment	30
3.2.1 Coordinate system and common kinematic variables	30
3.2.2 Design principle	31
3.2.3 Tracking system	32
3.2.4 Calorimeter system	33
3.2.5 Muon system	36
3.2.6 Trigger system	37
3.2.7 Data acquisition and processing	39
3.2.8 Luminosity measurement	40
<b>4 Particle reconstruction and identification in ATLAS</b>	<b>43</b>
4.1 Inner detector track reconstruction	43
4.2 Electrons	44

---

4.2.1	Reconstruction . . . . .	44
4.2.2	Identification . . . . .	45
4.2.3	Isolation . . . . .	47
4.2.4	Electron trigger . . . . .	47
4.2.5	Electron energy calibration . . . . .	47
4.3	Muons . . . . .	48
4.3.1	Reconstruction . . . . .	48
4.3.2	Identification . . . . .	49
4.3.3	Isolation . . . . .	49
4.3.4	Muon trigger . . . . .	50
4.4	Jets . . . . .	50
4.4.1	Reconstruction . . . . .	50
4.4.2	Jet energy calibration . . . . .	51
4.4.3	Suppression of pileup jets . . . . .	51
4.5	Missing transverse energy . . . . .	52
<b>5</b>	<b>Simulations and theoretical predictions</b>	<b>55</b>
5.1	Theoretical predictions . . . . .	55
5.2	Simulation of events at the LHC . . . . .	56
5.2.1	Physics simulation . . . . .	56
5.2.2	Detector simulation . . . . .	58
5.3	Simulated samples . . . . .	59
5.4	Experimental corrections applied to simulations . . . . .	61
5.4.1	Efficiency corrections . . . . .	61
5.4.2	Energy/Momentum scale and resolution corrections . . . . .	62
5.4.3	Correction of the pileup profile . . . . .	62
<b>6</b>	<b>Selection of <math>ZZ</math> candidates</b>	<b>65</b>
6.1	Selection overview . . . . .	65
6.2	Data Set . . . . .	66
6.3	Preselection . . . . .	68
6.3.1	Event cleaning . . . . .	68
6.3.2	Trigger selection and further event cleaning . . . . .	68
6.4	Analysis object selection . . . . .	69
6.4.1	Muon selection . . . . .	69
6.4.2	Electron selection . . . . .	70
6.4.3	Jet selection . . . . .	71
6.5	Event selection . . . . .	71
6.5.1	Overlap removal . . . . .	71
6.5.2	Further event cleaning . . . . .	72
6.5.3	Quadruplet selection . . . . .	73
6.5.4	Final Event selection . . . . .	74
6.6	Signal efficiency . . . . .	75
<b>7</b>	<b>Standard Model expectation</b>	<b>79</b>
7.1	Signal expectation . . . . .	79
7.2	Backgrounds . . . . .	80

---

7.2.1	Genuine background . . . . .	80
7.2.2	Single $Z$ pileup background . . . . .	81
7.2.3	Non-genuine background . . . . .	82
7.3	Systematic uncertainties . . . . .	101
7.3.1	Experimental uncertainties . . . . .	101
7.3.2	Luminosity uncertainty . . . . .	103
7.3.3	Pileup modeling uncertainty . . . . .	103
7.3.4	Theoretical uncertainties . . . . .	104
7.3.5	Impact of systematic uncertainties on the expectation . . . . .	105
7.4	Comparison of data and expectation . . . . .	108
7.4.1	Investigation of the $4e$ disagreement . . . . .	113
<b>8</b>	<b>Cross section determination</b>	<b>117</b>
8.1	Fiducial definition . . . . .	117
8.1.1	Fiducial phase space . . . . .	117
8.1.2	Signal definition . . . . .	119
8.2	Differential cross section determination . . . . .	119
8.2.1	Unfolding principle . . . . .	119
8.2.2	Choice of kinematic observables . . . . .	120
8.2.3	Binning choice . . . . .	121
8.2.4	Unfolding input . . . . .	122
8.2.5	Monte Carlo based closure check . . . . .	124
8.2.6	Systematic and statistical uncertainties . . . . .	124
8.2.7	Results . . . . .	126
8.3	Fiducial and total cross section . . . . .	128
8.3.1	Method . . . . .	129
8.3.2	Efficiency correction ( $C_{ZZ}$ ) . . . . .	130
8.3.3	Extrapolation to full on-shell phase space . . . . .	130
8.3.4	Results . . . . .	131
<b>9</b>	<b>Limits on anomalous neutral triple gauge couplings</b>	<b>135</b>
9.1	Signal parameterization . . . . .	135
9.1.1	Validation of the signal generator . . . . .	137
9.2	Input for the limit setting . . . . .	138
9.2.1	Choice of kinematic variable . . . . .	138
9.2.2	Binning optimization for highest sensitivity . . . . .	139
9.2.3	Comparison of data with expectation . . . . .	140
9.3	Limit setting procedure . . . . .	143
9.4	One and two dimensional exclusion limits . . . . .	145
9.4.1	Comparison to other results . . . . .	149
9.4.2	Outlook . . . . .	150
<b>10</b>	<b>Conclusion</b>	<b>153</b>
	<b>Appendix</b>	<b>159</b>
<b>A</b>	<b>Detailed information about simulated samples</b>	<b>159</b>

---

<b>B</b>	<b>Signal efficiencies</b>	<b>161</b>
<b>C</b>	<b>Event display</b>	<b>165</b>
<b>D</b>	<b>Background</b>	<b>167</b>
D.1	Data driven background . . . . .	167
D.1.1	Real lepton correction model uncertainty . . . . .	167
<b>E</b>	<b>Cross section</b>	<b>169</b>
E.1	Unfolding input parameter . . . . .	169
E.2	Monte Carlo based closure check . . . . .	173
E.3	Differential cross section tables . . . . .	174
E.4	Systematic bin correlations . . . . .	176
E.5	Differences between cross section measurements with 2015 and full 2015+2016 data	178
	<b>Bibliography</b>	<b>179</b>
	<b>Danksagung</b>	<b>193</b>

# Chapter 1

## Introduction

The question of what we and the world surrounding us consists of has already been bothering mankind for several thousands of years. Democritus, a Greek philosopher and pupil of Leucippus, answered this question as follows: “Sweet exists by convention, bitter by convention, colour by convention; atoms and Void alone exist in reality” [1]. This was one of the first theories that postulated the nature of matter formed by “indivisible” particles (atoms). About 2000 years later, this idea was continued by John Dalton, who postulated that each element consists of different types of indivisible atoms which can be reordered in chemical processes but not destroyed [2]. In 1904, after the discovery of the electron [3], J. J. Thompson devised an atom model where negatively charged electrons are equally distributed in a positive charged mass, which is also called “plum pudding model”. Only seven years later Ernest Rutherford showed in his scattering experiments that the positive charge must be localized in a compact core with surrounding electrons. In 1909 he continued his scattering experiments and found out, together with James Chadwick, that the core of the atom has a structure and discovered, thus, the proton [4]. X-ray scattering experiments on crystals carried out by Arthur Holly Compton showed the particle properties of photons [5] in 1923. About a decade later Chadwick found evidence for the existence of neutrons in nuclei scattering experiments [6]. Only four different types of particles, protons, neutrons, electrons and photons were known before the muon was discovered in 1937 by Carl D. Anderson and Seth Neddermeyer while studying cosmic radiation [7]. With advanced technology of particle accelerators and better detection of cosmic rays many new particles, later identified as hadrons, were found in the middle of the 20th century. Theorists made strong efforts to find an underlying structure of this *particle zoo* and developed the quark model [8, 9]. This model described the structure of these new particles as bound states of quarks. In 1960 it was possible to experimentally show, using electron-nucleon scattering, that the proton has an internal structure [10] which can also be explained by the quark model. Further developments in the theoretical description of the interaction of particles led to predictions of mediators of these interactions. One of them, the gluon, was found in 1979 by the electron-positron collider PETRA (Positron-Elektron Tandem Ring Anlage) at DESY (Deutsches Elektronen-Synchrotron) [11–14]. The mediators of the so-called weak force, which for example play a major role in radioactive  $\beta$ -decays, were found four years later at the Super-Proton-Antiproton Synchrotron (Sp $\bar{p}$ S) located at CERN (Conseil Européen pour la Recherche Nucléaire) [15–18].

---

This interplay of theoretical and experimental physics led to the development of the Standard Model of particle physics. It describes the fundamental structure of matter and the interaction of elementary particles via three different forces, the electromagnetic, weak and strong force. It also includes the description, how particles acquire masses by introducing the Higgs mechanism. With the discovery of the Higgs boson at the Large Hadron Collider (LHC) at CERN in 2012 [19, 20] all particles predicted by the Standard Model have been discovered by experiments. It is a very successful model which has been tested very intensively over the last years and no significant deviations between predictions and experiments had been found.

Nevertheless, there are limitations and experimental results that can not be described by the Standard Model. Among other topics it does not include the gravitational force, it can not explain why the masses of the elementary particles are so different or why we live in a world of matter despite the fact that there should have been a matter- anti-matter equilibrium in the beginning of the universe. There is also no explanation given by the Standard Model why the visible matter only amounts to about 5% in the universe whereas the rest is build of so-called *Dark Matter* and *Dark Energy* [21].

At the LHC two hadrons collide, which gives the possibility to test the Standard Model at never before reached energies and search for physics beyond the Standard Model. One possibility to search for such physics is to analyse data from proton-proton collisions for resonances of new particles for example in mass spectra. Another possibility is to search for couplings between particles that are not allowed in the Standard Model. When searching for new physics it is very important to have very precise predictions. There are many parameters in the prediction of processes that can not be calculated theoretically and therefore need to be extracted from data. In this thesis a measurement of the production of two  $Z$  bosons, the neutral mediators of the weak force, is performed. Only leptonic decays of the  $Z$  bosons to electron-positron or muon-antimuon pairs are considered since in these decay channels only very small background is expected. One motivation for a precise measurement of this process is that it is a dominating background for the Higgs production process:  $pp \rightarrow H + X \rightarrow ZZ^* \rightarrow \ell^+ \ell^- \ell'^+ \ell'^- + X$  ( $\ell = e, \mu$ ). Having a good knowledge of  $pp \rightarrow ZZ + X \rightarrow \ell^+ \ell^- \ell'^+ \ell'^- + X$  is therefore mandatory for making precise measurements of Higgs boson properties. Studies of  $ZZ$  processes at high energies are also important to probe the electroweak sector and especially the electroweak symmetry breaking of the Standard Model. For this reason the cross section is measured as function of different observables and compared to different theoretical predictions. The data used for this analysis was taken in 2015 and 2016 at a center of mass energy of  $\sqrt{s} = 13$  TeV.

Couplings of three neutral gauge bosons, such as  $\gamma^* ZZ$ , are not allowed in the SM, but it is possible to search for signatures of such anomalous triple gauge couplings. Those signatures are for instance enhancements in tails of distributions that are correlated to the energy of the outgoing leptons. This is why this search strongly profits from an increased center of mass energy compared to the operation of the LHC in 2012 where the center of mass energy was 8 TeV.

The thesis is structured as follows: In Chapter 2 theoretical foundations are described with focus on the Standard Model and  $pp$  collisions at the LHC. The following Chapter describes the experimental setup of the LHC and ATLAS experiment, containing descriptions of the sub-detectors, data triggering and data acquisition system which are relevant for this analysis. The calibration of data and identification of physical objects like electrons and muons is explained in Chapter 4. This is followed by a description of current theoretical predictions of  $ZZ$  production at the LHC and an explanation of the simulation of  $pp$  events in Chapter 5. The selection of



---

$ZZ$  events that is applied to data and simulation is shown in Chapter 6, followed by Chapter 7 where it is described, how Standard Model expectations are build and compared to data. In Chapter 8 the procedure of cross section extraction is discussed and results are compared to predictions from simulations and to results from other experiments. A description of the search for anomalous triple gauge couplings is given in Chapter 9 together with the presentation of results and a comparison to other experiments. In the last chapter, Chapter 10, the results are summarized and a short outlook for future projects is given.



# Chapter 2

## Theory foundations

This chapter gives a brief overview of the theoretical foundations that are needed to do a cross section measurement of  $ZZ$  production at the LHC and search for signatures from phenomena beyond our current understanding of the structure of matter and their interactions. In the first section the Standard Model of particle physics, with its elementary particles and interactions, is briefly described. The following section focuses on the theoretical description of proton-proton (pp) collisions, like they take place at the LHC. It covers also a description of the dynamical structure of the proton and outlines the theoretical aspects of multi boson production in  $pp$  collisions. The last section gives a motivation why the Standard Model is not enough to describe all observed phenomena and discusses the main aspects of models beyond the Standard Model that are relevant when looking at  $ZZ$  production at the LHC. The discussion is orientated on the description in [22]. Throughout this thesis neutral units are used, which means that  $\hbar$  and  $c$  is set to one and therefore masses and momenta are given in units of energy which in most cases is electron volts (eV).

### 2.1 The Standard Model of particle physics

The Standard Model (SM) of particle physics is currently the best model to describe the fundamental structure of matter and the interaction of elementary particles. It was tested in many different ways and passed all of them.

The SM describes all matter consistent of two fundamental, elementary point like particles: leptons and quarks. Both particles follow a Fermi–Dirac statistics [23, 24] and are therefore called fermions. They have half integer spin, which is an intrinsic form of angular momentum and like for example the charge of a particle, a quantum number describing its properties. In order to form more complex structures, leptons and quarks have to interact with each other. In the SM these interactions are described by three different forces: the electromagnetic, the weak and the strong force. The gravitational force, which is known to exist, is not included in the SM but for subatomic scales its strength is negligible compared to the other interactions. The mediators of the three forces, which are described by the SM, are a further fundamental group of particles that follow Bose–Einstein statistics [25] and therefore called gauge bosons and have integer spins.

Interaction	Boson	Mass [GeV]	couples to	rel. strength
strong	gluon ( $g$ )	0	color charge (r, g, b)	1
electromagnetic	photon ( $\gamma$ )	0	electric charge ( $e$ )	$10^{-2}$
weak	$W^\pm$	$\approx 80.4$	weak charge ( $g$ )	$10^{-6}$
	$Z$	$\approx 90.2$		

TABLE 2.1: Overview of the interactions and gauge bosons of the Standard Model of particle physics [26].

An overview of the different interactions and the correspondent mediators is shown in Table 2.1. The electromagnetic force, first described by Maxwell in 1873 [27], is mediated by massless photons ( $\gamma$ ). It interacts with electromagnetic charged particles but is itself uncharged. Additionally the range of the electromagnetic interaction is infinite and decreases with distance.

The weak interaction, first described by Fermi in 1934 [28], is mediated by three different gauge bosons: the electrically neutral  $Z$  boson and the charged  $W^\pm$  bosons. They couple to the weak charge (described in more detail in Section 2.1.3). All of them have masses in the GeV range, a short lifetime and therefore a short interaction range.

The strong force was first described by Fritsch and Gell-Mann in 1973 [29]. It is mediated by 8 gluons which couple to color charge, which they also carry themselves. This color charge, a quantum number introduced to describe the strong interaction, comes in three different colors: red, green and blue as well as the corresponding anti colors. Due to the self interaction of gluons, the range of the strong interactions is the shortest of all interactions.

Leptons, of which six exist, can be divided into three different families. Each family has a charged lepton and a corresponding neutrino which is electrically neutral but interacts weakly. In Table 2.2 the leptons are presented. The charged leptons<sup>1</sup>, electron ( $e$ ), muon ( $\mu$ ) and tau ( $\tau$ ) interact electromagnetic as well as via the weak interaction. The masses of the charged leptons increase with the generation. Therefore it is possible for leptons of higher generations to decay via the weak interaction into leptons of the generation below. Neutrinos are expected to be massless in the SM. Nevertheless it was shown, for example with neutrino oscillation experiments, that neutrinos have a very small mass [30]. So far it is not possible to measure the mass directly but to give upper limits on the mass, which are also shown in the table. In addition to the particles in the table, there is to each lepton an anti-lepton, which has the same mass but opposite additive quantum numbers.

Generation	Name	$T_3$	el. charge	Mass
1.	electron ( $e^-$ )	-1/2	-1	$\approx 0.5$ MeV
	electron neutrino ( $\nu_e$ )	+1/2	0	$< 2$ eV
2.	muon ( $\mu^-$ )	-1/2	-1	$\approx 106$ MeV
	muon neutrino ( $\nu_\mu$ )	+1/2	0	$< 0.19$ MeV
3.	tau ( $\tau^-$ )	-1/2	-1	$\approx 1777$ MeV
	tau neutrino ( $\nu_\tau$ )	+1/2	0	$< 18.2$ MeV

TABLE 2.2: Overview of the three lepton families of the Standard Model. Given are name, third component of the isospin  $T_3$ , electric charge and masses [31].

<sup>1</sup>This description holds also for charged anti-leptons.

Quarks can also be grouped into three families where each contains two different flavored quarks as well as the corresponding anti-quarks. In Table 2.3 the quarks are listed with their electric charge, the third component of the isospin and their mass. A specialty about quarks is that they have fractional electric charge, the up-type quarks have charge  $+2/3$  and the down-type quarks  $-1/3$ . The masses of quarks are increasing with the generation. The definition of the mass of a quark can be done in different ways. Either the current quark mass is quoted, which is the mass of the quark itself, or the constituent mass which contains in addition the mass of the gluon field around it. For heavy quarks ( $t, b, c$ ) these masses are very similar but for the low mass quarks ( $u, d, s$ ) this can be different. In the table the current mass is given.

Quarks also carry color charge and therefore participate in the strong interaction. They do not exist as free particles<sup>2</sup> but in color neutral bound states. These states can be split into two groups: mesons, which contain one quark and one antiquark, and baryons, containing three quarks with three different colors. Recently there was also observations of combined states with four and five quarks, called tetra- and pentaquarks [32–34].

Generation	Name	$T_3$	el. charge	Mass
1.	up u	+1/2	+2/3	$\approx 2.3$ MeV
	down d	-1/2	-1/3	$\approx 4.8$ MeV
2.	charm c	+1/2	+2/3	$\approx 1.3$ GeV
	strange s	-1/2	-1/3	$\approx 95$ MeV
3.	top t	+1/2	+2/3	$\approx 173.1$ GeV
	bottom b	-1/2	-1/3	$\approx 4.2$ GeV

TABLE 2.3: Overview of the three quark families of the Standard Model. Given are the name, the third component of the isospin  $T_3$ , the charge and the masses. The values are taken from [31].

For the quarks the constituent mass is shown. Anti particles are not listed explicitly.

Mathematically the Standard Model can be described by a gauge-invariant quantum field theory [35]. Particles of the SM are described in this theory as excitations of quantum fields. Fermions are represented by so-called (dirac)-spinors ( $\psi$ ) which are four component column vectors that satisfy the Dirac equation for a free fermion:

$$(i\gamma^\mu \partial_\mu - m)\psi = 0, \quad (2.1)$$

where  $\gamma_\mu$  are the gamma matrices,  $m$  the mass of a fermion and  $\partial_\mu$  the partial derivative. All the dynamics of a free fermion are described by this equation. The corresponding Lagrangian density function, short Lagrangian, is given by:

$$\mathcal{L} = \bar{\psi}(i\gamma^\mu \partial_\mu - m)\psi, \quad (2.2)$$

where  $\bar{\psi} = \psi^\dagger \gamma^0$ . This formalism should be gauge invariant under symmetry transformation<sup>3</sup>. This can be expressed by transforming the fermion field in the following way (for the case of a U(1) symmetry):

$$\psi \rightarrow e^{i\theta(x)}\psi. \quad (2.3)$$

<sup>2</sup>At least up to now they were never observed free

<sup>3</sup>One example from classical electrodynamics would be the freedom in choice of the reference potential when measuring a voltage.

---

The transformation is called global if the real phase  $\theta(x)$  is not dependent on the space coordinate  $x$  and local if it is. The change of the Lagrangian after inserting the transformed fermion field is:

$$\delta\mathcal{L} = -\bar{\psi}(x)\gamma^\mu\partial_\mu\theta(x)\psi(x), \quad (2.4)$$

and is therefore not invariant under local gauge transformations. In order to restore this invariance a new vector field ( $A_\mu(x)$ ) can be introduced which transforms like:

$$A_\mu(x) \rightarrow A_\mu(x) - \frac{1}{e}\partial_\mu\theta(x). \quad (2.5)$$

This field is incorporated into the Lagrangian by replacing:

$$\partial_\mu \rightarrow \mathcal{D}_\mu = \partial_\mu + ieA_\mu(x), \quad (2.6)$$

where  $\mathcal{D}_\mu$  is the so-called covariant derivative and  $e$  can be identified as a conserved charge of the particle described by  $\psi$ , following Noether's theorem [36]. When inserting Equation 2.6 in Equation 2.2 the resulting Lagrangian:

$$\mathcal{L} = \bar{\psi}(x)(i\gamma^\mu\partial_\mu - m)\psi(x) - e\bar{\psi}(x)\gamma^\mu A_\mu(x)\psi(x), \quad (2.7)$$

is invariant under local gauge transformations. This Lagrangian shows the dynamic of a fermionic field and in the second part of the equation, the interaction of the fermions with the gauge field  $A_\mu(x)$  which can be identified as the photon field. It is known that photons can also exist as free particles, not as part of an interaction, and therefore an additional term has to be added to get the full Lagrangian of Quantum Electrodynamics (QED):

$$\mathcal{L}_{QED} = \bar{\psi}(x)(i\gamma^\mu\partial_\mu - m)\psi(x) - e\bar{\psi}(x)\gamma^\mu A_\mu(x)\psi(x) - \frac{1}{4}F_{\mu\nu}F^{\mu\nu}, \quad (2.8)$$

where  $F_{\mu\nu}$  is the electromagnetic field tensor:

$$F_{\mu\nu} = \partial_\mu A_\nu(x) - \partial_\nu A_\mu(x). \quad (2.9)$$

In summary it was shown that by requiring local gauge invariance, a new vector fields, in the case of a  $U(1)$  symmetry group a photon field, is introduced that describes the interaction. A beautiful characteristic of this formalism is that the number of introduced vector fields, and thus the number of particles mediating the interaction, corresponds to the number of generators of the group. The Lagrangian of the complete SM is invariant under local gauge transformations of the  $SU(2)_L \times U(1)_Y \times SU(3)_C$  group. The first part  $SU(2)_L \times U(1)_Y$  corresponds to a combination of the electromagnetic and weak interaction which leads to the four gauge bosons corresponding to these interactions. Invariance under transformations under the second part,  $SU(3)_C$ , generate the eight gluons, mentioned before.

### 2.1.1 Feynman formalism

It is possible to calculate the amplitude of a process by using the so-called Feynman rules [37]. Feynman diagrams can be used to visualize processes and for guidance to calculate amplitudes. Fermions are displayed as straight lines with arrows that point in direction of time for particles

and in the opposite direction for anti-particles. Points, where three or more lines intersect are called vertices. Lines connecting two vertices are called propagators. In Figure 2.1 two different

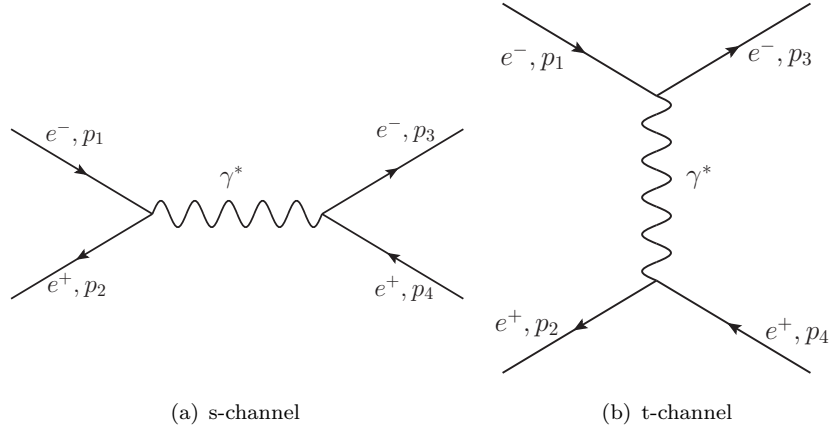


FIGURE 2.1: Different leading order feynman graphs for Bhabha-scattering. The time axis is horizontally adjusted.

exemplary diagrams are given which represent the process of  $e^+e^-$  scattering, called Bhabha-scattering. This is a process of QED therefore the propagator is in this case a (virtual<sup>4</sup>) photon. The left part of the Figure shows the s-channel where the electron and positron annihilate to a virtual photon, which then decays again into an electron-positron pair. The right side shows the t-channel, reflecting a scattering process of  $e^+, e^-$  via the exchange of a photon. At each vertex a factor proportional to the square root of the coupling constant ( $\alpha_{em}$ ) of the interaction is entering the amplitude. The coupling constant is a measure of the strength of the interaction and in case of QED directly proportional to the electron charge squared ( $\alpha_{em} = e^2/4\pi$ ). For the two diagrams shown this leads overall to an amplitude proportional to  $\sqrt{\alpha_{em}} \times \sqrt{\alpha_{em}} = \alpha_{em}$ . In order to connect the amplitude with a cross section, Fermi's Golden rule [38] can be used, which states that the cross section is given by the product of the squared, absolute value of the amplitude with the integral over the available phase space. The amplitude can be derived with Feynmans rules as shown before and the phase space is given by looking at the kinematic of the process. For the example of Bhabha-scattering the cross section is given by:

$$\sigma = \frac{1}{4\sqrt{(p_1 \cdot p_2)^2 - (m_1 m_2)^2}} \int |\mathcal{M}|^2 (2\pi)^4 \delta^4(p_1 + p_2 - p_3 - p_4) \times \prod_{j=3}^4 2\pi \delta(p_j^2 - m_j^2) \Theta(p_j^0) \frac{d^4 p_j}{(2\pi)^4}. \quad (2.10)$$

The four momenta  $p_i$  and the corresponding masses  $m_i$  are the momenta and masses of the incoming and outgoing leptons as already shown in Figure 2.1. The factor  $\delta^4(p_1 + p_2 - p_3 - p_4)$  ensures energy and momentum conservation and the delta function  $\delta(p_j^2 - m_j^2)$  constrains the particles to be on their mass shells. The Heaviside function  $\Theta(p_j^0)$  constrains the outgoing energy to positive values. Since the matrix amplitude  $\mathcal{M}$  is squared there is also the possibility for interference terms. In general the cross section can be expressed as a series expansion of the coupling constant:

$$\sigma = \sum_{i=1} \alpha^i \sigma^{(i)} \quad (2.11)$$

<sup>4</sup>Particles are virtual if their invariant mass does not correspond to the mass of the real (experimentally observable mass). Particles with such masses are also labeled as off-shell particles.

where  $\sigma^{(i)}$  indicates all contributing graphs to the order of  $\mathcal{O}(\alpha^i)$ . The graphs corresponding to the lowest order of  $\alpha^i$  are called leading order (LO), the second lowest, next to leading order (NLO) and so on. Examples of some NLO diagrams, that have to be taken into account when calculating the amplitude of the Bhabha-scattering, are shown in Figure 2.2. The first diagram shown in the top left is a correction to the decay vertex of the photon, called vertex correction. The top right one is an example of final state photon radiation and the bottom left for initial state radiation. An example for a (fermion) loop correction is shown in the bottom right diagram.

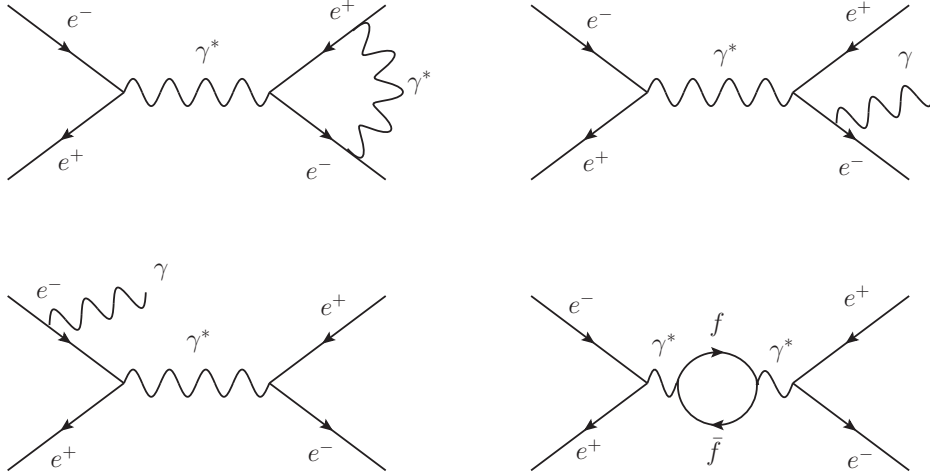


FIGURE 2.2: Some of the Feynman graphs contributing to the NLO correction of the process  $e^+e^- \rightarrow \gamma^* \rightarrow e^+e^-$ . The top left shows a vertex correction, the top right is an example of final state radiation (FSR), the bottom left is an example of initial state radiation (ISR) and the bottom right a fermion loop correction.

When calculating a cross section in principal all orders (see Equation 2.11) have to be taken into account. In practice this is not possible for theoretical calculations and one has to stop after a few orders<sup>5</sup>. When calculating higher order loop corrections, integrating over the momenta of particles in loops, can lead to divergences which are also called *ultra violet (UV)* divergences. It is possible to *regularize* the integrals by introduction of a cutoff scale  $\Lambda_{cutoff}$ . After solving the integral, two parts from the regularization are left, one term independent and one dependent on  $\Lambda_{cutoff}$ . This dependence can be seen as modification of the coupling:

$$\alpha_{em,physical} = \alpha_{em} + \delta\alpha_{em}. \quad (2.12)$$

In the limit  $\Lambda_{cutoff} \rightarrow \infty$ ,  $\delta\alpha_{em}$  also goes to infinity. The bare coupling  $\alpha_{em}$  must have therefore some compensating infinities. Illustrative might be the picture of having an infinite bare charge that is screened by charges from vacuum polarizations leading to a physical, measurable charge which is not infinite. In order to remove the dependency of the cutoff scale and make it possible to do predictions of physical quantities the regularized integrals have to be *renormalized*. During this procedure the dependence on the cutoff scale disappears but a new renormalization scale

<sup>5</sup>How many orders differs for different interactions and highly depends on the model and resources used to calculate the cross section but for strong interaction processes often NNLO calculations are currently the best possible theory predictions.



dependence shows up. This scale depends of couplings leads to the concept of the so-called “running couplings”. For QED the coupling constant increases for higher scales.

### 2.1.2 Strong interaction

Quantum Chromodynamics (QCD) is the quantum field theory description of the strong interaction. The underlying symmetry group  $SU(3)_C$  has 8 generators<sup>6</sup>. One representation of these generators are the Gell-Mann matrices  $\lambda^1, \dots, \lambda^8$  [39]. They fulfill the commutator relation:

$$[\lambda^a, \lambda^b] = 2if^{abc}\lambda^c \quad (2.13)$$

with  $f^{abc}$  as fully antisymmetric structure constants [40]. When local gauge invariance under symmetry transformation of the  $SU(3)_C$  is considered, the Lagrangian is given by:

$$\mathcal{L}_{QCD} = -\frac{1}{4}G_a^{\mu\nu}G_{\mu\nu}^a + \sum_f \bar{q}_f(i\gamma^\mu D_\mu - m_f)q_f, \quad (2.14)$$

with the covariant derivative:

$$D^\mu = \partial^\mu - ig_s \frac{\lambda^a}{2} G_a^\mu(x). \quad (2.15)$$

The eight different gluons are represented by  $G_a^\mu$ , where the small index  $a$  stands for the color. The sum iterates over all quark flavors  $f$  and  $g_s$  is connected to the fine structure constant of QCD via  $\alpha_s = g_s^2/4\pi$ . The field strength tensors  $G_a^{\mu\nu}$  in the first part of the Lagrangian are defined as:

$$G_a^{\mu\nu} = \partial^\mu G_a^\nu - \partial^\nu G_a^\mu + g_s f^{abc} G_b^\mu G_c^\nu \quad (2.16)$$

and show the self-coupling of gluons.

It is also possible to formulate Feynman rules for QCD processes and visualize them in Feynman diagrams. Figure 2.3 shows at the top two processes at leading order in  $\alpha_s$ . The top left shows a simple  $q\bar{q} \rightarrow q\bar{q}$  process with an gluon propagator in between. The top right side is an example of gluon gluon coupling. Examples of higher order corrections are shown at the bottom left side of the figure, where a  $q\bar{q}$  loop correction is shown, and on the bottom right side, illustrating a gluon loop correction.

Also here, similar to QED loops, divergences occur when trying to calculate these loop correction. As mentioned before the coupling ends up to have a dependency on a renormalization scale ( $\mu_R$ ). This scale is arbitrary and the measurable quantities, like the cross section, should be independent of it. This is given when all loop corrections are included, but since this is technically not possible when calculating a cross section a  $\mu_R$  dependence remains. A choice that is often made is to set  $\mu_R = Q^2$ . Variations of its choice are often used as an estimate of the size of the contribution of neglected terms.

<sup>6</sup>The  $C$  indicates the aspect of color in this theory.

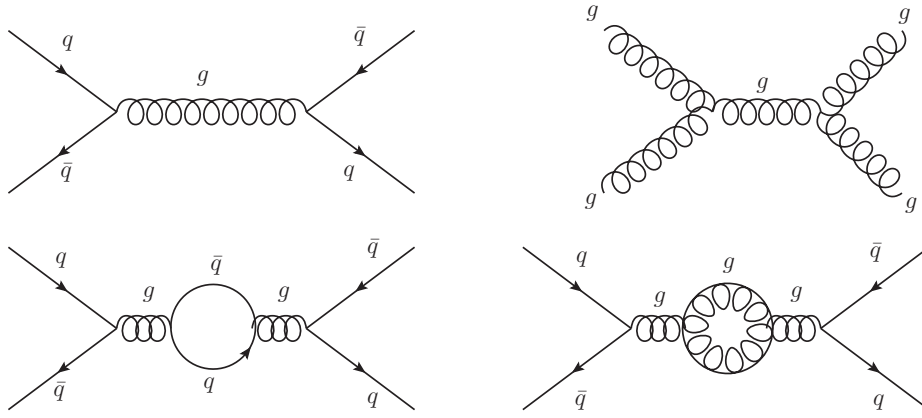


FIGURE 2.3: At the top two leading order QCD Feynman graphs are shown. On the top left side a  $q\bar{q} \rightarrow g \rightarrow q\bar{q}$  process and on the top right side an example for gluon gluon coupling. In the bottom left a NLO fermion loop correction and on bottom right a gluon loop correction is shown.

The  $Q^2$  dependency of  $\alpha_s$  can be expressed at LO by:

$$\alpha_s(Q^2) = \frac{\alpha_s(Q_0^2)}{1 - \frac{\beta_1 \alpha_s(Q_0^2)}{2\pi} \ln(Q^2/Q_0^2)}, \quad \beta_1 = \frac{2N_f - 33}{6}, \quad (2.17)$$

where  $Q_0$  stands for an energy scale where  $\alpha_s$  is known and  $N_f$  for the number of quarks with masses  $m_q^2 < Q^2$ . The  $\beta_1$  is the lowest order coefficient of the  $\beta$ -function which predicts the energy scale dependence of  $\alpha_s$  [40]. Equation 2.17 shows that  $\alpha_s$  decreases for large values of  $Q^2$ , which corresponds to small distances where it is possible to calculate observables perturbatively according to Equation 2.11. This behavior is called “asymptotic freedom”. For small values of  $Q^2$  (long distances) the coupling constant increases. In regions where  $\alpha_s$  is in the order of unity it is not possible to calculate observables as an expansion in powers of  $\alpha_s$ . The scale at which perturbative QCD is not possible anymore is called  $\Lambda_{QCD} \approx 220$  MeV. Measurements of  $\alpha_s(Q^2)$  at different energy scales  $Q$  are shown in Figure 2.4, which reflects the behavior from Equation 2.17.

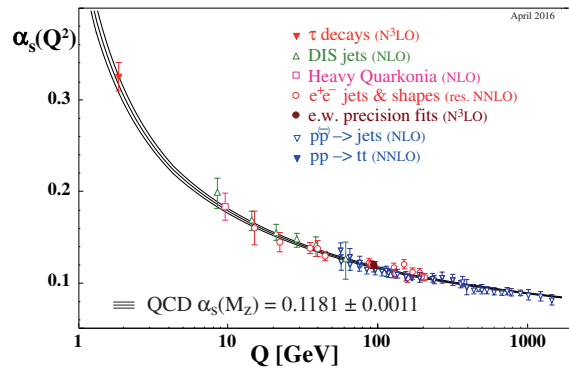


FIGURE 2.4: Measurements of  $\alpha_s(Q^2)$  at different energy scales  $Q$ . Figure is taken from [31].

---

A different way to think of this property of the QCD is by picturing a potential between a quark and an anti-quark in a meson. At small distances, corresponding to large  $Q^2$ , the quarks behave like two particles under the influence of a potential in the form of  $1/r$ . At larger distances the potential increases with  $r$ . With further increasing distance between the quarks, the energy of the field surrounding them gets so large that a new quark-antiquark is paired out of the vacuum, building new colorless bound states, which is called hadronization. This is the reason why no free quarks or gluons exist (at least none have been observed yet) which is called “confinement”. Even if a very high energetic parton (quark or gluon) is produced, for example at colliders, it starts to radiate additional gluons up a point where the energy scale is small and confinement occurs and hadrons are formed. These bundles of particles are called jets.

### 2.1.3 Electroweak interaction and symmetry breaking

The electromagnetic and weak interaction were treated at the beginning as two separate interactions. In 1967 Gashow, Salam and Weinberg [41] found a way to unify these two interactions into one: the electroweak interaction. In this unification new quantum numbers are introduced, the weak isospin ( $T$ ) and the weak hypercharge. Weak interactions preserve the third component of the isospin and only left-handed particles take part in weak interactions. The handedness is given by the chirality [42] which is for massless particle the projection of the spin to the momentum and therefore the same as the helicity. The left-handed fermions are grouped into isospin doublets with  $T = 1/2$  and  $T_3 = \pm 1/2$  and the right-handed into an isospin singlet with  $T = 0$  and  $T_3 = 0$ , which reflects that they do not undergo charged current interactions. A connection between the electromagnetic charge ( $Q$ ) and the third component of the weak isospin ( $T_3$ ) is done by introducing the weak hyper charge ( $Y$ ):

$$Y = 2(Q - T_3). \quad (2.18)$$

The underlying symmetry group of the electroweak interaction is a  $SU(2)_L \times U(1)_Y$  group [43]. The generators of the  $SU(2)_L$  group are the isospin operators  $T_i = \sigma_i/2$ , where  $\sigma_i$  are the Pauli matrices which can be associated with three bosonic vector fields  $W_\mu^a$ ,  $a = 1, 2, 3$ . The generator of the  $U(1)$  group is the hypercharge which can be associated with a singlet gauge field  $B_\mu$ . After requiring local gauge invariance, the Lagrangian can be formulated as:

$$\mathcal{L} = -\frac{1}{4}W_{\mu\nu}^a W^{\mu\nu,a} - \frac{1}{4}B_{\mu\nu}B^{\mu\nu} + \sum_j \bar{\psi}_j^L i\gamma^\mu D_\mu \psi_j^L + \sum_{j,\sigma} \bar{\psi}_{j\sigma}^R i\gamma^\mu D_\mu \psi_{j\sigma}^R, \quad (2.19)$$

where  $\psi^{L(R)}$  is the left- (right-) handed fermion field,  $j$  runs over the generations and  $\sigma$  is the component of the doublet (e.g. flavor in case of quarks).  $D_\mu$  is given by the covariant derivative:

$$D_\mu = \partial_\mu - ig_2 T_a W_\mu^a + ig_1 \frac{Y}{2} B_\mu, \quad (2.20)$$

which contains two coupling constants  $g_2$  and  $g_1$ . The vector fields  $W_\mu^a$ ,  $a = 1, 2, 3$  and  $B_\mu$  are contained in the field strength tensors  $W_{\mu\nu}^a$  and  $B_{\mu\nu}$ . The charged  $W$  bosons that where

introduced before in Table 2.1 are given by a linear combination of  $W_\mu^1$  and  $W_\mu^2$ :

$$W_\mu^\pm = \frac{1}{\sqrt{2}}(W_\mu^1 \mp iW_\mu^2). \quad (2.21)$$

A characteristic of the charged bosons is the possibility to change the quark flavor, also between generations. This behavior is described by the CKM-Matrix [31] formalism. The matrix elements of the CKM-Matrix hold the probabilities that a quark of flavor  $i$  transforms to a quark with flavor  $j$  by interacting via charged bosons. This is not possible for the neutral current, which is described by neutral bosons of the electroweak interaction. The unitary CKM-Matrix can be described with three mixing angles and one complex phase. This complex phase is the description of CP-violation of the weak interaction, which was first discovered in 1964 in the decay of neutral Kaons [44].

The neutral bosons,  $Z$  boson and photon, are connected to the electroweak vector fields via a matrix containing the weak mixing angle  $\theta_W$ :

$$\begin{pmatrix} Z_\mu \\ A_\mu \end{pmatrix} = \begin{pmatrix} \cos \theta_W & \sin \theta_W \\ -\sin \theta_W & \cos \theta_W \end{pmatrix} \begin{pmatrix} W_\mu^3 \\ B_\mu \end{pmatrix}. \quad (2.22)$$

The electroweak mixing angle can also be used to relate the electric charge with the electroweak coupling  $g_2$  via:

$$e = g_2 \cdot \sin \theta_W. \quad (2.23)$$

When replacing the vector fields  $W_\mu^a$  and  $B_\mu$  in the Lagrangian by  $Z_\mu$ ,  $A_\mu$  and the charged  $W^\pm$  bosons, terms appear that reflect self-interaction between bosons, which is expected by the non Abelian structure of  $SU(2)$ . Nevertheless there is no vertex with three or more neutral bosons included since the  $Z$  boson as well as the photon do not have any electromagnetic charge nor  $T_3 > 0$  and therefore can not interact with each other.

The requirement of local gauge invariance sets the masses of the weak gauge bosons to zero but in 1983 the  $W^\pm$  and  $Z$  boson had been discovered with non vanishing masses [15–18]. A solution to this problem is to spontaneously break the electroweak gauge symmetry by introducing a complex scalar doublet field, called Higgs doublet [45]:

$$\Phi(x) = \begin{pmatrix} \phi_+(x) \\ \phi_0(x) \end{pmatrix}. \quad (2.24)$$

The interaction of the Higgs bosons with the electroweak gauge bosons is described by the Lagrangian:

$$\mathcal{L}_H = (D_\mu \Phi)^\dagger (D^\mu \Phi) - V(\Phi), \quad (2.25)$$

with the Higgs potential:

$$V(\Phi) = -\mu^2 \Phi^\dagger \Phi + \frac{\lambda}{4} (\Phi^\dagger \Phi)^2, \quad \lambda > 0. \quad (2.26)$$

---

This potential, often quoted as “mexican hat” potential due to its functional form, is constructed in a way that  $\Phi$  has a degenerated ground state. When choosing the ground state to:

$$\langle \Phi \rangle = \frac{1}{\sqrt{2}} \begin{pmatrix} 0 \\ v \end{pmatrix} \text{ with } v = \frac{2\mu}{\sqrt{\lambda}}, \lambda > 0 \quad (2.27)$$

the  $SU(2) \times U(1)$  is spontaneously broken. After expanding  $\Phi$  around the vacuum expectation value,  $v$ , it follows:

$$\Phi(x) \approx \frac{1}{\sqrt{2}} \begin{pmatrix} 0 \\ v + H(x) \end{pmatrix}. \quad (2.28)$$

In this equation  $H(x)$  can be identified has the Higgs boson field with a mass of  $m_H = \mu\sqrt{2}$ . In July 2012 the Higgs boson was observed by ATLAS [19] and CMS [20]. The combined result for the mass is  $125.09 \pm 0.24$  GeV [46]. The three additional degrees of freedom of the Higgs doublet lead to the constrains on the mass terms of the electroweak gauge bosons:

$$m_\gamma = 0 \quad m_W = \frac{1}{2}vg_2 \quad (2.29)$$

$$m_z = \frac{1}{2}\sqrt{g_1^2 + g_2^2}v \quad (2.30)$$

and for the electroweak mixing angle it follows:

$$\cos \theta_W = \frac{M_W}{M_Z}. \quad (2.31)$$

This relation can be compared together with Equation 2.23 to results from experiments. The value of the mixing angle has been measured to  $\sin^2 \theta_W = 0.233 \pm 0.004(\text{exp.}) \pm 0.005(\text{theor.})$  [47], which is compatible with theory prediction. The Higgs mechanism can also be used to explain the masses of the fermions. The coupling of the fermions to the Higgs field is described by a Yukawa coupling [48].

## 2.2 $pp$ collisions

### 2.2.1 Phenomenology of $pp$ collisions

Quarks can not exist as free particles due to “confinement”, they form therefore color neutral hadrons, baryons and mesons. The only stable hadron that can exist freely is the proton<sup>7</sup>. In a quark model it consists of three so-called *valence quarks*: two u- and one d-quark. The valence quarks interact with each other through gluon exchange, whereas the gluons can convert to quark-antiquark pairs, which again annihilate into gluons. It is also possible that the gluons or the quarks radiate further gluons. The part of dynamical changing quarks is named *sea quarks*. Both parts, valence and sea together with the gluons are called partons.

The proton is therefore a very complex structure, but a good description of it is needed when analyzing proton-proton collisions. When the energy of the colliding hadrons is large enough,

---

<sup>7</sup>At least no proton decay was observed to far.

the collision can be inelastic which means that the structure of the proton is dissolved. The collision can be understood as a collision of partons from the proton. In Figure 2.5 a schematic view of such an interaction is shown. Two protons  $A$  and  $B$  contain two partons  $a$  and  $b$  which carry a momentum fraction  $x_a$  and  $x_b$ <sup>8</sup> of the proton. The probability to find partons with this momentum fraction is given by the parton distribution functions (PDF)  $f_{a/A}$  and  $f_{b/B}$ , respectively. The interaction between the two partons is called *hard process* and its cross section is given by  $\hat{\sigma}$  which is the part that can be calculated perturbatively.

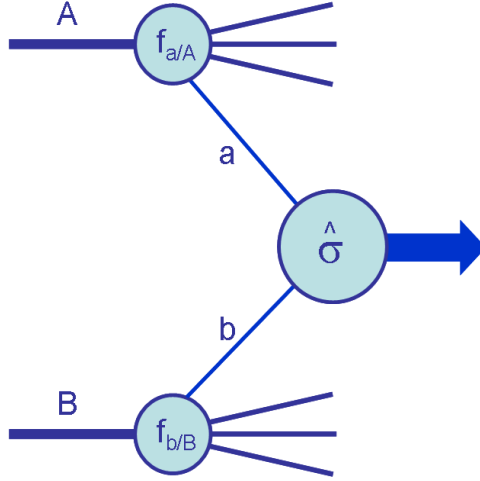


FIGURE 2.5: Schematic view of a pp-collision. The incoming protons are labeled with  $A$  and  $B$ . The parton distribution functions of the protons are given by  $f_{a/A}$  and  $f_{b/B}$ . The partons of the hard scattering process,  $a$  and  $b$ , interact with a cross section  $\hat{\sigma}$ . Figure is taken from [49].

In 1971 it was shown by S. Drell and T.-M. Yan in their factorization theorem [50] that it is possible to separate the cross section in a part from the hard interaction and one part from the PDFs, that can not be described perturbatively. The equation for a proton-proton cross section is therefore given by:

$$\sigma_{AB} = \sum_{a,b} \int dx_a \int dx_b f_{a/A}(x_a) f_{b/B}(x_b) \hat{\sigma}_{ab \rightarrow X}(x_a, x_b). \quad (2.32)$$

The remnants of the proton are left in color charged state since one parton of each proton takes place in the hard interaction and will therefore form colorless particles during hadronization. It is also possible that more than one hard interaction happens, which is then called multiple parton interaction. All these processes that are not part of the hard interaction are called *underlying event*. The complexity of proton-proton interactions is also a challenge when it comes to the simulation of those, which is discussed in more detail in Section 5.2.

---

<sup>8</sup> $x$  can be identified with Bjorken  $x$ .

## 2.2.2 Structure of the proton

The parton distribution functions describe the momentum distribution of the partons inside the proton and have therefore a dependence on the Bjorken variable  $x$ , but they also have a dependence on  $Q^2$ . This dependence can be understood by a better spatial resolution with higher  $Q^2$ . In Figure 2.6 a schematic picture is shown to demonstrate this effect. The substructure of the proton is not visible if the momentum transfer  $Q^2$  is smaller than a certain scale  $Q_{res}^2$ . With larger momentum the probability raises to resolve the vacuum polarizations which yields to changes of the PDF with  $Q^2$ .

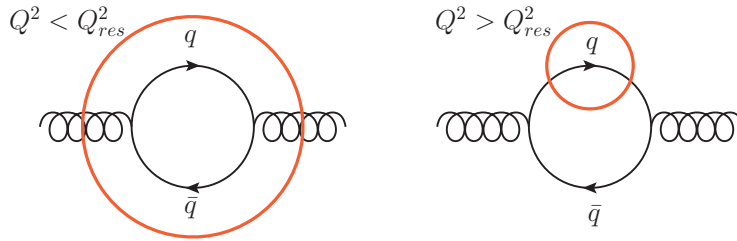


FIGURE 2.6: Schematic sketch of vacuum polarization inside the proton. The red circle indicates the resolution corresponding to a certain  $Q^2$ . On the left side of the figure the resolution is too small to resolve the quarks from the vacuum polarization, whereas on the right the  $Q^2$  is large enough to do so.

The resolving of further processes in the proton can also be interpreted as radiation of quarks or gluons before the parton takes place in the hard scattering. In Figure 2.7 a schematic view is shown, where a quark from a proton radiates a gluon before taking place in the hard interaction. When trying to calculate this process at leading order one gets a cross section that includes integrals in this form [51]:

$$\frac{\alpha_s}{2\pi} \int \frac{dk_{\perp}^2}{k_{\perp}^2} \int_x^1 \frac{dz}{z} P_{qq} \left( \frac{x}{z} \right) q(z), \quad (2.33)$$

where  $q(z)$  corresponds to a quark PDF and  $k_{\perp}$  corresponds to the projection of the gluon momentum to the quark momentum. The factor  $P_{qq}(x/z)$  is the so-called Altarelli-Parisi [52] splitting function which describes in this example the gluon emission from a quark. The whole term can be included into the PDF rather than the cross section of the hard interaction. The first integral diverges for small  $k_{\perp}$  or in other words collinear parton radiations create divergences. These divergences can be absorbed into a scale ( $\mu_F$ ) dependence of the PDF. The scale evolution of the parton distributions  $q_i$  and  $g$  is given by the DGLAP equations (Dokshitzer-Gribov-Lipatov-Altarelli-Parisi)

$$\frac{\partial q_i(x, \mu_F^2)}{\partial \log \mu_F^2} = \frac{\alpha_s}{2\pi} \int_x^1 \frac{dz}{z} \left\{ \sum_j P_{q_i q_j}(x/z) q_j(z, \mu_F^2) + P_{q_i g}(x/z) g(z, \mu_F^2) \right\} \quad (2.34)$$

$$\frac{\partial g(x, \mu_F^2)}{\partial \log \mu_F^2} = \frac{\alpha_s}{2\pi} \int_x^1 \frac{dz}{z} \left\{ \sum_j P_{g q_j}(x/z) q_j(z, \mu_F^2) + P_{g g}(x/z) g(z, \mu_F^2) \right\}, \quad (2.35)$$

where the sum iterates over all different quark flavors. The dependence on  $\mu_F$  vanishes when including all higher order corrections, but this is not possible. Currently the highest order, to which the splitting functions are calculated, is NNLO [53] which leads to a remaining  $\mu_F$

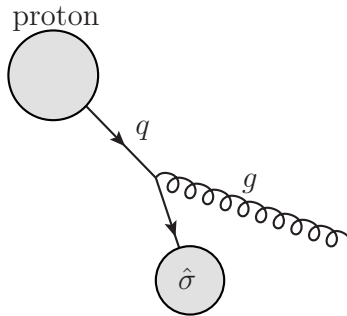


FIGURE 2.7: Schematic sketch of gluon radiation from a quark not as a part of the hard interaction process.

dependence of theory predictions. The choice of the factorization scale should be done in a way that the collinear (long-distance) physics is included in the PDF and the noncollinear (short-distance) physics in the hard scattering cross section. Often this choice is  $\mu_F^2 = Q^2$ , which corresponds to the momentum accessible in the hard interaction. Variations of this scale choice are then uncertainties that have to be taken into account.

**Determination of PDFs** It is not possible to predict the  $x$  dependency of PDFs. Therefore data is used to make a global fit including several free parameters. The principal is to start with a  $x$  dependent parameterization at a chosen  $Q_0^2$ , which is often in the order of 1-2 GeV<sup>2</sup><sup>9</sup>. This parameterization is then evolved to the  $Q^2$  scale where the measurement is done using the DGLAP equations and convoluted with the partonic cross section of the hard interaction. The perturbative order of the partonic cross section determines also the referred order of an PDF and should match the order of the DGLAP equations. This predicted cross section is then compared to measurements by calculating a  $\chi^2$ . The parameters are determined by minimizing the  $\chi^2$ . It is then possible to evolve the determined parameterization at  $Q_0^2$  to any  $Q^2$  using again the DGLAP equations. For the fitting, data from many different experiments over a large  $x$  and  $Q^2$  range is used. Precise measurements especially in the low  $x$  region were done by H1 [54] and ZEUS [55]. In higher  $x$  ranges fixed target experiments lead to precise measurements using data from deep inelastic scattering events (DIS) [56]. The parameterization of the  $x$  dependence can be done in different ways which leads to PDFs from different groups, which use different parameterizations, different fit techniques and also different data. Examples of those groups that provide PDFs are NNPDF 3.0 [57], CT10 [58] or MSTW [59].

The fit parameters of the parameterizations have also uncertainties for example due to the uncertainties of the measurements. It is not possible to propagate the uncertainties of the single parameters directly to the observables, like a cross section, since the parameters can be correlated. Therefore the fit parameters are transformed into an orthogonal eigen basis using a Hessian approach [60]. This makes it possible to vary each of the transformed parameters up and down within a value corresponding to either 68% C.L. or 90% C.L.<sup>10</sup>, which leads to a set of  $2n$  PDF variations for both confidence levels, where  $n$  is the number of uncertainty sources. The propagation of these variations to, for example, a cross section is then quoted as a PDF

<sup>9</sup>The starting scale should not be in the range where the measurements to which the fit is performed is done but above  $\Lambda_{QCD}$ .

<sup>10</sup>Confidence Level



uncertainty.

An example of PDFs at two different  $Q^2$  is shown in Figure 2.8 for PDFs from the CT10 group. In both cases the valence quarks dominate high  $x$  regions whereas for low  $x$  the sea part dominates. For higher  $Q^2$  the sea part is much higher compared to  $Q^2$  at 2 GeV which reflects the behavior of resolving more of the vacuum polarizations at small distances (high  $Q^2$ ).

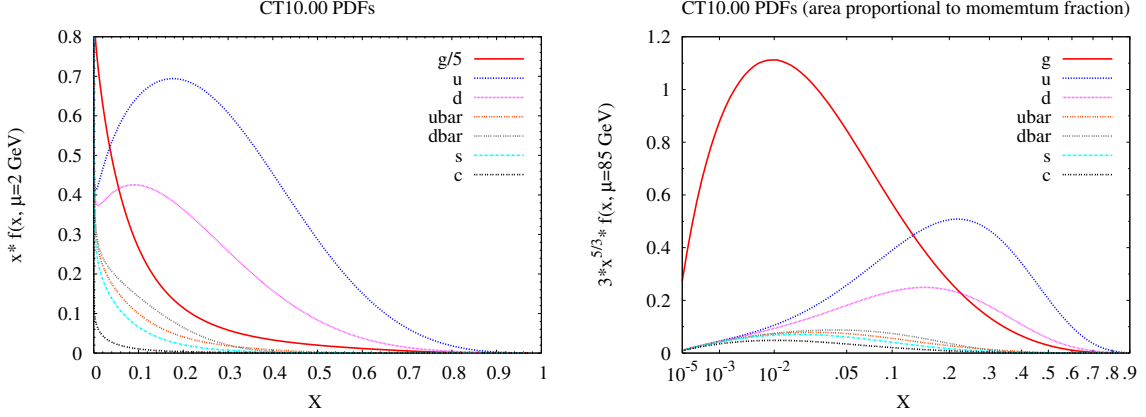


FIGURE 2.8: CT10 PDF times  $x$  (y-axis) as function of  $x$  (x-axis) for  $Q^2 = 2 \text{ GeV}$  on the left side and  $Q^2 = 85 \text{ GeV}$  on the right side. Plots taken from [58].

### 2.2.3 LHC kinematics

Most hard processes at the LHC are processes of two incoming partons with four momenta  $p_1$  and  $p_2$  and  $n$  outgoing particles with momenta  $p_3, \dots, p_n$ . A schematic sketch of this process is shown in Figure 2.9.

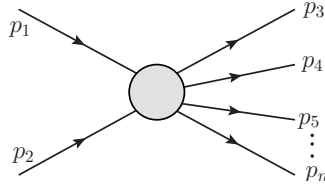


FIGURE 2.9: Schematic sketch of a process with two incoming partons, having a four momenta of  $p_1$  and  $p_2$  and  $n$  outgoing particles with momenta  $p_3, \dots, p_n$ .

The partonic center of mass energy ( $\hat{s}$ ) for such a process is given by:

$$\sqrt{\hat{s}} = \sqrt{(p_1 + p_2)^2} = \sqrt{(p_3 + \dots + p_n)^2}, \quad (2.36)$$

which is the same as the invariant mass ( $m_{inv}$ ) of the system when considering four momenta conservation. The partonic center of mass energy is connected to the center of mass energy ( $\sqrt{s}$ ) of the protons by:

$$\hat{s} = x_1 x_2 s. \quad (2.37)$$

Therefore the momenta of the incoming partons can be chosen to (assuming  $m_{parton} = 0$ ):

$$p_1 = \frac{\sqrt{s}}{2} \begin{pmatrix} x_1 \\ 0 \\ 0 \\ x_1 \end{pmatrix}, \quad p_2 = \frac{\sqrt{s}}{2} \begin{pmatrix} x_2 \\ 0 \\ 0 \\ -x_2 \end{pmatrix}. \quad (2.38)$$

This can be used to put into the definition of the rapidity  $y = \frac{1}{2} \log\left(\frac{E+p_z}{E-p_z}\right)$ , which yields to:

$$y = \frac{1}{2} \log\left(\frac{x_1}{x_2}\right). \quad (2.39)$$

This can be used to extract  $x_1$  and  $x_2$ :

$$x_1 = \frac{m_{inv}}{\sqrt{s}} e^y, \quad x_2 = \frac{m_{inv}}{\sqrt{s}} e^{-y}. \quad (2.40)$$

This relation shows that it is possible to probe different  $x$  when measuring the invariant mass, build from the four momenta of the outgoing particles and the rapidity of the system. In Figure 2.10 the relationship between  $x$  and  $Q^2$  for different masses and  $y$  is shown. It is shown that DIS experiments are able to reach lower  $Q^2$  compared to the LHC. The advantage of the LHC is the possibility to probe the region of high  $Q^2$ , especially above the  $Z$  boson mass which could be used, for example, to improve the understanding of PDFs.

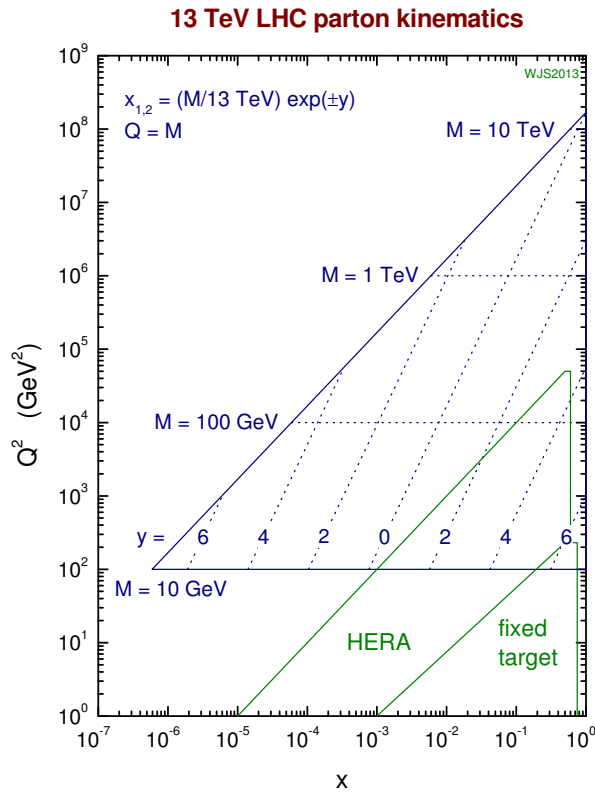


FIGURE 2.10: Schematic plot to illustrate the kinematic coverage of LHC with a center of mass proton energy of 13 TeV, HERA and fix target experiments. Shown is the  $x, Q^2$  plane together with different invariant masses and correspondent rapidity ( $y$ ) values. The plots is taken from [61].

## 2.2.4 $Z$ boson pair production at the LHC

At the LHC the main diboson production channel is a  $q\bar{q}$  initiated process. For  $ZZ$  production this is only the t- and u-channel since a s-channel would imply a vertex with three neutral gauge bosons, which is not allowed in the Standard Model at leading order. For other diboson production like  $WZ$  or  $W^+W^-$  the s-channel exists due to the non Abelian structure of the electroweak symmetry group. In Figure 2.11 the main leading order SM Feynman diagrams for  $ZZ$  production are shown. Besides of the  $q\bar{q}$  initiated process there is the  $gg$  induced process via a fermion loop, which contributes roughly 10% to the total cross section. The electroweak production of  $ZZ$  in association with jets is shown in (c) and (d) of the figure. These processes are suppressed due to being a higher order electroweak process. The masses of  $Z$  bosons make it possible for a Higgs boson to couple to them, which is also shown in the figure. This was also one of the first Higgs decay channels where the observation of the particle was done [19].

About half of the  $ZZ$  events decay hadronically but, in experiments, often only the decay

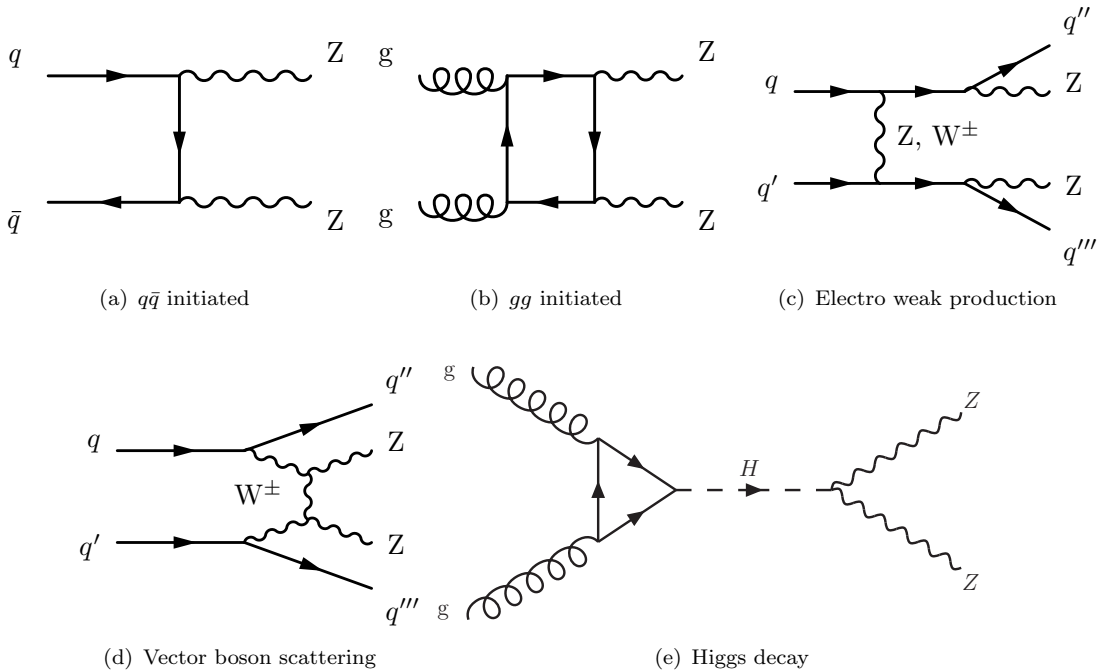


FIGURE 2.11: Example diagrams for  $ZZ$  production at the LHC. Figure (a)-(d) are taken from [62].

into electrons and muons is chosen. Only 0.5% [31] of the  $ZZ$  events decay into this final state. The main reason to choose this channel is the small expected background, which makes the experimental analysis much easier. Also electrons and muons are objects easy to detect, compared to neutrinos which evade most detectors undetected or jets where the energy resolution is bad compared to those from electrons or muons.

In Figure 2.12 a simulated differential cross section as function of the invariant mass of the four leptons ( $m_{4\ell}$ )<sup>11</sup> is shown. The simulations are based on SHERPA [63, 64], which is explained in more detail in Chapter 5<sup>12</sup>. It can be seen that the largest contribution is given by the  $q\bar{q}$

<sup>11</sup> $\tau$  leptons are excluded.

<sup>12</sup>During generation of simulated events small phase space restrictions are already applied which is also explained in Chapter 5.

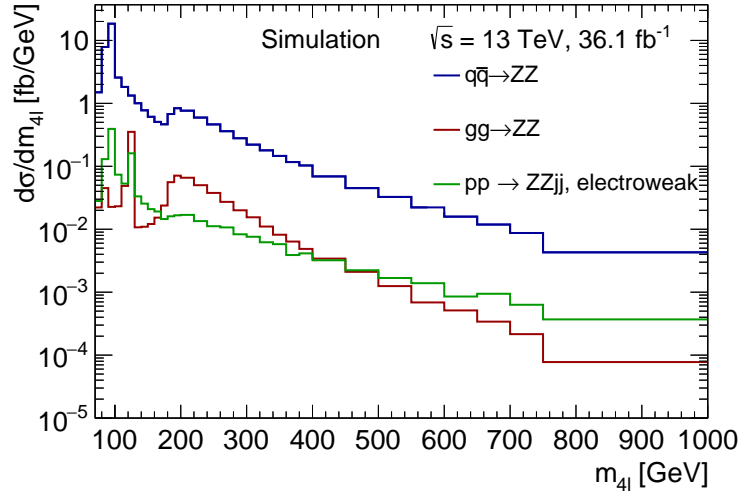


FIGURE 2.12: Expected differential cross section as function of the invariant mass of four leptons  $m_{4\ell}$ . The simulations are done with SHERPA [63, 64].

initiated process. The shape of the distribution show a resonance at about 90 GeV which is caused by single  $Z$  production with a radiated  $Z$  from a lepton. A Feynman diagram for such a process is shown in Figure 2.13. At about 125 GeV the resonance of the Higgs boson is visible in the  $gg$  induced process and in the electroweak  $ZZjj$  production which both contain Higgs related production. At about 182 GeV, two times the  $Z$  pole mass, the cross section has a sharp raising edge since it is at this point kinematically possible to produce two on shell  $Z$  bosons. Towards higher  $m_{4\ell}$  the cross section decreases but the slope for the electroweak  $ZZjj$  production is different which shows possible higher sensitivity to this process at high masses. In this thesis only the production of two on-shell  $Z$  bosons is considered which suppresses most contributions from Higgs and  $Z \rightarrow \ell^+ \ell^- \ell'^+ \ell'^-$ .

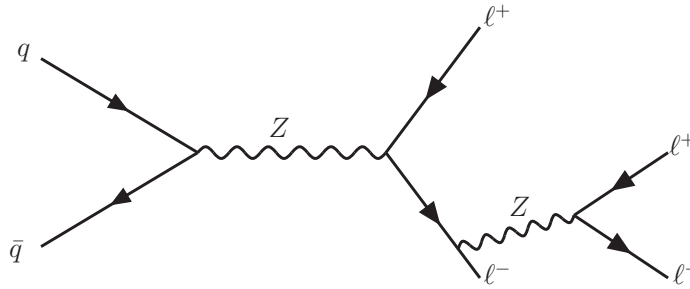


FIGURE 2.13: Leading order Feynman diagram for  $Z \rightarrow \ell^+ \ell^- \ell'^+ \ell'^-$  through radiation of a further  $Z$  boson from decay products of the initial  $Z$  boson.

---

## 2.3 Physics beyond the Standard Model

### 2.3.1 Limitations of the Standard Model

The Standard Model is one of the best theories in physics. Many observations of the last decades were done based on the structure of the Standard Model, for example the Higgs or top-quark discovery. Also testing the precession of the Standard Model predictions shows good agreement between experiment and theory. One example is the magnetic moment of the electron which is measured up to the 10 decimal place and in agreement with the prediction [65, 66]. But there are some limitations to the Standard Model that are listed in the following.

The neutrinos are considered massless in the Standard Model, but the observation of neutrino oscillation showed that they have a mass. A naive inclusion of mass terms of neutrinos would result in a right-handed spinor if it is assumed that neutrinos are Dirac particles. The right-handed neutrinos would not be seen from any of the three interactions described by the Standard Model which seems unsatisfactory. In addition it is not clear why the masses of the neutrinos are so much smaller than the masses of other leptons.

Another problem that can not be described with the Standard Model is the current matter-antimatter asymmetry. In the Big Bang, matter and antimatter should have been created in almost the same amount, but today we live in world where matter dominates. The CP violation that is included in the Standard Model can explain the asymmetry to some extent but this is by far not enough to explain the observed asymmetry. Therefore additional CP violation is needed which is beyond the Standard Model.

Furthermore the Standard Model can not explain the question of different scales of the interaction. The weak force is, for example,  $10^{24}$  times as strong as gravity. Technically the question about this hierarchy problem is the question of the small size of the Higgs mass. In the Standard Model the effective Higgs mass gets correction with  $\mathcal{O}(\Lambda^2)$  via loop processes of heavy quarks, where  $\Lambda$  is the energy scale up to which the Standard Model is valid. When it is considered that it is valid over a very large energy range, the mass would be tremendously much larger as it is observed. In order to get to the observed mass the bare mass of the Higgs boson must be extremely fine tuned so that it cancels out most of these corrections. This fine-tuning of parameters seems very unnatural and can not be explained by the Standard Model.

The visible amount of matter in the universe is also a problem that leads to questions which can not be solved by the Standard Model. Measurements of the rotation velocity of luminous matter in galaxies as function of the distance from the galactic center showed a rather constant behavior from a certain distance on [67]. This contradicts the expectation that the velocity should decrease further away from the center. A solution to this problem would be another kind of matter that exists besides of the visible one. The existence of so-called dark matter is supported by many other observations from astrophysical experiments, for example measurements of the cosmic microwave background [21] or observations of gravitational lensing [68]. It is expected that dark matter has a very weak interaction with other matter otherwise it would have been observed. This makes neutrinos the only explanation that is given within the Standard Model but it was shown that neutrinos can only account only for a very small fraction of dark matter. Recent results from measurements of the cosmic microwave background [69] showed that the universe consists only to 5% of ordinary matter, 27% are dark matter and 68% dark energy. Dark energy is so far very little understood. It is an idea to explain the observation that the

universe expansion is accelerating for which some kind of (dark) energy is necessary. There are different ways to search for effects of physics beyond the standard model. One way is by building a concrete theory that predicts new particles which can be searched for experimentally. One popular theory of this kind is Supersymmetry (SUSY) [70] which relates bosons and fermions and gives solutions for most of the above problems. In this theory each particle is associated with a supersymmetric partner. These supersymmetric partners are predicted to be in the energy range of electroweak symmetry breaking ( $\mathcal{O}(100)$  GeV). It is possible to search for such particles for example at colliders. So far no SUSY particles have been found but it is possible to tune parameters of the theory in such a way that the scale of the SUSY particles is higher and not yet reached in experiments. Therefore it seems like even with SUSY some fine tuning is needed.

Another way to look for new physics is the interaction between Standard Model particles in a novel way, for example the interaction of three neutral gauge bosons which is discussed in the next section.

### 2.3.2 Anomalous triple gauge couplings

The non Abelian structure of the Standard Model allows for self-coupling between gauge bosons as it was explained in Section 2.1.3. For neutral gauge bosons a vertex, like it is shown in Figure 2.14 is forbidden, but it is possible to search for such couplings when analyzing multiboson final states. There are different approaches to parameterize such couplings. Two common approaches are discussed in the following.

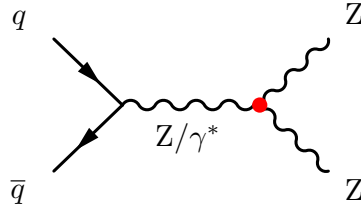


FIGURE 2.14:  $ZZ$  production via s-channel which is forbidden in Standard Model.

A general parametrization of the  $Z(q_1)Z(q_2)V(P)$  vertex with  $V = Z, \gamma$ , where  $q_1, q_2, P$  stands for the momenta of the particles, is given by [71]:

$$g_{ZZV}\Gamma_{ZZV}^{\alpha\beta\mu} = e \frac{P^2 - m_V^2}{m_Z^2} \left[ i f_4^V (P^\alpha g^{\mu\beta} + P^\beta g^{\mu\alpha}) + i f_5^V \epsilon^{\mu\alpha\beta\rho} (q_1 - q_2)_\rho \right]. \quad (2.41)$$

Here two dimensionless complex couplings  $f_4^V$  and  $f_5^V$  with dependence on  $q_1, q_2, P$  are introduced. The couplings  $f_4^V$  violate CP symmetry whereas  $f_5^V$  conserve it. In the SM at LO both couplings are zero<sup>13</sup>. The term  $P^2 - m_V^2$  leads to a statically increasing cross section with higher parton cross sections  $\sqrt{\hat{s}}$  which would lead to violation of unitarity at higher energies. In order to restore unitarity, a  $\sqrt{\hat{s}}$  dependence of the couplings is introduced by using a generalized form

<sup>13</sup>When taking higher order fermion loop corrections into account the CP conserving couplings get contributions that are in the order of  $\mathcal{O}(10^{-4})$ .

factor approach [72]:

$$f_i^V(\hat{s}) = \frac{f_{i0}^V}{(1 + \hat{s}/\Lambda_{FF}^2)^n} \quad i = 4, 5, \quad (2.42)$$

where  $\Lambda_{FF}$  corresponds to an arbitrary scale related to new physics which generates the anomalous  $ZZV$  couplings. The power of the form factor  $n$  has to be larger than  $3/2$  to fulfill unitarity [73]. Still, there is a choice dependency on  $n$  and  $\Lambda_{FF}$  which makes it difficult to compare results from different experiments when different parameters are chosen. Therefore a choice often made is to set  $\Lambda_{FF}$  to infinity (or  $n = 0$ ) in order to get results for  $f_{i0}^V$  which can be compared better. This choice is also made in this analysis unless claimed otherwise.

The typical signature of anomalous triple gauge couplings (aTGCs) are enhancements in tails of distributions that are sensitive to  $\hat{s}$ , which is for example the invariant mass of a system. When calculating these contributions, linear and quadratic terms in  $f_i^V$  appear, but due to the CP violating properties of  $f_4^V$  the linear terms, which reflect SM interference, vanish. Therefore it is not possible to distinguish between the positive and negative sign of  $f_4^V$ . For  $f_5^V$  it is expected that observables show differences for different signs but the linear terms that contain the interference grow only with  $(\sqrt{\hat{s}}/M_Z)^3$  whereas the quadratic terms grow with  $(\hat{s}/M_Z^2)^3$  which leads to very small interference effects for energies where the LHC operates [73]. Possible differences between  $f_i^Z$  and  $f_i^\gamma$  are controlled by the couplings of the  $Z$  or  $\gamma$  propagator to the initial partons which means that the sensitivity to aTGC parameter can be different for a lepton collider compared to a hadron collider.

There is a more modern approach to describe anomalous couplings: Effective field theories [74]. In this approach the SM is treated as the most general theory of quark, lepton and Higgs fields that interact via  $SU(3)_C \times SU(2)_L \times U(1)_Y$  gauge symmetry. The operators, which are the product of fields, have in the SM a mass dimension of four or less. The SM Lagrangian is then extended by adding operators of higher dimension which can be written as:

$$\mathcal{L} = \mathcal{L}_{SM} + \sum_{d>4} \sum_i \frac{C_i}{\Lambda^{d-4}} \mathcal{O}_i^d, \quad (2.43)$$

where  $d$  is the dimension<sup>14</sup> of operator  $\mathcal{O}_i^d$ ,  $\Lambda$  the mass scale of new physics and  $C_i$  a measure of the coupling strength of new physics to the SM. An advantage of such a generic approach is that no specific assumption about the new physics have to be done. It could be anything, for example new particles, extra spacetime dimensions or even non ordinary quantum field theories like string theory. The EFT approach describes the interaction of “low” energy particles of the SM with new physics that lives at mass scales of  $\Lambda$ , where “low” means the experimental reachable energies especially smaller than  $\Lambda$ . A great advantage of this approach compared to the before described vertex function approach is that it is not needed to introduce an arbitrary scale to ensure unitarity. Here the unitarity is automatically given due to terms in the amplitude that grow with  $\hat{s}/\Lambda^{d-4}$  at least for  $\hat{s} < \Lambda$ , but this is given by construction.

The first non vanishing higher order operators besides the SM one are dimension six operators that describe the self interaction of electroweak gauge bosons beyond SM with charged bosons. The first neutral triple gauge boson ( $nTGC$ ) couplings are described by dimension

<sup>14</sup>Only even dimensions are allowed, when lepton and baryon number conservation is considered [74].

---

eight operators. The EFT Lagrangian can be written as [75]:

$$\mathcal{L}^{nTGC} = \mathcal{L}_{SM} + \sum_i \frac{C_i}{\Lambda^4} (\mathcal{O}_i + \mathcal{O}_i^\dagger), \quad (2.44)$$

where  $\mathcal{O}_i^\dagger$  is the complex conjugate and transposed of the operator  $\mathcal{O}_i$ . There are four different operators describing the interaction that come with four coefficients:  $\frac{C_{WW}}{\Lambda^4}$ ,  $\frac{C_{BW}}{\Lambda^4}$ ,  $\frac{C_{BB}}{\Lambda^4}$ ,  $\frac{C_{\tilde{B}W}}{\Lambda^4}$ . A detailed description of the mathematical form of the operators and a description of the transformation of the EFT parameter  $\frac{C_i}{\Lambda^4}$  to the vertex function parameter  $f_i^V$  can be found in [75].

It had been searched for aTGCs also at other experiments before e.g. at the Large Electron-Positron Collider (LEP). Also LHC data from collisions below  $\sqrt{s} = 13$  TeV was used to find evidence for aTGCs. So far no significant differences between Standard Model predictions and data was found. Therefore different exclusion limits on the couplings had been set which are presented together with the results of this analysis in Chapter 9.



## Chapter 3

# The LHC and the ATLAS experiment

This chapter gives an overview of the Large Hadron Collider (LHC) and the ATLAS<sup>1</sup> experiment. The first section focuses on the design and performance of the LHC. In the next section a summarizing description of the ATLAS experiment with each of its components, relevant for this analysis, is presented.

### 3.1 The LHC

The Large Hadron Collider [76] is a hadron-hadron collider constructed at CERN<sup>2</sup> in Geneva (Switzerland). It is designed to reach very high center of mass energies and high luminosities in order to search for new physics or do precise measurements of Standard Model processes in phase spaces that could not be probed before. It can operate in two setups, proton beams or heavy ion beams. It was initially designed to reach proton beam energies up to 7 TeV and luminosities up to  $10^{34} \text{ cm}^{-2}\text{s}^{-1}$ . The LHC currently is the particle accelerator with the highest ever reached center of mass energy of  $\sqrt{s} = 13 \text{ TeV}$ .

#### 3.1.1 Design of the LHC

It is not possible to directly accelerate particles with one collider to such high energies like they are at the LHC. Several pre-accelerators are needed before the protons can be filled into the LHC. In Figure 3.1 a schematic view of the accelerator complex is given, including all the pre-accelerators. Together with the maximum beam energy also the year of the initial startup and the circumference of the individual pre-accelerators are shown. The initial acceleration is done by Linac 2, a linear accelerator, where ionized hydrogen is filled in. On a length of 33 m the protons are accelerated in bunches to 50 MeV. After that the protons run through a chain

---

<sup>1</sup>A Toroidal Lhc ApparatuS

<sup>2</sup>Conseil Européen pour la Recherche Nucléaire

of further accelerators: the Booster, the Proton Synchrotron (PS) and the Super Proton Synchrotron (SPS) after which they reach an energy of 450 GeV and are filled into the LHC. The filling is done in a clockwise and counterclockwise direction. In the LHC the beams are further accelerated to energies of up to 6.5 TeV per beam<sup>3</sup>.

The LHC itself is build in a 27 km long tunnel which is up to 175 m below the surface. The tunnel was used before by the LEP<sup>4</sup>. The acceleration itself is done by eight super conducting radiofrequency cavities. In order to keep the proton bunches on a circular track, 1232 superconducting dipole magnets are integrated in the accelerator ring. The magnets are cooled down to about 1.9 K and reach a magnetic field strength of up to 8.3 T. The orientation of the magnetic field is in opposite direction to the two beam pipes, since the bunches in the pipes are orbiting in opposite directions. The focusing of the beams is done by 392 quadrupole magnets and beams are brought to collision at four interaction points where the experiments are stationed.

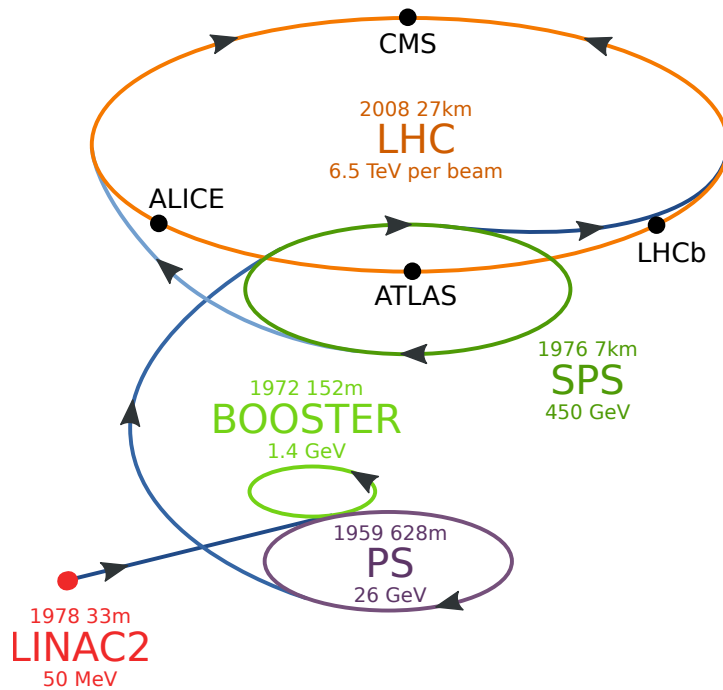


FIGURE 3.1: Schematic view of the LHC acceleration complex. The maximum beam energy is shown together with the year of the initial startup and the circumference of the individual accelerator. The figure is taken from [77].

### 3.1.2 Performance of the LHC

The beam energy is one aspect of an accelerator, but it is also important to get a high rate of collisions in order to get optimized data gathering per time. A variable that directly connects the rate ( $R$ ) with the cross section ( $\sigma$ ) of a physical process is the instantaneous luminosity ( $\mathcal{L}$ ):  $R = \mathcal{L} \cdot \sigma$ . It can be defined as:

$$\mathcal{L} = \frac{N_p^2 n_b f_r \gamma}{4\pi \epsilon_n \beta^*} F, \quad (3.1)$$

<sup>3</sup>The initial design was to reach up to 7 TeV per beam, but that was not yet reached.

<sup>4</sup>Large Electron Positron collider

where  $N_p$  is the number of protons in a bunch,  $n_b$  the number of colliding bunches per proton beam,  $\gamma$  the relativistic  $\gamma$ -factor and  $f_r$  the revolution frequency which for the LHC is about 11.2 kHz. The transverse emittance  $\epsilon_n$  and  $\beta^*$ , which is the beta function at the interaction point, describe the brightness of the beam. At the interaction points the beams are brought to collision with a small crossing angle which is reflected by the geometrical factor  $F$ . In Table 3.1 the parameters are listed which were reached during the 2015 and 2016 operation of the LHC. In 2015 the bunch spacing was decreased to 25 ns for the first time which brings the number of bunches very near to the design value. The emittance and  $\beta^*$  in 2015 were significantly lower than 2016 and especially lower than the design values which results in a peak luminosity below the design value. In 2016 these parameters could be improved and for the first time the LHC reached the design peak luminosity.

In 2015 an integrated luminosity of  $\mathcal{L}_{int} = \int \mathcal{L} dt = 4.2 \text{ fb}^{-1}$  had been delivered by the LHC in

Year	$E_{Beam}$ [TeV]	$N_p$	$n_b$	$\epsilon_n$ [ $\mu\text{m}$ ]	$\beta^*$ [cm]	Bunch spacing [ns]	Peak luminosity [ $\text{cm}^{-2}\text{s}^{-1}$ ]
2015	6.5	$1.15 \times 10^{11}$	2244	3.5	80	25	$5.0 \times 10^{33}$
2016	6.5	$1.15 \times 10^{11}$	2220	2.0	40	25	$1.4 \times 10^{34}$
Design	7	$1.15 \times 10^{11}$	2808	3.75	55	25	$1.0 \times 10^{34}$

TABLE 3.1: LHC parameters during the 2015 and 2016 operation [78, 79] together with the design values.

a data taking period between May and November. A lot of time in that year had been used for development and commissioning to optimize settings for running with  $\sqrt{s} = 13 \text{ TeV}$  and 25 ns bunch spacing. In 2016 the development and commissioning paid off by having a total delivered luminosity of  $38.5 \text{ fb}^{-1}$ .

### 3.1.3 LHC experiments

The beams are brought to collisions at four interaction points where the four large LHC experiments are located: ATLAS [80], CMS<sup>5</sup> [81], LHCb [82] and ALICE<sup>6</sup>. ATLAS and CMS are two general purpose detectors which are designed to cover a large range of physics measurements and searches for physics beyond the Standard Model, based on proton-proton and heavy ion collisions. LHCb focuses on physics where bottom quarks are involved. The ALICE experiment is designed specially to investigate heavy nuclei collisions.

There are also further, smaller experiments around the LHC. One of them is the TOTEM [83] experiment which focuses on detecting elastic proton-proton scattering which happens at the CMS interaction point. That is why it is build very near to the beam pipe, close to the CMS experiment. Another experiment is LHCf (LHC-forward) [84] which is installed 140 m away from ATLAS. It is mostly designed to study neutral pions. This can be used to test simulation models for proton air showering which are for example used in simulations of the cosmic rays in the earth atmosphere. Also to mention is the MoEDAL<sup>7</sup> experiment [85] which is build

<sup>5</sup>Compact Muon Solenoid

<sup>6</sup>A Large Ion Colliding Experiment

<sup>7</sup>Monopole and Exotics Detector at the Lhc

near LHCb and designed to search for highly ionizing avatars of new physics such as magnetic monopoles.

## 3.2 The ATLAS experiment

The ATLAS experiment is one of the four large experiments at the LHC. It is a general purpose detector to precisely measure electrons, photons, muons,  $\tau$ -leptons and jets in a large kinematic range. A schematic sketch of the experiment where its individual components are visible is shown in Figure 3.2. In the following the components are explained in more detail. Also the coordinate system is introduced together with common kinematic variables.

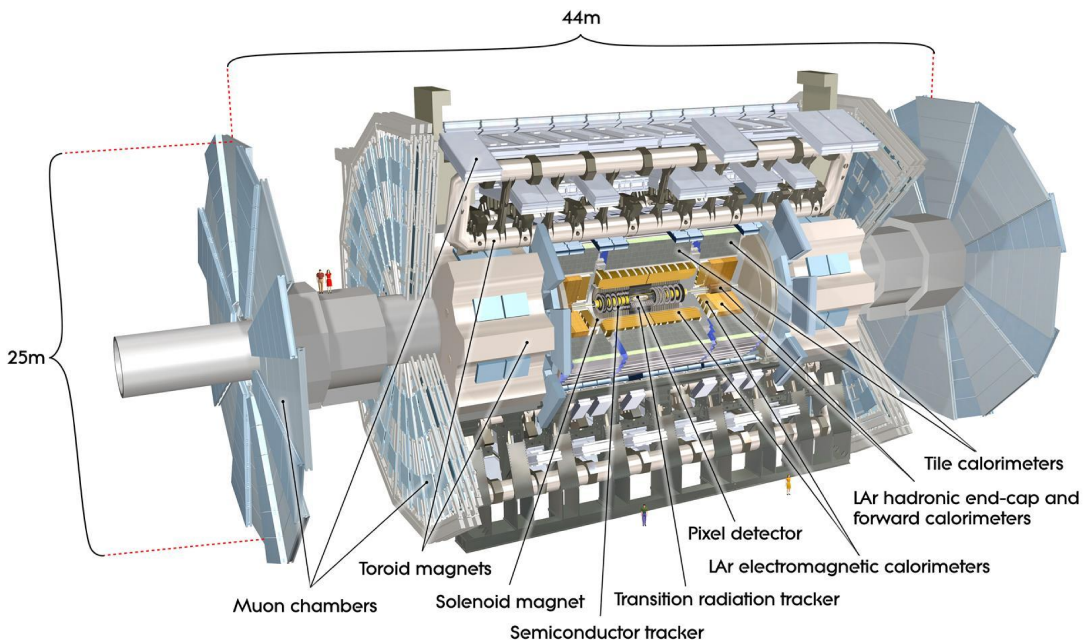


FIGURE 3.2: Cut-away view of the ATLAS experiment. The different components are marked in different colors. It is about 25 m high and 44 m long and weights 7000 t. The figure is taken from [80].

### 3.2.1 Coordinate system and common kinematic variables

At ATLAS a right handed Cartesian coordinate system with origin at the nominal interaction point is used. The  $x$ -axis points towards the LHC center, the  $y$ -axis in the direction of the surface and the  $z$ -axis counterclockwise along the beam axis. In polar coordinates the azimuthal angle  $\phi$  is defined around the beam axis in the  $x - y$  plane ranging from  $-\pi$  to  $\pi$  with  $\phi = 0$  pointing in direction of the  $x$ -axis. In most cases the polar angle  $\theta$  is replaced by the pseudorapidity  $\eta$  which is given by  $\eta = -\ln(\tan(\theta/2))$ . Pseudorapidity differences are, in contrast to differences in  $\theta$ , invariant under Lorentz transformation which makes it a better variable to express angle differences, since it is independent of the choice of the inertial system.

---

The rapidity of a particle, which is a measure of a particles boost along the beam axis, can be given in ATLAS coordinates as:

$$y = \frac{1}{2} \ln \left( \frac{E + p_z}{E - p_z} \right), \quad (3.2)$$

where  $E$  is the energy of a particle and  $p_z$  the momentum along the beam axis. For massless particles it is the same as the pseudorapidity, which for most final state particles at LHC energies is a good approximation. Energies and momenta are often given in the transverse plane, since in this plane it is possible to use momentum conservation. The vectorial sum of all outgoing particles should compensate to zero in the transversal plane since the transversal component of the initial partons of the proton have, to first approximation, no transverse momentum.

Distances in the  $\eta, \phi$  plane are often given by the variable  $\Delta R$  which is defined as:

$$\Delta R = \sqrt{\Delta\eta^2 + \Delta\phi^2}. \quad (3.3)$$

### 3.2.2 Design principle

The ATLAS detector is built shell-like around the beam axis, where each component has a different purpose to measure the momentum, energy or direction of the produced particles.

The innermost part is the inner detector (ID) which consists of three subsystems, the pixel detector, followed by the Semi Conductor Tracker (SCT) and the Transition Radiation Tracker (TRT). The main purpose of the ID, which has a coverage of up to  $|\eta| = 2.5$ , is the precise measuring of tracks. This is achieved by a solenoidal magnet that produces a 2 T strong magnet field that bends the trajectories of charged particles in the transversal plane which is used to extract the transverse momentum. The innermost layer of the pixel detector, the *Insertable b-layer* had been assembled in a long shutdown between 2012 and 2015. More details of the ID are given in Section 3.2.3.

The next subdetector in radial direction is the calorimeter system. It is build out of two main components, the electromagnetic liquid argon (LAr) sampling calorimeter with a full  $\phi$  coverage and  $|\eta|$  coverage up to 3.2 and the hadronic calorimeter. The hadronic calorimeter consists of a *scintillator tile* calorimeter in regions up to  $|\eta| = 1.7$  and also a LAr calorimeter for the endcap ( $1.5 < |\eta| < 3.2$ ) regions. The forward region ( $3.2 < |\eta| < 4.9$ ) is also covered by a LAr calorimeter measuring both, electromagnetic and hadronic objects. A detailed description of the calorimeter is given in Section 3.2.4.

The outermost part of the ATLAS experiment is the muon spectrometer (MS) which contains tracking chambers and a toroid system, built out of a long barrel and two endcap magnets. The toroid magnets have an air-core and generate a strong magnetic field over a large volume to bend the tracks of the muons and make their momentum measurement more precise. The tracking chambers are organized in three layers and cover regions of  $|\eta| < 2.7$ . The muon system also contains trigger chambers that range up to  $|\eta| < 2.4$ . More detailed information of the MS is given in Section 3.2.5.

The rate of  $pp$  collisions is about 1 GHz, considering a design luminosity of about  $\mathcal{L} = 10^{34} \text{ cm}^{-2}\text{s}^{-1}$ , but it is only possible to record events with a rate of about 1 kHz. This reduction of event rate is obtained by a two level trigger system. The first stage is a hardware based trigger that only uses reduced detector information and decides which events are interesting to keep based on this information. The rate of about 100 kHz after the first stage is reduced

further with a software based trigger to the needed order of event rate.

CMS and ATLAS are both built to measure mostly the same physical processes, but there are some differences in the construction of the experiments. One main difference is the magnet system. CMS only uses a single solenoidal magnet with a strength of 3.8 T which is achieved by the usage of an iron return yoke. This higher magnetic field strength results in a better momentum resolution for the tracking system compared to ATLAS. Although ATLAS can compensate this to some extent by having a second magnet. Another difference is the electromagnetic calorimeter where CMS has a homogeneous calorimeter built from crystals of lead tungstate which is not a sampling calorimeter like the one from ATLAS.

### 3.2.3 Tracking system

It is essential for a tracking system to have a high momentum and vertex resolution. Since the track density at ATLAS is very high, a fine granularity is needed. The tracking system or inner detector [86] consists of three sub-components: The pixel detector, the Semi Conductor Tracker (SCT) and the Transition Radiation Tracker (TRT). In Figure 3.3 on the left side an overview of the inner detector is given. The right side of the figure shows a cut-out view of the inner detector with its individual components. The solenoid magnet, which generates the magnetic field to bend the tracks for momentum measurements, is 5.3 m long and has a diameter of 2.5 m. The relative momentum resolution of the ID is  $\sigma_{p_T}/p_T \approx 0.05\% p_T [\text{GeV}] \oplus 1\%$ , where the first term reflects the difficulty to measure the momentum if the track is less bent due to higher  $p_T$ . The second term describes a constant term due to electronic noise and  $\oplus$  symbolizes the quadratic sum of both terms. In the following the several sub-components are explained in more detail.

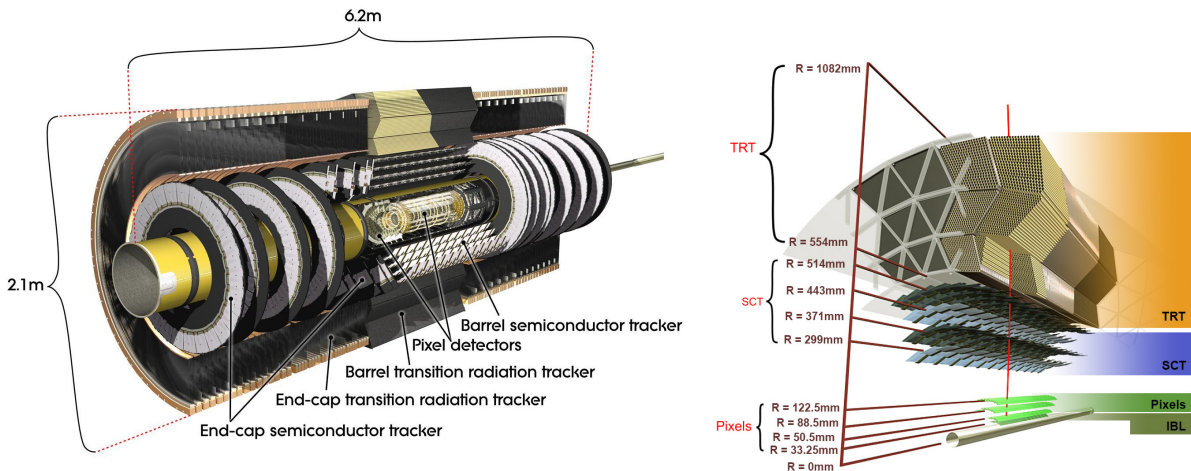


FIGURE 3.3: The left part of the figure, taken from [80], shows a cut-away view of the ATLAS inner detector. The right side, taken from [87], shows the schematic view of the components in the  $r - \phi$  plane.

**Pixel detector** The pixel detector [88] consists of four layers in the barrel region and three layers in the endcap region. It allows track measurement in a pseudorapidity range of  $|\eta| < 2.5$ . The silicon pixel modules in the barrel region are cylindrical mounted around the beam axis,



---

whereas in the endcap region three discs, mounted perpendicular to the beam axis, are used. The fine granularity of the pixel detector allows high resolution track measurement and reconstruction of the interaction point and secondary vertices from decays of long-lived particles. The IBL [89] is placed 33.25 mm away from the beam axis. Its main purpose is the improvement of the reconstruction of secondary vertices. The pixel modules of the IBL have a size of  $50 \mu\text{m} \times 250 \mu\text{m}$  whereas the other layers have a larger pixel size of  $50 \mu\text{m} \times 400 \mu\text{m}$ . The position resolution of the pixel detector is  $10 \mu\text{m}$  in the  $r - \phi$  plane,  $115 \mu\text{m}$  in  $z$  for central regions and  $115 \mu\text{m}$  in  $r$  for endcap regions.

**Semi Conductor Tracker (SCT)** Between 299 mm and 514 mm away from the beam axis the second layer of the ID is installed, the SCT. It covers a region of  $|\eta| < 2.5$  and is built out of silicon microstrips. In central regions the strips are orientated parallel to the beam axis to measure the  $r - \phi$  position. There are also stereo strips which are arranged with a small angle relative to the beam axis to be able to measure both coordinates. In the endcap region radially orientated strips are used. The spacial precision that is reached in the central region is  $17 \mu\text{m}$  in the  $r - \phi$  plane and  $580 \mu\text{m}$  in  $z$ .

**Transition Radiation Tracker (TRT)** The TRT is built out of straw tubes with a diameter of 4 mm and provides a coverage of  $|\eta| < 2.0$ . In the central region the tubes are arranged parallel to the beam axis and have a length of 144 cm. In the endcap regions, radially arranged, 37 cm long tubes are placed in wheels. With this number of tubes it is possible to provide a large number of hits (up to 36 per track). The TRT measures the  $r - \phi$  position with a precision of about  $130 \mu\text{m}$ . This worse resolution per point compared to the silicon detectors is compensated by the large number of hits and the larger track length. The tubes are filled with a Xe-based gas mixture and nested in polypropylene fibres in the barrel region or polypropylene foils for endcap regions which serve as transition material. When charged particles propagate through the TRT, the transition material radiates energy which is proportional to the Lorentz factor  $\gamma = E/m$ . Since the electron has a very low mass compared to massive hadrons, it is possible to distinguish between those.

### 3.2.4 Calorimeter system

The calorimeter system of ATLAS consists of two different parts, the electromagnetic calorimeter and the hadronic calorimeter. A schematic view of the system is given in Figure 3.4. The sampling calorimeters consist of alternating active and passive material. Particles, that propagate through the dense, passive material, build showers, whose energy is measured in the active material.

The shower that evolves in the electromagnetic calorimeter differs from the hadronic shower. Electromagnetic showers are formed by incoming electrons or photons. They start to evolve in the passive material and divide their energy between daughter-particles, which is in the case of an electron a radiated photon (Bremsstrahlung) and in the case of an incoming photon an electron and a positron due to pair production. This shower evolves up to the point where the daughter-particles are stopped through ionization. The decrease of energy of an incoming electron or photon with distance  $x$  is given by  $E(x) = E_0 e^{-x/X_0}$ , where  $X_0$  is the material

dependent radiation length.

Hadronic showers evolve differently. The incoming hadron loses energy through successive, inelastic scattering via the strong force in the calorimeter material. A typical material dependent quantity to measure the length of a hadronic shower is the absorption length  $\lambda$ . In general hadronic showers are broader and longer compared to electromagnetic showers.

When the signals of the cells are read out, it can happen that signals of particles from other bunch crossings contribute, which is called *out-of-time pileup*. In addition it happens that signals of particles from different interaction within one bunch crossing overlay, which is called *in-time pileup*. In order to reduce these effects the readout signals are shaped in a special way and different digital filtering techniques are applied which are described in detail in [90].

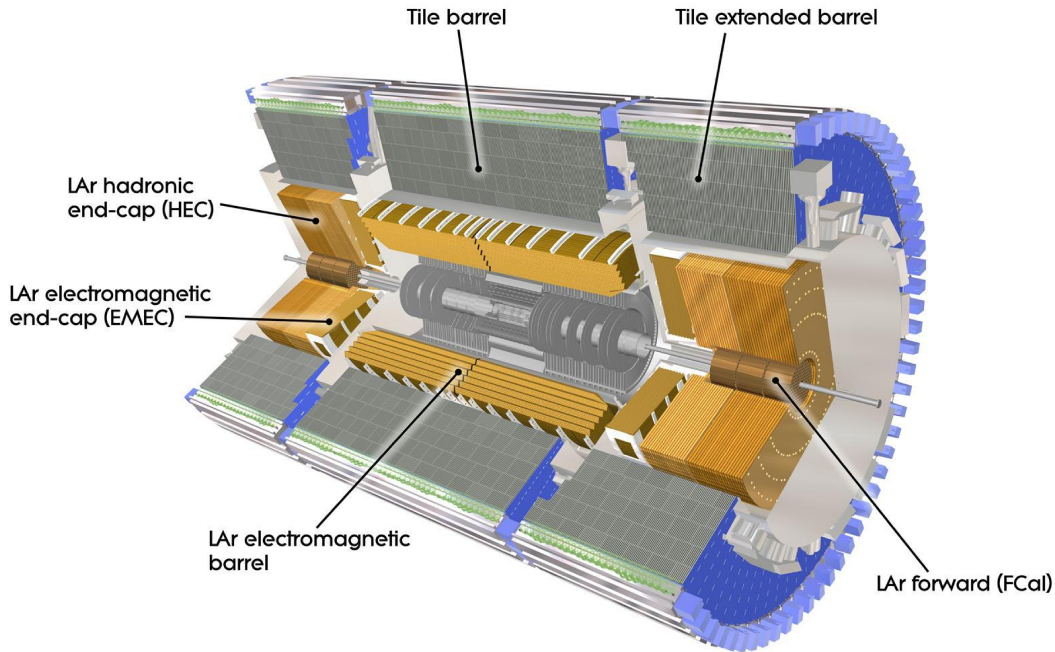


FIGURE 3.4: Cut-away view of the ATLAS calorimeter system. Figure taken from [80].

**Electromagnetic Calorimeter** In the central region ( $|\eta| < 1.475$ ) the electromagnetic calorimeter [91] (EM) can be divided into two half-barrels that cover a diameter of 2.8 m to 4 m in radial direction which corresponds to about  $22 X_0$ . Each half-barrel consists of 16 modules, where each module covers a region of  $\Delta\phi = 22.5^\circ$ , leading to a full coverage in  $\phi$ . The region between  $|\eta| = 1.375$  and  $|\eta| = 3.2$  is covered by the electromagnetic endcap calorimeters (EMEC). Those are installed in two coaxial wheels, the outer wheel covering  $1.375 < |\eta| < 2.5$ , and the inner wheel from  $|\eta| = 2.5$  to  $|\eta| = 3.2$ . Each wheel is segmented into eight wedge-shaped modules and extends over radii from 0.3 m to 2.1 m. In the very forward region,  $3.1 < |\eta| < 4.9$ , the first module (on each side) of the so-called forward calorimeter (FCAL) can also be used for electromagnetic measurements. It is made out of copper as passive medium and also uses LAr as active material. In the region  $|\eta| < 3.2$  the calorimeter uses lead as absorber and liquid Argon (LAr) with kapton electrodes as active layer which are arranged in a special accordion-geometry



to provide uniform coverage in  $\phi$ .

The part of the calorimeter with  $|\eta| = 2.5$  has a special longitudinal segmentation to have very fine granularity which is necessary for the precise measurement of electrons. It consists of three layers, which is visible in Figure 3.5, where a schematic view of a barrel module is shown. In front of the first layer a 11 mm thick layer of liquid argon is installed in regions with  $|\eta| < 1.8$ . This layer, also called pre-sampler, has the purpose to measure the energy loss of a particle before it enters the EM. The following layer, also called “strip-layer”, has a granularity of  $0.0031 \times 0.0982$  in  $\eta \times \phi$ . This fine granularity makes it possible to distinguish also very close-by particles, for example two photons from a  $\pi_0$  decay. The second layer is about  $16 X_0$  thick and has a granularity of  $0.025 \times 0.0245$  in  $\eta \times \phi$ . This is the layer where most energy is deposit. The third layer is again built with a coarser granularity and designed to correct for the overlap of the energy deposition in the following hadronic calorimeter. Together with the pre-sampler cells, a barrel module has 3424 read-out channels and a module in the EMEC about 4000.

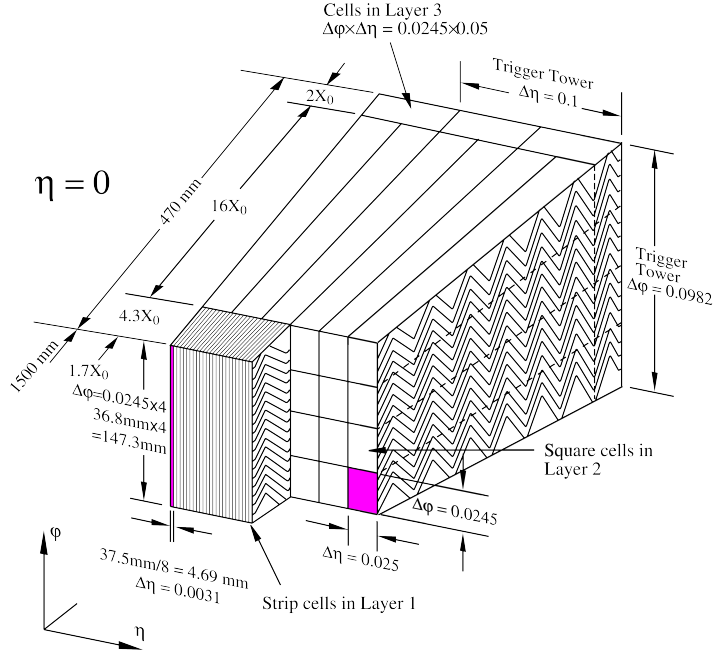


FIGURE 3.5: Schematic view of a barrel module visualizing different layers and the accordion-geometry. Figure is taken from[80].

An important feature of a calorimeter is a good energy resolution. For an electromagnetic sampling calorimeter the relative energy resolution can be parameterized in the following way:

$$\frac{\sigma_E}{E} = \frac{a}{\sqrt{E}} \oplus \frac{b}{E} \oplus c. \quad (3.4)$$

The parameter  $a$  is the so-called sampling term which is at low  $|\eta|$  about  $10\%/\sqrt{E[\text{GeV}]}$  [92]. For higher  $|\eta|$  the term is expected to increase due to more material before the calorimeter. The second term describes the noise from electronics in the readout chain. It is about  $350 \times \cosh(\eta)$  MeV for a typical cluster in the barrel, given a mean number of interactions per bunch

---

crossing of  $\langle\mu\rangle = 20$ . Both terms decrease with energy and approach the constant term which is about 0.7% [92].

**Hadronic Calorimeter** In ATLAS three different hadronic calorimeters are included depending on the respective detector region.

In the central region the tile calorimeter [93] is installed. It consists of a central barrel with coverage up to  $|\eta| < 1.0$  and two extended barrels that cover the region  $0.8 < |\eta| < 1.7$ . Like the EM calorimeter it is a sampling calorimeter, but uses steel as absorber and scintillating tiles as active material. The inner radius of the tile calorimeter is 2.28 m and ends at a radius of 4.25 m. It consists of three layers with different values of interaction lengths ( $\lambda$ ) which for the barrel region are 1.5, 4.1 and 1.8, respectively. In the extended barrel the values of the interaction lengths are 1.5, 2.6, 3.3. The readout is done by photomultipliers that are mounted on wavelength shifting fibers which are build on both sides of the detector.

In the hadronic endcap calorimeter (HEC) also LAr is used as active medium and copper as absorber. It is placed behind the ECAL and uses the same cooling cryostats for the LAr as the EMEC. Both wheels, one on each detector side, are built out of 32 wedge-shaped modules and cover a region of  $1.5 < |\eta| < 3.2$ . The jet energy resolution of barrel and endcap hadronic calorimeters is given by [93]:

$$\frac{\sigma_E}{E} = \frac{50\%}{\sqrt{E[\text{GeV}]}} \oplus 3\%. \quad (3.5)$$

In the very forward region,  $3.1 < |\eta| < 4.9$ , the second and third layer of the FCAL [94] (on each side) are placed to measure the energy of hadronic particles. They are made out of tungstend and have a relative energy resolution of [94]:

$$\frac{\sigma_E}{E} = \frac{100\%}{\sqrt{E[\text{GeV}]}} \oplus 10\%. \quad (3.6)$$

### 3.2.5 Muon system

Muons are, besides of neutrinos, the only (so far known) particles that escape the detector. Their energy deposition in the calorimeters is small, typically about 3 GeV. In order to be able to measure, reconstruct and identify muons, a system of trigger and high-precision tracking chambers [95] is build, surrounding the calorimeters. The muon momentum measurement is based on the magnetic deflection of muon tracks using three large superconducting air-core toroid magnets [96]. In regions of  $|\eta| < 1.4$  this bending is done by the large barrel toroid [97] which has a bending power of 1.5 to 5.5 Tm. In the range of  $1.6 < |\eta| < 2.7$  the magnetic field is generated by two endcap magnets [98] which are inserted into the ends of the barrel toroid. In the transition region an overlap of both magnetic fields provides deflection of the muons with reduced power. The orientation of the magnetic field is done in such a way that it is mostly orthogonal to the muon trajectories. An overview of the muon system is given in Figure 3.6. A summary of the different muon chambers is given in the following which follows largely the description from [80].

In the barrel region Monitored Drift Tube (MDT) chambers are placed in three layers on and between the superconducting barrel toroid magnet. Their main purpose is the measurement of the track of the muon in the bending plane. The first layer has a coverage of  $|\eta| < 2.0$  whereas

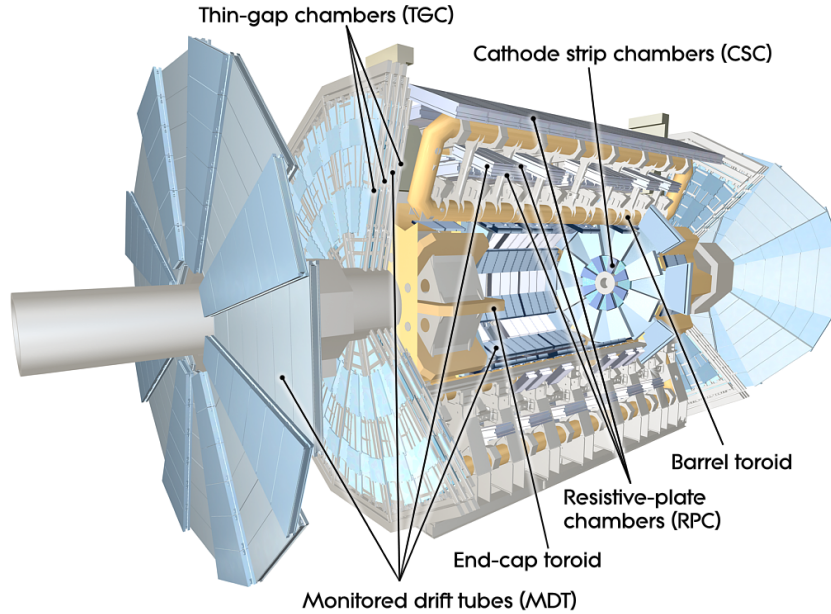


FIGURE 3.6: Overview of the ATLAS muon system. The figure is taken from [80].

the second and third layer cover regions up to  $|\eta| = 2.7$ . In the center of the detector  $|\eta| < 0.1$  a small gap is left in order to allow for services of the solenoid magnet, the calorimeters and the ID. Each MDT chamber has between three to eight layers of drift tubes which have an average resolution of  $80 \mu\text{m}$  per tube leading to a resolution of about  $35 \mu\text{m}$  per chamber.

For more forward regions,  $2.0 < |\eta| < 2.7$ , the first layer is built out of Cathode-Strip Chambers (CSC). These multi-wire propositional chambers are able to measure two coordinates at the same time due to orthogonal organized strips. They reach precisions of  $40 \mu\text{m}$  in the bending and  $5 \text{ mm}$  in the transverse plane. They have higher granularity and better time resolution compared to the MDTs which better fits the requirement of higher track densities in the more forward region.

In addition to the before mentioned precision-tracking chambers, there also are fast muon chambers that are used for triggering. They can deliver signals within  $15\text{-}25 \text{ ns}$  after a particle propagated through them and thus it is possible to use them for decisions for each bunch crossing. It is also possible to retrieve information in both coordinates and get well-defined momentum information of the tracks. Two different techniques are used for the trigger chambers. In the barrel region, Resistive Plate Chambers (RPCs) are used which reach resolutions of about  $10 \text{ mm}$  in both planes, bending and non-bending. The endcap region is instrumented with Thin Gap Chambers (TGCs) which reach a precision of  $2\text{-}7 \text{ mm}$  in  $\eta$  and  $3\text{-}7 \text{ mm}$  in  $\phi$ .

### 3.2.6 Trigger system

Starting from 2015 the ATLAS trigger system [99] is a two level<sup>8</sup> system with the important task to reduce the event rate from about  $40 \text{ MHz}$  to about  $1 \text{ kHz}$ . The first stage, the Level-1 (L1) trigger, is a hardware based component made from custom-made electronics. The decisions

<sup>8</sup>For run 1 the trigger system had three stages, but the last two were merged for run 2.

of the L1 are given to the High Level Trigger (HLT). The HLT forms then the decision if an event is recorded or not. An schematic overview of the trigger system and its interplay with the data acquisition system is shown in Figure 3.7. In the following the two levels are explained in more detail mainly following the descriptions given in [99].

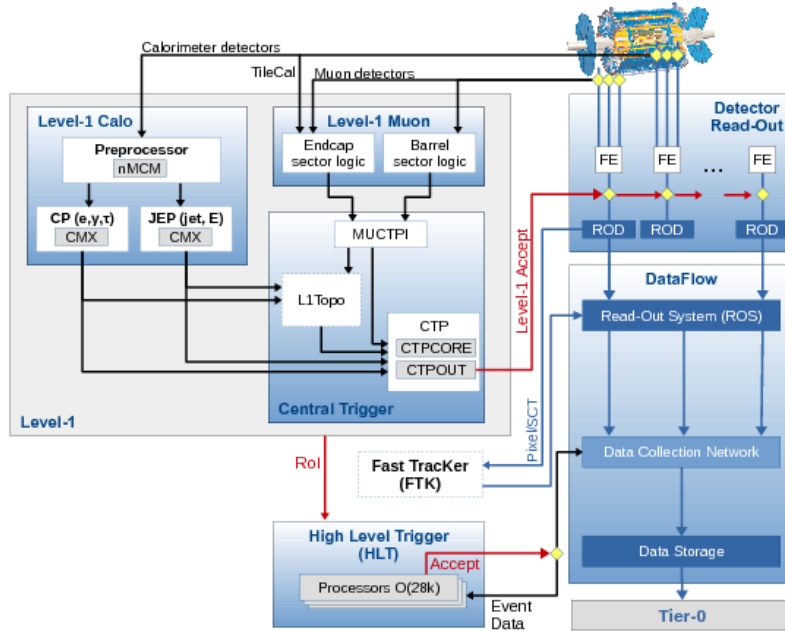


FIGURE 3.7: Schematic sketch of the ATLAS trigger and data acquisition system. L1Topo and FTK are not included for the data used in this analysis since they were being commissioned. The Figure is taken from [99].

**Level-1 Trigger** The time for the L1 trigger to decide, whether an event should be processed further, is only about  $2.5 \mu\text{s}$  which is the reason, why it can not include all detector components in full granularity. But during this time all detector information is stored in temporary pipeline memories. Only information from the calorimeters and the muon trigger chambers is used for the first trigger stage. It can be divided into three parts: The calorimeter trigger L1Calo, the muon trigger L1Muon and the Central Trigger Processor (CTP). In the following these single parts are explained in more detail.

The calorimeter trigger [100] does not use the signals of the cells with full granularity, but instead uses output signals of electronics on the detector that provide the sum of all calorimeter cells in a window of about  $\Delta\eta \times \Delta\phi = 0.1 \times 0.1$ . These energy sums are called trigger towers. The size is also illustrated in Figure 3.5. These analog signals are first digitized in the pre-processor using fast 10-bit Analog-to-Digital Converters (ADCs). Afterwards the digitized signals are converted to transverse energy values using lookup tables. The transverse energy values are then send to the jet/energy processor (JEP) and cluster processor (CP) which, like most parts of the L1 trigger system, rely heavily on firmware programmable FPGAs. The CP scans with a window of  $2 \times 2$  trigger towers for local energy maxima above a programmable threshold, from possible electron, photon or  $\tau$ -lepton candidates, by using a sliding-window technique (similar to a technique explained later in Section 4.2). These regions of interest (RoI) are stored and

---

also used as input for the HLT. Also jet candidates are formed this way by the JEP system. But instead of a window size of  $2 \times 2$  trigger towers, window sizes of  $4 \times 4$ ,  $6 \times 6$  and  $8 \times 8$  trigger towers are used. The JEP also provides the total scalar transverse energy and the missing transverse energy of each event using all cells of the calorimeter acceptance up to  $|\eta| < 4.9$ .

The L1Muon trigger uses information from the RPCs in the barrel region and the TGCs in the endcaps. It defines muon candidates for six different  $p_T$  thresholds from 5 GeV to 35 GeV using a simple track finding algorithm. This algorithm is based on finding coincidences of hits along the path of a possible muon from the interaction point. The width of the path where coincidences are searched is larger for low  $p_T$  muons due to a bigger curvature of the muon tracks and smaller for high  $p_T$  muons. The combination of the RPC and TGC information is done in the Muon to CTP Interface (MuCTPI) and sent to the CTP.

The CTP then combines the information of the L1Muon and L1Calo and does the actual trigger decision based on the trigger menu. For example it searches for two high  $p_T$  objects in the list of objects send from the L1Calo system. This first trigger level reduces the rate from 40 MHz to about 100 kHz and sends its decision together with the regions of interest further to the High Level Trigger.

The topological trigger L1Topo is also a component of the Level-1 trigger system. It can combine information of the calorimeter and muon trigger to form decisions on complex objects like the invariant mass or angular variables. Since this device was still in commissioning phase for the data gathered between 2015 and 2016, information from this trigger is not used for this analysis.

**High Level Trigger** The HLT can be divided into two main processes. In a first process the full granularity of the detector is used but only in the regions of interest. Based on this information together with information from reconstructed tracks (see Section 4.1) from the ID it is decided, if the event is processed further. If so, the complete event is reconstructed using all available informations and several calibrations and identification criteria (see Chapter 4) can already be applied, if required by the pre-defined trigger menu. When events pass this latest stage, full detector information is recorded.

The definition and the multiplicity of the objects for which the L1 and also the HLT trigger are searching at which  $p_T$  threshold can be adjusted during data taking. This is done in a way that the available bandwidth of about 1 kHz is not overloaded. On the one hand it is possible to reduce the bandwidth of a single trigger by increasing e.g. the  $p_T$  threshold, on the other hand, it is possible to introduce so-called pre-scales. Those pre-scales only allow the recording of each  $n$ -th event, where the trigger decision is positive, where  $n$  is the pre-scale factor.

In the future a new FastTracKer [101] (FTK) system will provide global ID track reconstruction at very fast rates. This will speed up the HLT rate a lot since the track building is not based on computationally intensive fits and pattern recognition on CPU but FPGA-based track fits. This system is still under commissioning and therefore not included in this analysis. It is planned to be fully integrated by the end of 2018.

### 3.2.7 Data acquisition and processing

The data taking system is controlled by the RunControl system (RC) [102]. Only if all detectors are in operational state and the LHC declares stable beams, the data taking is started. The

---

data is grouped into different runs with an unique run ID, where one run normally corresponds to one fill of the LHC. A fill of the LHC represents the time until the beam is dumped and new proton bunches are filled to the LHC, which lasts from several hours up to one day. The runs are further divided into several luminosity blocks that contain data of about one minute of recording, where the instantaneous luminosity is approximately constant. The luminosity blocks where all components of the detector for a certain analysis are in good condition can be grouped and later selected by so-called Good Runs Lists. Several runs are grouped into different periods which are labeled alphabetically and have a length of days to weeks often dependent on the beam settings with which the LHC operated.

As it was mentioned before all detector information has to be stored during the trigger decision. During the L1 trigger decision this information is stored at buffer pipelines that are placed directly on the detector components. If an event is accepted by the L1 trigger decision, the data is readout by 1574 readout links, digitized and send to the data acquisition (DAQ) system. The DAQ system stores the information temporarily in local buffers where it can be read by the HLT to build further decisions and reconstruct the event. The complete event is then, after a positive HLT decision, stored in a so-called RAW format on magnetic tapes in the CERN computer center.

Further processing of the RAW data happens using the LHC Computing Grid [103, 104]. This computing grid is a network distributed all over the world with several levels also called Tiers. The first Tier, Tier-0, applies reconstruction algorithms and calibration, which is discussed in more detail in Chapter 4, and transforms the raw data format into information for physics objects called Event Summary Data (ESD). The ESD are then distributed to Tier-1 centers where further processing, for example recalibration, can be done. The ESD are then transformed to a format that contains only information about objects relevant for physics analysis, like muons, electrons and jets. This Analysis Object Data (AOD) is transformed into xAODs which is a format that can be read with the analysis software ROOT [105] and stored at Tier-2 centers. Tier-2 centers can also be used for production of simulated samples and running physics analysis. The xAOD format is further processed to match the requirements of different analyses. It is for example possible only to filter out events with three electron candidates or reduce the size of each event by selecting only the needed information about the detector. These so-called derivated AODs (DAODs) build the nominal input samples of an physics analysis like it is done here. They are also stored at Tier-2 centers, but can be transfered to local Tier-3 centers like the *mainzgrid* which is part of the high performance computing cluster *mogon* [106].

### 3.2.8 Luminosity measurement

A measure of the amount of data that is delivered is the instantaneous luminosity. In Section 3.1.2 it was already explained, how the integrated luminosity is connected to parameters of the LHC. Equation 3.1 can also be written as:

$$\mathcal{L} = \frac{n_b f_r N_1 N_2}{2\pi \Sigma_x \Sigma_y}, \quad (3.7)$$

where  $n_b$  is the number of colliding bunches,  $N_i$  the number of protons in bunch  $i$  and  $\Sigma_x$  and  $\Sigma_y$  a measure of the horizontal and vertical convoluted beam width.

In addition the luminosity can be defined as the ratio of the rate ( $R_{inel}$ ) and cross section ( $\sigma_{inel}$ )

---

of inelastic  $pp$  collisions:

$$\mathcal{L} = \frac{R_{inel}}{\sigma_{inel}}. \quad (3.8)$$

When taking into account that the rate can be expressed as the product of the number of average interactions per bunch crossing ( $\mu$ ) times the number of bunches ( $n_b$ ) and the revolution frequency it yields:

$$\mathcal{L} = \frac{\mu n_b f_r}{\sigma_{inel}}. \quad (3.9)$$

There are several methods and algorithms to measure the luminosity within ATLAS and as well as special detectors like LUCID [107] or ALFA [108] which are based on measuring  $\sigma_{inel}$ . When trying to measure  $\sigma_{inel}$  and the average interaction per bunch crossing, the parameters have to be corrected for acceptance and efficiency effects of the detector by:  $\sigma_{inel} = \sigma_{meas}/\epsilon$  and  $\mu = \mu_{meas}/\epsilon$ . Therefore the determination of the luminosity is equivalent to determining the cross section  $\sigma_{meas}$ . Now, combining Equation 3.7 and 3.9 leads to:

$$\sigma_{meas} = \mu_{meas} \frac{2\pi \Sigma_x \Sigma_y}{N_1 N_2}. \quad (3.10)$$

The product  $N_1 N_2$  is given by the LHC group from beam current measurements. The other parameters are measured in beam separation scans, also called *van der Meer* (vdM) scans [109]. During these scans the beams are horizontally and vertically separated in well defined steps and the visible interaction rate is measured. The peak of the resulting curve then gives  $\mu_{meas}$  and the width  $\Sigma_x$  and  $\Sigma_y$  dependent on the axis of the separation. More details about this procedure can be found in [107].

The results from the different detectors and methods are compared with each other and a systematic uncertainty is applied which for the combined luminosity of 2015 and 2016 is 3.2%. The largest part of the uncertainty is coming from the vdM calibration and the extrapolation from the condition during these scans to the conditions during collision.





## Chapter 4

# Particle reconstruction and identification in ATLAS

This chapter gives a short summary of particle reconstruction and identification in ATLAS. The first section is about track reconstruction using elements of the inner detector. In Section 4.2 the reconstruction and identification of electrons is explained, followed by a section describing the reconstruction and identification of muons. Subsequently it is described how jets are reconstructed and how the contamination from pileup jets can be reduced. The last section gives a brief introduction on how it is possible to get kinematic information of neutrinos that do not interact with the detector, by estimating the so-called missing transverse energy.

### 4.1 Inner detector track reconstruction

The main purpose of track reconstruction is to determine the path of charged particles from hits in dedicated detector elements located in the inner detector. It is based on a sequence of different tracking algorithms that are explained in detail in [110]. Further track properties that can be measured using the muon system are described in Section 4.3.

As a first step, three dimensional space points are formed in the pixel and SCT detectors. In the TRT it is not possible to form three dimensional space points since there is no information about the coordinate along the straw direction. Here, track segments can be formed using a projection to the  $r - \phi$  plane and the  $r - z$  plane for the barrel and endcap regions, respectively. In this case additional timing information is used. With this information, two different track-finding approaches are performed.

The first approach applies an inside-out track finding algorithm which uses combinations of space points of the pixel detector. One combination of three space points is called a seed. These seeds are then extrapolated to the TRT using a Kalman-filter [111]. The track candidates are then fitted to the actual hits in the pixel detector, SCT and TRT. This inside-out approach mainly aims to reconstruct tracks from particles that are directly produced in the  $pp$  collision or from decaying particles that have a lifetime less than  $3 \times 10^{-11}$ s.

A second algorithm is run using the track segments from the TRT as a starting point and extending the segments inwards by including the hits in the pixel detector. This outside-in

---

approach is mainly used to reconstruct tracks from decays of converted photons or long-lived particles that do not necessarily produce hits in the inner-most layers of the detector.

With the reconstructed tracks as inputs, vertex finding algorithms are used to assign vertices to the tracks. In general, a vertex is defined to have at least two associated tracks. The vertex with the highest  $\sum p_T^2$  is defined as the primary vertex.

More information about the track reconstruction and its performance using  $\sqrt{s} = 13$  TeV data from 2015 can be found in [112], for the vertex performance see [113].

An important quality criterion of tracks is the transverse impact parameter  $d_0$ , which is the distance between the reconstructed primary vertex or the beam spot and the (extrapolated) track in the transverse plane. The beam spot is obtained by measuring the primary vertex position over several collisions and using the mean of their (Gaussian) distribution. Cuts are frequently placed in the  $d_0$  significance, which is defined as the nominal value divided by its uncertainty. Another variable is the longitudinal impact parameter  $z_0$  which is the distance from the track to the primary vertex in the  $z$ -plane. Restricting these variables reduces the contributions from particles that come from secondary particle decays such as muons from  $\tau$ -lepton decays.

## 4.2 Electrons

This section describes the reconstruction of electrons and positrons. Since positrons differ from electrons only by the curvature of their tracks, all of the presented criteria apply to both, electrons and positrons. For the remainder of this analysis, the term electrons is supposed to also include positrons, unless charge information is explicitly mentioned. Furthermore only electrons are used in this analysis that are reconstructed in a central region of the detector  $|\eta| < 2.47$ . The forward calorimeters are not used for electrons.

### 4.2.1 Reconstruction

The starting point of the electron reconstruction is the search for *clusters* of energy depositions in the electromagnetic calorimeter. This search is done using a so-called *sliding-window* [114] algorithm. This algorithm divides the cells in the second calorimeter layer into a matrix with element sizes of  $\Delta\eta \times \Delta\phi = 0.025 \times 0.0245$ . Then, a window which has a size of  $3 \times 5$  elements is running over the matrix. In each iteration it integrates the energies of all containing cells and searches for transverse energies above 2.5 GeV. Windows whose energy exceeds this threshold are labeled as clusters. The clusters are then associated to a track by extrapolating from the last track point to the first layer of the calorimeter. The distance between the track impact and the cluster center is required to be smaller than 0.05 in  $|\Delta\eta|$  and  $|\Delta\phi|$ . If no matching track is found the electron candidate is discarded. If more than one track is found, the track with smaller  $\Delta R$  and more hits in the pixel detector and SCT is chosen. The criteria of pixel and SCT hits is placed to reduce the amount of electrons originating from photon conversion.

After a successful assignment of track and cluster, the window of the energy cluster is increased to a size of  $3 \times 7$  elements in the barrel region and  $5 \times 5$  in the endcap region and the energy of the cluster is rebuild. This increased window can account better for Bremsstrahlung losses. The energy is then corrected for different effects, such as losses in dead material or leakage to

regions beyond the electromagnetic calorimeter. More details on the electron reconstruction can be found in [92, 115, 116].

### 4.2.2 Identification

Many of the reconstructed electrons are not real electrons. Jets can also deposit parts of their energy in the electromagnetic calorimeter with tracks that are associated to this cluster. Therefore, there is a large fraction of objects which are in fact jets that are reconstructed as electrons. In order to reduce this contribution, further criteria are applied to reconstructed electrons. The main challenge is to reject large fractions of the wrongly reconstructed electrons while keeping the efficiency of selecting real electrons high (signal efficiency). There is a large number of variables that can be used to reject incorrectly reconstructed electrons. A schematic view of the detector components that are used to build these variables is shown in Figure 4.1. There are algorithms provided by ATLAS that combine these variables using a multivariate likelihood approach. They are tuned to different working points to deliver specific signal efficiencies and background rejection rates. Some of the variables used to build the working points are described briefly in the following, a more detailed explanation can be found in [117].

The first variable is the ratio of the transverse energy measured in electromagnetic calorimeter and the hadronic calorimeter. This parameter is also referred to as the hadronic leakage. It is expected that jets have a large energy deposition in the hadronic calorimeter since jets contain large number of hadrons, while electrons dominantly deposit their energy in the electromagnetic calorimeter. Another possibility is to reduce photons from  $\pi_0 \rightarrow \gamma\gamma$  decays by including the variable  $E_{ratio}$  in the likelihood. To build this variable it is looked for the largest and second largest energy deposition in a cluster using only the first layer of the electromagnetic calorimeter. The ratio of the difference of these two deposition over the sum of both is the definition of  $E_{ratio}$ . The energies of the two photons from the  $\pi_0$  decay are expected to have a similar

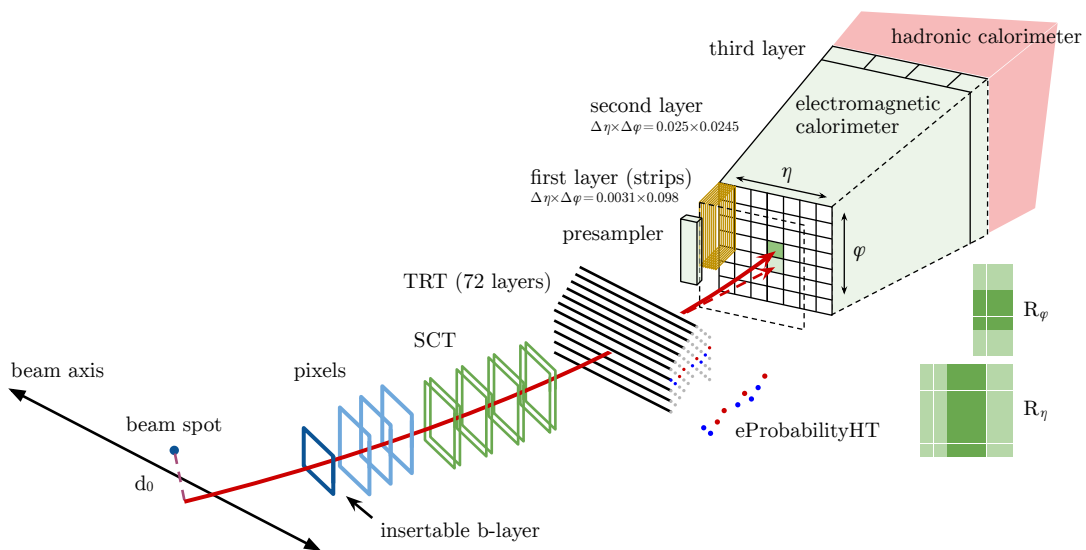


FIGURE 4.1: Illustration of electron reconstruction and identification at ATLAS. Figure is taken from [117].

amount of energy and therefore  $E_{ratio}$  should be smaller compared to electrons. A different set of variables is sensitive to the shower width in the middle layer of the calorimeter. For example it is made use of the fact that hadronic showers e.g. from jets are expected to be symmetric in  $\eta$  and  $\phi$ . Electromagnetic showers from electrons are expected to be larger in  $\phi$  than in  $\eta$  due to Bremsstrahlung effects that happen dominantly in the  $\phi$ -plane. Moreover, track quality variables like the  $d_0$  and the  $d_0$  significance are included in the likelihood as well as parameters that quantify how well tracks and clusters match. An example of such a variable is the distance of the cluster center to the track which is often smaller for electrons than for jets. Also decisions based on the TRT hits<sup>1</sup> are included in the likelihood. For each input variable signal and background probability density functions are estimated using simulations. Chapter 5 describes these simulations in greater detail. A discriminant,  $d_{\mathcal{L}}$ , is calculated:

$$d_{\mathcal{L}} = \frac{\mathcal{L}_S}{\mathcal{L}_S + \mathcal{L}_B}, \quad \mathcal{L}_S(\vec{x}) = \prod_{i=1}^n P_{S,i}(x_i), \quad (4.1)$$

where  $P_{S,i}$  is the value of the signal probability density function of the  $i^{\text{th}}$  variable, evaluated at  $x_i$ . The likelihood of the background  $\mathcal{L}_B$  is defined the same way as  $\mathcal{L}_S$  but evaluating the background probability density function  $P_{B,i}$  at  $x_i$ .

The various working points of the electron identification differ by the value at which the discriminant is cut. In addition, cuts are also applied on the number of hits in the pixel detector and the SCT. At this stage the specific cuts on  $\mathcal{L}$  and the number of hits are chosen to obtain certain efficiencies for each identification level. The efficiencies directly correspond to background rejection rates associated with the identification levels. The levels are defined such that electrons selected by a certain identification level would have also been selected by the looser identification criteria. The loosest level, **LHVeryloose**, has an efficiency of about 95% at  $E_T = 20$  GeV (based on estimates using a simulation of  $pp \rightarrow Z + X \rightarrow e^+ e^- + X$  processes) and a background rejection of about 80% (using dijet simulations [117]). The next identification level, **LHLoose**, has a signal efficiency and background rejection rate of about 92%, followed by the **LHMedium** identification level which has 87% signal efficiency and a background rejection rate of 95% at electron  $p_T$  of 20 GeV. The most stringent identification level, **LHTight**, contains cuts on additional variables. The first one is the ratio of  $E/p$ , which is the cluster energy divided by the track momenta. A cut on this ratio is meant to ensure that the track and the cluster are coming from the same object. Furthermore a cut is placed on  $w_{\text{stot}}$ . It is a measure of the shower width and defined as:

$$w_{\text{stot}} = \sqrt{\frac{\sum_i E_i (i - i_{\text{max}})^2}{\sum_i E_i}}, \quad (4.2)$$

where  $i$  is the index of the strip in the first layer of the EM calorimeter and  $i_{\text{max}}$  is the index of the strip with the highest energy. Jets have broader shower widths than electrons. The efficiency of the **LHTight** identification level is about 78% and the background rejection about 96% for 20 GeV electrons.

In addition to the likelihood based identification criteria, there are also cut based identifications which put restrictions directly on the variables which are used to build the likelihood. They were mostly used in ATLAS at  $\sqrt{s} = 8$  TeV and have lower efficiencies and background rejection rates.

<sup>1</sup>The TRT decision is also based on a (different) likelihood.

---

### 4.2.3 Isolation

The energy deposition of electrons from the hard interaction is expected to be centered in the cluster. Showers from electrons formed inside jets often have contributions from energy depositions from other particles in the jet and thus broader showers. Therefore, it is possible to put restrictions on the energy contained in a cone with a certain size of  $\Delta R$  around the central deposition of the electron candidate. This can be used to distinguish between isolated electron candidates and electron candidates from jets. It is also possible to use the tracks surrounding the track of the electron candidate and put isolation criteria on those. The track isolation has the advantage that it allows to build very small cones around the track of the electron candidate. This is not possible in the calorimeter due to the cell sizes. Often a variable cone size is used for the track isolation which gets smaller for higher  $p_T$ . Isolation criteria are not included in any of the identification levels and have to be applied separately. Nevertheless, correlations between identification and isolation are possible. The ATLAS isolation group provides a tool<sup>2</sup> that uses these isolation variables and puts restriction on them. There are different working points defined in this tool that are either optimized to have a certain target efficiency by varying the requirements for different  $p_T$  and  $\eta$  regions or have constant cuts applied on the isolation variables. More information on the electron isolation can be found in [117].

### 4.2.4 Electron trigger

As discussed in Section 3.2.6, there are Level-1 triggers which require one or multiple electromagnetic calorimeter trigger objects above a certain threshold. These are used as seeds for the electron trigger. At the HLT level it is possible to apply identification and isolation criteria which are following the definitions described before, but are always a bit looser, so that no events are lost that would pass the “offline” selection.

### 4.2.5 Electron energy calibration

The energy of electrons is built from the energy of the clusters in the electromagnetic calorimeter and is calibrated using multivariate techniques based on simulation. This first calibration procedure is described in detail in [116]. Preliminary cuts are made on the energy after this initial calibration step to reduce the data size. A second calibration of data is done at a later point, when a detailed analysis is done. To do this,  $\eta$ -dependent corrections are applied to recalibrate the energy. The correction values are calculated by comparing invariant mass spectra around selected  $Z$ - and  $J/\Psi$ -candidates between data and simulation. The corrections are below one percent and provided in a tool<sup>3</sup> by the ATLAS electron performance group [116].

---

<sup>2</sup>In this analysis the tool version is: *IsolationSelection-00-06-05*.

<sup>3</sup>The tool version is: *ElectronPhotonFourMomentumCorrection-02-03-00*

---

## 4.3 Muons

In this section the reconstruction, identification and isolation of muons is briefly described following a more detailed description that can be found in [118]. As it is the case for electrons, there are no relevant differences between muons and anti-muons that would require a separate treatment in the following procedures. Thus, the term muons is meant to refer to anti-muons as well, unless the charge is explicitly pointed out.

### 4.3.1 Reconstruction

The reconstruction of muons begins with a search of hit patterns in each muon chamber to form segments. The procedure searches for hits in the MDT and trigger chambers that are aligned on a trajectory in the bending plane of the detector by using a Hough transform [119]. The segments are then built by fitting a straight line to those hits. In the CSC the segments are built using other search algorithms. The track candidates are then built by fitting hits from the segments of the different layers. It is started in the middle layer, subsequently including more and more hits from the outer and inner layers. At least hits from two segments are required to build a track candidate.

The combination of ID tracks with the muon tracks can be done using different algorithms. Four types of reconstructed muons can thereby be built dependent on which subdetectors are used:

- Combined (CB) muons: The independently reconstructed tracks of the ID and MS are combined using a global refit to the hits from both tracks. To do this, an outside-in approach is chosen which starts in the MS and then extrapolates inwards searching for matching ID tracks. The opposite, an inside-out approach starts with the ID tracks, which are extrapolated to match the MS tracks. This result complements the tracks of the other approach.
- Segmented-tagged (ST) muons: An ID track is identified as a muon track, when the extrapolation of the ID track points to a track segment in the MDT or CSC chamber. This method aims to reconstruct very low  $p_T$  muons, that only cross one layer of the MS chambers and muons in regions with reduced MS acceptance.
- Calorimeter-tagged (CT) muons: The MS spectrometer is only partially instrumented in regions with  $|\eta| < 0.1$ . In order to recover some acceptance in this region, muon tracks are formed when a track in the ID points to an energy deposit that is compatible with a minimum-ionizing particle. The purity of such reconstructed muons is the lowest compared to the other muon types.
- Extrapolated (ME) muons: Tracks in the MS are extrapolated to the interaction point, taking the energy loss of the muon in the calorimeters into account. The tracks are required to propagate through at least two layers of MS chambers in the central region and three layers in the forward region. Since the ID covers only regions with  $|\eta| < 2.5$ , ME muons are used to extend the muon acceptance to  $|\eta| = 2.7$ .

---

In order to exclude any overlap of the muon types in case they share the same ID track, preference is given to CB muons, then to ST and finally to CT muons. Overlapping ME muons with other tracks in the MS system are resolved by choosing the track with better fit quality and larger number of hits.

### 4.3.2 Identification

Some of the reconstructed muons are not prompt muons. They originate from secondary vertices like pion or kaon decays. In order to reduce these background muons while keeping a high signal efficiency, identification criteria are applied.

A characteristic of muon candidate tracks that originate from in-flight decays of charged hadrons is a distinctive “kink” of the reconstructed track in the ID. Therefore the fit quality is often poor and the momentum measured in the ID will not match as well with the measured momentum by the MS. One variable which is used for CB muons and useful to distinguish background from signal muons is the normalized  $\chi^2$  of the combined track fit. Another variable is the  $q/p$  significance. It is defined as the absolute value of the difference between the ratio of the charge and momentum of the muons measured in the ID and MS divided by the quadratic sum of the corresponding uncertainties. A related variable is  $\rho'$  which is the absolute value of the difference between the transverse momentum measurement in the ID and MS divided by the  $p_T$  of the combined track. In order to ensure a robust momentum measurement, requirements can be placed on the number of hits in the ID and MS. Furthermore, at least one pixel hit, at least five SCT hits and less than three pixel or SCT holes are required. A hole is defined as an active sensor where the track passes through but contains no hit. For  $0.1 < |\eta| < 1.9$ , which is the acceptance of the TRT, at least 10% of the original TRT hits are required to have ended up in the final fit.

These variables are used to define four identification selections (*loose*, *medium*, *tight*, *High- $p_T$* ). The categories are inclusive, which means that a muon identified as medium would also pass the loose category. In this analysis only the loose identification is used in order to have the highest efficiencies possible. The following requirements are set on the aforementioned variables for the loose category. The CB muons have to have more than three hits in at least two MDT layers, except for tracks in the  $|\eta| < 0.1$  region, where tracks with at least one MDT layer but no more than one MDT hole are allowed. ME muons have to have hits in at least three MDT/CSC layers and are only used for regions  $2.5 < |\eta| < 2.7$ . The  $q/p$  significance of CB muons has to be smaller than 7. CT and ST muons are restricted to regions with  $|\eta| < 0.1$  and account for about 2.5% of the muons in regions  $|\eta| < 2.5$  when taking CB muons into account [118]. The efficiency of the *loose* and *medium* identification to select real muons from the hard interaction was tested with simulation and is above 98% for most of the region covered by the MS.

### 4.3.3 Isolation

Muons can also appear in jets from charged hadron decays. In order to reduce this amount of muons, track isolation cuts can be applied. The procedure is the same as it was explained for the electron track isolation in Section 4.2.3 but using the muon track instead.



---

### 4.3.4 Muon trigger

As explained in Section 3.2.6, triggers are used to select events that contain one or more muons at Level-1. In the HLT also MDT chamber information is used to build simple tracks from the MS hits by using a parameterized function. These tracks are combined with the ID tracks and the transverse momentum is recalculated. If it passes a certain threshold, the event is recorded. In addition, it is also possible to apply a simple track isolation criterion at the HLT level which corresponds to the “offline” isolation but is slightly looser in order not to affect the efficiencies.

## 4.4 Jets

Jets were introduced before as collimated bundles of hadrons emerging from fragmentation of partons. In this section, it is explained how jets are reconstructed from the energy depositions of these hadrons in the calorimeter. In addition, it is explained how reconstructed jets can be distinguished from jets that do not originate from  $pp$  collisions or jets from pileup processes. The discussion is largely based on [120].

### 4.4.1 Reconstruction

The reconstruction of jets uses topological calorimeter clusters (*topo-clusters*) [121]. This clustering is based on the signal-to-noise ratio ( $S/B$ ) of each calorimeter cell, where the noise includes electronic noise and contributions from pileup. It starts with a cell that has  $S/B > 4$  and iteratively adds neighboring cells with  $S/B > 2$ , including the first one that has a value smaller than two but stopping there. If all cells are processed and all clusters are formed, it is checked for overlaps between clusters. If overlapping clusters are found, they are split. The splitting is based on searching a local maximum cell with energy above 500 MeV and forming a new cluster around it, only considering the cells of the parent cluster. Cells that end up in different clusters formed from local maxima are added to the clusters with a weight that depends on their energy and distance to the respective cluster center. The energy of a topo-cluster is defined as the sum of all included cell energies and the position is given by weighting the  $\eta$  and  $\phi$  of all constituent cells with their energy. The mass of a topo-cluster is set to zero. Topo-clusters built this way are at the baseline scale of the energy deposit in the calorimeter, called electromagnetic scale (EM scale). The ATLAS calorimeter is non-compensating, which means that the energy of hadronic showers is lower than the true energy. There are techniques to correct this but those are not used in this analysis.

The topological clusters are the input to a jet finding algorithm that is often used in ATLAS as well as in this analysis, which is called anti- $k_t$  algorithm [122]. This algorithm is proven to fulfill the requirement that the jets formed by it are not (or very weakly) dependent on radiation of partons with low energies under small angles. This property is called infrared and collinear safety. The main principle of the algorithm is the recombination of jet constituents, which are the topo-clusters in this case. The combination is based on distance measures. Two distances are defined, one between constituent  $i$  and  $j$ ,  $d_{i,j}$ , and one between constituent  $i$  and the beam ( $B$ ),  $d_{iB}$ . If the distance  $d_{i,j}$  is smaller than  $d_{iB}$ , the two constituents are combined, if  $d_{iB}$  is smaller



---

the constituent is considered a jet and removed from the list. The procedure is repeated until all constituents are processed. The definitions of the distances used in this analysis are:

$$d_{ij} = \min(k_{t,i}^{-2}, k_{t,j}^{-2}) \frac{\Delta_{ij}^2}{R^2}, \quad d_{iB} = k_{t,i}^{-2}, \quad (4.3)$$

where  $\Delta_{ij}^2 = (y_i - y_j)^2 + (\phi_i - \phi_j)^2$  and  $k_{t,i}$ ,  $y_i$ , and  $\phi_i$  are the transverse momentum, rapidity, and azimuth angle of particle  $i$ , respectively. The radius parameter, describing the size of the jets, is given by  $R$ . The choice of  $R$  is a compromise between having jets that are large enough to contain all relevant constituents and not being affected too much by pileup effects or the underlying event. In this analysis jets with  $R = 0.4$  are used.

#### 4.4.2 Jet energy calibration

The jet energy scale is calibrated in several steps. First an offset correction of the energy is done due to pileup interactions. Then the origin is corrected to point to the vertex instead of the nominal interaction point. Finally a residual correction is applied using in-site techniques. These techniques are based on transverse momentum measurements in balancing processes like  $pp \rightarrow Z(e^+e^-) + jets + X$ , where the jets have to compensate the momentum of the reconstructed  $Z$  boson in the transverse plane. All these corrections are provided by the ATLAS jet performance group [123] and implemented in a tool <sup>4</sup>.

#### 4.4.3 Suppression of pileup jets

In the jet reconstruction a correction for energy from pileup effects is already done by subtracting an averaged energy amount from the calorimeter cells. However, local fluctuations in the pileup activity can still result in reconstructed jets from pileup effects. It is possible to reduce the amount of pileup jets by putting restrictions on the so-called jet-vertex-fraction ( $JVF$ ). This is the sum of the scalar transverse momentum of the tracks that are associated with a jet and originate from the primary vertex divided by the scalar transverse momentum sum of all associated tracks. For jets from pileup, this variable tends to zero, whereas for jets from the hard interaction the variable tends to one. Another variable that is sensitive to pileup jets is the scalar  $p_T$  sum of the tracks that are associated with the jet and originate from the primary vertex, divided by the fully calibrated jet  $p_T$  ( $R_{pT}$ ). For pileup jets, the distribution of  $R_{pT}$  peaks at zero and steeply falls towards higher values. At these higher values only small contributions from jets from the hard interaction are expected. Both variables,  $R_{pT}$  and a corrected<sup>5</sup> version of  $JVF$ , are used to build a likelihood, called jet-vertex-tagger ( $JVT$ ). Different cuts on this variable results in different efficiencies to select jets from the hard interaction and accordingly different fake rates of jets from pileup. For example tests with simulations show a fake rate of 1% for signal efficiencies of 90% [124]. A more detailed description can be found in [124]. The functionality is built in a tool provided by the ATLAS jet performance group and is used in this analysis.

---

<sup>4</sup>In this analysis the version of the tool is: *JetCalibTools-00-04-76*

<sup>5</sup>The efficiency to select jets from the hard interaction is falling when applying a cut on the nominal  $JVF$  which is not the case for the corrected version.

---

The previously mentioned tagging technique is only possible in the detector region of the ID,  $|\eta| < 2.5$ , where tracking information is available. However, jets are reconstructed up to values of  $|\eta| < 4.9$  which can also originate from pileup processes. The pileup jets in the forward region can be classified into two different categories: *QCD pileup jets* which are jets that originate mostly from a single pileup interaction and *stochastic jets* which combine particles from different pileup interactions. Stochastic jets differ in the shape from hard interaction jets which can be used for discrimination. QCD pileup jets do not differ fundamentally from the hard interaction jets. For those a different approach is used. The assumption is made that the transverse momentum of each pileup interaction is balanced. When adding up all QCD pileup jets in the central region ( $|\eta| < 2.5$ ), it is expected that any imbalance comes from a QCD pileup jet in the forward region, which then can be rejected. In order to filter the QCD pileup jets in the central region, techniques similar to the JVT are used and tuning those parameters results in different rejection rates of forward pileup jets. This functionality is implemented in a tool from the ATLAS jet performance group [125]. The efficiency for jets between  $20 \text{ GeV} < p_T < 50 \text{ GeV}$  from the hard interaction is about 92% and the rejection rate of forward pileup jets is about 40%. More details on forward pileup jet tagging can be found in [125].

## 4.5 Missing transverse energy

Neutrinos are very unlikely to deposit energy in the detector and therefore it is not possible to reconstruct them directly. It is, however, possible to use momentum conservation in the transverse plane to draw conclusions on the energy and the direction of the neutrino in the  $x - y$  plane. This section is largely based on the descriptions given in [126, 127].

The components of the missing transverse energy ( $E_T^{\text{miss}}$ ) can be calculated as:

$$E_{x(y)}^{\text{miss}} = E_{x(y)}^{\text{miss},e} + E_{x(y)}^{\text{miss},\gamma} + E_{x(y)}^{\text{miss},\tau} + E_{x(y)}^{\text{miss},jets} + E_{x(y)}^{\text{miss},\mu} + E_{x(y)}^{\text{miss},soft}, \quad (4.4)$$

where each component is given by the negative vectorial sum of the transversal energies of the respective reconstructed calibrated objects. In order to avoid situations where energy depositions in the calorimeter are taken into account multiple times for different objects, the association of the energy depositions is done in the following order: electrons, photons, hadronically decaying  $\tau$ s, jets and finally muons. The default selection applied to single objects by the reconstruction software of ATLAS is briefly described in the following.

Electrons (photons) have to have  $p_T > 10 \text{ GeV}$ ,  $|\eta| < 2.47$  and pass a medium (tight) identification criterion. The identification criteria of photons are similar to the ones of electrons lacking the track information.  $\tau$  leptons have to be within  $|\eta| < 2.5$  and  $p_T > 20 \text{ GeV}$ . In addition, they have to pass a medium identification level. This reduces the amount of hadronically decaying  $\tau$ -leptons. Jets are reconstructed using the anti- $k_t$  algorithm with  $R = 0.4$  and have to be within  $|\eta| < 5$ . In order to suppress pileup jets in the central region  $|JVF| > 0.25$  is required for jets with  $p_T < 50 \text{ GeV}$  and  $|\eta| < 2.4$ . Muons are required to pass the loose identification, have a  $p_T > 2.5 \text{ GeV}$  and a certain amount of hits in ID and MS tracking detectors. The last term,  $E_{x(y)}^{\text{miss},soft}$ , contains any tracks that are not considered by any of the other objects. The tracks of this term have to pass  $p_T > 0.5 \text{ GeV}$ , have at least 6 hits in the SCT and 1 hit in the pixel detector and be associated with a primary vertex by requiring cuts on  $d_0$  and  $z_0$ .

From the  $x$  and  $y$  components, it is then possible to get the transverse component of the missing

---

energy and the azimuthal angle  $\phi^{\text{miss}}$  as:

$$E_{\text{T}}^{\text{miss}} = \sqrt{(E_{\text{x}}^{\text{miss}})^2 + (E_{\text{y}}^{\text{miss}})^2}, \quad \phi^{\text{miss}} = \arctan(E_{\text{y}}^{\text{miss}}/E_{\text{x}}^{\text{miss}}). \quad (4.5)$$



## Chapter 5

# Simulations and theoretical predictions

The first section of this chapter presents different theoretical predictions for on-shell  $ZZ$  production at the LHC. In the following sections it is described how events at the LHC are simulated, including detector simulation. After this, fully simulated Monte Carlo samples are listed and described, which are later used for comparison with data. In the last section experimental corrections, which are applied to simulations, are described.

### 5.1 Theoretical predictions

There are different theoretical predictions for the cross section of  $pp \rightarrow ZZ + X$  processes which are used in this analysis that are listed in the following.

**MATRIX** MATRIX [128] can calculate  $pp \rightarrow ZZ + X$  cross sections in next-to-next-to leading order in QCD and leading order in EW. This includes  $q\bar{q}$ ,  $qg$  and  $gg$  initiated processes but no electroweak production of  $ZZjj$ . It is possible to apply different kinematic restrictions in order to get a cross section in a fiducial volume, for example the coverage of the ATLAS detector. The program can also provide differential cross sections as function of different variables. The renormalization and factorization scale is set to  $m_{ZZ}/2$ , where  $m_{ZZ}$  is the invariant mass of the  $ZZ$  system. The description of the PDFs is done using NNPDF 3.0 [57] PDFs.

**SHERPA** SHERPA 2.2.1 [63, 64] calculates cross sections at NLO in QCD and LO in EW. In addition two and three parton emission is included in the matrix element. Only  $q\bar{q}$  and  $qg$  initiated processes are included in this calculation. The PDF used for the calculation is also NNPDF 3.0. It is possible to place kinematic cuts and get differential cross sections.

The  $gg$  initiated process is simulated with SHERPA 2.1 at LO in QCD, which means for this process  $\alpha_s^2$ . These calculations contain also contributions with Higgs propagators and uses CT10 PDFs [58].

Contributions from electroweak  $ZZjj$  production to the cross section are available by using

---

SHERPA 2.1 at LO in QCD. Also contributions from processes like  $pp \rightarrow ZZV + X \rightarrow ZZjj + X$  are included in this calculation. This calculation uses CT10 PDFs.

**POWHEG** It is also possible to use POWHEG [129–131] to calculate cross sections of the  $q\bar{q}$  initiated process at NLO in QCD (which contains also  $gg$  initiated processes). POWHEG does not include further parton radiation in the matrix element, uses CT10 PDFs and sets the renormalization and factorization scale to  $m_{ZZ}$ . Similar to SHERPA, kinematic restrictions can be placed and differential cross section calculation is possible.

The NNLO calculation without the  $gg$  initiated process of MATRIX is used to calculate corrections to the NLO cross section. These corrections, also called *k-factors*, are ratios of differential cross sections where the numerator is simulated at NNLO and the denominator at NLO. They can be applied as function of an observable, like the invariant mass of the  $ZZ$  system, to NLO calculations, for example the POWHEG cross section. The application to SHERPA is not possible directly since SHERPA already includes further parton radiations in the matrix element which would lead a double counting of real parton emissions from higher order QCD effects.

Also the  $gg$  initiated process had been calculated at NLO ( $\alpha_s^3$ ) in QCD. The NLO/LO k-factor is  $1.67 \pm 0.25$  [132] and is applied to the prediction of SHERPA and MATRIX as an overall factor, since the k-factor is not provided differentially. There are also calculations of the  $q\bar{q}$  initiated cross section at LO in QCD but NLO order in EW [133, 134] which are used to get k-factors that can be applied to LO EW calculations. The corrections are provided as function of different kinematic properties in a restricted phase space which matches the criteria of this analysis. Integrated the NLO EW correction is in the order of 0.95.

## 5.2 Simulation of events at the LHC

It was already described in Section 2.2.1 that the hard interaction is only one aspect of proton-proton collisions. In order to get predictions that can be compared to measured data, simulations on an event-by-event basis are needed that include these aspects. This can be split in two parts. The first one is the physics simulation, including all generated particles. The second part is the simulation of the detector response to the simulated particles. The resulting samples are then treated like actual data.

### 5.2.1 Physics simulation

The simulation of the physics processes of proton-proton collisions can be split into different steps:

1. **Hard process**
2. **Parton shower**
3. **Underlying event**

---

#### 4. Hadronization

#### 5. Unstable particle decays

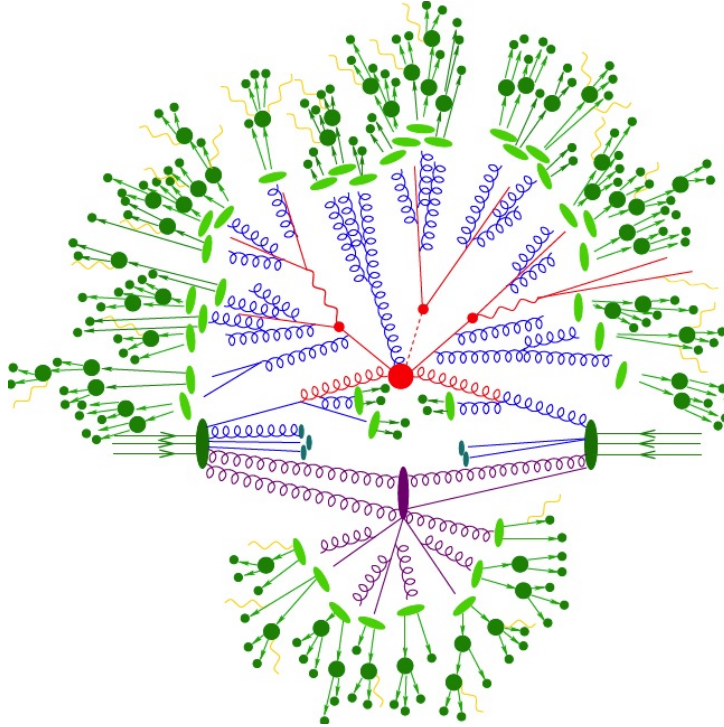


FIGURE 5.1: Illustration of the structure of proton-proton collisions. The colors indicate different stages that are needed to simulate an event. Figure is taken from [135].

In Figure 5.1 a schematic view of a proton-proton collision is shown. The colors of the figure correspond to the colors of the processes listed before.

An event simulation starts with the calculation of the cross section of the hard process at a certain order of perturbation theory. This is convoluted with the PDFs of the incoming partons where choices of the factorization and renormalization scales have to be made. In order to calculate the cross section, a numerical procedure called *Monte Carlo* integration is used, which is also why the simulations are called Monte Carlo simulations. The results are events that contain four-vectors of outgoing particles which kinematic properties follow the convoluted cross section. The shape information is often given as weight to a generated event. In this way it is possible to sample the same amount of events in areas of phase space with very different cross sections which is reflected by a strong variation of the weight. It is also possible to put phase space restrictions on the event generation so that only certain kinematic phase spaces are populated. This can be used to generate only events that will fall in a phase space that is relevant for certain analyses which saves times and enhances the number simulated events in relevant kinematic regions. Another possibility is a filtering of events after they are generated. This saves the time of the detector simulation that is explained in the next section.

The incoming and outgoing partons of the hard interaction are color charged and can therefore radiate gluons that can split further into quark anti-quark pairs or two gluons, leading to an extended shower. In case of the incoming partons this is called initial state radiation (ISR) and for the case of the outgoing partons, final state radiation (FSR). The growth of such parton showers can be simulated step-by-step using the DGLAP equations similar to the splitting

---

described in the PDFs. The evolution starts at a scale of the hard interaction down to a scale where a perturbative description is possible any more and hadrons are formed due to confinement. The probability to radiate a gluon or splitting into quark anti-quark is given by  $1-S_a(t)$ , where  $S_a(t)$  is the so-called *Sudakov form factor* [136] and  $t$  can be interpreted as a time for the shower development. This description of parton showers is valid in the collinear and soft limit, which means that the radiation should happen within a small angle relative to the radiating particle and with low energy. A further challenge that is put on the parton shower modeling is a matching to the hard process. If the hard process is calculated at higher order in  $\alpha_s$  it contains real emissions of (hard) partons. There exist several methods to avoid any double counting. SHERPA [64] uses a different method compared to POWHEG [130].

The color charged remnants can also interact or form further parton showers as it was already described in Section 2.2.1 which is called underlying event. It is not possible to calculate these processes perturbatively which makes a phenomenological description necessary. In those models several free parameter exist which have to be tuned using data.

When the energy scale of a parton shower is at a point where perturbation theory does not work any more hadronization models simulate the forming of colorless hadrons, which can be measured in the detector if they do not decay further. Two often chosen models are the so-called *string model* [137, 138] and the *cluster model* [139]. The main difference between those two is that the cluster model forms intermediate cluster that form hadrons whereas in the string model the hadrons are directly formed from the partons. Both models have free parameters that need to be tuned to data since a perturbative description is not possible.

Many of the final particles, hadrons and leptons are not stable and decay before they reach the detector volume which is simulated also.

## 5.2.2 Detector simulation

After the simulation of all outgoing particles from a  $pp$  collision it is necessary to simulate the interaction of these particles with the detector in order to compare it to data. A brief explanation of the different steps of the detector simulation is given in the following.

The physics simulation of the outgoing particles delivers events in a standardized format called HepMC [140]. In these events the “truth” information is stored with the whole history of simulated processes, for example decays of  $W^\pm$ ,  $Z$  bosons or  $\tau$  leptons. The events at this level of simulation are often referred to as events at generator level. The particles are then read in by GEANT4 [141] which simulates the path and interactions of the particles through the detector. This needs a detailed model of the whole detector which includes materials, geometry and also the magnetic fields. The interaction of the particles with the detector is completely simulated, for example Bremsstrahlung or particles in an electromagnetic or hadronic shower. This results in a precise record of where and when energy is deposited in which part of the detector and thus written to so-called hit files.

These hit files are then read in to simulate the response of the detector components to the energy depositions which includes also the electronics of the readout system. Known problems with some readout modules or defective components of the detector, corresponding to the state of the detector during data taken, are also taken into account. This raises the need to redo the simulations from time to time, when the condition of the detector changed for another data taking period. Fortunately the setup is done in a way that not all steps have to be done from the



---

beginning but only the simulation of the detector response. Pileup effects are taken into account by using hit files from different events that are overlaid to the one containing the hard interaction. For the overlay so-called inelastic minimum bias events are used which can be diffractive and non-diffractive<sup>1</sup>. The simulation of these kind of events have to be tuned with data since a lot of non perturbative processes are involved. Often the energy signature of minimum bias events is below any trigger threshold since no hard interaction happened where the outgoing particles carry most of the momentum transfer. Therefore the events are gathered by randomly firing triggers. How many pileup interactions are overlaid to the interaction containing the hard scattering is dependent on the pileup profile. In order to change the pileup profile, when for example the pileup profile of data changes, it is not necessary to run all the simulation steps of before. It is also possible to adjust the simulation after the pileup in data is known, using a reweighting technique which is explained in more detail in Section 5.4.3.

The digitized detector information is used to emulate the trigger decision and the reconstruction. The trigger decision will not discard events but store its result so that it is possible to do trigger studies like estimating trigger efficiencies. The reconstruction is exactly the same as it is for data but in addition to the final reconstructed properties also the truth information is kept.

The generation of events can be quite CPU time consuming. For example the generation of an event:  $pp \rightarrow W^\pm + X \rightarrow e^\pm \nu_e + X$  can take about 19 minutes<sup>2</sup> [143] where the largest time is spent on the simulation of the detector response. The simulation of the electromagnetic and hadronic shower in the calorimeters take the majority of that time. There are possibilities to reduce these simulation times by using some parameterization of the shower shapes [143] inside the calorimeters instead of simulating it, but in this analysis only fully simulated samples are used.

### 5.3 Simulated samples

There are different event generators that are able to include all of the physics and detector simulation steps mentioned before which leads to simulated samples that can be compared to data. A brief explanation of the relevant generators of this analysis is given in the following.

One of the general-purpose event generators, that can simulate events for different processes is PYTHIA. It is not only capable of simulating  $pp$  collisions like they happen at the LHC, it can also simulate  $e^+e^-$ ,  $ep$  and  $p\bar{p}$  collisions like they happened at LEP, HERA and the Tevatron. Therefore it is one of the most used generators in high energy physics. There are two versions that are mainly used at ATLAS, PYTHIA 6 [144], which is based on Fortran 77, and PYTHIA 8 [145], which is a complete rewrite of the former in C++. It can generate over 200 different Standard Model and beyond Standard Model hard interactions at LO in QCD together with the simulation of the parton shower, hadronization, underlying event modeling and particle decays. It is also possible to interface to PYTHIA, for example by generating the hard interaction with an other generator and using the parton shower, underlying event, etc. from PYTHIA.

POWHEG is not only able to calculate cross sections at NLO in QCD, it can also generate events from  $pp$  collisions. But unlike PYTHIA it does only simulate the hard interaction without taking the parton shower etc. into account. Therefore it is possible to interface to POWHEG via the

---

<sup>1</sup>In non-diffractive events the initial protons are broken up and the outgoing particles hit the detector.

<sup>2</sup>The time is normalized to kSI2K seconds [142].

Les Houches Event interface [146]. In ATLAS POWHEG is often used to get the hard interaction at NLO in QCD and then interface it with PYTHIA for the parton shower, hadronization, underlying event modeling and particle decays.

Also SHERPA is a general-purpose event generator like PYTHIA. Processes are defined in SHERPA with respect to the outgoing stable particles from the hard interaction and it calculates all (wanted) contributions to the matrix elements. Since it also contains the simulation of parton shower, hadronization, parameterization of the underlying event and particle decays, it is not necessary to interface it with another generator.

MadGraph [147] is a generator that is capable of simulating hard interactions at NLO in QCD. Like POWHEG it does not contain a simulation of the needed phenomena besides the hard interaction, like parton shower. Therefore it is often interfaced with PYTHIA to include these processes in the simulation.

In this analysis only the decay of both  $Z$  bosons to electrons and muons ( $\ell$ ) is investigated. The hard interaction and the PDFs of the  $ZZ$  signal samples that are used in this analysis were already described in Section 5.1. In order to search for phenomenas from anomalous triple gauge couplings samples are needed that include these processes. Three different samples were generated at LO using SHERPA. A detailed table of all signal samples, containing the amount of generated events and the total cross section of the simulations is given in Appendix A. There are also further samples listed that are needed for background estimates which is discussed in more detail in Section 7.2. As it was mentioned before it is possible to generate events only in a certain phase space to reduce the number of events where analyses are not interested in. Also for the signal samples that are used in this analysis different kinematic cuts where applied that are listed in Table 5.1.

Sample	Kinematic cuts on outgoing particles
$q\bar{q} \rightarrow \ell^+\ell^-\ell'^+\ell'^-$ POWHEG + PYTHIA	$m_{\ell\ell'} > 4.0$ GeV
$q\bar{q} \rightarrow \ell^+\ell^-\ell'^+\ell'^-$ SHERPA	$p_{T,\ell} > 5$ GeV; $m_{\ell\ell'} > 4.0$ GeV
$gg \rightarrow \ell^+\ell^-\ell'^+\ell'^-$ SHERPA	$m_{\ell\ell'} > 10.0$ GeV; $m_{4\ell} > 100$ GeV
$q\bar{q} \rightarrow \ell^+\ell^-\ell'^+\ell'^-jj$ (EW $ZZjj$ ) SHERPA	$p_{T,\ell} > 5$ GeV; $ \eta_\ell  < 2.7$ GeV; $m_{\ell\ell'} > 0.1$ GeV
Signal samples with aTGCs	
$q\bar{q} \rightarrow \ell^+\ell^-\ell'^+\ell'^-$ (with aTGC) SHERPA	$p_{T,\ell} > 5$ GeV; $m_{\ell\ell'} > 4.0$ GeV

TABLE 5.1: Kinematic cuts on outgoing particles that are placed on signal Monte Carlo samples in order to enhance the production of events in phase space regions that are more relevant for this analysis. The invariant mass of the dilepton system ( $m_{\ell\ell'}$ ) refers to all possible combinations of the four outgoing leptons. The invariant mass of the four lepton system is labeled as  $m_{4\ell}$ .

When a distribution of the simulation is compared to a data distribution it is necessary to weight the simulation to the amount of data. To do this, the simulated distribution is scaled by the following factor:

$$w_{lumi} = \frac{\epsilon_{filter}\sigma_{gen}L_{int}}{\sum_i w_i}. \quad (5.1)$$

In this equation  $\epsilon_{filter}$  takes possible efficiencies into account due to event filters applied during simulation (see Section 5.2). The cross section of the simulated process is given by  $\sigma_{gen}$ .  $L_{int}$  is the integrated luminosity of the data to which the simulation is compared to. The sum in the denominator iterates over all event weights. An event weight contains a generator specific

---

weight due to technical treatments of generating (higher order) processes which can be different from one.

## 5.4 Experimental corrections applied to simulations

### 5.4.1 Efficiency corrections

The efficiency of objects to pass particular reconstruction and selection steps can differ between data and simulation. In the following it is explained how these differences are corrected, for objects used in this analysis.

For electrons, corrections on the reconstruction, identification and isolation efficiency ( $\epsilon$ ) are taken into account by using a correction factor (also called scale factor)  $w_{SF} = \epsilon_{data}/\epsilon_{MC}$  for each criterion. The data efficiency is obtained in events where a  $Z$  boson decays to electrons, using a so-called “tag and probe method”. In this method one electron is selected with very strict identification and isolation criteria, called tag electron, and another is selected that does not pass the needed criterion for which the efficiency should be measured. The invariant mass of the two electron candidates has to be within the  $Z$  mass window which is a region with mostly real electrons. The Monte Carlo efficiency ( $\epsilon_{MC}$ ) is obtained using the same method but instead of data a  $pp \rightarrow Z + X \rightarrow e^+e^- + X$  sample is used. All efficiency corrections are estimated by the ATLAS electron performance group [117] and provided in a tool<sup>3</sup>. The corrections are binned in  $p_T$  and  $\eta$  of the electron and are applied as a weight when histogramming variables. The corrections are in the order of one percent.

Also the muon reconstruction and isolation efficiency is corrected using the tag and probe method for events, where the  $Z$  boson decays to muons. In order to probe lower  $p_T$  regions also  $J/\Psi \rightarrow \mu^+\mu^-$  events are taken into account. A detailed description of the corrections is given in [118]. The order of the corrections is here also in a range of a few percent. They are provided in a tool<sup>4</sup> from the ATLAS muon performance group [118].

In principal it is also necessary to correct for efficiency differences concerning the trigger selection. But it was tested within the ATLAS  $ZZ$  analysis group [62] that the impact of these correction factors are below 0.1% when the trigger efficiency is near 100%, which is the case for this analysis. Therefore no correction due to differences in the trigger selection efficiency is applied.

The efficiency to suppress jets from pileup processes using the jet vertex tagger (see Section 4.4) can differ between data and simulation. The efficiency of the suppression is estimated using also a tag and probe method.  $pp \rightarrow Z + X \rightarrow \mu^+\mu^- + jets + X$  events are selected where the jet with highest  $p_T$  has a back-to-back topology with the reconstructed  $Z$  bosons candidate ( $|\Delta\phi(Z, jet)| > 2.8$ ). This increases the probability for selecting recoil jets from the hard interaction. The efficiency is then defined as the ratio:

$$\epsilon = \frac{N_j^{pass}}{N_j - N_{PU}}, \quad (5.2)$$

---

<sup>3</sup>The electron efficiency correction tool version used in this analysis is: *ElectronEfficiencyCorrection-00-01-94*.

<sup>4</sup>The muon efficiency correction tool version used in this analysis is: *MuonEfficiencyCorrections-04-00-11*.

---

where  $N_j$  is the number of jets in the signal region and  $N_j^{pass}$  the number of jets in the signal region that pass the jet vertex tagging criterion. The term  $N_{PU}$  corrects for pileup jets in the signal region which is estimated by using a control region and simulation. The simulation efficiency is estimated the same way but using a  $Z \rightarrow \mu\mu$  MC sample. More details about the procedure can be found in [124]. The efficiency corrections are up to 2% for low  $p_T$  jets.

### 5.4.2 Energy/Momentum scale and resolution corrections

It was already described in Section 4.2 how the energy scale of electrons is calibrated in data to match to simulation. The resolution of the electron energy is too optimistic in MC simulation. Therefore the energy is smeared with a correction that follows a Gaussian distribution. Also here  $Z$  and  $J/\Psi$  events are used and the widths of mass peaks are compared and correction factors are estimated. These corrections are also provided in the tool from the egamma performance group. The corrections are generally in the order of one per mille but grow slightly higher around the transition region between the barrel region of the detector and the end caps. The uncertainties of these corrections are in the order of 0.01%.

For the muon momentum scale and resolution correction the same procedure as for electrons is used. The ATLAS muon combined performance group [118] provides a tool<sup>5</sup> with correction factors binned in  $\eta$  of the muon. The momentum scale corrections are in the per mille range with an accuracy of about 0.1%. The momentum resolution correction is in the low percentage range with uncertainties in the per mille range for muons with  $|\eta| < 2.0$  and in the percent range for muons with  $|\eta| > 2.0$ . More details are given in [118].

In principle reconstructed jets (see Section 4.4) can show differences in the energy scale and resolution between data and simulation after calibration. But it was found that the simulation is describing data good enough so that no further corrections have to be applied [123].

### 5.4.3 Correction of the pileup profile

In order to have a good description of  $pp$  collisions it is necessary to include also pile up effects. A good description of the in-time pileup is the number of primary vertices ( $n_{PV}$ ). Primary vertices are reconstructed interaction points with more than two reconstructed tracks. The inner detector is fast enough not to be effected by out-of-time pileup. An observable sensitive to the out-of-time-pileup is the number of interactions averaged over one bunch train  $\langle\mu\rangle$ <sup>6</sup> and luminosity block. Both properties are highly dependent on the beam settings of the LHC, like the number of protons in a bunch or the spacing between the different bunches. Often these settings change during data taking but simulations are done before data taking. Therefore the simulations are done with generic, approximative distributions which can be reweighted on an event-to-event basis to match to the data pileup profile. The reweighting is implemented in a tool<sup>7</sup> which is provided by ATLAS [148]. The tool compares the  $\langle\mu\rangle$  distribution of data and simulation and returns the ratio of both as weight which is then used to fill variables into histograms in the analysis. In order to take also the number of primary vertices into account,

<sup>5</sup>The tool version that is used is: *MuonMomentumCorrections-01-00-60*

<sup>6</sup>One bunch train has 72 bunches of protons.

<sup>7</sup>In this analysis version *PileupReweighting-00-04-01* of the tool is used.

---

$n_{PV}$  as function of  $\langle\mu\rangle$  had been compared to data beforehand and differences are applied as a correction factor to  $\langle\mu\rangle$ . This correction factor comes with an uncertainty. The variation of the correction factor by one standard deviation up and down is referred to as Pileup uncertainty.



# Chapter 6

## Selection of $ZZ$ candidates

In this chapter the selection of  $ZZ$  candidates is described. Firstly, Section 6.1 gives a short overview about how the analysis is done and what the aims are. Secondly the data set used for the analysis is discussed in Section 6.2 together with a description of the used trigger information. The selection of physics objects like electrons or muons is shown in Section 6.4. The selected objects are then used in the event selection which is described in Section 6.5. The last Section presents the signal efficiency, the fraction of  $ZZ$  events that is kept after each different selection steps.

### 6.1 Selection overview

In this analysis the fully leptonic decay of two  $Z$  bosons into electrons or muons is considered<sup>1</sup>. The main advantage is that there are not many other Standard Model processes that contribute to a four electron/muon final state and therefore a small background is expected. Also the energy resolution for leptons is much better than for jets which makes the selection of on-shell  $ZZ$  events easier. In fact it would not be possible to distinguish between  $W$  and  $Z$  bosons in the invariant mass distribution due to the low energy resolution of jets. The disadvantage is, that the branching fraction is low (about 0.45 %) and thus only a limited number of selected events are expected. Therefore it is mandatory to enhance the statistical power as much as possible e.g. by going with the  $p_T$  threshold and identification criteria of the leptons as low as possible. Also the selection of additional jets in  $ZZ \rightarrow \ell^+ \ell^- \ell'^+ \ell'^-$  events can be of great interest to probe directly effects from higher order QCD contributions. Therefore it is also discussed how these jets are selected.

The selection is following the procedure that is also described in the ATLAS publication [62] which is partially synchronized with the analysis of  $pp \rightarrow H + X \rightarrow ZZ + X \rightarrow \ell^+ \ell^- \ell'^+ \ell'^- + X$  [149] where  $ZZ$  production is the major background contribution. All selection criteria are summarized in Table 6.1 but explained in the following sections in more detail.

---

<sup>1</sup>In the following leptons refer only to electrons or muons and not  $\tau$ -leptons unless it is stated otherwise.

Category	Cut Name	Requirement
Event preselection	Trigger Vertex	See Table 6.3 At least one vertex reconstructed with 2 or more tracks
Baseline electrons	$p_T$ $\eta$ ID Object Quality $ z_0 \sin \theta $	$> 7$ GeV $ \eta  < 2.47$ Silicon and Pixel Hits requirements of <b>LHVeryLoose</b> working point Not from a bad cluster $< 0.5$ mm
Baseline muons	$p_T$ $\eta$ ID $ z_0 \sin \theta $ $ d_0 $	$> 5$ GeV (15 GeV if calo tagged) $ \eta  < 2.7$ Loose $< 0.5$ mm if muon is not StandAlone $< 1$ mm if muon is not StandAlone
Baseline jets	Clustering $p_T$ Jvt cut forward JVT cut	AntiKt4EMTopo $> 30$ GeV (60 GeV if $2.4 <  \eta  < 2.5$ ) JVT $< 0.59$ if $p_T < 60$ GeV and $ \eta  < 2.4$ medium WP if $p_T < 60$ GeV and $ \eta  > 2.5$
Overlap Removal		Lepton favoring Working Point (see section 6.5.1)
Quadruplet selection	$p_T$ Electron Quality Muon Quality	$p_T^{l,1} > 20$ GeV, $p_T^{l,2} > 15$ GeV, $p_T^{l,3} > 10$ GeV No more than two electrons fail <b>LHLoose</b> identification Number of Standalone or Calo tagged $\mu < 2$
Quadruplet ranking	Minimal $\Delta m_Z$	Select quadruplet with smallest $ m_{12} - m_Z  +  m_{34} - m_Z $
Selection event	$\Delta R$ Quarkonia Veto Electron ID Impact parameter Isolation  $Z$ Window	$> 0.1$ between same-flavour leptons in quadruplet, $> 0.2$ between different-flavour $m_{12,34,14,23} > 5$ GeV All $e$ in quadruplet pass <b>LHLoose</b> working point $ d_0^{\text{BL}}/\sigma(d_0^{\text{BL}})  < 5$ (3) for $e$ ( $\mu$ ) in quadruplet All leptons in quadruplet pass <b>FixedCutLoose</b> working point $66 < m_{12,34} < 116$ GeV

TABLE 6.1: Summary of event and object selections used in the analysis.

## 6.2 Data Set

The data set used in this analysis was taken in the years 2015 and 2016 at  $\sqrt{s} = 13$  TeV at the LHC with the ATLAS experiment. The 2015 data taking period went from June 2015 until November 2015 with a total recorded integrated luminosity of  $3.9 \text{ fb}^{-1}$ . This can be seen in Figure 6.1 on the left side where the collected luminosity per day is shown. The first month of data taking had been done with a time spacing between the proton bunches of 50 ns whereas the rest of 2015 and 2016 was done with a 25 ns bunch spacing. Since the different bunch spacings would have to be modeled in Monte Carlo simulations to make a comparison to data possible, only data with 25 ns bunch spacing is taken into account. The 2016 data set, collected between April and October 2016 has a recorded integrated luminosity of  $35.6 \text{ fb}^{-1}$ . It is almost 10 times



as large as the 2015 data set as it can be seen on the right side of Figure 6.1. This is on the one hand achieved due to a long data taking period and on the other hand due to a higher instantaneous luminosity. As a result the interactions per bunch crossing increased in 2016 due to out-of-time pileup (see Section 5.2.2) which is shown in Figure 6.2.

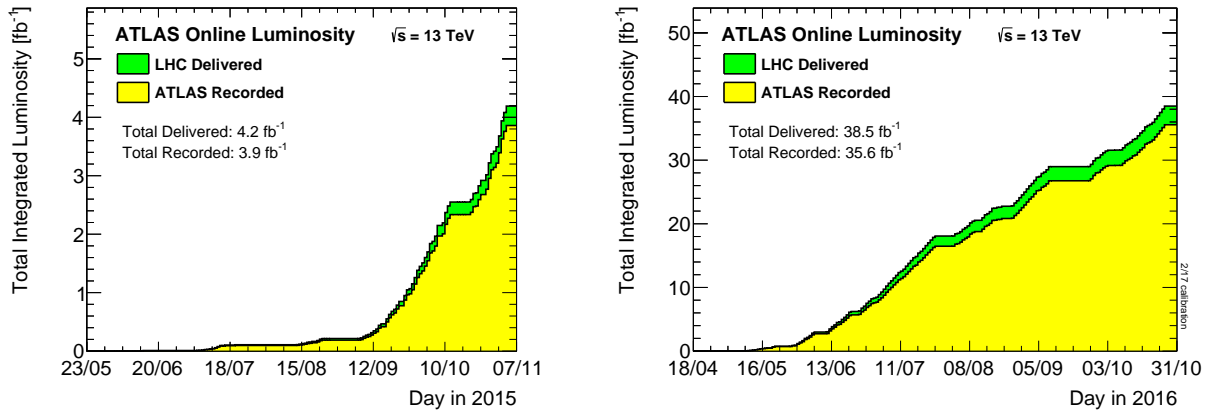


FIGURE 6.1: Left side shows the sum of integrated luminosity by day for data taking in 2015 and the right side for 2016. In green the sum of the integrated luminosity delivered by the LHC is shown. The sum of the integrated luminosity record by ATLAS is shown in yellow. Figures are taken from [150].

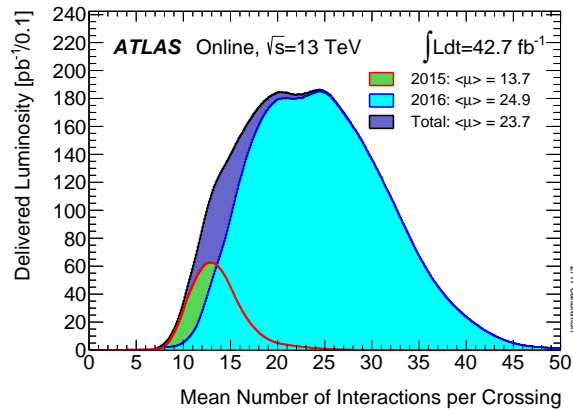


FIGURE 6.2: The plot shows the delivered luminosity as function of the mean number of interactions per bunch crossing for 2015 in green and 2016 in cyan together with the combination in blue. The figure is taken from [150].

---

## 6.3 Preselection

### 6.3.1 Event cleaning

In Section 3.2.7 it was already explained that the complete data set would be very large, therefore in this analysis a derived data set is used. Only events are used with at least two reconstructed electrons or muons with  $p_T > 15$  GeV and  $\eta < 2.6$ , where the electrons must pass at least the `LHLoose` criteria (see Section 4.2), or events with at least two electrons with  $p_T > 20$  GeV passing the `LHVeryLoose` criteria. The two muons also have to pass some quality criteria based on track properties which are looser than the identification criteria described in Section 4.3.

As mentioned before, data is split into different periods and luminosity blocks. In order to ensure that only data is used when all detector components had been working, the luminosity blocks have to be in the Good Runs Lists(GRL)<sup>2</sup>. In addition to rejecting complete luminosity blocks, quality criteria are also applied on single events. One of these criteria is the rejection of events where noise bursts occur in the electromagnetic or hadronic calorimeter. Noise bursts happen due to large statistical fluctuations of the electronic background noise and can fake energy depositions, making it impossible to measure the energy accurately. Furthermore events are rejected where the information of the SCT might be corrupt due to ionizing particles going through electronic modules. Sometimes the trigger system has to be restarted during data taking. During such a restart not all detector information might be accessible and therefore events are rejected that are recorded during the restart.

In Table 6.2 it is shown, how much data events are removed due to the different quality criteria. The reduction of events after the removing of luminosity blocks not in the GRL is very small ( $\approx 1\%$ ). The reduction due to the GRL is about 2.6 %. After quality cuts applied, data corresponding to an integrated luminosity of  $36.1 \text{ fb}^{-1}$  are left, which is the number quoted for this data set.

### 6.3.2 Trigger selection and further event cleaning

One of the main goals of the selection is a high signal efficiency, because the number of events are expected to be limited due to the small cross section and branching fraction. Therefore it is important to take every recorded event that could possibly be categorized as event with four leptons into account. Since it is not possible to record every event, the trigger system decides which events to record (see Section 3.2.6). Every trigger chain has possibly some (small) inefficiencies, in order to minimize those, a combination of different triggers can recover some of those inefficiencies. The recovery is only possible if more than one trigger is firing the events after the complete selection. This was tested with the  $q\bar{q} \rightarrow ZZ$  simulated sample from POWHEG by checking the amount of events after the full selection, where only one of the many triggers fired. The fraction was found to be  $< 0.5\%$  which is low enough to justify the assumption of efficiency enhancement.

The trigger itself is also a limiting factor of how loose the analysis selection can be. The selection has to be more stringent than the criteria of the unprescaled trigger with the lowest  $p_T$  threshold

---

<sup>2</sup>In this analysis the GRL of 2015 is: `data15_13TeV.periodAllYear_DetStatus-v79-repro20-02.DQDefects-00-02-02_PHYS_StandardGRL_All_Good_25ns.xml` and for 2016: `data16_13TeV.periodAllYear_DetStatus-v80-pro20-08.DQDefects-00-02-02_PHYS_StandardGRL_All_Good_25ns.xml`

Quality criteria	Remaining events (rel. amount)
Total events in data set	219,059,760 (100%)
Events pass Good Runs List	213,461,445 (97,4%)
Veto events due to noise burst in the electromagnetic calorimeter	213,159,656 (99.9%)
Veto events due to noise burst in the hadronic calorimeter	213,159,571 ( $\approx 100.0\%$ )
Veto events due to trigger restart	213,159,571 (100.0%)
Veto events with incomplete tracking information	213,154,437 ( $\approx 100.0\%$ )

TABLE 6.2: Remaining events after each quality cut. The number in brackets show the relative amount of events with respect to the previous selection step. A preselection is applied beforehand to reduce the size of the data set needed for this analysis.

and identification criteria. In addition not all triggers stayed un-prescaled during the complete data taking periods, for example the  $p_T$  thresholds had to be raised for 2016 compared to 2015 since the number of protons per bunch were higher and thus the event rate. Table 6.3 shows a full list of which triggers are used for each data taking period. After the trigger requirement an event must have at least one reconstructed vertex that has two or more tracks coming out of the vertex.

## 6.4 Analysis object selection

### 6.4.1 Muon selection

All reconstructed muons have a corrected momentum scale and resolution as described before in Section 4.3. These muons are used for a basic selection using the loose selection criteria provided by the central ATLAS muon selector tool [118]. This working point is optimized for maximum reconstruction efficiency by ensuring good quality muon tracks. It also includes a general cut of  $|\eta| < 2.7$  on the muons which is the coverage of the muon system. In the coverage of the inner detector ( $|\eta| < 2.5$ ) about 97.5% of the muons are combined muons. In regions  $|\eta| > 2.5$  extrapolated muons are used. The trigger system only covers  $|\eta| < 2.4$  but at a later selection stage of the analysis at most one stand alone (SA) muon is allowed which means all other muons have to have  $|\eta| < 2.5$ . This remains with a gap of  $\Delta\eta = 0.1$  which is not covered by the trigger system and therefore events could possibly not be recorded if the muons are in this region. It has been studied that this inefficiency is below 0.1% and therefore negligible. Furthermore a basic  $p_T$  cut of 5 GeV is applied, which is the lowest threshold where calibrated muons are provided by the ATLAS muon working group [118]. One additional source of muons

	Trigger name	Run Range	Time
$e$	e24_lhmedium_L1EM20VH	→284484	only for 2015
	e60_lhmedium	→284484	
	e26_lhtight_nod0_ivarloose	296939 →	only for 2016
	e60_lhmedium_nod0	296939 →	
$\mu$	mu20_iloose	→300287	2015 + 2016 period A
	mu24_ivarmedium	296939 →302393	2016 period A-C
	mu26_ivarmedium	296939 →	
	mu40	→300287	Up to 2016 period A
	mu50	All runs	
$ee$	2e12_lhloose_L12EM10VH	→284484	
	2e17_lhvloose_nod0	296939 →	
$\mu\mu$	mu18_mu8noL1	→284484	
	mu20_mu8noL1	→ 302393	Up to 2016 period C
	2mu10	→300287	
	2mu14	All runs	
	mu22_mu8noL1	All runs	
	mu20_nomucomb_mu6noL1_nscan03	296939 →302393	
$e\mu$	e17_lhloose_mu14	→284484	
	e17_lhloose_nod0_mu14	296939 →	
$3e$	e17_lhloose_2e9_lhloose	→284484	
	e17_lhloose_nod0_2e9_lhloose_nod0	296939 →	
$3\mu$	3mu6	All runs	

TABLE 6.3: Triggers used in the analysis together with the associated runs. The name of the triggers includes the  $p_T$  threshold and possible identification and isolation requirement.

that can contribute to background that is not covered by simulation are cosmic muons. In order to reduce those, a restriction on the longitudinal distance,  $|\Delta z_0|$ , between the track of the inner detector<sup>3</sup> and the position of the vertex with highest  $\sum p_T$ , is placed. Since the muons in the more forward region are expected to have a larger error on  $|\Delta z_0|$ , the cut is placed at  $|\Delta z_0 * \sin \theta| < 0.5$  mm, where  $\theta$  is the angle between the track and the beam axis. In addition a cut on the transverse impact parameter at  $d_0 < 1$  mm is done, to further reduce the cosmic background.

### 6.4.2 Electron selection

Electron candidates that are used for the selection must be reconstructed and calibrated as it is explained in Section 4.2. In order to ensure that the tracking information is available, the  $|\eta|$  of the energy deposition in the calorimeter has to be less than 2.47. The coverage of the tracking detector is  $|\eta| < 2.5$ , but to be sure that the whole cluster is inside the "inner wheel" of the electromagnetic calorimeter the cut is set to  $|\eta| < 2.47$ . There is also a transition region between the barrel and endcap electromagnetic calorimeters which has worse energy resolution and lower reconstruction efficiencies. To maximize signal efficiency this region is included and

<sup>3</sup>The cut is not applied on SA muons since these do not have a track in the inner detector.

---

the simulation is corrected accordingly. The minimal  $p_T$  that is required is 7 GeV which is the lowest threshold where electron efficiency corrections for the simulation are provided from the central ATLAS calibration group [117]. The  $p_T$  value chosen here is calculated by the energy measurement of the calorimeter and the  $\eta$  information from the associated track. Furthermore electron candidates are removed where it is known that some parts of the calorimeter did not operate well in that time and special region of the cluster. This can happen due to malfunction of some electronic component or problems with the power supply. Only about 0.4% of the electrons after the  $p_T$  cut are removed by this criterion. In addition the electron candidates have to fulfill the cut on the number of hits in the pixel and silicon detector that are done by using the `LHVeryLoose` identification criteria described in 4.2. Also electron candidates have to pass the same  $|\Delta z_0 * \sin \theta|$  cut as the muons, but the reason here is to reduce electrons from secondary decay vertices.

### 6.4.3 Jet selection

In this analysis jets are used that are reconstructed with the anti- $k_T$  algorithm with a radius parameter of  $R = 0.4$  (see Section 4.4 for more details). The kinematic restrictions of the jets are  $p_T > 30$  GeV to suppress jets from pileup that are more common at low  $p_T$ . The cut is also in line with the selection of the  $pp \rightarrow H + X \rightarrow ZZ^* + X \rightarrow \ell^+ \ell^- \ell'^+ \ell'^- + X$  analysis. The  $|\eta|$  of the jets is restricted to be smaller than 4.5 to match the region covered by the calorimeter<sup>4</sup>. To gain further reduction of pileup jets, discriminating power of the JVT (see Section 4.4) is used. For central jets ( $|\eta| < 2.4$ ) with  $p_T < 60$  GeV the JVT threshold has to be above the default value of 0.59. In the forward regions ( $|\eta| > 2.5$ ) the forward JVT is used for jets with  $p_T < 60$  GeV at the medium working point. In the transition region ( $2.4 < |\eta| < 2.5$ ) all jets have to have a  $p_T > 60$  GeV.

## 6.5 Event selection

### 6.5.1 Overlap removal

In order to avoid the double counting of objects (e.g. counting one signature as electron and a jet) an overlap removal is carried out. The objects used for this overlap removal are the selected objects described before. Only electrons are taken into account that pass the full `LHLoose` identification criterion to avoid that electrons failing the `LHLoose` criterion, which are removed at a later point in the event selection, remove other objects. There are different overlap criteria which are implemented in an ATLAS overlap removal tool. In this analysis a lepton favored working point is used, which is summarized in Table 6.4. The procedure is thereby sequential, starting with an electron-electron overlap removal where the electrons with the highest  $p_T$  are kept when they share a track or have overlapping calorimeter cluster with other electrons. After that, calorimeter tagged muons are removed which share a track with electrons. Then electrons are removed which share tracks with remaining muons. In the end jets are removed if they have a

---

<sup>4</sup>Indeed the calorimeter covers regions up to  $|\eta| = 4.9$ , but in order to ensure that the complete cluster of an energy deposition is inside the calorimeter the cut is placed at smaller values than the coverage.

	Reference objects	Criteria
Remove electrons	electrons	Share a track or have overlapping calorimeter cluster. Keep higher $p_T$ electron
Remove muons	electrons	Share track and muon is calo-tagged
Remove electrons	muons	Share track
Remove jets	electrons	$\Delta R_{e-jet} < 0.4$
	muons	$\Delta R_{\mu-jet} < 0.4$ or muon track is ghost-associated to jet

TABLE 6.4: Overlap removal criteria between baseline objects in the analyses. The overlap removal follows the order shown in this table. Once an object has been marked as removed, it does not participate in the subsequent stages of the overlap removal procedure.

distance of  $\Delta R_{e-jet} < 0.4$  to electrons or muons or if tracks from a muon are "ghost-associated" to the jet. This "ghosting" technique [151] uses the four momenta of the muon tracks as an additional input for the jet clustering algorithm (see Section 4.4) after setting the  $p_T$  calculated from the muon tracks to zero. If a muon track is clustered into a jet it is "ghost-associated". The impact of the overlap removal on objects in data is shown in Table 6.5. It can be seen that almost no muons are removed, 1.7% of electrons and about half of the jets. This large removal of jets is reasoned by the fact that most electrons are also reconstructed as a jet.

Objects	Before OR	After OR	Relative amount removed
Electrons	224054550	220324847	1.6%
Muons	233071422	233064553	< 0.01%
Jets	274991028	140886535	48.8%

TABLE 6.5: Impact of overlap removal (OR) on the different objects used in the analysis. The number before overlap removal corresponds to the number of objects after the applied object selection criteria.

### 6.5.2 Further event cleaning

It is possible that proton losses before the interaction point build cascades that reach the detector which results in measurable energy depositions in the calorimeter. Also calorimeter noise and cosmic rays can deposit energy in the calorimeter which is not from the hard scattering process. Jets that are build by such depositions can also fulfill the before mentioned selection and enter as background the analysis. Most of this background is already reduced by event cleaning cuts but a small fraction remains. To get rid of this background an ATLAS tool is used that removes events with bad jets. The definition of bad jets is based on different quantities e.g. the jet energy deposition along the expected direction of the calorimeter shower (more information can be found in [152]). The operating point is optimized for 99.5% efficiency to select events with jets from proton-proton collision. In this analysis only 0.2% of events are removed.

---

### 6.5.3 Quadruplet selection

In order to select  $pp \rightarrow ZZ + X \rightarrow \ell^+ \ell^- \ell'^+ \ell'^- + X$ <sup>5</sup> events there have to be at least four selected muons or electrons which could be paired to at least two SFOC<sup>6</sup> pairs (called quadruplets), on which further selection criteria are applied. If electrons are present in a quadruplet, at least two have to pass the LHLoose identification criterion. The reason not to apply this cut to all electrons if more than two are present is due to the fact that for some background estimations, that are explained later in Section 7.2.3, the identification criteria is reverted for one or two electrons. The  $p_T$  of the leptons in the quadruplets must satisfy a hierarchical  $p_T$  cut which is 20 GeV for the hardest lepton, 15 GeV for the second hardest and 10 GeV for the third hardest lepton. This cut is mostly motivated by the thresholds of the trigger, where the lowest multi electron trigger is one with a  $p_T$  requirement of 17 GeV for at least one electron. The trigger is not fully efficient close to the threshold (which is shown in [153]) and therefore the cut in the analysis is set to 20 GeV. The other  $p_T$  thresholds are synchronized with the  $pp \rightarrow H + X \rightarrow ZZ^* + X \rightarrow \ell^+ \ell^- \ell'^+ \ell'^- + X$  analysis, but it was checked (using signal simulation) that the  $p_T$  threshold of the second and third hardest lepton could be even harder without losing much  $ZZ$  on-shell events. Furthermore only quadruplets are kept that have at most one calo tagged or stand alone muon because those muons are not very well calibrated and more than one would give worse energy resolution. It is still possible that there are more than one quadruplet at this point, especially when at least four leptons have the same flavor. Therefore the quadruplet is chosen, which minimizes the sum:

$$|m_{\ell\ell,a} - m_Z| + |m_{\ell\ell,b} - m_Z| , \quad (6.1)$$

where  $m_{\ell\ell,a}$  is the invariant mass of one same flavor lepton pair and  $m_{\ell\ell,b}$  of the other one and  $m_Z$  the pole mass of the  $Z$  boson [31]. This procedure is found to give a slightly better signal efficiency ( $\approx 2\%$ ) in the on-shell region, compared to a “lexographic” ranking. In a lexographic ranking the pairs with the invariant mass nearest and second nearest to the  $Z$  pole mass are chosen as  $Z$  candidates. After choosing two pairs the one nearer to the  $Z$  pole mass is called primary and the one more far away secondary, the one with higher transverse momentum is called leading and the other one subleading pair.

Table 6.6 shows the remaining events after requiring at least two, three and four leptons together with the number of events, where at least one quadruplet remains after the selection step. It is visible that by increasing the lepton multiplicity the number of events decreases drastically. It is also shown that about half of the events with four leptons have not two same flavor opposite charge pairs, which is mostly caused by not applying isolation criteria or further identification on the leptons at this stage and thus many of the four lepton events come from objects faking the leptons, e.g. jets faking electrons. The size of the fake contributions after the complete selection is estimated later in Section 7.2.3. After the quadruplet selection about 8.5 million events are remaining.

---

<sup>5</sup>In the following often the short notation for the final  $\ell^+ \ell^- \ell'^+ \ell'^-$  state:  $4\ell$  is used.

<sup>6</sup>Same Flavor Opposite Charge

### 6.5.4 Final Event selection

All leptons have to be well separated from each other requiring an  $\Delta R$  between same flavor objects larger than 0.1 and for different flavor objects larger than 0.2. There are possible resonances of particles that can occur within a jet due to parts of the parton shower that decay leptonically and thus passing the selection before. These resonances, dominantly quarkonia e.g.  $J/\Psi$ , are removed by rejecting events with invariant masses of the pairs  $< 5$  GeV. Thereby, not only the pairs coming from the pairing algorithm are used, but also the cross pairings, in the case of selecting four leptons with the same flavor. Additionally, events are removed where not all leptons are isolated, using an ATLAS provided tool at a working point called `FixedCutLoose`. This isolation requirement is build out of two parts. One is build by adding the transverse energy in the calorimeter in a cone with  $\Delta R < 0.2$  around the lepton (excluding the energy of the lepton) and require this divided by the  $p_T$  of the object to be less than 0.3. The other one is a track isolation requirement doing the same but using the tracks for the  $p_T$  instead of the calorimeter cells and a  $\Delta R < 0.3$  with a cut value of 0.15. Also now all electrons have to pass the `LHLoose` criteria and all leptons have to pass a cut on the  $d_0$ -significance (see Section 4.2 for definition) of 5 (3) for electrons (muons). In the very end the two  $Z$  boson candidates are required to be on-shell which means the invariant mass of the di-lepton pairs has to be between 66 GeV and 116 GeV. This mass window is a rather wide choice and mostly historically reasoned and makes it easier to compare to previous results from ATLAS. The mass cut is illustrated in Figure 6.3 where the leading di-lepton pair is shown against the subleading di-lepton pair before the on-shell cut is applied. The pink boxes correspond to the prediction of the  $q\bar{q}$  induced process from POWHEG. The sizes of the boxes are proportional to the number of expected events in each bin. The dashed lines symbolize the on-shell cuts. It can be seen that most of the selected events are in the on-shell region.

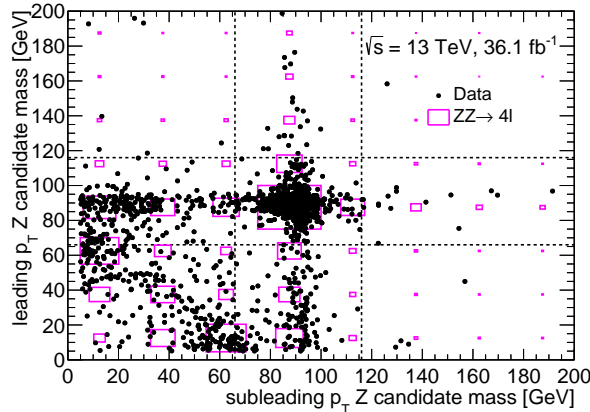


FIGURE 6.3: Invariant mass of the leading  $Z$  boson candidate vs. the invariant mass of the subleading  $Z$  boson candidate before the on-shell requirement. All other selection steps have been applied. Data is shown as black dots and prediction of the  $q\bar{q}$  induced signal process is shown as pink boxes. The sizes of the boxes are proportional to the number of expected events in each bin.

The impact of the single cuts on the number of data events is shown at the bottom of Table 6.6. The events are now split into three different channels, one with four electrons, one with two electrons and two muons and a last one with four muons. The largest reduction is done by the



requirement of having all electrons passing the `LHLoose` working point which reflects that up to that point many electrons can come from fake sources. Also the  $d_0$  significance requirement reduced the number of events, showing that events beforehand included leptons which originate more likely from secondary particle decays. In the end one ends up with only 1017 events in the signal region, 249 events in the channel with four electrons, 465 in the mixed channel and 303 events in the muon channel. One of the selected events in the mixed channel is shown in

Event preselection	# events passing			
Cleaning	213,154,437			
Trigger	181,518,741			
Vertex	181,518,734			
Jet cleaning	181,478,233			
$\geq 2$ selected leptons	157,974,555			
$\geq 3$ selected leptons	65,630,012			
$\geq 4$ selected leptons	30,764,508			
Quadruplet selection	# events with $\geq$ one quadruplet passing			
Contains SFOC pairs	14,024,248			
Electron quality	11,442,369			
Hierarchical $p_T$ cut	8,580,192			
Muon quality	8,580,023			
Event selection	# events passing			
	4e	2e2 $\mu$	4 $\mu$	Combined
$\Delta R$	1,354,304	2,086,303	17,683	2,745,645
Quarkonia Veto	1,063,914	1,396,883	12,305	1,942,643
Electron ID	482	2,745	3,394	6,621
Impact Parameter	449	1,358	1,115	2,922
Isolation	351	809	571	1,731
66 GeV $< m_{12,34} < 116$ GeV	249	465	303	1,017

TABLE 6.6: The table is split in four parts. The first part shows the number of events remaining after different pre-selection steps. The second part shows the remaining events after requiring different lepton multiplicities of selected leptons. The third part of the table shows the events where at least one quadruplet remains the selection criterion. At the end of the quadruplet selection one pair of lepton pairs is chosen as  $Z$  boson candidates. Which is why after this step it is possible to split events into different channels unambiguously as it done in the bottom part of the table for further event selection steps.

Figure 6.4. The energy depositions of the electrons in the calorimeter are shown in yellow. The tracks are shown in green for the electrons and in red for the muons. The  $p_T$  of the four lepton system is only 5 GeV which leads to a nice back-to-back topology of the decay products of the  $Z$  bosons in the  $r - \phi$  plane. Another event display for an event from 2016 can be found in Appendix C.

## 6.6 Signal efficiency

One main goal of the selection is the reduction of background while keeping the signal efficiency as high as possible. All of the described selection steps before are the loosest criteria

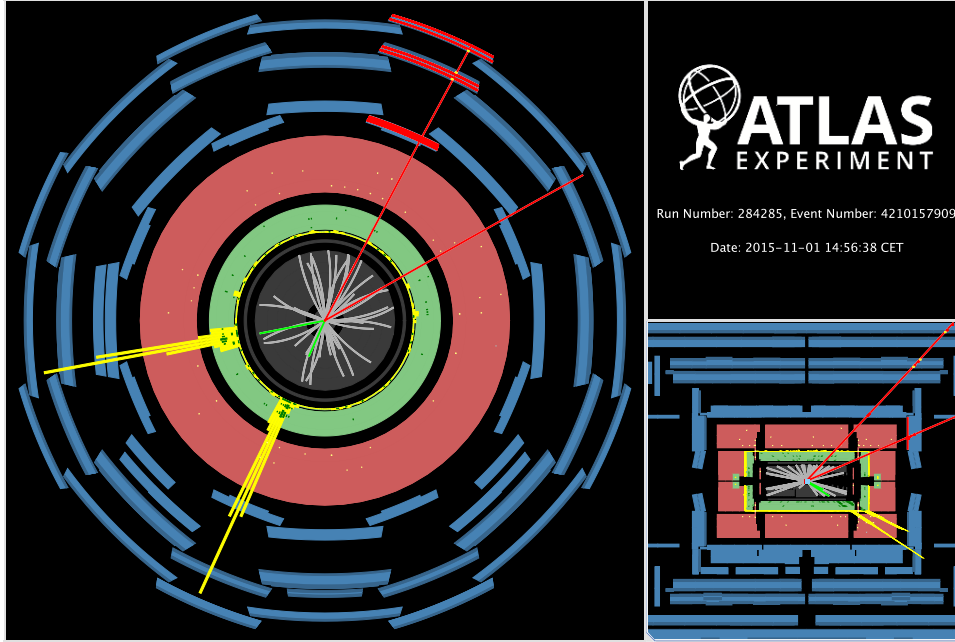


FIGURE 6.4: Event display of an event recorded in 2015. The left panel shows the  $r - \phi$  plane and the right panel the  $z - \eta$  plane. The energy depositions of the electrons in the calorimeter are shown in yellow. The tracks of the electrons are shown in green and the one of the muons in red. Inner detector tracks with a transverse momentum larger than 2 GeV are shown in gray. The four lepton system has an invariant mass of 408 GeV, transverse momentum of 4 GeV, and a rapidity of 1.3. The first  $Z$  boson candidate is reconstructed from two oppositely charged electrons ( $p_T = 116$  GeV,  $\eta = 1.45$  and  $p_T = 87$  GeV,  $\eta = 1.21$ ), has a mass of 95 GeV and transverse momentum of 181 GeV. The other candidate has a mass of 88 GeV, a transverse momentum of 183 GeV and is reconstructed from two oppositely charged muons ( $p_T = 83$  GeV,  $\eta = 0.84$  and  $p_T = 107$  GeV,  $\eta = 1.58$ ). The figure is taken from [154].

recommended by the different performance groups of ATLAS to keep as many signal events as possible. But nonetheless there are inefficiencies of those criteria, including also the one of the reconstruction, that can not be minimized further and due to the high lepton multiplicity enter with higher power. For giving an example the reconstruction efficiency per electron could be up to 99% in some kinematic region (see [117]) but when having four electrons in the final state this would lead to an event efficiency of  $0.99^4 = 0.96 \stackrel{\Delta}{=} 96\%$ . It is therefore beneficial to check at which criteria the signal efficiency suffers most. This study includes simulated events from three  $ZZ$  signal processes:  $q\bar{q}$  initiated,  $gg$  initiated and the electroweak  $ZZjj$  contribution, which are combined, taking the respective cross sections into account. The estimation of the efficiency is done on a subset of events that fulfill the fiducial definition (applied on generator level) not to be biased from acceptance effects. Table 6.7 shows the event selection efficiencies for different selection steps. The efficiencies quoted in the table are with respect to the previous selection step with the exception of the first row, which is calculated with all events passing the fiducial selection in the denominator. The last row shows the total selection efficiency. Technically the efficiency is calculated by building the ratio:

$$eff = \frac{N_{cut,i}}{N_{cut,i-1}}, \quad (6.2)$$

Selection step	Relative event efficiency			
Trigger	99.449 ± 0.014			
Vertex	100.0 ± 0.0			
Jet Cleaning	99.9836 ± 0.0025			
≥ 2 selected leptons	99.919 ± 0.005			
≥ 3 selected leptons	98.959 ± 0.018			
≥ 4 selected leptons	88.42 ± 0.06			
Contains SFOC pairs	94.70 ± 0.04			
Electron Quality	99.9797 ± 0.0031			
Hierarchical $p_T$ cut	99.930 ± 0.006			
Muon Quality	99.940 ± 0.005			
	4e	2e2μ	4μ	combined
$\Delta R$	99.914 ± 0.014	99.541 ± 0.022	99.993 ± 0.004	99.756 ± 0.010
Quarkonia Veto	99.802 ± 0.020	99.948 ± 0.007	99.973 ± 0.006	99.923 ± 0.005
Electron ID	76.53 ± 0.21	87.98 ± 0.11	100 ± 0	88.65 ± 0.07
Impact Parameter	99.32 ± 0.04	98.93 ± 0.04	98.76 ± 0.05	98.957 ± 0.023
Isolation	92.97 ± 0.14	92.615 ± 0.100	90.82 ± 0.13	92.11 ± 0.06
On-shell	99.25 ± 0.05	99.153 ± 0.033	98.56 ± 0.05	99.012 ± 0.021
overall	48.44 ± 0.21	59.49 ± 0.15	71.15 ± 0.19	59.77 ± 0.09

TABLE 6.7: Event selection efficiency for combined signal expectation. The  $q\bar{q} \rightarrow ZZ \rightarrow 4\ell$  contribution is calculated using the POWHEG sample. The efficiencies are given with respect to the previous selection step, except the first row which is in relation to all events in the fiducial region and the last row which shows the combined efficiency of all selection steps. The uncertainties only account statistical uncertainties due to the finite sample size.

where  $N_{cut_i}$  is the  $i$ -th cut. The numerator is a subset of the denominator, therefore the uncertainty is given by the binomial uncertainty:

$$\Delta eff = \frac{1}{N_{cut,i-1}} \sqrt{N_{cut,i}(1 - N_{cut,i}/N_{cut,i-1})}. \quad (6.3)$$

The results in the table show that for most selection criteria the efficiency is 95% or better. One exception is the requirement of having four or more leptons, which reflects that at this point the efficiency of the electron and muon selection enters completely. Requiring three or more selected leptons still gives the chance for one of the four generated leptons from the  $Z$  boson decay not to be selected and thus pushing the efficiency, which is not any more the case when having four or more selected leptons. Furthermore about 5% of the remaining signal events get cut away by requiring same flavor opposite charge pairs for at least one quadruplet in an event. This is mostly caused due to allowing quadruplets with a very loose electron identification criteria and therefore having events with quadruplets where one or more lepton is faked by e.g. a jet. The behavior of having quadruplets with one or more leptons not from the hard interaction is also visible in low efficiencies of the electron ID and isolation on event level which can be up to 24%. It does not have to be the case that the efficiency is the same for the all three signal processes. Indeed the  $gg$  initiated process has an about 3% higher overall signal efficiency compared to the  $q\bar{q}$  initiated process as it is shown in Table B.2 and Table B.1 of appendix B. That is justified by the fact that the  $gg$  initiated process has more leptons in the central region compared to the  $q\bar{q}$  initiated process. The efficiency of the electroweak  $ZZjj$  process is lower because the

---

two jets from the hard interaction have larger  $p_T$  compared to jets from e.g. pileup processes and thus can be easier wrongly identified as e.g. electron. One rather simple improvement of the signal efficiency would be the application of the `LHLoose` electron identification criteria already on object level. This would increase the overall efficiency (taking all signal processes into account) in the 4e channel for 1.5% but making a background determination less consistent (and technically more challenging) and therefore not considered.

# Chapter 7

## Standard Model expectation

This chapter describes the expectation based on Standard Model processes and compares it with selected data. As already mentioned the background is presumed to be small and most of the Standard Model expectation is build by the signal  $ZZ \rightarrow \ell^+ \ell^- \ell'^+ \ell'^-$  contribution, that is described in Section 7.1. Another part of the expectation is background, which are contributions that pass the signal selection but are not originating from the  $ZZ \rightarrow \ell^+ \ell^- \ell'^+ \ell'^-$  signal process in question. This is split in two parts. On the one hand there is background with at least four genuine leptons which is described in Section 7.2.1 and on the other hand there is background where up to two leptons are not from genuine sources which is described in Section 7.2.3. Systematic uncertainties from experimental and theoretical sources are described in Section 7.3. The last section of this chapter compares the total Standard Model prediction to data.

### 7.1 Signal expectation

In order to check how well the expectation describes data, a good understanding of the signal expectation is needed. It was already mentioned before that three different signal contributions,  $q\bar{q}$  initiated,  $gg$  initiated and electroweak  $ZZjj$  production are used, to build the signal expectation. The distributions and yields, after applied selection, are weighted to the integrated luminosity of data as described in Section 5.3. Table 7.1 shows the expected yields for the different signal processes. The  $q\bar{q}$  initiated process has the four lepton mass dependent NNLO QCD k-factor and NLO EW k-factor applied. The  $gg$  initiated process is scaled by the NLO

Channel	$4e$	$2e2\mu$	$4\mu$	Total $4\ell$
$q\bar{q} \rightarrow 4\ell$ (SHERPA)	$168.2 \pm 1.6$	$398.8 \pm 2.3$	$247.7 \pm 1.8$	$814.7 \pm 3.3$
$q\bar{q} \rightarrow 4\ell$ (POWHEG)	$160.4 \pm 1.6$	$381.2 \pm 2.4$	$238.5 \pm 1.9$	$780.2 \pm 3.4$
$gg \rightarrow 4\ell$	$21.35 \pm 0.22$	$50.32 \pm 0.34$	$29.74 \pm 0.26$	$101.4 \pm 0.5$
$q\bar{q} \rightarrow 4\ell jj$ (electroweak)	$4.36 \pm 0.34$	$10.3 \pm 0.5$	$6.5 \pm 0.4$	$21.1 \pm 0.7$
Combined (using POWHEG)	$186.2 \pm 1.6$	$441.8 \pm 2.5$	$274.7 \pm 2.0$	$903 \pm 4$

TABLE 7.1: Expected number of signal events with four isolated genuine leptons in the final state estimated with simulation. Only statistical uncertainties are shown.

k-factor of 1.67 as described in Section 5.1. The dominant contribution is given by the  $q\bar{q}$  initiated process, as expected. Followed from the gluon initiated process with about 11% and 2% from the electroweak production of  $ZZjj$ . In this table also differences in the yields between the SHERPA and POWHEG predictions of the  $q\bar{q}$  initiated process are visible. The SHERPA yield is higher since no EW k-factors are applied on this sample and SHERPA includes further real parton emission in the matrix level which increases the cross section of the simulated process. Additionally, there is the part of double parton interaction (see Section 2.2.1) where two partons of one proton interact with two partons of the other proton via single  $Z$  production which could also end up in four charged leptons. This process is also part of the signal definition but not included in the simulations mentioned before. In order to get an estimate for the size of this contribution one can use the formula [155]:

$$\sigma_{Z+Z}^{\text{tot}} = \frac{\sigma_Z^{\text{tot}} \times \sigma_Z^{\text{tot}}}{2\sigma_{\text{eff}}}, \quad (7.1)$$

where  $\sigma_Z^{\text{tot}}$  is the cross section to produce one on-shell  $Z$  boson and  $\sigma_{\text{eff}}$  an effective area parameter for double parton scattering. The effective area parameter has been measured by ATLAS using data recorded at  $\sqrt{s} = 7$  TeV to  $15_{-3}^{+6}$  mb [156]. Various measurements at different center of mass energies [157–164] suggest no significant dependence on the center of mass energy nor the final state particles. The total on-shell single  $Z$  boson cross section times the leptonic branching ratio was measured at 13 TeV [165] to  $1869 \pm 173$  pb. After correcting for the leptonic branching fraction of 3.36% [31] the resulting total double parton scattering cross section for two  $Z$ 's is then  $\sigma_Z^{\text{tot}} = 0.103_{-0.033}^{+0.045}$  using gaussian error propagation of the uncertainties of the input parameters. Compared to the total cross section obtained with MATRIX, presented in Chapter 5.1, this is  $0.61_{-0.22}^{+0.31}\%$ . Assuming the acceptance and efficiency correction is the same as for all signal processes, less than 1% of the signal expectation is from double parton scattering.

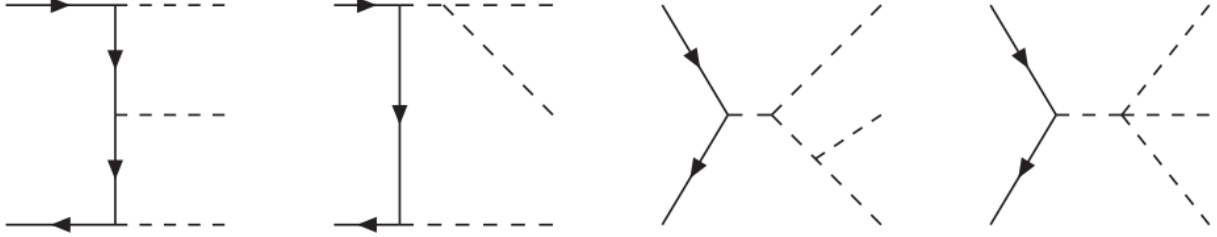
## 7.2 Backgrounds

### 7.2.1 Genuine background

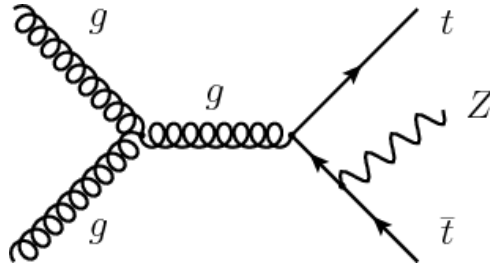
There are further Standard Model processes with at least four isolated genuine leptons from boson decays. One of these backgrounds is the  $ZZ$  process where at least one boson decays to  $\tau$ -leptons which then decay leptonically. This contribution is estimated by using the  $q\bar{q}$  initiated  $ZZ$  sample from POWHEG which is also used for the signal estimation but filtering only for events with at least one  $Z$  boson decaying to  $\tau$ -leptons which decay further to electrons or muons. A further contribution is triboson production ( $ZZZ, WZZ, WWZ$ ) with all leptonically decaying bosons leading to at least four leptons in the final state. Examples of how three bosons can be produced in the  $q\bar{q}$  initial state is shown in Figure 7.1(a). Processes where the third boson decays hadronically are considered as signal and included in the before mentioned electroweak process of  $ZZjj$  production which is simulated with SHERPA. Furthermore  $gg \rightarrow t\bar{t}Z$  can contribute when the top-quarks and the  $Z$  boson decay leptonically. The dominant production diagram is shown in Figure 7.1(b).

After full selection is applied the expected yield, weighted to an integrated luminosity of

36.1 fb<sup>-1</sup> is shown in Table 7.2. The uncertainties include only the statistical uncertainties of the simulated samples.



(a) Leading order processes contributing to  $q\bar{q} \rightarrow VVV$  with  $V$  being  $W$  or  $Z$ . Quarks are marked with straight lines and bosons with dashed lines. Graphics are taken from [166]



(b) Dominant contribution of the  $gg \rightarrow t\bar{t}Z$  background. Graphic is taken from [167].

FIGURE 7.1: Leading order production graphs contributing to the genuine background.

Channel	$4e$	$2e2\mu$	$4\mu$	Total $4\ell$
Triboson	$0.729 \pm 0.019$	$1.613 \pm 0.029$	$1.033 \pm 0.025$	$3.375 \pm 0.042$
$ZZ \rightarrow \tau\tau[ll, \tau\tau]$	$0.614 \pm 0.098$	$0.552 \pm 0.083$	$0.575 \pm 0.094$	$1.74 \pm 0.16$
$t\bar{t}Z$	$0.975 \pm 0.047$	$2.229 \pm 0.074$	$1.704 \pm 0.069$	$4.91 \pm 0.11$
Combined	$2.32 \pm 0.11$	$4.39 \pm 0.12$	$3.31 \pm 0.12$	$10.03 \pm 0.20$

TABLE 7.2: Yield of background with four isolated genuine leptons in the final state estimated with simulation. Only statistical uncertainties are shown.

## 7.2.2 Single $Z$ pileup background

In principle it is possible that four leptons, which pass the selection, originate from single  $Z \rightarrow \ell^+\ell^-$  decays from different  $pp$  interactions in the same event due to pileup effects. Cuts that are placed on the parameters ( $d_0, |\Delta z_0 * \sin(\theta)|$ ) are expected to reject most of this background. Nevertheless, the total cross section of single  $Z \rightarrow \ell^+\ell^-$  production is larger by a factor of about 1300 compared to the on-shell  $ZZ$  production and therefore also very small fractions of initial  $Z \rightarrow \ell^+\ell^-$  events might be a relevant background contribution. An estimate of this background was calculated by members of the ATLAS  $ZZ$  analysis group [62] by using single  $Z \rightarrow \ell^+\ell^-$  events generated with PYTHIA. The prediction for 36 fb<sup>-1</sup> is  $< 1$  event and therefore negligible.

## 7.2.3 Non-genuine background

### 7.2.3.1 Methodology

Processes where at least one lepton is either misidentified or originating from leptonic decays of hadrons can also contribute to the background. Leptons from such contributions are called fake leptons ( $F$ ) in the following. Prompt leptons from  $Z$  decays in the hard interaction are called real leptons ( $R$ ). An example of misidentification of electrons are jets that mimic the electron properties and pass the signal selection. An example of misidentification for muons is the leptonic decay of hadrons. These contributions can be split into two categories: Events with two fake lepton, which originate mainly from  $Z$ +jets,  $t\bar{t}$ ,  $W^+W^-$ +jets ( $N_{RRFF}$ ) and events with one fake lepton mainly from  $WZ$ +jets ( $N_{RRRF}$ ). Contributions with three and four fake leptons are assumed to be much smaller and are therefore neglected.

Since the fake contributions are not modeled very well in simulation a data driven approach is chosen. One problem is that the true number of events with one or two fake leptons is not directly accessible in data but it is possible to relate them to measurable quantities. The measurable quantities are based on certain selection criteria: Leptons passing all signal selection criteria, called “selected leptons” (denoted by  $L$ ) or leptons failing one (or both for muons) of the following cuts:

- isolation or impact parameter (or both) for muons,
- isolation or LHLoose identification (but not both) for electrons

which are called “lepton-like” leptons (denoted by  $J$ ). The connection between the measurable quantities and the real numbers can be done by introducing a matrix. This matrix contains the efficiency of a fake lepton passing the signal selection ( $f$ ), the efficiency of a real lepton passing the signal selection ( $e$ ), the efficiencies of real leptons passing the inverted selection ( $\bar{e} = 1 - e$ ) and the efficiency of a fake lepton passing the inverted selection ( $\bar{f} = 1 - f$ ). In the following the assumption is made that  $e$  is 1 and therefore  $\bar{e} = 0$ . A correction for this assumption is applied later on. Writing down the complete matrix with up to two fakes and 4 leptons yields:

$$\begin{pmatrix} N_{LLLL} \\ N_{JLLL} \\ N_{LJLL} \\ N_{LLJL} \\ N_{LLLJ} \\ N_{JJLL} \\ N_{JLJL} \\ N_{JLLJ} \\ N_{LJJL} \\ N_{LJLJ} \\ N_{LLJJ} \end{pmatrix} = \begin{pmatrix} 1 & f_1 & f_2 & f_3 & f_4 & f_1f_2 & f_1f_3 & f_1f_4 & f_2f_3 & f_2f_4 & f_3f_4 \\ 0 & \bar{f}_1 & 0 & 0 & 0 & \bar{f}_1f_2 & \bar{f}_1f_3 & \bar{f}_1f_4 & 0 & 0 & 0 \\ 0 & 0 & \bar{f}_2 & 0 & 0 & f_1\bar{f}_2 & 0 & 0 & \bar{f}_2f_3 & \bar{f}_2f_4 & 0 \\ 0 & 0 & 0 & \bar{f}_3 & 0 & 0 & f_1\bar{f}_3 & 0 & f_2\bar{f}_3 & 0 & \bar{f}_3f_4 \\ 0 & 0 & 0 & 0 & \bar{f}_4 & 0 & 0 & f_1\bar{f}_4 & 0 & f_2\bar{f}_4 & f_3\bar{f}_4 \\ 0 & 0 & 0 & 0 & 0 & \bar{f}_1\bar{f}_2 & 0 & 0 & 0 & 0 & 0 \\ 0 & 0 & 0 & 0 & 0 & 0 & \bar{f}_1\bar{f}_3 & 0 & 0 & 0 & 0 \\ 0 & 0 & 0 & 0 & 0 & 0 & 0 & \bar{f}_1\bar{f}_4 & 0 & 0 & 0 \\ 0 & 0 & 0 & 0 & 0 & 0 & 0 & 0 & \bar{f}_2\bar{f}_3 & 0 & 0 \\ 0 & 0 & 0 & 0 & 0 & 0 & 0 & 0 & 0 & \bar{f}_2\bar{f}_4 & 0 \\ 0 & 0 & 0 & 0 & 0 & 0 & 0 & 0 & 0 & 0 & \bar{f}_3\bar{f}_4 \end{pmatrix} \begin{pmatrix} N_{RRRR} \\ N_{FRRR} \\ N_{RFRR} \\ N_{RRFR} \\ N_{RRRF} \\ N_{FFRR} \\ N_{FRFR} \\ N_{FRRF} \\ N_{RFFR} \\ N_{RFRF} \\ N_{RRFF} \end{pmatrix}$$

The first line reflects the number of events in the signal region. By using the other lines and putting them into the first line it yields:



$$\begin{aligned}
N_{LLLL} = N_{RRRR} + N_{JLLL} \frac{f_1}{\bar{f}_1} + N_{LJLL} \frac{f_2}{\bar{f}_2} + N_{LLJL} \frac{f_3}{\bar{f}_3} + N_{LLLJ} \frac{f_4}{\bar{f}_4} \\
- N_{JJLL} \frac{f_1}{\bar{f}_1} \frac{f_2}{\bar{f}_2} - N_{JLLJ} \frac{f_1}{\bar{f}_1} \frac{f_3}{\bar{f}_3} \\
- N_{JLLJ} \frac{f_1}{\bar{f}_1} \frac{f_4}{\bar{f}_4} - N_{LJLL} \frac{f_2}{\bar{f}_2} \frac{f_3}{\bar{f}_3} \\
- N_{LJLL} \frac{f_2}{\bar{f}_2} \frac{f_4}{\bar{f}_4} - N_{LLJL} \frac{f_3}{\bar{f}_3} \frac{f_4}{\bar{f}_4}
\end{aligned} \tag{7.2}$$

which is often written in a short notation

$$N_{LLLL} = N_{RRRR} + N^{\ell\ell j} \frac{f_i}{\bar{f}_i} - N^{\ell\ell jj} \frac{f_i}{\bar{f}_i} \frac{f_j}{\bar{f}_j}. \tag{7.3}$$

The first term,  $N_{RRRR}$ , is reflecting the signal contribution in the selected events. The other terms show the background contribution due to fakes. The lower case  $\ell$  and  $j$  terms together with the  $f_i$ 's and  $f_j$ 's stand for the sum of the terms with one or two leptons passing the inverted selection from Equation 7.2. To compensate any real lepton contribution in the events with fakes (or in other words compensating the effect of the  $e = 1$  assumption) contributions from  $ZZ \rightarrow \ell^+ \ell^- \ell'^+ \ell'^-$  processes are subtracted using simulation, leading to following equation for the background with fake contributions:

$$N_{\text{bkg}}^{\text{misid. leptons}} = N^{\ell\ell j} \frac{f_i}{\bar{f}_i} - N_{ZZ}^{\ell\ell j} \frac{f'_i}{\bar{f}'_i} - \left( N^{\ell\ell jj} \frac{f_i}{\bar{f}_i} \frac{f_j}{\bar{f}_j} - N_{ZZ}^{\ell\ell jj} \frac{f'_i}{\bar{f}'_i} \frac{f'_j}{\bar{f}'_j} \right), \tag{7.4}$$

where  $f'_i$  and  $f'_j$  indicate that the fake factor is applied separately to data events and the real lepton correction. The inversion of the cuts to get  $N^{\ell\ell j}$  and  $N^{\ell\ell jj}$  is done on event level after the quadruplet selection. On the one hand this is done due to technical reasons. On the other hand it is preferable to split between background and signal events after as many selection steps as possible are applied. This ensures that all other selection criteria are applied on signal events and events in the  $N^{\ell\ell jj}$  ( $N^{\ell\ell j}$ ) category in the same way.

### 7.2.3.2 Fake factor determination

One ingredient for Equation 7.4 is the ratio:  $f/\bar{f}$  which is called fake factor ( $F_{\text{mis-ID}}$ ) and is defined as:

$$F_{\text{mis-ID}} = \frac{N_L}{N_J}, \tag{7.5}$$

where  $L$  and  $J$  are defined as before. The  $F_{\text{mis-ID}}$  is determined for electrons and muons separately in a  $pp \rightarrow Z + X \rightarrow \ell^+ \ell^- + X$  control sample. The idea is to select a rather clean set of  $pp \rightarrow Z + X \rightarrow \ell^+ \ell^- + X$  events and take all additional objects, which are assumed to be objects from fake sources, to probe the fake factor. This is done separately with objects that are either reconstructed as electrons or muons but without further applied identification cuts. The event selection for this sample is given in Table 7.3. Events with at least two selected muons or two selected electrons are selected. The two selected leptons that are used to form the  $Z$

---

Either 2 selected muons or 2 selected electrons with $p_T > 20$ GeV
Oppositely charged leptons
2 trigger-matched leptons
$ m_{\ell\ell} - m_Z  < 20$ GeV
$E_T^{\text{miss}} < 25$ GeV

---

TABLE 7.3: Summarized selection criteria to obtain a  $pp \rightarrow Z + X \rightarrow \ell^+\ell^- + X$  control sample.

boson candidate have also to fulfill the requirements that are inverted for the additional objects. Furthermore the two leptons have to have  $p_T > 20$  GeV to match the trigger requirements of the lowest unpre-scaled trigger. After requiring that the two same flavor leptons have opposite charge, they have to be matched to the object that actually fired the trigger. Since it is more important to catch pure  $Z \rightarrow \ell^+\ell^-$  events than probing high invariant dilepton masses the invariant mass of the two leptons has to be within 20 GeV of the pole mass of the  $Z$  boson<sup>1</sup>. In the end,  $E_T^{\text{miss}}$  is required to be below 25 GeV in order to suppress  $pp \rightarrow W + X \rightarrow \ell\nu$  events.

Figure 7.2 shows the invariant mass ( $m_Z$ ) and the transverse momentum ( $p_{T,Z}$ ) of the dilepton

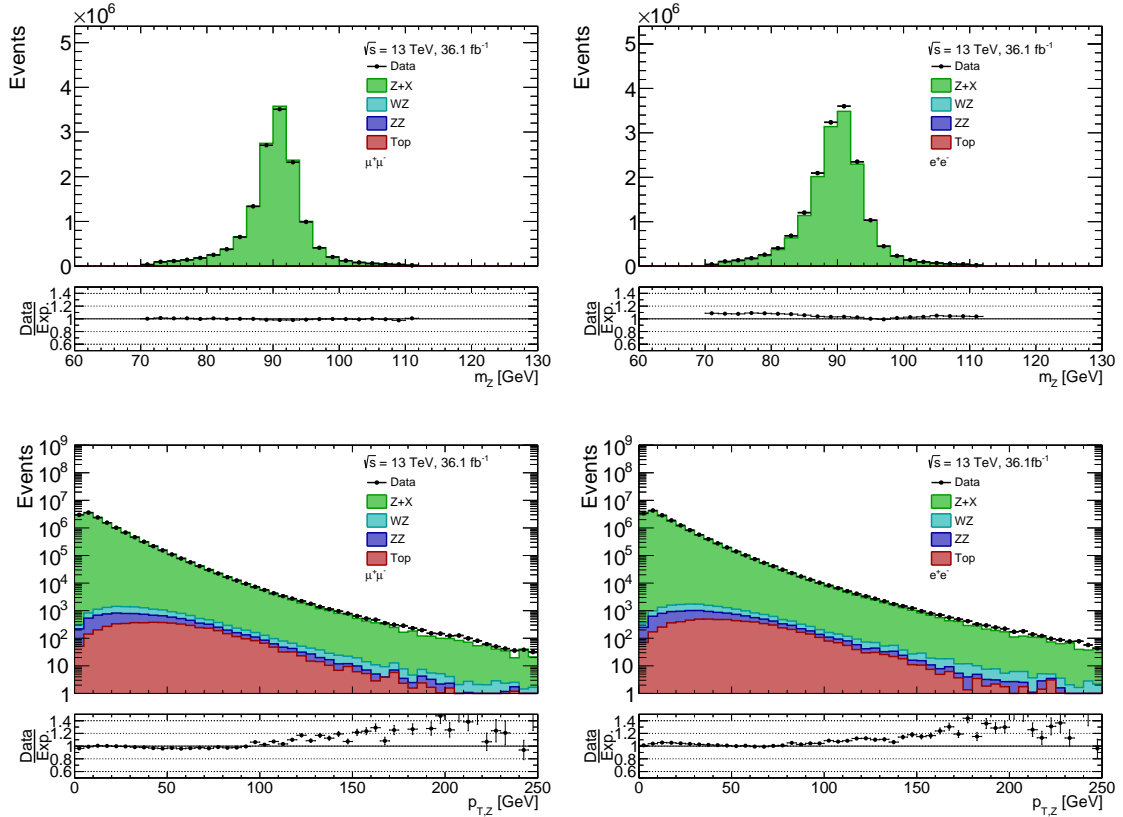


FIGURE 7.2: Comparison of lepton pairs after  $Z$  boson selection between data and Monte Carlo simulation. Left: Muon pairs forming  $Z$  boson candidate. Right: Electron pairs forming the  $Z$  boson. Top: Invariant mass of the lepton pairs. Bottom: transverse momentum of the lepton pairs.

system for muons on the left side, and for electrons on the right side in order to check if

<sup>1</sup>The value of the pole mass is taken from [31]

---

the selected events are consistent with the expectation. The  $ZZ$  contribution that is shown in the figure contains all different signal processes mentioned before. The contribution for  $pp \rightarrow WZ + X$  (labeled as  $WZ$ ) includes all decays of the bosons that lead to at least two genuine leptons that could pass the  $Z$  candidate selection. Contributions from  $pp \rightarrow t\bar{t} + X$  where at least one top quark decays leptonically are also included using a simulation done with SHERPA. More information of the different MC samples that were used are given in Appendix A. It can be seen that overall there is good agreement between data and simulation. The small disagreement in the low mass region of the dielectron system indicates that the simulation is missing (partially) photon radiation from leptons. Also the tail of the dilepton transverse momentum is not very well described by simulation which is due to missing higher order QCD corrections that would contribute more in this kinematic region. But since it is not important for the fake factor determination that the simulation matches perfectly to the data no further corrections are applied.

Now, having a sample of events with mostly  $Z$  bosons, the additional objects are used for the fake factor calculation.<sup>2</sup> In general the fake factor is not expected to be constant over the whole kinematic range. In order to investigate possible kinematic dependencies it is necessary to analyze the single contributions of the fake factor differentially. Therefore the  $\eta$  and  $p_T$  distribution of the electron-like and muon-like objects, which are the additional objects that fail identification criteria, are shown in Figure 7.3. The corresponding distributions for the selected additional objects is shown in Figure 7.4. Together with data also predictions from simulations are shown. The contribution to the simulations are the same as before, but additionally the  $ZZ$  contribution also contains events where one  $Z$  bosons decays hadronically. In all distributions the Monte Carlo description of the data is bad, which emphasizes the motivation to use a data-driven approach.

---

<sup>2</sup>In order to determine the  $F_{\text{mis-ID}}$  in an orthogonal sample of events to the one where it is later applied to, only events with exactly one additional object are used.

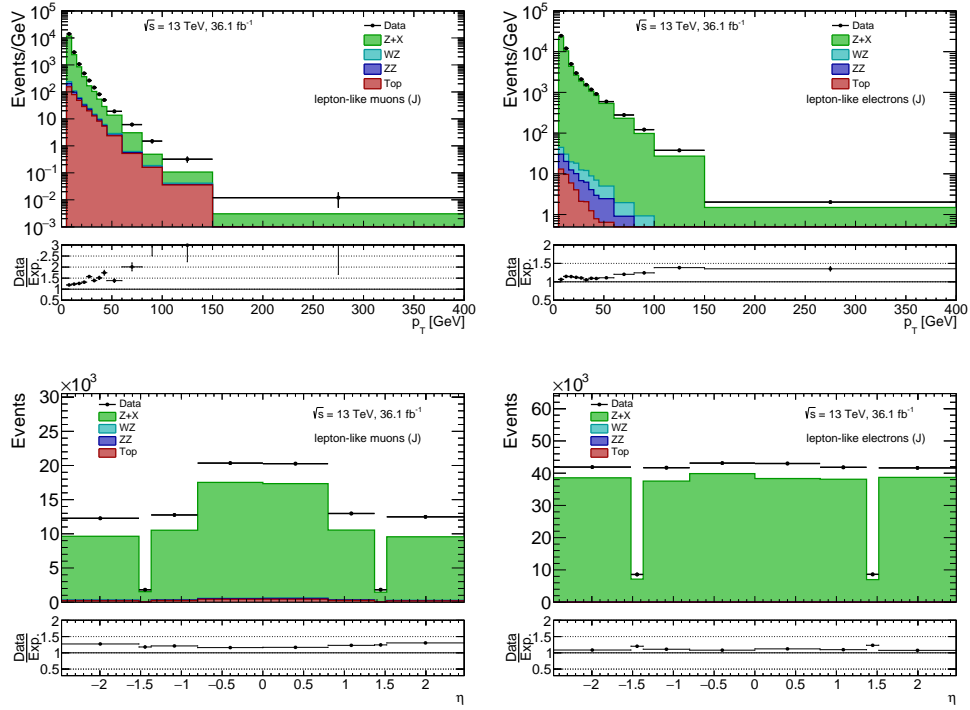


FIGURE 7.3: Additional leptons (besides of those forming the  $Z$  boson) that fail certain identification criteria (lepton-like objects) as a function of  $\eta$  and  $p_T$ . Left side shows muons and right side electrons.

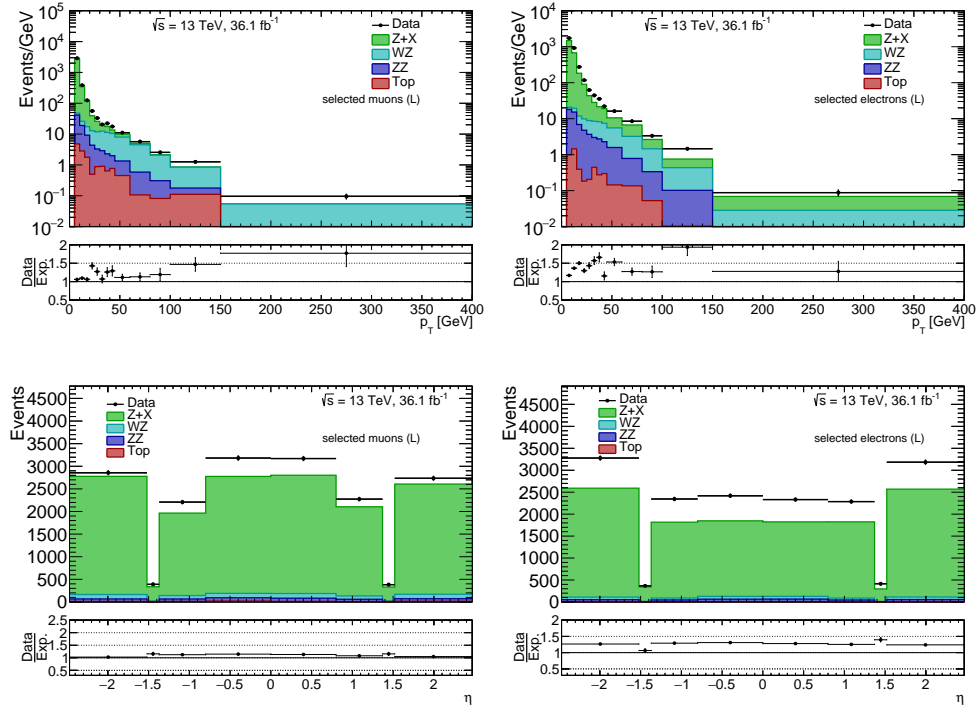


FIGURE 7.4: Additional leptons (besides of those forming the  $Z$  boson) that pass all identification criteria (selected leptons) as a function of  $\eta$  and  $p_T$ . Left side shows muons and right side electrons.

The resulting fake factor is now calculated separately for electrons and muons as:

$$F_{\text{mis-ID}} = \frac{N_{L(\ell)}^{\text{data}} - N_{L(\ell)}^{\text{MC WZ,ZZ}}}{N_{J(\ell)}^{\text{data}} - N_{J(\ell)}^{\text{MC WZ,ZZ}}}, \quad (7.6)$$

where  $N_{L(\ell)}^{\text{data}}$  is the number of selected leptons using data and  $N_{J(\ell)}^{\text{data}}$  is the number of objects passing the inverted selection in data. The subtractive terms  $N_{L(\ell)}^{\text{MC WZ,ZZ}}$  and  $N_{J(\ell)}^{\text{MC WZ,ZZ}}$  correct for real lepton contributions (also called “real lepton dilution”) and is estimated with  $pp \rightarrow WZ + X$  and  $pp \rightarrow ZZ + X$  simulations where all bosons decay leptonically. This real lepton correction is shown in Figure 7.5 for selected and lepton-like objects as function of  $p_T$  and  $\eta$ . Integrated over  $p_T$  and  $\eta$  the dilution for  $N_{L(\ell)}$  is about 3% for electrons and 5% for muons. The  $N_{J(\ell)}$  dilution is less than 0.1% for electrons and muons. As a function of  $p_T$  the  $N_{L(\ell)}$  dilution increases very fast to about 40% for electrons and 70% for muons in the highest  $p_T$  bin. This could introduce a model dependency of the fake factor. It was tested to use SHERPA instead of POWHEG for the dilution and it was found to get similar results within statistical uncertainties. It was also tested to vary the dilution 50% up and down but the impact was less than the later described systematic uncertainties and therefore no further treatment of model dependency is done here.

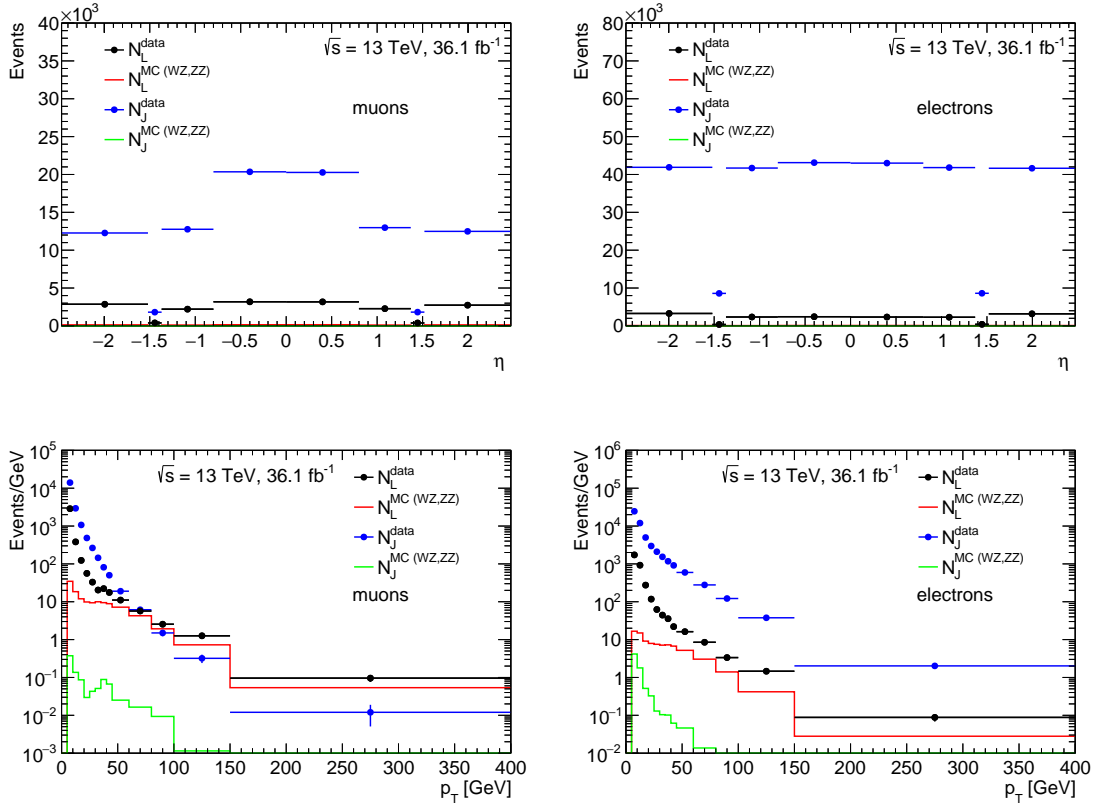


FIGURE 7.5: Fake factor contributions as a function of  $\eta$  and  $p_T$  as quoted in Equation 7.6. Left side shows muons and right side electrons.

The resulting fake factors are shown as a function of  $\eta$  and  $p_T$  in Figure 7.6 for electrons and muons separately. The  $\eta$  binning of electrons is chosen to have bin borders at  $|\eta| = 1.37$  where the barrel part of the electromagnetic calorimeter ends and at  $|\eta| = 1.52$  where the endcap starts including a bin for the transition region  $1.37 < |\eta| < 1.52$ . The fake factors range from approximately 0.02-0.08 for electrons and for muons from about 0.1-0.2 and have a large  $p_T$  dependency in both cases and a rather constant behavior in  $\eta$ . It is also visible that the fake factors are much larger for muons than for electrons. However, the numbers are not directly comparable since the cuts used for inversion are very different and the sources of objects with inverted selection are also different. For electron-like objects typically a hadronic jet is misidentified as an electron. Muon-like objects are often real muons from a secondary decay inside a jet that gets misidentified as an isolated, prompt muon. Since the number of events,  $N_{L(\ell)}^{\text{data}}$  and  $N_{J(\ell)}^{\text{data}}$ , are too low to apply the fake factor binned in a  $p_T$  and  $\eta$  binning simultaneously<sup>3</sup> the fake factors are applied using:

$$F_{\text{mis-ID}}(p_T, \eta) = \frac{F_{\text{mis-ID}}(p_T) \times F_{\text{mis-ID}}(\eta)}{\langle F_{\text{mis-ID}}(p_T, \eta) \rangle}, \quad (7.7)$$

where  $\langle F_{\text{mis-ID}}(p_T, \eta) \rangle = (F_{\text{mis-ID}}(p_T) + F_{\text{mis-ID}}(\eta))/2$  is the average over both  $p_T$  and  $\eta$  of the fake factors.

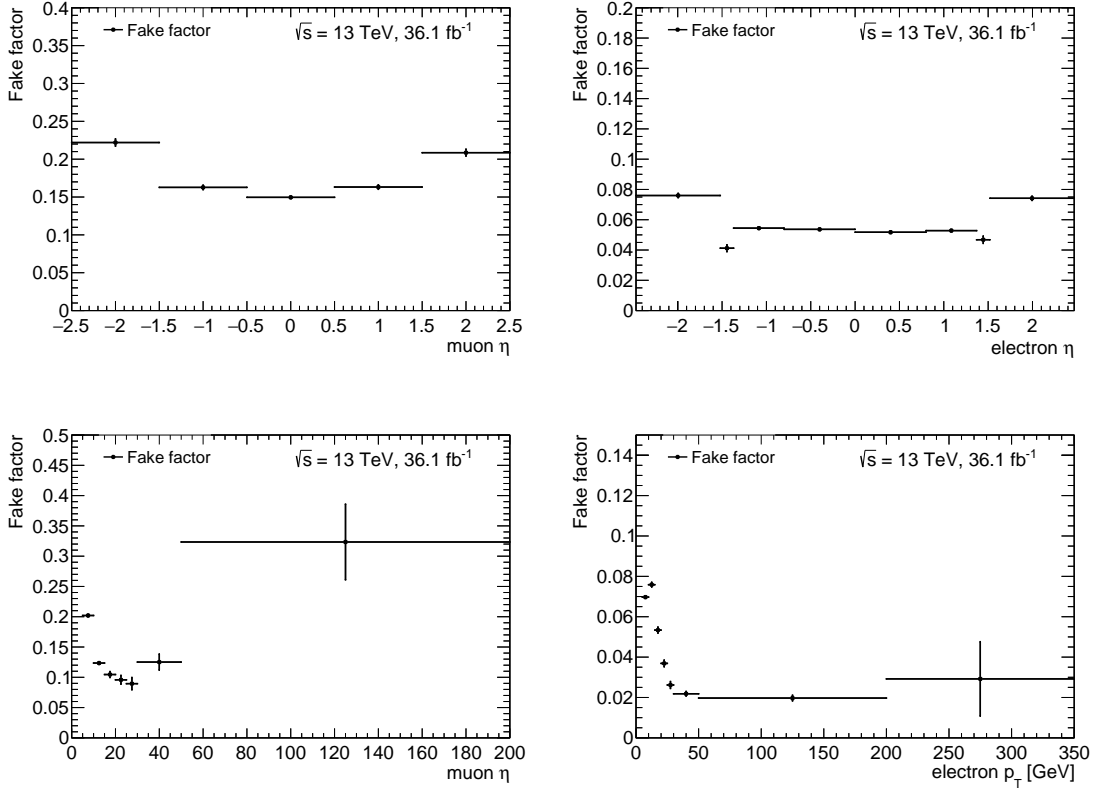


FIGURE 7.6: Fake factor as a function of  $p_T$  and  $\eta$ . Left side shows muons and right side the electrons. The uncertainty reflect only the statistical uncertainty from data.

<sup>3</sup>The impact using a (very coarse) 2D binning has been investigated. It was found to be smaller than the difference when propagating the statistical uncertainties of the fake factors.

In principle the fake factor could also depend on other variables like the number of additional jets in a  $ZZ$  event ( $N_{jets}$ ). The jet selection is described in Section 6.4.3 and it has been taken care that all jets are removed that overlap with a lepton from the  $Z$  boson or the additional object. The resulting distributions for selected leptons or objects with inverted selection are shown in Figure 7.7 together with the MC prediction. The description of data due to MC simulation is poor since fake leptons are not expected to be modeled well in MC simulation and the  $pp \rightarrow Z + X$  MC simulation is only at NLO in QCD. The real lepton dilution as a function of  $N_{jets}$  is shown in Figure 7.8. It can be seen that it is rather constant and in the order of 5%. The resulting  $F_{mis-ID}$  are shown in Figure 7.9. It can be seen that for the electron case there is a rather flat behavior whereas for muons there is a  $N_{jets}$  dependency which is covered by later discussed systematic variation of the fake factor and therefore not taken into account when the fake factor is applied.

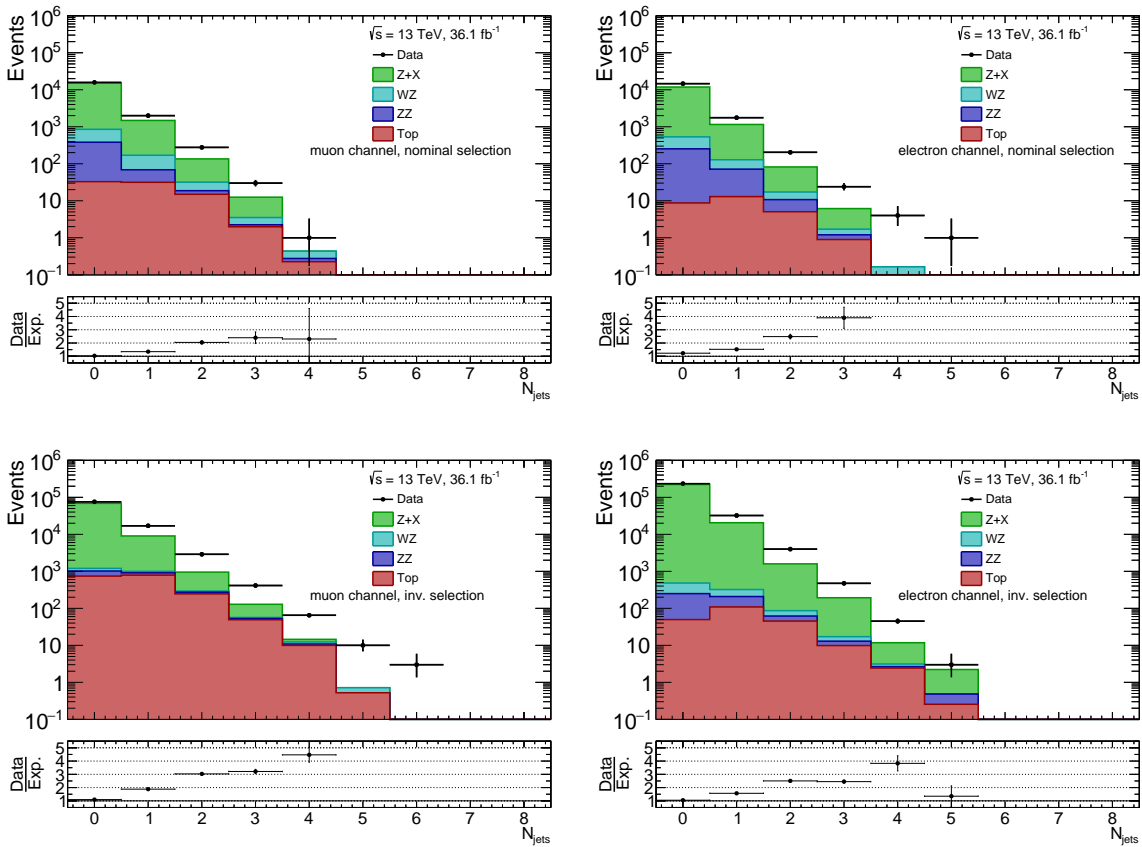


FIGURE 7.7:  $N_{jets}$  distribution for events with additional leptons (besides of the one forming the  $Z$  boson). The left side shows the case when the additional object is a muon and the right side if it is an electron. The top plots show the case if the additional object is a selected lepton, the bottom plots, when the additional object is passing the inverted selection.

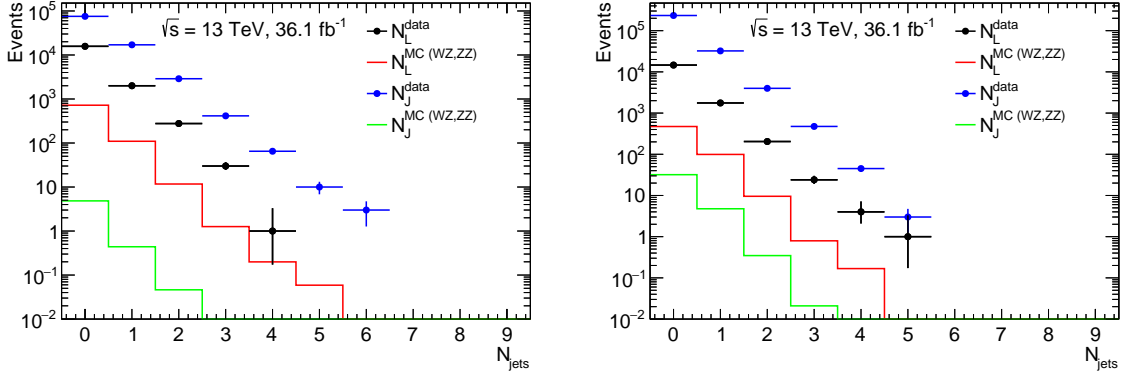


FIGURE 7.8: Fake factor contributions as a function of  $N_{jets}$ . The labels of the contributions correspond to the nomenclature of Equation 7.6. The left side shows the distribution for the case when the additional object is reconstructed as a muon and the right side when it is reconstructed as an electron.

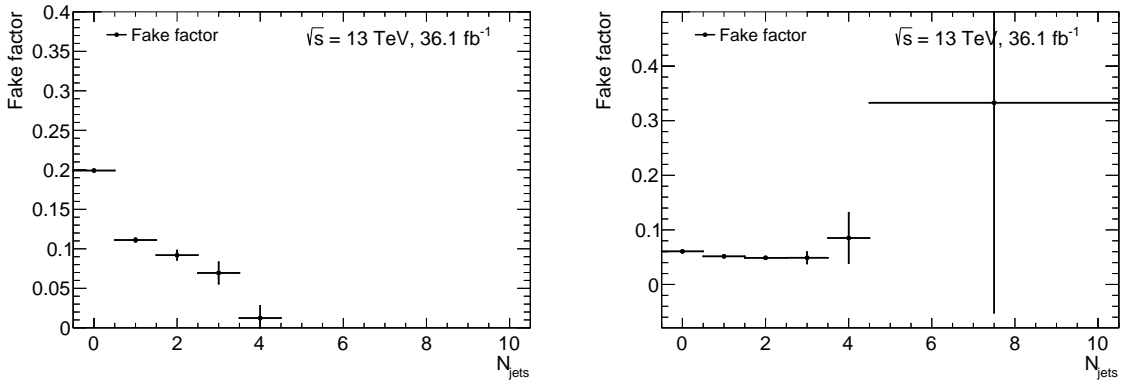


FIGURE 7.9: Fake factor as a function of  $N_{jets}$ . The left side shows the distribution for the case when the additional object is reconstructed as a muon and the right side when it is reconstructed as an electron.



### 7.2.3.3 Background yield and shape determination

Other parts of Equation 7.4, besides the fake factors, are  $N^{\ell\ell j}$  and  $N^{\ell jj}$ . The size of these contributions are shown in Table 7.4.

Contribution	$4e$	$2e2\mu$ fake $\mu$	$2e2\mu$ fake e	$2e2\mu$ fake e fake $\mu$	$4\mu$
$N^{\ell\ell j}$	106	51	109	–	77
$N_{ZZ}^{\ell\ell j}$	$37.7 \pm 0.8$	$20.0 \pm 0.6$	$43.1 \pm 0.8$	–	$23.0 \pm 0.6$
$N^{\ell jj}$	370	54	349	60	154
$N_{ZZ}^{\ell jj}$	$4.97 \pm 0.30$	$0.35 \pm 0.07$	$0.99 \pm 0.11$	$2.06 \pm 0.17$	$4.31 \pm 0.27$

TABLE 7.4: Raw yield (not weighted by the fake factor) of the inverted selection split into the different components and channels used for the final background estimate. The uncertainty of the real lepton correction shows only the statistical uncertainty of the simulation.

Also shown are the contributions correcting for real leptons that fail the cuts for inversion. Since the fake sources and the cuts for inversion are different for electrons and muons, here the  $2e2\mu$  channel is split in events where the fakes are from electrons only, muons only or both<sup>4</sup>. These numbers show that there are more events with one or more electron passes the inverted selection. Also  $N^{\ell jj}$  is higher compared to  $N^{\ell\ell j}$ . As mentioned before, a way to end up with two genuine leptons and at least two jets in the final state is for example  $Z$ +jets and  $t\bar{t}$  production. A generic way to get three genuine leptons and one jet is dominantly  $WZ$ +jet production. The cross section for the latter process is lower compared to the former ones and therefore more events end up in  $N^{\ell jj}$ . There are also contributions where a jet from  $Z$ +jets production is identified as a lepton and therefore ends up in  $N^{\ell\ell j}$  which is included in this method. The estimate of non-genuine background is found by combining the events of each category weighted by the fake factor and using Equation 7.4. The fake factors are applied depend on the  $p_T$  and  $\eta$  of the leptons passing the inverted selections. The results can be found in Table 7.5 along with the associated statistical uncertainties.

Contribution	$4e$	$2e2\mu$	$4\mu$	$4\ell$
$(+)N^{\ell\ell j} \times F_{i,\text{mis-ID}}$	$4.3 \pm 0.4$	$12.0 \pm 1.2$	$12.2 \pm 1.4$	$28.5 \pm 1.9$
$(-)N_{ZZ}^{\ell\ell j} \times F'_{i,\text{mis-ID}}$	$1.493 \pm 0.034$	$4.68 \pm 0.09$	$3.38 \pm 0.09$	$9.56 \pm 0.14$
$(-)N^{\ell jj} \times F_{i,\text{mis-ID}} F_{j,\text{mis-ID}}$	$0.74 \pm 0.04$	$2.40 \pm 0.21$	$3.62 \pm 0.30$	$6.8 \pm 0.4$
$(+)N_{ZZ}^{\ell jj} \times F'_{i,\text{mis-ID}} F'_{j,\text{mis-ID}}$	$0.0073 \pm 0.0005$	$0.0231 \pm 0.0024$	$0.095 \pm 0.006$	$0.125 \pm 0.007$
Background estimate, $N_{\text{bkg}}$	$2.1 \pm 0.4$	$4.9 \pm 1.2$	$5.3 \pm 1.5$	$12.3 \pm 2.0$

TABLE 7.5: Non-genuine background estimate split into different contributions and channel. Only statistical uncertainties are shown. The  $2e2\mu$  channel contains the contributions from fake muons and fake electrons.

The statistical uncertainty on the non-genuine background estimate for each channel was calculated by adding the statistical uncertainty for  $N^{\ell\ell j}$ ,  $N_{ZZ}^{\ell\ell j}$ ,  $N^{\ell jj}$  and  $N_{ZZ}^{\ell jj}$  in quadrature. The combined result is given by the sum of the different channels and the quadratic sum of the uncertainties. The size of the background is found to be about 2% of the signal expectation which shows that the non-genuine background, like the genuine background is small. Additionally, the MC correction for real leptons is up to 40%, which introduces a modeling dependency

<sup>4</sup>Fakes are leptons that pass the inverted cuts.

that will be discussed in the next section. The contributions (weighted by their fake factor) as a function of the invariant mass of the four lepton system can be found in Figure 7.10 for events with one object passing the inverted selection and in Figure 7.11 for events with two objects passing the inverted selection. In all distribution the description by MC are not very good modeled, which reflects the difficulty to simulate fake leptons correctly. The contributions from real leptons (e.g.  $ZZ \rightarrow 4\ell$ ) are already subtracted here. For the real lepton subtraction a matching between leptons at generator level and leptons passing the inverted selection is done. A small fraction of events do pass this matching and remain in the inverted selection which is also visible in the figures.

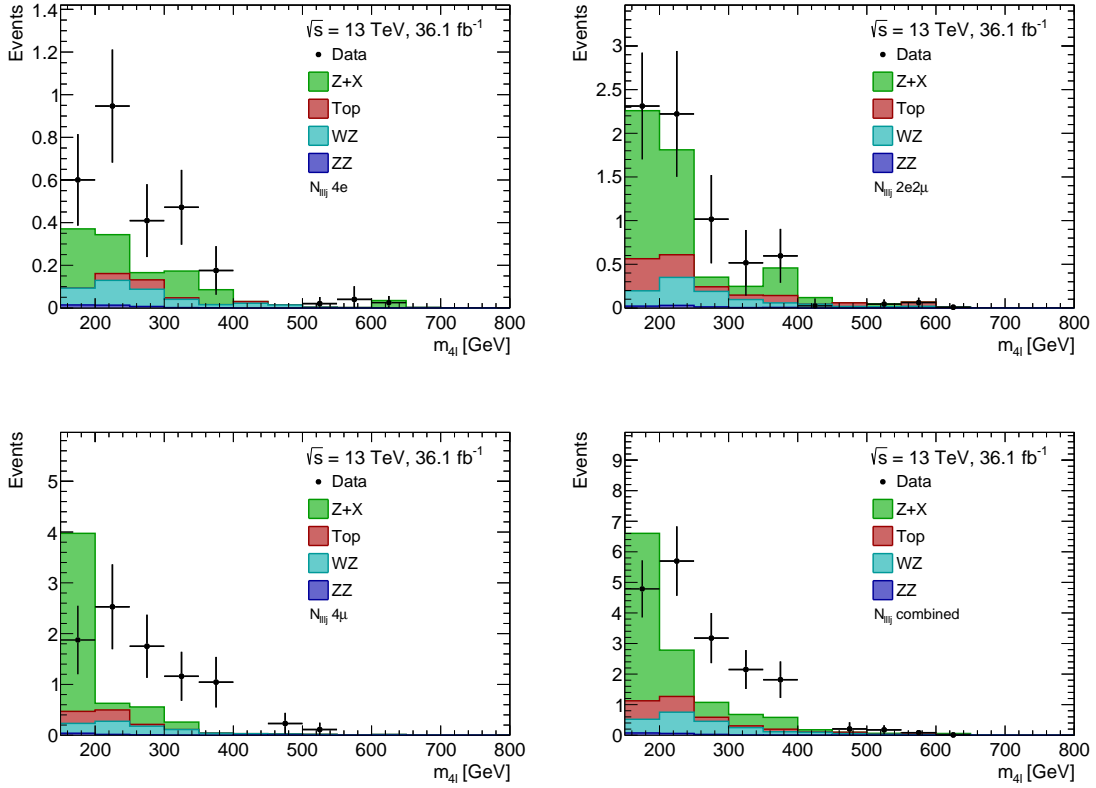


FIGURE 7.10: Events with one object passing the inverted selection, split into different channels weighted by  $F_{\text{mis-ID}}$  (one part of Equation 7.4). Also different MC predictions that can contribute in this region are added. The real lepton contribution from  $ZZ \rightarrow 4\ell$  is subtracted here using MC (POWHEG).

In order to have background predictions when looking at differential distributions it is necessary to have the shape of the background. The data yield for  $N^{\ell\ell j}$  and  $N^{\ell\ell jj}$  per bin can be quite low and therefore the prediction per bin can get negative after the correction for real  $ZZ \rightarrow 4\ell$  events (see Equation 7.4). Therefore the shape is taken using the  $N^{\ell\ell jj}$  distribution with the fake factor applied scaled to the total yield. As an example Figure 7.12 shows the distributions for  $m_{4l}$  and  $p_{T, \text{lead} Z}$  of the leading  $Z$  boson. The plots show also the impact when  $N^{\ell\ell j}$  is used instead of  $N^{\ell\ell jj}$ . It can be seen that the impact is negligible within the statistical uncertainty. Further distributions, including jet properties, were checked and the difference between the two shapes was found to be negligible in all cases.

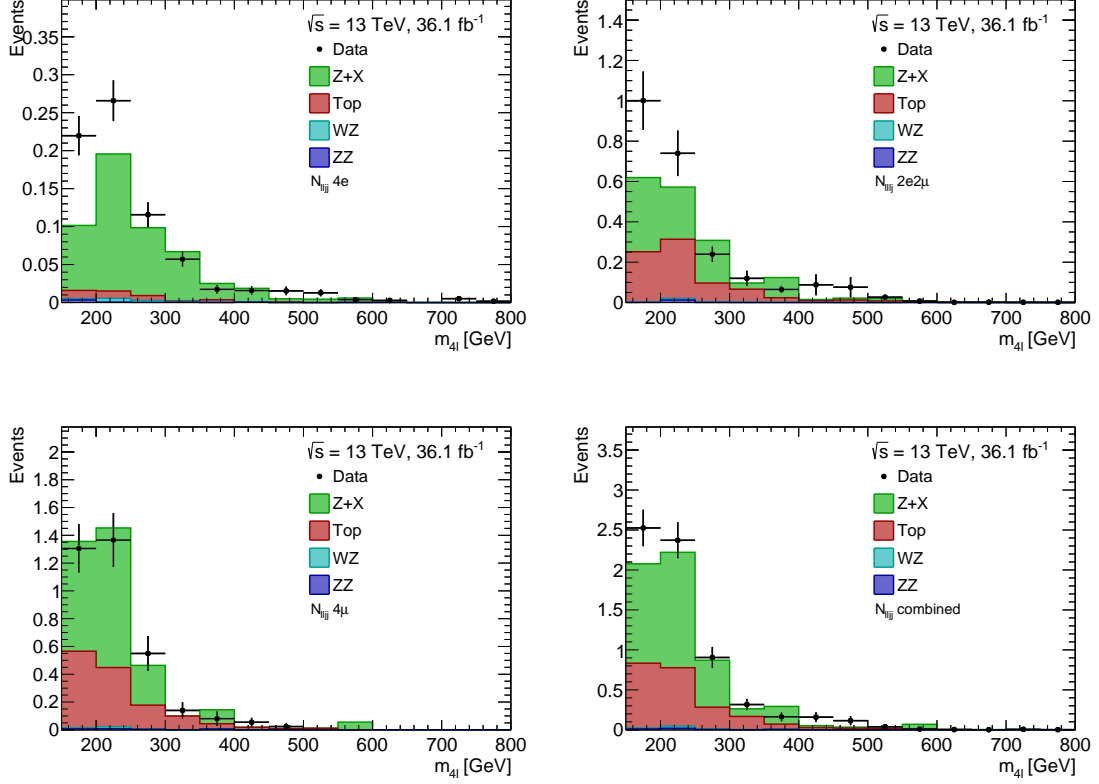


FIGURE 7.11: Events with two objects passing the inverted selection, split into different channels weighted by  $F_{\text{mis-ID}}$  (one part of Equation 7.4). Also different MC predictions that can contribute in this region are added. The real lepton contribution from  $ZZ \rightarrow 4\ell$  is subtracted here using MC (POWHEG).

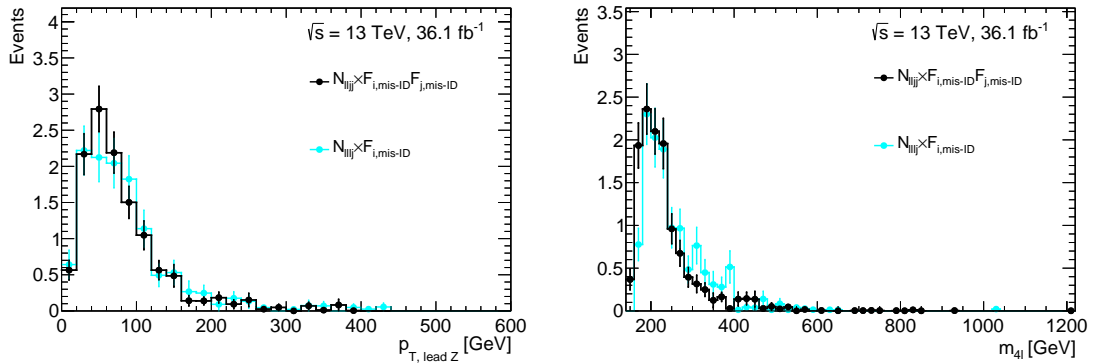


FIGURE 7.12: Data driven background shape as a function of  $m_{4l}$  and  $p_{T,\text{lead } Z}$  of the  $Z$  boson candidate with higher transverse momentum. The real lepton contribution is not subtracted. The distributions are normalized to the total background prediction shown in Table 7.5.

### 7.2.3.4 Systematic uncertainties

The estimated background also comes with different systematic effects that are presented in the following. One systematic uncertainty is the statistical error of the fake factors which is propagated. Another systematic uncertainty is estimated by applying the fake factor in a non  $p_T$  or  $\eta$  depended way (averaging over both). Furthermore the assumption is made that the contributing process to the background is mainly  $Z+X$ , which is the region where the fake factor is measured. As it can already be seen in Figure 7.10 and Figure 7.11 this is not the case for the single contributions needed to estimate the background. For further investigation Figure 7.13 shows the comparison of data to background simulation for events with one object passing the inverted selection, split into different channels. These distributions show that in general the contribution from  $Z+X$  is larger for events with fake electrons compared to distributions with fake muons. It is also visible that the contribution from real leptons ( $ZZ \rightarrow 4\ell$ ) is large (up to 40%). In Figure 7.14 events with two leptons passing the inverted selection are shown for different channels. There, the contribution from real leptons is much smaller, but the differences in the contributions from  $Z+X$  and  $t\bar{t}$  to the different channels is much larger. This is clearly visible in the large  $t\bar{t}$  contribution in the  $4\mu$  channel compared to the  $4e$  channel, where the  $Z+X$  contribution is more dominant. It is considered that the fake factor is different for different processes and it has to be taken care of the compositions of the processes.

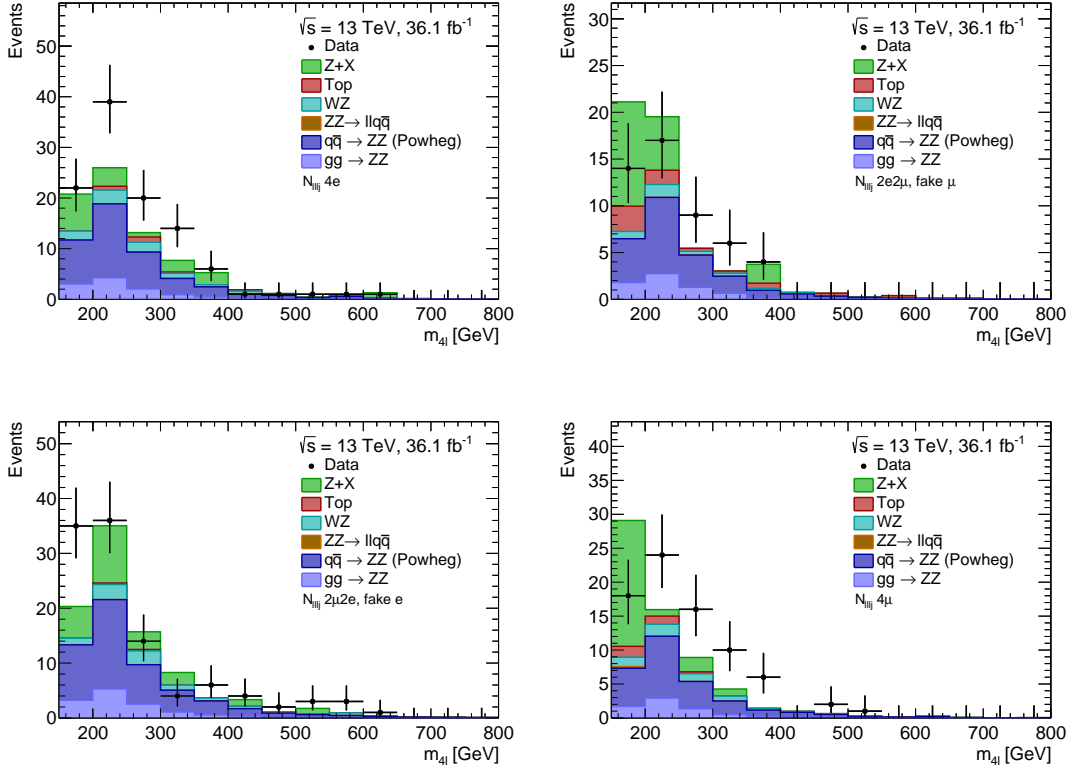


FIGURE 7.13: Events with one object passing the inverted selection. Different MC predictions that contribute in this region are also added. The  $2e2\mu$  channel is split into parts where the object passing the inverted selection is a muon ( $2e2\mu$ ) and where it is an electron ( $2\mu2e$ ). No fake factor is applied and the real lepton contribution is not subtracted.

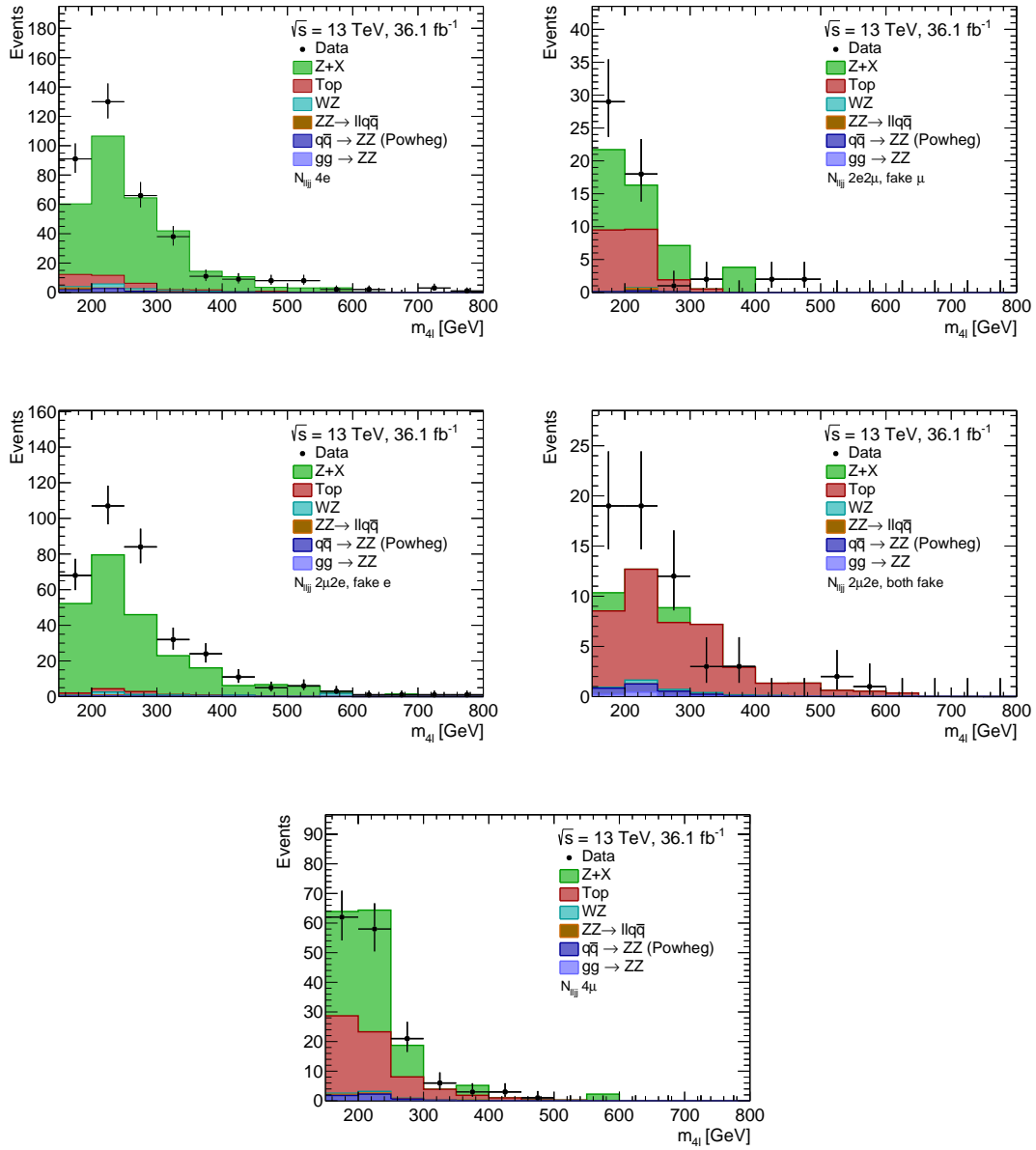


FIGURE 7.14: Events with two objects passing the inverted selection. Different MC predictions that contribute in this region are also added. The  $2e2\mu$  channel is split into parts where both object passing the inverted selection are muons ( $2e2\mu$ ), where one object is an electron and one is a muon ( $2e2\mu$  both fake) and where both are electrons ( $2\mu2e$ ). No fake factor is applied and the real lepton contribution is not subtracted.

Not only the compositions due to different processes influences the background estimation. Also the composition due to different fake sources can be different in the region where the fake factors are measured and where they are applied to. In order to investigate this, the MC simulations have been used to track down where the lepton passing the inverted selection originates from. This is done by using a tool<sup>5</sup> that splits the origin of a particles into different categories. This is possible in simulation because the information where a reconstructed particle is originated from is available which is not the case for data. It is differentiated between following categories:

<sup>5</sup>The version of the tool is: *MCTruthClassifierTool-00-01-53-02*.

- Leptons from light flavor hadron decays (LF), which are present for example in jets,
- Leptons originated from heavy flavor hadron decays (HF), also possible decays in a jet
- Hadrons faking the signature of a lepton, like a jet faking a lepton
- Photons that convert to two leptons
- Real leptons from the hard interaction

Figure 7.15 shows the composition for  $N^{\ell\ell j}$  and  $N^{\ell\ell jj}$  for the different channels when adding the  $Z + X$ ,  $t\bar{t}$  and  $WZ$  contributions.

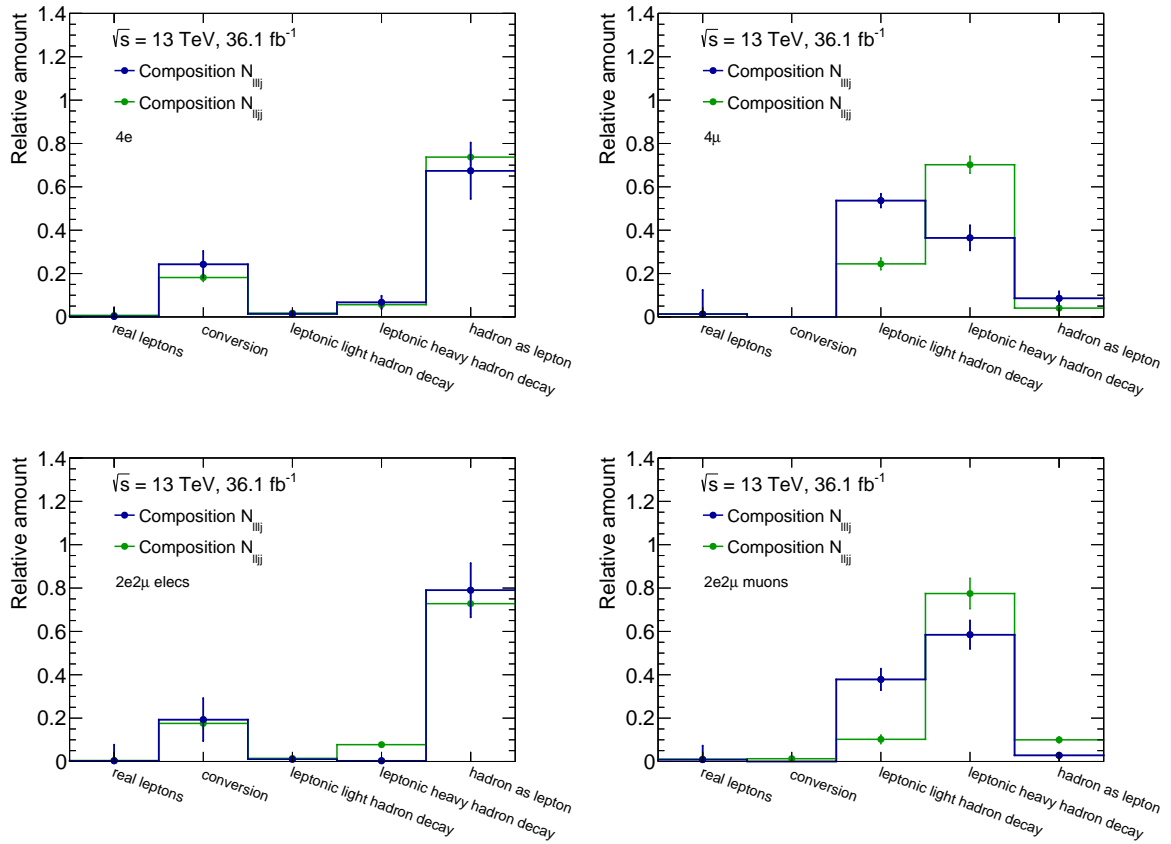


FIGURE 7.15: Origins of the leptons passing the inverted selection split into different categories for different channels. The mixed channel is split into one part with fakes from muons (bottom right) and another part with fakes from electrons (bottom left). The real lepton contribution from  $ZZ \rightarrow 4\ell$  is already subtracted. The uncertainties show only the statistical ones due to limited number of simulated events.

In the distributions with fake electrons it can be seen that the major part (about 70%) is faked by hadrons which is expected, because the signatures from jets and electrons in the detector can be quite similar. Another part (about 20%) of fake electrons originate from photon conversion. For muons the main source of fakes is heavy and light flavor hadron decays. The comparison between  $N^{\ell\ell j}$  and  $N^{\ell\ell jj}$  shows good agreement for fake electrons but differences for fake muons. This is mainly caused by larger top contribution to  $N^{\ell\ell jj}$  compared to  $N^{\ell\ell j}$  for muons. Since top quarks decay into bottom quarks which form so-called b-jets in the detector, it is more

likely that fake muons originate from heavy hadron decays when the top contribution is higher. Figure 7.16 shows the composition for the  $Z + X$  region, where the fake factor is measured, split in electrons and muons separately summing over all MC simulations ( $Z + X$ ,  $t\bar{t}$  and  $WZ$ ). The differences in the compositions between the selected and lepton-like objects show the impact of the inversion cuts. Ideally the distribution of the lepton-like objects should match with the distributions where the fake factor is applied on which were shown in Figure 7.15. For electrons they match quite well, but for muons there are larger differences visible.

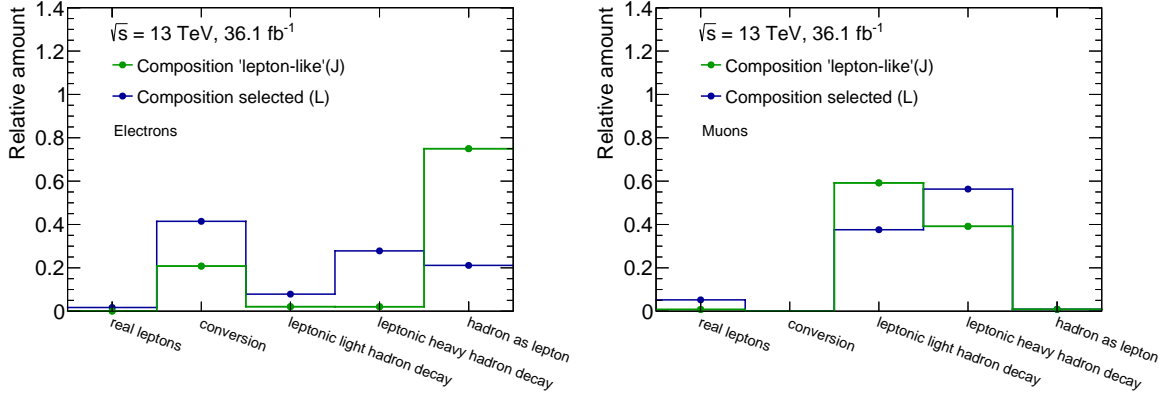


FIGURE 7.16: Fake composition for electrons and muons in the region where the fake factor is estimated. The real lepton contribution from  $ZZ \rightarrow 4\ell$  and  $WZ \rightarrow 3\ell$  is already subtracted. The uncertainties show only the statistical ones due to limited number of simulated events.

In order to check the impact of all these differences on the final background estimate, the fake factor is calculated for the three major contributions ( $Z + X$ ,  $t\bar{t}$  and  $WZ$ ) using MC simulation and within those split further into the different origins. Figure 7.17 shows the electron fake factors as a function of  $p_T$  and  $\eta$  after the splitting. It can be seen that there are large differences for different origins and MC simulations. This is specially visible for the fake factors determined with the  $Z + X$  simulation which differ over a large range for different origins. The fake factor for electrons from heavy flavor decays is larger than one in some bins, especially in the lowest  $p_T$  bin. This shows that the chosen cuts for inversion are not very efficient to suppress those fake electrons, but as it was shown before, the fraction of fake electrons from heavy flavor decays is low for  $N^{\ell\ell j}$  and  $N^{\ell j j}$ . In some categories the number of simulated events is very low and therefore bins can have no entries or large uncertainties. The fake factor for different processes and fake origins is shown in Figure 7.18 for muons. Similar to the electron case there are differences of the fake factors depending on the processes and the origins.

Summarized there are two effects that have to be taken into account and were discussed before. One effect are differences in the contributions of single processes, e.g.  $Z + X$  between the different selection channels. The other effect are differences in the distributions of sources of fake leptons between the region where fake factor is measured and where it is applied. In order to consider both effects, weights in the region with inverted selection are calculated for each background process (e.g.  $Z + X$ ) and origin (e.g. conversion) in each channel (e.g.  $4e$ ) and “event type” ( $N^{\ell\ell j}$ ,  $N^{\ell j j}$ ). The fake factors are then added by taking these weights into account, resulting in four different fake factors per lepton (one per channel and “event type”). The resulting fake factors can be seen in Figure 7.19.

The difference of the resulting background yield compared to the nominal case is shown in

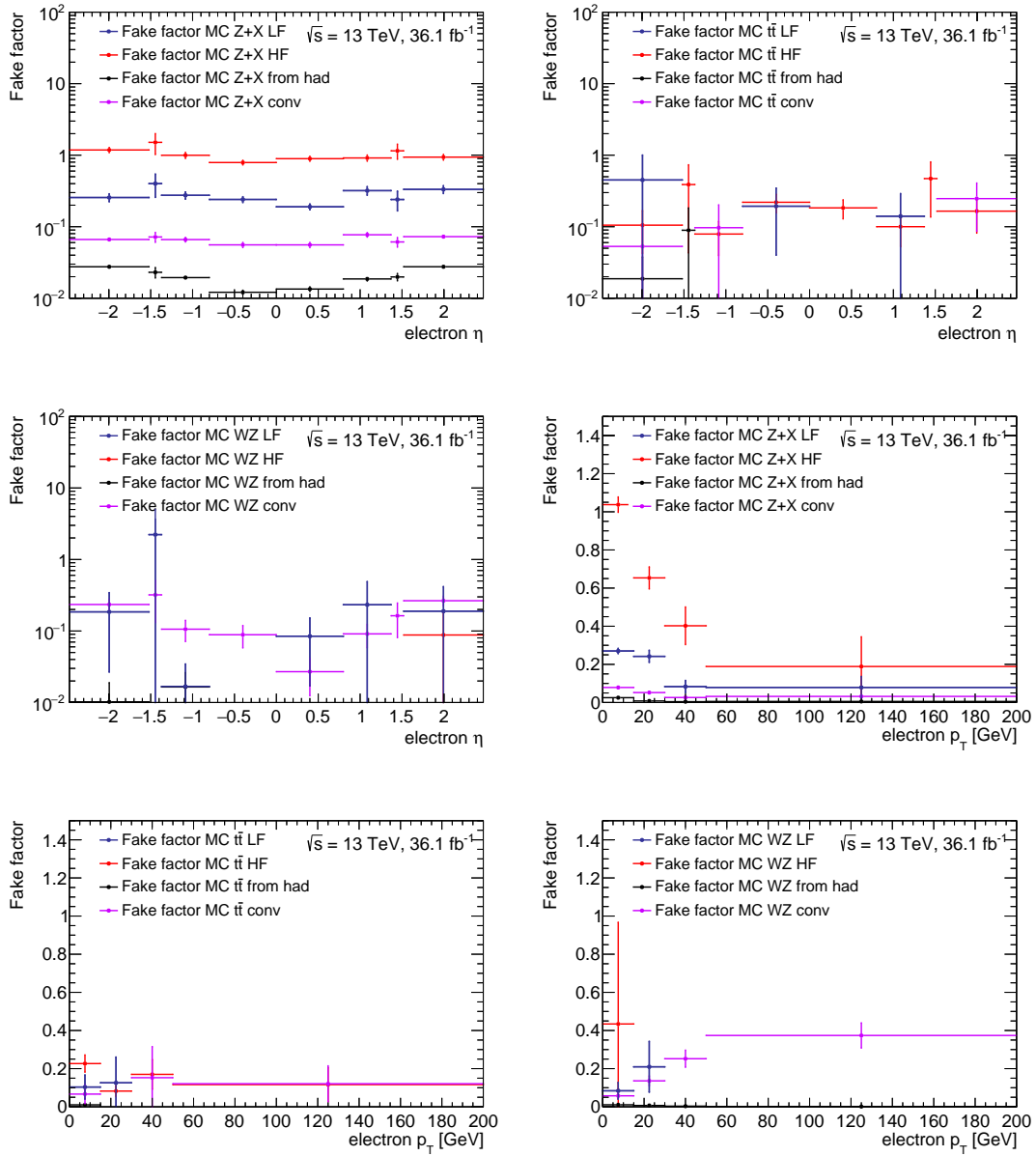


FIGURE 7.17: Electron fake factor estimated with different MC simulations for different sources of fakes. Contributions from real leptons are not taken into account.

Table 7.6 together with the outcome of the systematic uncertainties mentioned before. It can be seen that the impact of using the fake factors from simulation is largest for channels with muon fakes. This reflects that the extrapolation of the fake factor region to the region where the fake factors are applied is higher for channels with muon fakes compared to channels with electron fakes. Also it is possible that the modeling of the  $Z + X$  contribution can differ a lot using a different generator. Therefore the procedure described before is repeated using MadGraph as generator for the  $Z + X$  contribution. The impact of this variation on the background yield is also included in Table 7.6.

Furthermore, the modeling of the real contribution which is subtracted from  $N^{\ell\ell j}$  and  $N^{\ell\ell jj}$  introduces a further source of systematic uncertainty. In the table two further variations are



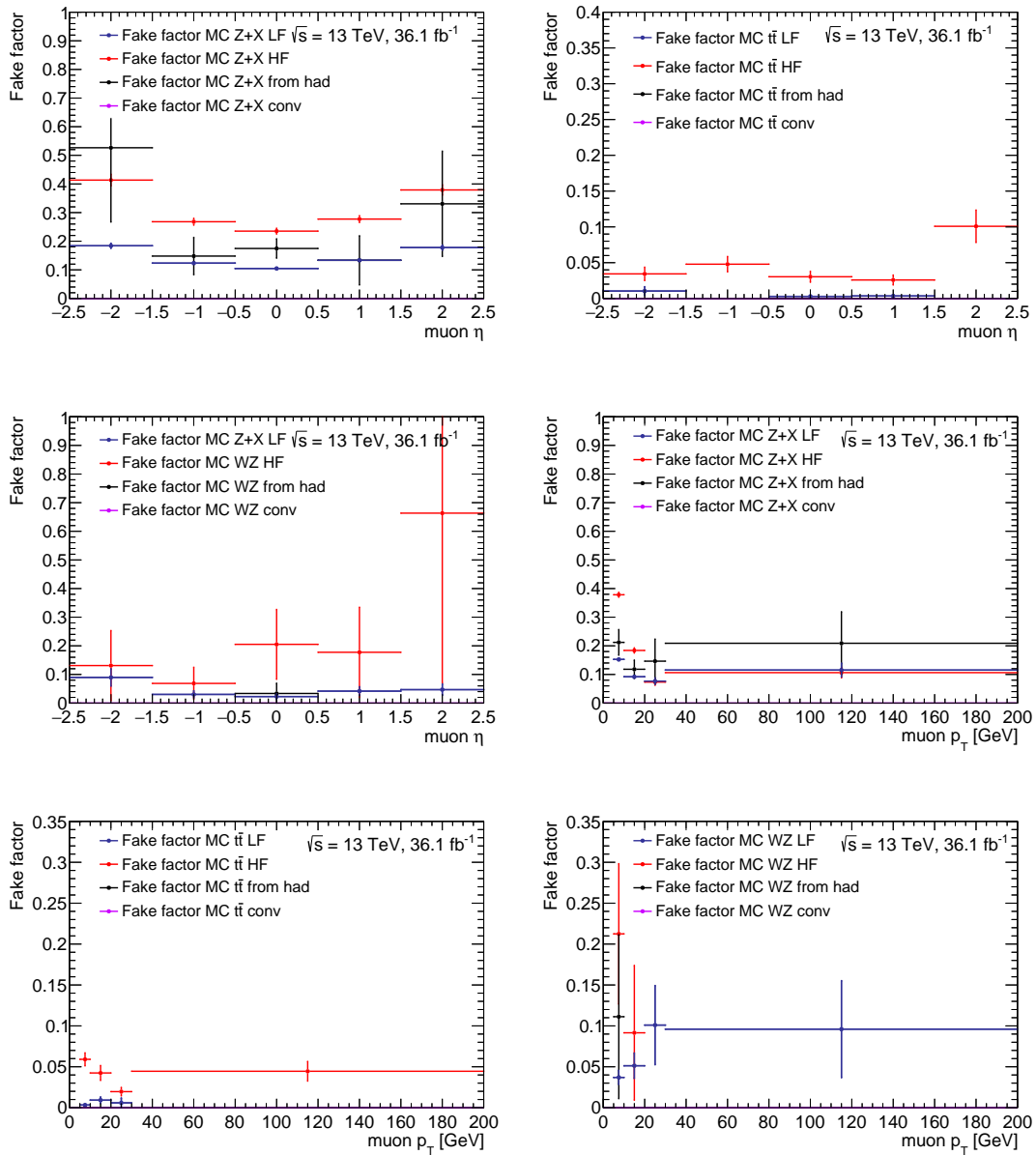


FIGURE 7.18: Muon fake factor estimated with different MC simulations for different sources of fakes. Contributions from real leptons are not taken into account.

shown that show the result of varying the real lepton contribution to account for this model uncertainty. More information on how this systematic is estimated, is shown in Appendix D.1.1. The combined uncertainty is estimated by taking the envelope of each statistically depended group and add those in quadrature.

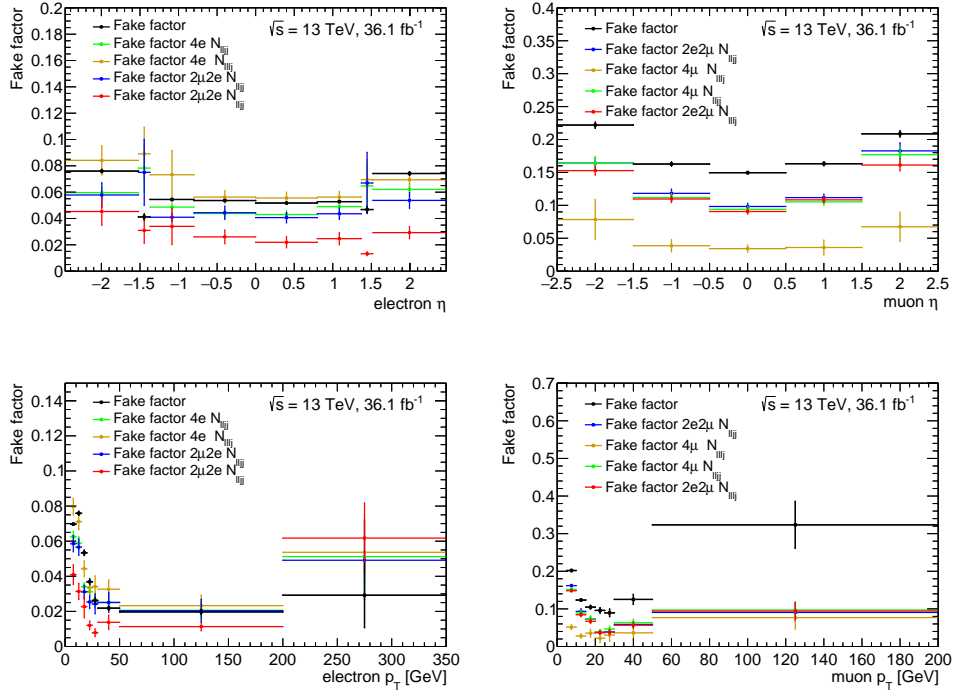


FIGURE 7.19: Black points show the fake factor when using the default approach with data. The colored points show MC simulation based fake factors that are applied to the corresponding channel (e.g.  $4e$ ) and “event type” ( $N^{\ell\ell jj}, N^{\ell\ell jj}$ ) for estimation of systematic uncertainties.

	$4e$	$2e2\mu$	$4\mu$	$4\ell$
Nominal fake background estimate	$2.1 \pm 0.4$	$4.9 \pm 1.2$	$5.3 \pm 1.5$	$12.3 \pm 2.0$
Vary $F_{\text{mis-ID}}$ stat. uncertainty down	2 %	2 %	3 %	2 %
Vary $F_{\text{mis-ID}}$ stat. uncertainty up	-2 %	-2 %	-2 %	-2 %
Use average $F_{\text{mis-ID}}$	-28 %	-16 %	8 %	-7 %
Use MC $F_{\text{mis-ID}}$	-32 %	42 %	80 %	46 %
Use MC $F_{\text{mis-ID}}$ stat up	-47 %	38 %	70 %	38 %
Use MC $F_{\text{mis-ID}}$ stat down	-15 %	46 %	90 %	55 %
Use MC (MG) $F_{\text{mis-ID}}$	-75 %	-34 %	9 %	-22 %
Use MC (MG) $F_{\text{mis-ID}}$ stat up	-98 %	-53 %	0 %	-37 %
Use MC (MG) $F_{\text{mis-ID}}$ stat down	-49 %	-14 %	19 %	-5 %
Real lepton correction up	-36 %	-47 %	-31 %	-38 %
Real lepton correction down	36 %	47 %	31 %	38 %
Combined	100%	71%	95%	66%

TABLE 7.6: Data driven background systematic uncertainties. The statistical uncertainty of the fake factor ( $F_{\text{mis-ID}}$ ) is propagated. Also the impact of using the  $F_{\text{mis-ID}}$  averaged over  $p_T$  and  $\eta$  is shown. The largest variation is resulting when using a MC simulation based  $F_{\text{mis-ID}}$  that takes relative difference of contributing processes in the different channels into account. Also the statistical uncertainty of this MC simulation based  $F_{\text{mis-ID}}$  (due to limited MC statistics) is taken as further variations. To account for differences between generators for this variation a further estimate, using MadGraph for the  $Z + X$  simulation has been considered (marked as MG in the table). In order to have a conservative estimate of the mis-modeling uncertainty of the real lepton contamination, the simulation is scaled by 50% up and down. The combined uncertainty is estimated by taking the envelope of each statistically dependent group (indicated by horizontal lines) and add those in quadrature.

---

## 7.3 Systematic uncertainties

In an experimental data analysis, especially in a cross section measurement, it is crucial to estimate the size of systematic effects to quantify agreement between data and expectation. In this section it is described how systematic uncertainties from different sources are estimated. First the experimental uncertainties are discussed and split into origins from reconstruction and identification of electrons, muons and jets. The second part discusses theoretical uncertainties from PDFs, choice of the QCD factorization and renormalization scale and higher order electro weak corrections. The impact of the different uncertainties on the signal and background expectation is presented in the last part of the section.

### 7.3.1 Experimental uncertainties

#### 7.3.1.1 Electron uncertainties

**Electron efficiencies** The efficiency corrections that are applied to the simulated predictions come with different uncertainties. They are provided by the ATLAS electron performance group [117] and estimated by variations applied to the tag and probe method (see also Section 4.2), for example changing the mass window cut that is applied on the dilepton invariant mass. More details how the uncertainties are estimated can be found in [117]. All the effects can be applied to the analysis by varying the scale factors by one standard deviation of each uncertainty source up and down which results in many variations on the final selected four lepton events. It is also possible to use a combined uncertainty set which has only one up and down variation that is propagated. The disadvantage of this procedure is that possible correlations between different uncertainties are not taken into account and the combined uncertainty might be too conservative. It was checked, that the uncertainties for the isolation and reconstruction efficiency corrections are sufficiently small when using the combined uncertainties, whereas for the identification the fully decorrelated set is taken into account using 22 separate variations. Since no correction is applied to account for mis-modeling of trigger efficiencies also no systematic variations are applied.

**Electron energy scale** The ATLAS performance group provides different nuisance parameter as function of  $\eta$  and  $p_T$  that estimate systematic effects when determining the energy scale correction. Typical values for the electron energy scale uncertainty at 40 GeV are about 0.04%. The scale is corrected in data but the systematic variations are done in simulation since the number simulated events is higher compared to selected data events. More details which systematic effects are considered can be found in [92]. In total there are 60 different kinds of those nuisance parameter decorrelated in  $\eta$ . It was checked that this analysis is not dominantly sensitive to the scale correction uncertainties. Therefore a simplified model is used which provides one nuisance parameter that considers full correlation in different  $\eta$  bins which is built by the quadratic sum of all 60 parameters. This leads to a more conservative result compared to the fully decorrelated approach.

---

**Electron energy resolution** Differences between data and simulation in the resolution of the electron energy are taken into account by applying a smearing on MC simulation. Systematic uncertainties on the smearing have also been investigated by the ATLAS performance group [92]. The uncertainties range from about 10% for  $E_T < 50$  GeV to about 40% at higher energies. The group provides several decorrelated nuisance parameter for different  $\eta$  regions that are used to study the impact of the uncertainties on selected four lepton events. Since the number of nuisance parameter is quite large and the analysis is not sensitive to such uncertainties, a simplified approach is used. This follows the procedure described for the energy scale uncertainties leading to a presumably more conservative uncertainty on the  $ZZ$  expectation.

### 7.3.1.2 Muon uncertainties

**Muon efficiencies** The muon efficiency correction together with its uncertainties is measured using the tag and probe method with  $Z \rightarrow \mu^+\mu^-$  and  $J/\Psi \rightarrow \mu^+\mu^-$  events. They are provided by the ATLAS muon performance group [118]. The uncertainties are provided separately for the reconstruction, isolation and track to vertex association split into a statistical component (due to the finite data and MC sample size) and a systematic component from varying e.g. the tag and probe selection. Both parts are varied separately for all efficiency corrections and the effect on the final expectation is studied. Additionally the uncertainties of the reconstruction efficiency corrections are split into a low  $p_T$  part and a high  $p_T$  part.

**Muon momentum scale** Although the MC samples contain a precise simulation of the ATLAS detector, differences in the momentum scale between data and simulation are present and have to be corrected. The ATLAS muon performance group [118] provides these corrections as a function of muon  $p_T$  and  $\eta$ , estimated using  $Z \rightarrow \mu^+\mu^-$  and  $J/\Psi \rightarrow \mu^+\mu^-$  events. Different systematic effects are considered when the scale correction is determined, for example changing the mass window or the background parametrization. More details about the source of the systematic uncertainty are given in [118]. The uncertainty of the muon momentum correction is in the order of 0.05%. The impact on the selected events in this analysis is estimated by shifting the muon momentum scale by one standard deviation up and down.

**Muon momentum resolution** The muon momentum resolution has to be smeared to be equal between data and simulation, as it was explained in Section 5.4.2. The uncertainties for the smearing are also provided by the ATLAS muon performance group and are in the low momentum scale in the order of 0.2%. The impact on the selected four lepton events of this analysis is estimated by increasing and decreasing the smearing by one standard deviation of the resolution parameter.

### 7.3.1.3 Jet uncertainties

**Jet energy scale** The jet energy scale has to be corrected in simulation to match to data. The ATLAS jet performance group [168] provides this correction together with its systematic

---

uncertainties which can range from 1%-4.5% dependent on the energy. The systematic uncertainties consist of a reduced set of 21 nuisance parameters that take for example different pileup suppression techniques into account. More information about which systematic effects are addressed with the nuisance parameter can be found in [168]. These nuisance parameter are varied up and down by one standard deviation to investigate the impact on this analysis.

**Jet energy resolution** The jet energy resolution matches in data and simulation within the uncertainty, therefore no correction of the central value is done. Nevertheless the impact of changing the resolution within the uncertainty is investigated. Therefore the ATLAS jet performance group provides a nuisance parameter that increases the energy resolution. More details are given in [123]. The uncertainties vary from about 6% at  $p_T = 20$  GeV down to 1% for  $p_T = 200 - 1800$  GeV.

**Jet vertex tagger** Jet vertex tagging suppresses pileup jets as it was explained in Section 4.4. The efficiency of the cut on the discriminating variable can be different in data compared to simulation. In order to account for such differences a  $p_T$  dependent correction factor is applied which is provided by the ATLAS JVT group [124]. Systematic uncertainties on the scale factor are extracted, for example by taking differences between different generators into account. More details on how the systematic uncertainties on the correction factor are estimated can be found in [124]. The influence on the selected events of this analysis are estimated by varying the correction factor one standard deviation up and down.

### 7.3.2 Luminosity uncertainty

The luminosity enters when the expectation is normalized to the data yield. The uncertainty on the luminosity of 3.2% therefore affects the normalization of the simulated samples. It is derived from a preliminary calibration of the luminosity scale using x-y beam-separation scans performed in August 2015 and May 2016. More details about the methodology of the uncertainty determination can be found in Section 3.2.8 and [169].

### 7.3.3 Pileup modeling uncertainty

In Section 5.4.3 it was described how the pileup profile is reweighted to match to data. The ratio between the predicted and measured inelastic cross section is included in the pileup reweighting as correction factor. Systematic uncertainties of this ratio are covered by varying this correction factor up and down by one standard derivation and checking the impact on the analysis.

---

### 7.3.4 Theoretical uncertainties

#### 7.3.4.1 PDF uncertainties

The PDFs used to generate samples come with an error set. For the CT10 PDF, which is used in the POWHEG simulation of  $q\bar{q}$  initiated  $ZZ$  processes, this error set comes with 26 variations ( $N_{\text{variations}}$ ). The variations are estimated using the method described in [58]. Each variation consists of an up ( $O^{+,i}$ ) and down ( $O^{-,i}$ ) part. The variations can be accessed through different weights which are applied to each event when processing the simulation. The combined uncertainty due to the PDF error sets on an observable is given by:

$$\Delta O^\pm = \sqrt{\sum_i^{N_{\text{variations}}} [\max(\pm(O^{+,i} - O), \pm(O^{-,i} - O), 0)]^2}. \quad (7.8)$$

The resulting uncertainties correspond to a 90% confidence interval and therefore have to be translated to a 68% confidence interval (one standard deviation) by dividing them by 1.645. Additionally variations using the central values of the NNPDF3.0 [57] or MMHT2014 [170] PDF as nominal PDF set are calculated. The envelope of these deviations and the set-internal error from the CT10 set is taken as the PDF uncertainty for each observable. The relative uncertainty estimated with the POWHEG  $q\bar{q}$  signal sample is also applied to the  $q\bar{q}$  SHERPA signal prediction. PDF uncertainties on the other signal processes like  $gg$  induced  $ZZ$  production as well as effects on the genuine background are not considered since the size of these contributions is smaller.

#### 7.3.4.2 Renormalization and factorization scale uncertainties

The choice of the renormalization and factorization scale has an impact on the physical observable when generating events at higher order in QCD. Therefore the scales are varied to estimate the size of the effect. Combinations of doubling the scales and dividing them by 2 are propagated to the observable. This results in six different variations when excluding the cases where one scale is doubled and one is halved. The envelope of all variations is then taken as uncertainty on the signal prediction. Also here the uncertainty is estimated using the POWHEG sample for  $q\bar{q}$  induced process only, neglecting contributions from other signal and background simulations.

#### 7.3.4.3 Higher order corrections

It was described in Chapter 5.1 how higher order QCD and EW corrections were applied. Doing it this way implicates that the two corrections factorize completely which is not necessarily the case. In order to account for this, variations based on the QCD activity in an event are done which is inspired by the procedure described in [171]. Events do have high QCD activity when  $|\sum_i \vec{p}_{T,i}| > 0.3 \sum_i |\vec{p}_{T,i}|$ , where the sum runs over the leptons from the hard interaction on generator level. Systematic variations are estimated by either applying no EW k-factor to these events or applying a factor double of the size:  $(1 + 2(\text{k-factor} - 1))$ . The deviation to the nominal case is taken as systematic uncertainty. In principle also the higher order QCD k-factor

has uncertainties from e.g. the renormalization and factorization scale variations, but to avoid double counting with the before mentioned ones those are not taken into account.

The contribution from  $gg$  induced  $ZZ$  production is also scaled with a NLO QCD k-factor which has an uncertainty of 15% [132] and applied as a normalization uncertainty.

#### 7.3.4.4 Cross section uncertainties on background samples

To account for cross section uncertainties of the  $t\bar{t}Z$  and triboson background a flat 30% uncertainty is included for these processes which is also used by the official ATLAS  $ZZ$  measurement [62].

#### 7.3.5 Impact of systematic uncertainties on the expectation

The different variations discussed before are propagated and the impact on the invariant mass of the combined four lepton system is presented. The uncertainties are symmetrized by using the larger of the up or down variation. The total uncertainty is the quadratic sum of all single variations for example all 15 variations of the electron identification efficiency uncertainty. The  $q\bar{q}$  initiated process is here taken from SHERPA due to having more simulated events which reduces statistical fluctuations when investigating systematic effects. For all other uncertainties POWHEG is used for the  $q\bar{q}$  initiated process.

Figure 7.20 shows the experimental related uncertainties. The dominating electron uncertainty

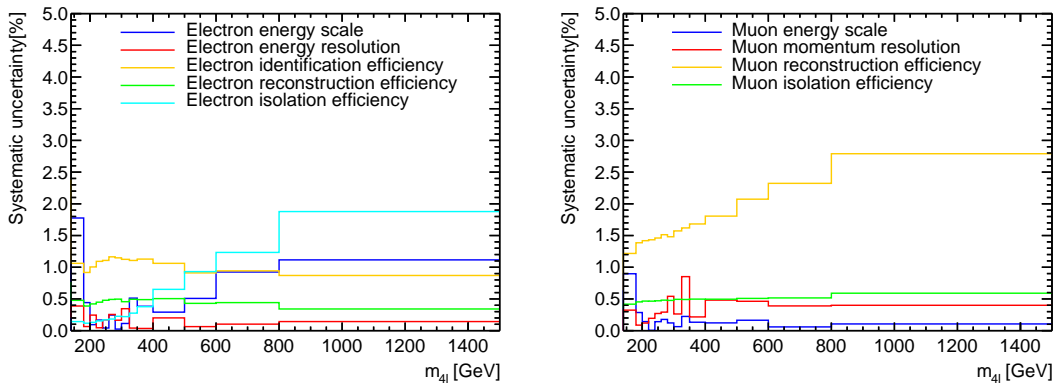


FIGURE 7.20: Relative experimental systematic uncertainties related to leptons on the total expectation in the combined channel as function of the four lepton mass. The left (right) side shows electron (muon) related systematic uncertainties.

in the region up to 500 GeV is the identification efficiency uncertainty. At that point the uncertainty of the electron isolation efficiency correction starts to dominate since the correction is only measured up to 150 GeV and above that, an uncertainty of 2% per electron is applied. This results in an increasing behavior since the electrons have to have higher  $p_T$  to get higher  $m_{4l}$ . Also the energy scale uncertainty increases for higher  $m_{4l}$  from 0.5% to about 1%. The values in the first bin for the energy scale and resolution uncertainty are unexpectedly high, since the number of simulated events in this bin is very low and migration of some events out of this bin can lead to large differences.

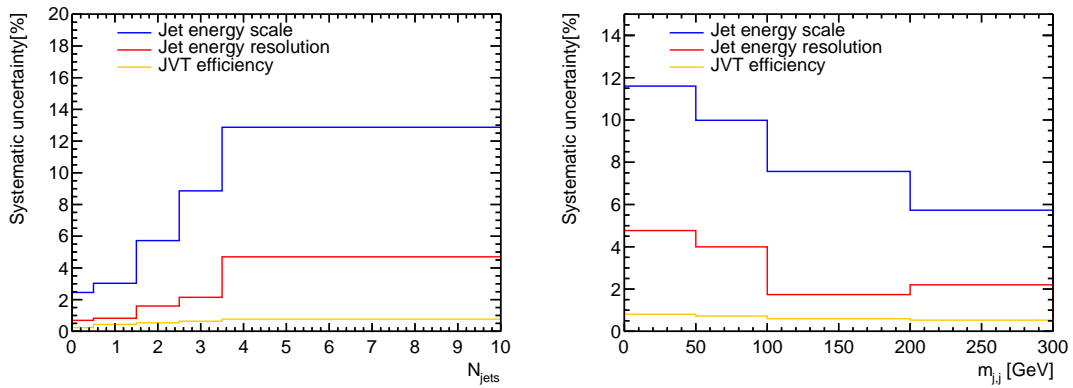


FIGURE 7.21: The left side shows jet related relative systematic uncertainties as function of the number of additional jets in four lepton events. The last bin includes events with four or more jets. The right side shows the uncertainties as function of the invariant mass built with two additional jets in four leptons events that have highest and second to highest  $p_T$ .

The reconstruction efficiency correction uncertainty is the most dominant muon related uncertainty. It rises from about 1% in the low  $m_{4l}$  region to about 3% in the high mass region. This is the case because the efficiency is only measured up to muon momenta of 100 GeV and extrapolated for higher momenta with a larger uncertainty. This effect is enhanced due to having two or four muons in the final state. The isolation efficiency correction is measured up to 500 GeV. Therefore not such a strong increasing behavior is visible. The momentum scale and resolution contribute less than 0.5% to the total uncertainty.

Jet uncertainties only enter the analysis where additional jets in selected four lepton events are present. The impact of the uncertainties on jet observables is shown in Figure 7.21. On the left side the uncertainties are shown as function of the number of additional jets and on the right side as function of the invariant mass, built with the two highest  $p_T$  jets. The jet energy scale uncertainty is the dominating one which starts at 2.5% for events with zero additional jets and goes up to 13% for events with 4 or more jets. The dependency as function of the invariant mass of the two hardest jets shows a decrease from 11.5% to 6%, because the determination of the jet energy scale is more difficult for low energetic jets due to high contamination with pileup jets.

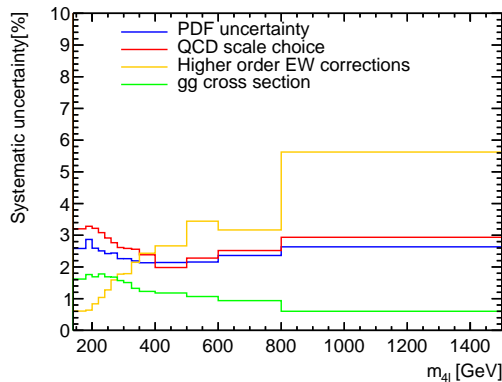


FIGURE 7.22: Relative systematic uncertainties from theory related sources as function of the four lepton mass.



The theory uncertainties as function of the four lepton mass are shown in Figure 7.22. It can be seen that for masses up to about 300 GeV the PDF and QCD scale uncertainties dominate with about 3%. The uncertainties from higher order electroweak corrections starts to dominate for higher masses going up to about 6%. The k-factor uncertainty of the  $gg$  induced  $ZZ$  contribution is about 1.5% in the low mass region and 0.5% in the high mass region.

The relative contribution of the background uncertainties as function of the invariant four lepton mass is shown in Figure 7.23. The largest contribution is from background due to fake leptons. It has uncertainties of 6% in the lowest  $m_{4l}$  bin which sharply drop below 1% at higher masses.

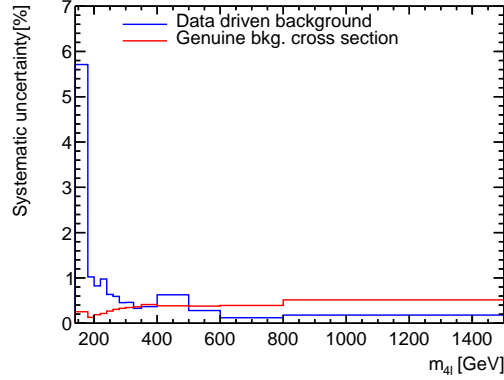


FIGURE 7.23: Relative systematic uncertainties from background related sources as function of the four lepton mass.

Table 7.7 shows a summary of all systematic uncertainties per channel. The largest uncertainty is 3.7% from QCD scale and PDF variations. The largest experimental uncertainty besides the luminosity uncertainty is given by the efficiency uncertainties. The total uncertainty amounts about 4-5%. This is larger than the relative statistical uncertainty from data in the combined channel which is about 3%.

Systematic	$4e$	$2e2\mu$	$4\mu$	combined
Monte Carlo statistics	0.8 %	0.5 %	0.7 %	0.4 %
Higher order EW corrections	1.3 %	1.4 %	1.4 %	1.4 %
$gg$ initiated cross section	1.6 %	1.6 %	1.6 %	1.6 %
QCD scales & PDFs	3.7 %	3.7 %	3.7 %	3.7 %
Electron efficiency	2.6 %	1.3 %	/	1.2 %
Electron energy scale & reso.	0.2 %	< 0.1 %	/	< 0.1 %
Muon efficiency	/	1.5 %	3.0 %	1.6 %
Muon momentum resolution	/	< 0.1 %	< 0.1 %	< 0.1 %
Background	0.6 %	0.5 %	0.8 %	0.5 %
Pileup modeling	1.2 %	0.9 %	2.2 %	1.3 %
Luminosity	3.2 %	3.2 %	3.2 %	3.2 %
Combined	5.7 %	5.2 %	5.4 %	5.2 %

TABLE 7.7: Summary of the systematic uncertainties on integrated expected yields.

## 7.4 Comparison of data and expectation

It is now possible to compare selected data with the expectation. Table 7.8 shows the event yield per channel for the single contributions together with the total prediction using SHERPA or POWHEG for the  $q\bar{q}$  induced contribution in comparison to data. Both total predictions agree within their uncertainty, but SHERPA predicts about 3.5% more in the combined channel. One reason for this is that SHERPA does not include higher order electroweak corrections. The largest difference is found in the  $4e$  channel with about 25% more data than expected. In order to check how significant this deviation is, the probability is calculated to have an observation of 249 events or more when expecting  $198 \pm 11$  events using a poisson model that takes also uncertainties of the prediction into account [172]. The result is a probability of 0.3% which corresponds to a significance of  $2.7 \sigma$ . More about the disagreement in this channel is given in Section 7.4.1. Differences between data and expectation in the other channels are below  $< 1\sigma$ .

Contribution	$4e$	$2e2\mu$	$4\mu$	Combined
Data	249	465	303	1,017
Total prediction [SHERPA]	$198 \pm 11$	$469 \pm 26$	$293 \pm 19$	$957 \pm 54$
Total prediction [POWHEG]	$191 \pm 11$	$451 \pm 27$	$283 \pm 19$	$925 \pm 54$
Signal ( $q\bar{q}$ -initiated) [POWHEG]	$160.4 \pm 10.0$	$381 \pm 24$	$239 \pm 16$	$780 \pm 48$
Signal ( $q\bar{q}$ -initiated) [SHERPA]	$168.2 \pm 9.3$	$399 \pm 22$	$248 \pm 14$	$812 \pm 44$
Signal ( $gg$ -initiated)	$21.4 \pm 3.3$	$50.3 \pm 7.8$	$29.7 \pm 4.7$	$101 \pm 16$
Signal (EWK $ZZjj$ )	$4.36 \pm 0.53$	$10.31 \pm 0.86$	$6.45 \pm 0.66$	$21.1 \pm 1.4$
$ZZ \rightarrow \tau\tau[l\ell, \tau\tau]$	$0.61 \pm 0.14$	$0.55 \pm 0.14$	$0.58 \pm 0.14$	$1.74 \pm 0.24$
Triboson	$0.73 \pm 0.22$	$1.61 \pm 0.49$	$1.03 \pm 0.31$	$3.4 \pm 1.0$
$t\bar{t}Z$	$0.98 \pm 0.30$	$2.23 \pm 0.68$	$1.70 \pm 0.52$	$4.9 \pm 1.5$
Misid. lepton background	$2.1 \pm 2.1$	$4.9 \pm 3.6$	$5.3 \pm 5.1$	$12.3 \pm 8.2$

TABLE 7.8: Observed and predicted yields. The uncertainties contain all statistical and systematic contributions.

Also interesting is the comparison between data and expectation as a function of different kinematic variables. First variables to look at are kinematic properties of the selected electrons and muons. Figure 7.24 shows  $p_T$ ,  $\eta$  and  $\phi$  of the selected electrons and muons in the combined channel. In addition to the  $q\bar{q}$  induced prediction from POWHEG also the total prediction using SHERPA is shown. The panels at the bottom of each plot show the ratio of data and the two total predictions. The uncertainties shown there only reflect the statistical uncertainty of the data. The  $p_T$  distribution shows the expected step falling behavior and good agreement between data and expectation for the muons. For electrons between 20 GeV and 70 GeV data lies above expectation, which is further discussed later. The  $\eta$  distributions have a maximum at  $\eta = 0$  and decrease to higher  $|\eta|$  values. The agreement between data and expectation is good for muons. An offset of about 15% can be seen for electrons. The  $\phi$  distributions shows the expected flat behavior and no shape differences between data and expectation but also the

offset for electrons.

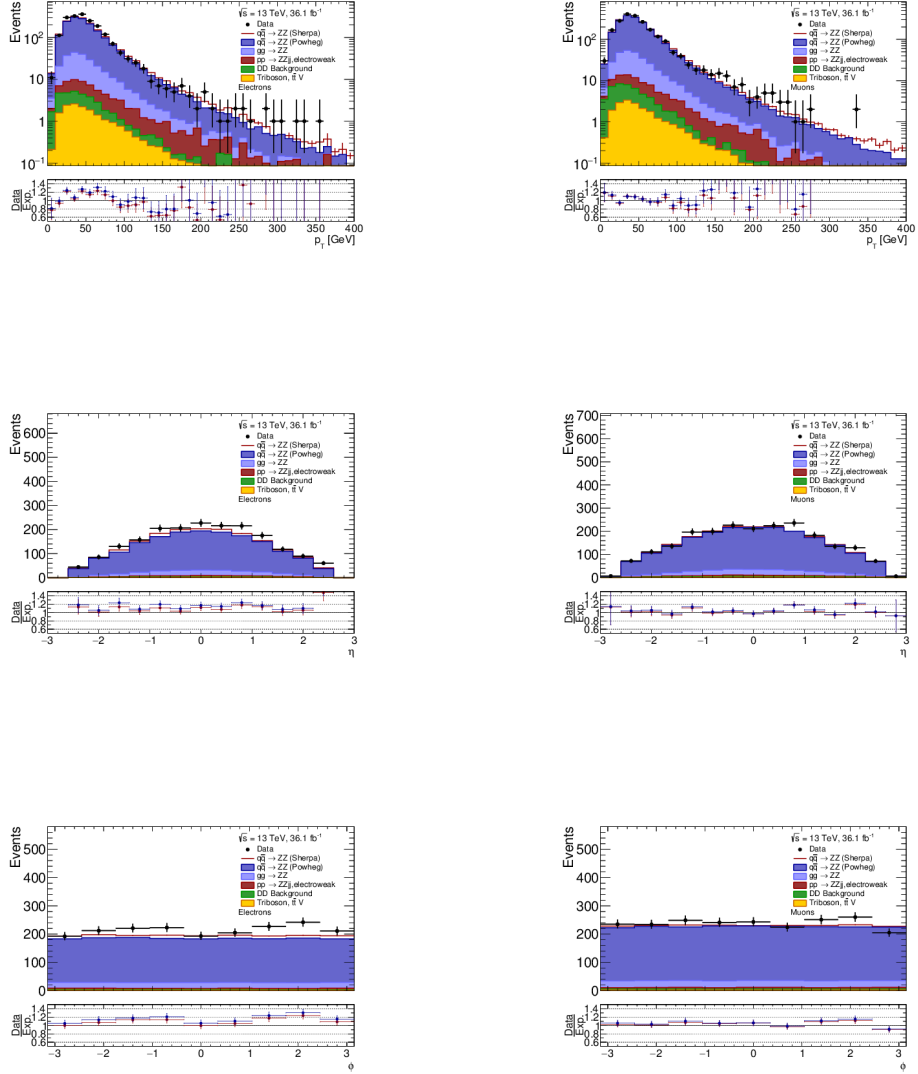


FIGURE 7.24: Comparison between data and expectation for different kinematic properties of electrons (left) and muons (right) after signal selection. The predicted contributions of the individual parts are stacked on each other. Additionally to the POWHEG prediction also a total prediction using SHERPA for the  $q\bar{q}$  initiated process is shown. The bottom panels show the ratio between data and expectations, in blue for  $q\bar{q}$  induced process using POWHEG and in red using SHERPA.

A variable that is build from the four selected objects is the invariant mass of the four lepton system, which is a direct measure of the energy of the hard interaction. It is shown in Figure 7.25 for the different selection channels. The shape of the spectrum shows increasing behavior for masses lower than 200 GeV caused by the on-shell requirement. Above 200 GeV the typical expected steeply falling behavior is visible. Data shows good agreement with the expectations except in the  $4e$  channel where a deviation of up to 40% is visible at low masses. When comparing the POWHEG expectation with the SHERPA one, good agreement is found at low masses

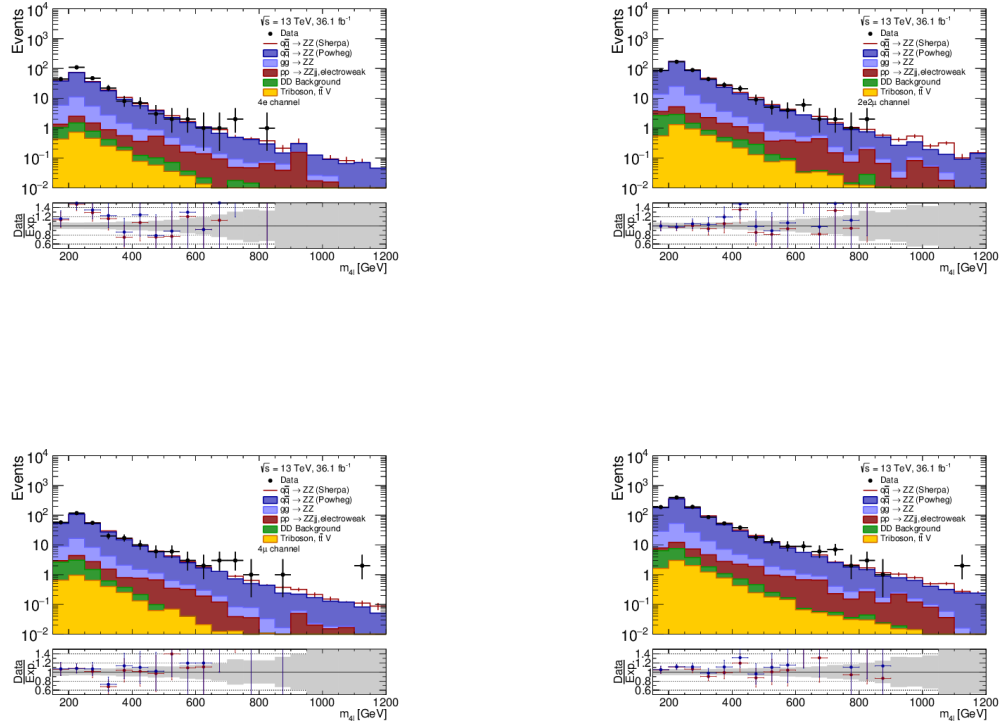


FIGURE 7.25: Comparison between data and expectation as function of the four lepton mass for different selection channels. The predicted contributions of the individual parts are stacked on each other. In addition to the  $q\bar{q}$  induced prediction from POWHEG also the total prediction using SHERPA is shown. The bottom panels show the ratio between data and expectations, in blue for  $q\bar{q}$  induced process using POWHEG and in red using SHERPA. The relative systematic uncertainty is shown as gray band.

but some differences are visible at higher masses which is also caused by not applying the EW k-factor to the SHERPA sample. Applying those impacts dominantly higher masses by pulling the expectation down.

A comparison of data and expectation as a function of the transverse momentum of the four lepton system  $p_{T,4l}$  is shown in Figure 7.26. This observable measures the recoil against other particles and is therefore sensitive to jet radiation from higher order QCD processes or electroweak effects. The sensitivity to electroweak radiation is also the reason why the difference between the SHERPA and POWHEG expectation is larger at high momenta compared to the high  $m_{4l}$  region. The general agreement between data and expectation is good in the low momentum region (also here the 4e channel builds an exception) but in the region  $p_{T,4l} > 50$  GeV the expectation is underestimating data.

Two observables that show angular properties of the  $ZZ$  system are the azimuth angle  $|\phi_{4l}|$  and the rapidity  $y_{4l}$  shown in Figure 7.27 for the combined channel. The absolute value of the azimuth angle shows the expected flat behavior for data and expectation. Differences between data and expectation in this distribution, would be a sign of detector effects that are not modeled in simulation, for example due to not well working detector components. The rapidity of

the four lepton system is connected with the  $z$ -component of the total momentum of the initial state partons. Therefore it also contains information about the PDFs. The comparison between data and expectation shows good agreement except for the first bin where a small deviation is visible.

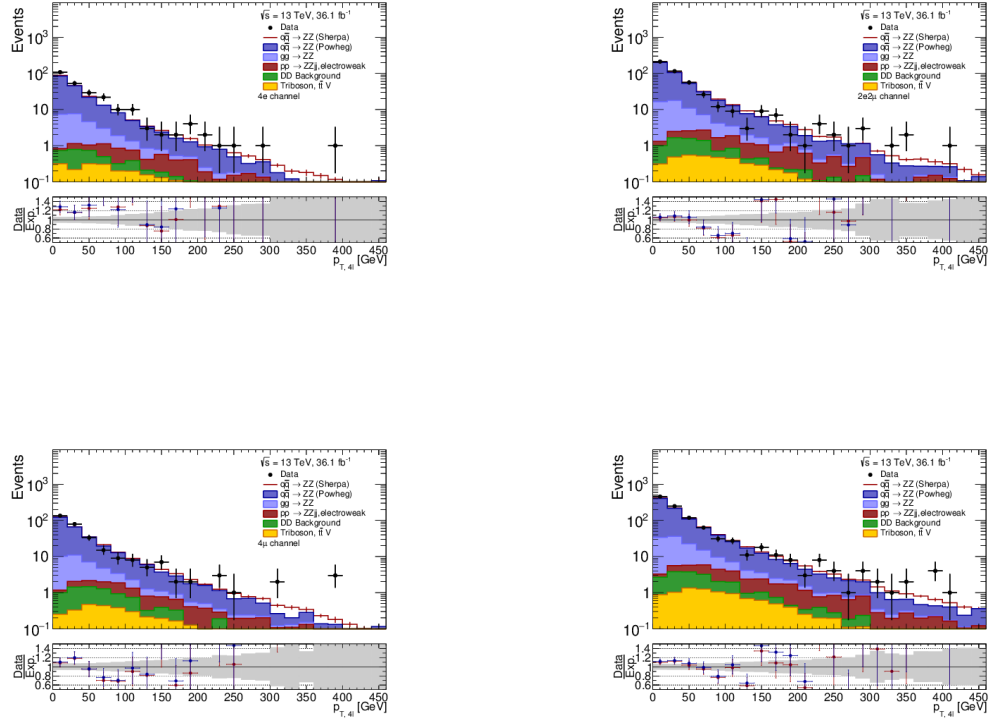


FIGURE 7.26: Comparison between data and expectation as function of the four lepton transverse momentum for different selection channels. The predicted contributions of the individual parts are stacked on each other. In addition to the  $q\bar{q}$  induced prediction from POWHEG also the total prediction using SHERPA is shown. The bottom panels show the ratio between data and expectations, in blue for  $q\bar{q}$  induced process using POWHEG and in red using SHERPA. The relative systematic uncertainty is shown as gray band.

The mass ( $m_{\text{lead}Z}$ ) and the transverse momentum ( $p_{T,\text{lead}Z}$ ) of the leading reconstructed  $Z$  boson candidate is shown for the combined channel in Figure 7.28. The  $Z$  boson resonance at about 90 GeV is clearly visible with good agreement between data and expectation. The transverse momentum has a sharp rising edge due to the kinematic requirements of the leptons. Then a steeply falling behavior to higher momenta is visible. Also here the agreement between data and expectations is good within the uncertainties.

Observables related to additional jets in selected four lepton events are shown in Figure 7.29. The comparison between data and the POWHEG and SHERPA expectations of the number of additional jets in four lepton events show that the agreement is good up to two jets, but then starts to differ more and more. This behavior reflects differences of the modeling in the parton shower between POWHEG and SHERPA which impacts most for high jet multiplicities. It is also visible that the electroweak  $ZZjj$  production has its maximum at  $N_{\text{jets}} = 2$  due to the two

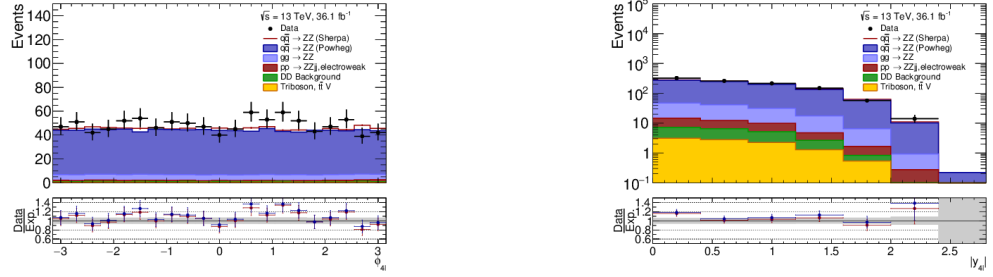


FIGURE 7.27: Comparison between data and expectation as function of angle  $\phi_{4\ell}$  (left) and rapidity (right) of the four lepton system. The predicted contributions of the individual parts are stacked on each other. In addition to the  $q\bar{q}$  induced prediction from POWHEG also the total prediction using SHERPA is shown. The bottom panels show the ratio between data and expectations, in blue for  $q\bar{q}$  induced process using POWHEG and in red using SHERPA. The relative systematic uncertainty is shown as gray band.

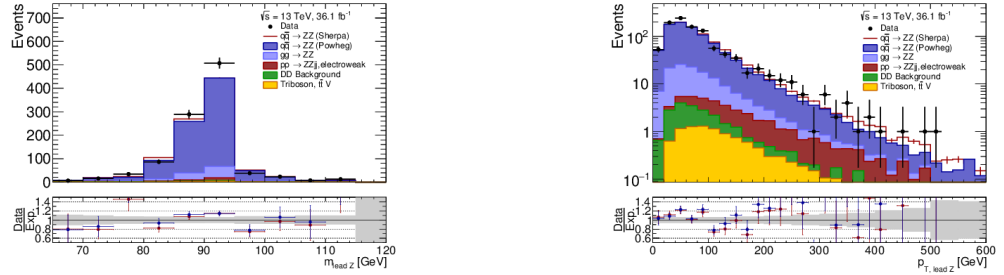


FIGURE 7.28: Comparison between data and expectation as function of the mass (left) and transverse momentum (right) of the leading reconstructed  $Z$  boson candidate. The predicted contributions of the individual parts are stacked on each other. In addition to the  $q\bar{q}$  induced prediction from POWHEG also the total prediction using SHERPA is shown. The bottom panels show the ratio between data and expectations, in blue for  $q\bar{q}$  induced process using POWHEG and in red using SHERPA. The relative systematic uncertainty is shown as gray band.

outgoing partons in the hard scatter process. Also the genuine background has its maximum at  $N_{\text{jets}} = 2$  since  $t\bar{t}V$  comes with two jets from the top decay. The disagreement between POWHEG and SHERPA in the  $N_{\text{jets}} = 2$  bin is also visible as a normalization difference when building the invariant mass and the rapidity difference of the two hardest (highest  $p_T$ ) jets. This is shown at the top right side and bottom of Figure 7.29. The number of events in these distributions is limited and therefore a conclusion about the agreement of the shapes is difficult. Within the uncertainties good agreement is observed in both distributions. Also the contribution of the electroweak  $ZZjj$  production is visible, which is higher at higher invariant masses and rapidity differences.

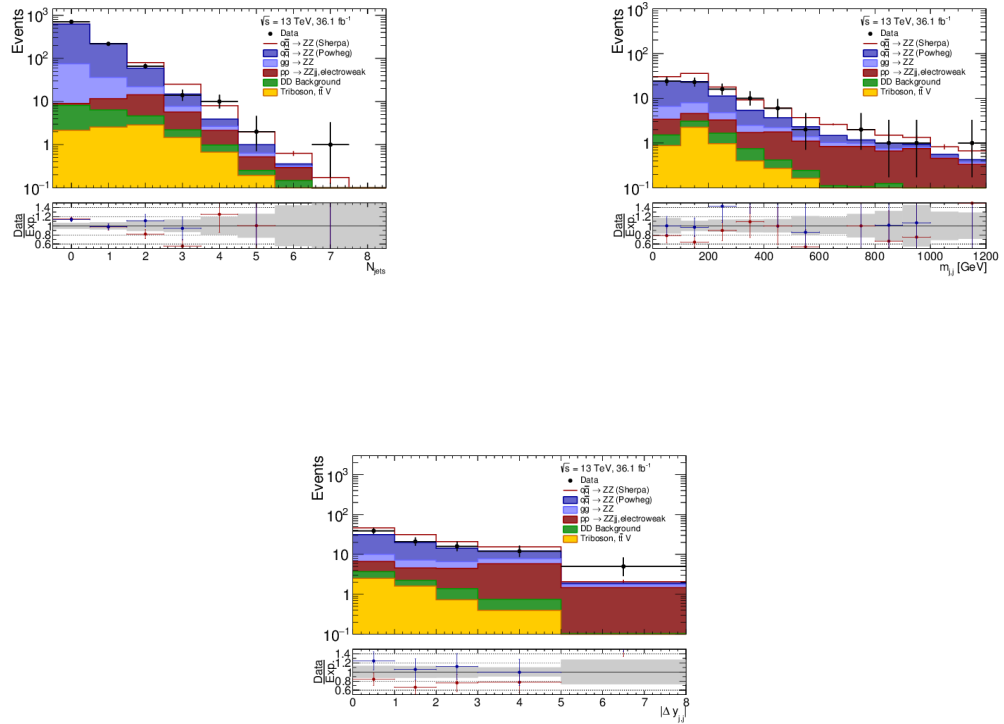


FIGURE 7.29: Comparison between data and expectation for observables including additional jets in four lepton events. The top left shows the number of additional jets, top right the invariant mass of the hardest two jets and at the bottom the rapidity difference between the two hardest jets. The contributions of the individual parts are stacked on each other. In addition to the  $q\bar{q}$  induced prediction from POWHEG also the total prediction using SHERPA is shown. The bottom panels show the ratio between data and expectations, in blue for  $q\bar{q}$  induced process using POWHEG and in red using SHERPA. The relative systematic uncertainty is shown as gray band.

#### 7.4.1 Investigation of the $4e$ disagreement

The disagreement between data and expectation in the  $4e$  channel could be a sign of a systematic effect that is not taken into account. Since the other channels have good agreement it could be assumed that there are problems that increase with electron multiplicity. In Figure 7.25 it was already shown that the disagreement is largest between 200 GeV and 300 GeV in  $m_{4l}$  and in regions  $< 70$  GeV in  $p_{T,4l}$ . In order to investigate the disagreement in the transverse four lepton momentum more in-depth, Figure 7.30 shows the distributions for the  $4e$  and  $2e2\mu$  channel in a finer binning. Using this binning shows that the largest disagreement in the  $4e$  channel is between 20 GeV and 30 GeV. The prediction in that bin using the SHERPA sample for the  $q\bar{q}$  initiated process is higher but not high enough to describe the data well. For comparison, the right side of the Figure shows the mixed channel. It can be seen that here the data in the second bin is well described by both expectations. In order to see if the disagreement is connected to kinematic properties of the electrons, it is necessary to compare data and expectation in electron related distributions. Therefore the  $p_T$ ,  $\eta$  and  $\phi$  spectrum of the electrons in the  $4e$  channel is

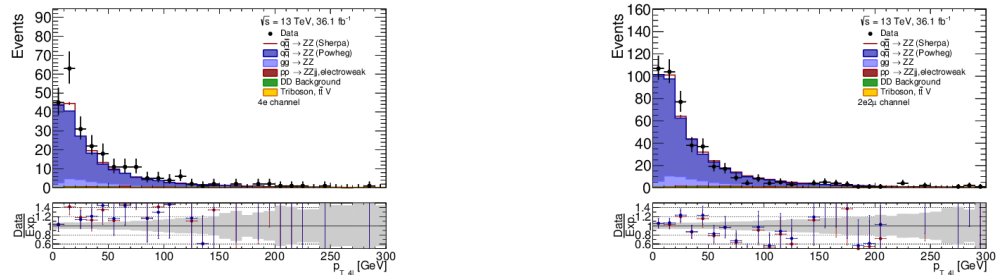


FIGURE 7.30: Comparison between data and expectation as function of the four lepton transverse momentum for the  $4e$  channel (left side) and the  $2e2\mu$  channel (right side) using 10 GeV bins. The contributions of the individual parts are stacked on each other. In addition to the  $q\bar{q}$  induced prediction from POWHEG also the total prediction using SHERPA is shown. The bottom panels show the ratio between data and expectations, in blue for  $q\bar{q}$  induced process using POWHEG and in red using SHERPA. The relative systematic uncertainty is shown as gray band.

shown in Figure 7.31. The angular spectra ( $\eta$  and  $\phi$ ) show that the disagreement is distributed equally in these observables which features that there is no problem with some specially location in the detector, like a broken cell in the calorimeter. The shape difference in the  $d_0$  significance was investigated by experts of the electron calibration group of ATLAS and is already corrected for in the scale factors that are applied as function of  $\eta$  and  $\phi$  (see chapter 5.4.1). In the  $p_T$  distribution it is visible that the deviation is mostly located between 20 GeV and 70 GeV. In order to separately check this region in more detail, Figure 7.32 shows the  $p_T$  distribution of only one electron per event that has the smallest  $p_T$  compared to the other three<sup>6</sup>. It is clearly visible that the deviation is located between 20 GeV and 30 GeV.

Now it is clearer where the deviation is located but the reason is not clarified. One possible explanation could be a major underestimation of the background with fakes. Given the size of the deviation the background would have to be wrong by a factor of 15 or more. This is very unlikely since other background estimations were done inside the ATLAS  $ZZ$  analysis group [62] which yield to the same magnitude of background. Another explanation could be an effect due to the usage of many triggers. Although it is checked that there are no events where only one of the included triggers fired, it might be possible that all data events are gathered by triggers in a kinematic region where they are not fully efficient. If that is the case small differences in the trigger efficiencies between data and simulation could lead to large deviations. Therefore the selection was redone using only one single electron trigger (HLT\_e26\_lhtight\_nod0\_ivarloose). Also the selection was modified to match the requirements of the trigger. This means the  $p_T$  threshold of the hierarchical  $p_T$  cut was raised to 30 GeV for the lepton with the highest  $p_T$ . The electron identification was set to the `LHTight` level and it was required that the electron with the highest  $p_T$  is matched to the object that fired the trigger. In addition the electron identification was moved from the quadruplet level to the object level to reduce the chance to pick a fake electron over a real one during quadruplet formation. The resulting  $p_T$  distribution

<sup>6</sup>The data driven background is here left out due to its small size.



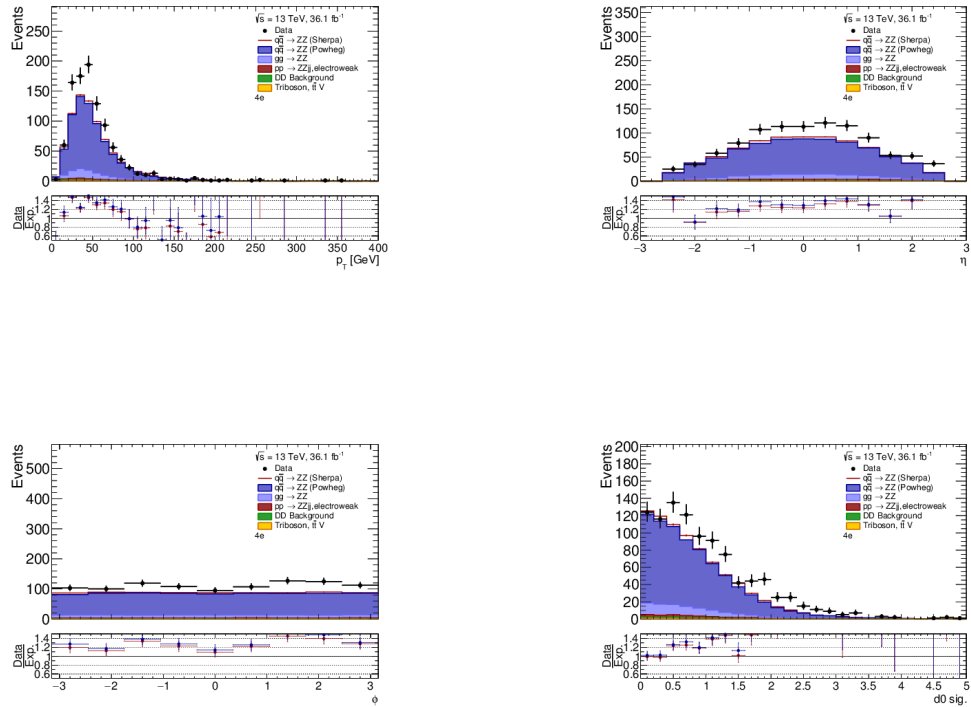


FIGURE 7.31: Comparison between data and expectation for  $p_T$  (top left),  $\eta$  (top right),  $\phi$  (bottom left) and the  $d_0$  significance (bottom right) of the electrons in the  $4e$  channel. The contributions of the individual parts are stacked on each other. In addition to the  $q\bar{q}$  induced prediction from POWHEG also the total prediction using SHERPA is shown. The bottom panels show the ratio between the expectations and data, in blue for  $q\bar{q}$  induced process using POWHEG and in red using SHERPA.

of the electron with the smallest transverse momentum is shown in Figure 7.33. Besides of having an overall smaller yield the deviation still remains and the reason is not given by the trigger selection mentioned before.

An analysis searching for resonant structures in high invariant masses of the four lepton system [173] also sees this excess which makes it less probable that it is caused by a technical mistake in the selection algorithm. It was checked by the ATLAS  $ZZ$  analysis group that a different modeling of the final state photon radiation is not reducing the excess. Also many more distributions including isolation variables, track parameter variables and other performance observables were checked and discussed with experts of the ATLAS electron calibration group, but nothing striking had been found. Therefore it is assumed that this deviation is an interaction of small effects from above mentioned reasons together with a large (unfortunate) statistical fluctuation. As mentioned before the probability of observing this amount of events is 0.3% which is small but not impossible.

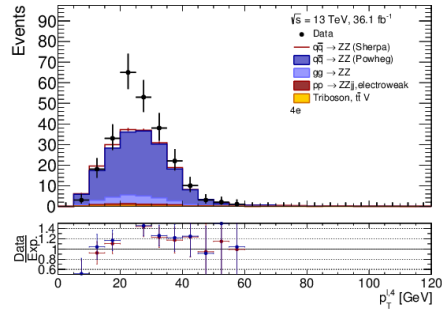


FIGURE 7.32: Comparison between data and expectation as function of the transverse momenta of the electron with the smallest  $p_T$  in a  $4e$  event. The contributions of the individual parts are stacked on each other. In addition to the  $q\bar{q}$  induced prediction from POWHEG also the total prediction using SHERPA is shown. The bottom panels show the ratio between the expectations and data, in blue for  $q\bar{q}$  induced process using POWHEG and in red using SHERPA.

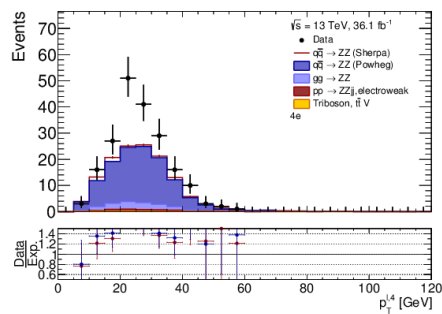


FIGURE 7.33: Comparison between data and expectation as function of the transverse momenta of the electron with the smallest  $p_T$  in a  $4e$  event after applying a modified selection. The contributions of the individual parts are stacked on each other. In addition to the  $q\bar{q}$  induced prediction from POWHEG also the total prediction using SHERPA is shown. The bottom panels show the ratio between the expectations and data, in blue for  $q\bar{q}$  induced process using POWHEG and in red using SHERPA.

# Chapter 8

## Cross section determination

The comparison of Standard Model expectations with data shows how good the level of understanding of the processes at the LHC is. For instance these comparisons can be done by comparing the number of observed events with an expectation built on simulation that includes all detector effects as it was shown in Section 7.4. The disadvantage of this comparison is the dependence on detector effects. Therefore this chapter describes, how cross sections can be extracted that are mostly independent on detector effects, which makes a comparison to theory predictions easier. First the fiducial definition, which describes the kinematic region where the cross sections are measured (also named fiducial phase space) is described in Section 8.1. Then the correction of detector effects with the resulting differential cross sections as a function of different kinematic observables is shown in Section 8.2. Integrated cross sections per channel are shown in Section 8.3. In this section also the extrapolation to the full on-shell region, without further kinematic requirements, is presented, compared to theory predictions and results from other analyses.

### 8.1 Fiducial definition

#### 8.1.1 Fiducial phase space

The fiducial phase space defines the kinematic region where the cross section is measured. It should be close to the selection applied to data to minimize possible extrapolation effects which depend highly on simulation. Theoretical uncertainties of the simulation effect the cross section more when doing an extrapolation. The fiducial phase space is the equivalent of the selection of reconstructed objects applied on particles on generator level. It is defined on prompt final state particles before detector simulation. Final state particles have a lifetime larger than  $c\tau_0 > 10$  mm as explained in Chapter 5. Prompt leptons do not originate from hadrons,  $\tau$  leptons, or any material interaction. This definition follows the ATLAS definition explained further in [174]. Like it is done for the selection of reconstructed leptons, at least four prompt electrons and/or muons should be present in an event. In order to mimic electromagnetic final state radiation (FSR) that occurs for charged leptons, prompt photons are added (*dressed*) to the four momenta of the electrons or muons if they are within  $\Delta R = 0.1$  of the lepton. The dressed leptons have

to have  $p_T > 5$  GeV and  $|\eta| < 2.7$ . This introduces a small extrapolation for electrons where the  $|\eta|$  cut is at 2.47 for reconstructed electrons. In order to keep the fiducial phase space more simple, also in terms of lepton universality, this disadvantage is accepted. With the remaining electrons and muons all possible quadruplets (same flavor, opposite charge dilepton pairs) are formed. The three highest  $p_T$  leptons of the quadruplets have to fulfill  $p_T > 20$  GeV, 15 GeV, 10 GeV, respectively. If more than four leptons are present, the quadruplet that minimizes  $|m_{\ell\ell,a} - m_Z| + |m_{\ell\ell,b} - m_Z|$  is selected, where  $m_{\ell\ell,a}$ ,  $m_{\ell\ell,b}$  is the invariant mass of the dilepton pair and  $m_Z$  the  $Z$  pole mass [31]. The leptons of the selected quadruplet have to be well separated and therefore  $\Delta R(l_i, l_j) > 0.1$  for same flavor leptons or  $\Delta R(l_i, l_j) > 0.2$  for different flavor leptons is required. Any combination of same flavor, opposite charge dileptons from the quadruplet has to have an invariant mass of greater than 5 GeV to match the requirement of the selection of reconstructed events, which is motivated by reducing the background from leptonically decaying hadrons. In the end an on-shell requirement on the  $Z$  boson is applied by requiring the invariant masses to be  $66 \text{ GeV} < m_{\ell\ell} < 116 \text{ GeV}$ . The classification in the  $4e$ ,  $2e2\mu$  and  $4\mu$  channel is done based on the chosen quadruplet, if necessary.

In order to provide differential cross sections for observables including additional jets in the event, also a jet definition in the fiducial phase space is necessary. Therefore all final state particles excluding all prompt leptons, prompt neutrinos and prompt photons are clustered to jets using the anti- $k_t$  algorithm [175] with a radius parameter of 0.4. The kinematic requirements on the jets are  $p_T > 30$  GeV and  $|\eta| < 4.5$ . When jets fall in  $\Delta R = 0.4$  of any selected fiducial lepton they are removed.

The fiducial phase space is the same as the one defined in the ATLAS publication of the  $ZZ$  on-shell measurement [62] and is summarized in Table 8.1

Type	Input or requirement
Leptons ( $e, \mu$ )	Prompt Dressed with prompt photons within $\Delta R = 0.1$ (added to closest prompt lepton) $p_T > 5$ GeV $ \eta  < 2.7$
Quadruplets	Two same-flavor opposite-charge lepton pairs Three leading- $p_T$ leptons satisfy $p_T > 20$ GeV, 15 GeV, 10 GeV
Events	Only quadruplet minimizing $ m_{\ell\ell,a} - m_Z  +  m_{\ell\ell,b} - m_Z $ is considered Any same-flavor opposite-charge dilepton has mass $m_{\ell\ell} > 5$ GeV $\Delta R > 0.1$ (0.2) between all same-flavor (different-flavor) leptons Dileptons minimizing $ m_{\ell\ell,a} - m_Z  +  m_{\ell\ell,b} - m_Z $ are taken as $Z$ boson candidates $Z$ boson candidates have mass $66 \text{ GeV} < m_{\ell\ell} < 116 \text{ GeV}$
Jets	Clustered from all non-prompt particles Anti- $k_t$ algorithm with $R = 0.4$ $p_T > 30$ GeV $ \eta  < 4.5$ Rejected if within $\Delta R = 0.4$ of a fiducial lepton

TABLE 8.1: Fiducial phase space definition. Table is taken from [62]

---

### 8.1.2 Signal definition

In general the signal is defined as processes that pass the fiducial phase space selection. This includes processes with a semi-leptonically decaying vector boson  $ZZV \rightarrow 4\ell jj$  which are included in the SHERPA EW  $4\ell jj$  sample. Processes with higher boson multiplicities or additionally produced Higgs bosons, for example  $ZZVV$  or  $ZZH$ , are also included in the signal definition but not present in the theory prediction. Double parton scattering in the same  $pp$  collision is also part of the signal definition but not included in the theory prediction. It is expected to be at most 1% of the signal contribution as already explained in Section 7.1.

From this definition, processes with four prompt leptons and any additional lepton, neutrino or photon are subtracted and considered as background which was discussed in more detail in Section 7.2. Examples of such processes are  $ZZW^+ \rightarrow 4\ell + \ell^+ \nu_l$  and  $WWZ \rightarrow 4\ell + \nu_l \bar{\nu}_l$ . Those processes are only in the order of 1% relative to the signal processes due to the higher order in the electroweak coupling constant.

## 8.2 Differential cross section determination

This section focuses on the determination of the differential cross sections. It starts with a general description of the unfolding of detector effects on data and its implementation. It is continued with a section describing the input of the unfolding after which the final differential cross sections are presented.

### 8.2.1 Unfolding principle

The general idea of unfolding is the correction for three different effects. Firstly, the limited detector efficiency leads to events in the fiducial phase space that are not being reconstructed. The second correction takes bin migration effects into account when events at particle level are reconstructed in a different kinematic bin on detector level. Thirdly, the correction for events that pass the selection on reconstruction level but not the fiducial phase space which can happen due to detector resolution effects or contribution from other sources like pileup. In general it is expected that this correction is rather small. All these effects can be described by a response matrix  $R$ , where the elements give the probability of an event in true bin  $j$  to be observed in bin  $i$ . This can be written as:

$$x_i = R_{ij} t_j, \quad (8.1)$$

where  $x$  is the measured distribution, after background subtraction and  $t$  the true distribution. In principle it is possible to get the unfolded (true) distribution by matrix inversion of the response matrix. But this inversion can be technically or even mathematically challenging. For example, the matrix is not necessarily singular and therefore an inverse matrix is not defined. Also the inversion can lead to large fluctuations of the unfolded distribution leading to unphysical results like negative differential cross sections. Therefore in this analysis an iterative unfolding method based on Bayes' theorem [176] is used which uses regularization to numerically stabilize the solution. The main idea of this method is the connection of the true number of events in

---

bin  $j$  with the measured number of events in bin  $i$  via the probability of a measured event in bin  $i$  ending up in bin  $j$  ( $P(t_j|x_i)$ ):

$$t_j = \frac{1}{\epsilon_j} \sum_{i=1}^n x_i P(t_j|x_i), \quad (8.2)$$

where  $\epsilon_j$  is the efficiency in bin  $j$  of total  $n$  bins. By using Bayes' theorem,  $P(t_j|x_i)$  can be replaced which then yields to:

$$t_j = \frac{1}{\epsilon_j} \sum_{i=1}^n \frac{P(x_i|t_j)P_0(t_j)}{\sum_k P(x_i|t_k)P_0(t_k)} x_i. \quad (8.3)$$

This equation depends on the likelihood  $P(x_i|t_j)$  which are the entries of the response matrix and a prior  $P_0(t_j)$  which is here chosen to be the true distribution from simulation. This procedure is repeated several times but using the posterior distribution of  $t_j$  as prior for a following iteration. The choice of the initial prior introduces a bias which is reduced by using more iterations, but with increasing iterations also the statistical uncertainty tends to increase since statistical fluctuations can be amplified. In this analysis three iterations are chosen. Studies of the official ATLAS analysis work group [62] showed that two to three iterations, dependent on the kinematic variable are a good trade-off between the statistical uncertainty and the bias from the initial chosen prior.

Statistical uncertainties of the data are estimated by generating 2000 sets of random pseudodata following a Poisson distribution with a mean at the number of events in each bin. The unfolding is repeated for each of the pseudodatasets and the root mean square (RMS) of the results is taken as data statistical uncertainty. In order to take uncertainties due to the finite number of generated events in MC simulations into account, a set of response matrices is generated by fluctuating the content randomly according to the MC statistical uncertainty. Again the RMS is taken as MC statistical uncertainty.

Further experimental and theoretical-modeling uncertainties are taken into account by using the accordingly varied response matrix. The difference to the nominal unfolding result is then taken as systematic uncertainty. Uncertainties from background are estimated by shifting the background by the uncertainty before subtracting it and taking the difference of the unfolded result to the nominal unfolded result as uncertainty.

An additional systematic uncertainty to account for uncertainties in the unfolding method is taken into account by using different number of iterations, either two or four and take the envelope of these variations.

All of the above described functionality is implemented in the *EWUnfold* software package that uses RooUnfold [177] which is a library within ROOT [105].

### 8.2.2 Choice of kinematic observables

In principle it is interesting to unfold all kinematic observables since then it is possible to see how well a theory prediction models a certain variable, but there are some variables of special interest that are used for the unfolding in this analysis.

The invariant mass of the four lepton system ( $m_{4\ell}$ ) is a direct measure of the energy of the system. It can be used to test theory predictions over a large energy range. Also models that

include physics beyond the Standard Model, like anomalous gauge couplings can make use of the differential cross section as function of the four lepton mass. Furthermore cross sections as function of the transverse momentum of the four lepton system ( $p_{T,4\ell}$ ) are interesting to measure since it gives a direct measure of the recoil kinematics against other particles produced in the collision. Therefore it can be used to test the modeling and understanding of QCD effects, like jet radiation or electroweak radiation over a large energy scale. The rapidity of the four lepton system ( $y_{4\ell}$ ) holds information of the  $z$ -component of the total momentum of the initial state particles and is therefore sensitive to PDFs. The  $p_T$  of the leading dilepton pair ( $p_{T,lead Z}$ ) is, as the four lepton mass, sensitive to contributions from possible BSM physics.

Variables that directly involve the kinematics of additional jets in the event (also called jet exclusive variables) like the number of jets in an event ( $N_{jet}$ ) give information about the jet activity and can be used to see how jet radiation is modeled by Parton Shower models in theory predictions. The invariant mass ( $m_{j,j}$ ) and the rapidity differences ( $\Delta y_{j,j}$ ) of the two leading (highest  $p_T$ ) jets are especially sensitive to contributions from electroweak production of  $ZZjj$  like vector boson scattering, which tends to have higher values in these variables than other  $ZZ$  production channels.

Therefore this set of seven observables is chosen to unfold and provide differential cross sections which are compared to theory predictions.

### 8.2.3 Binning choice

The choice of binning is a compromise of having fine bins which give more information, but have large uncertainties due to limited events per bin and larger bins with less information but smaller statistical uncertainties. Larger bins also have the advantage that migration effects play a smaller role, which makes the regularization easier. Therefore some criteria are placed on the binning. First the bins should contain all the data, so there should be no data in underflow or overflow bins. Each bin should also contain at least 10 expected events which corresponds to an expected statistical uncertainty of  $< 33\%$ . The expected rises and drops in distributions, for example the peak like structure in the  $m_{4\ell}$  spectrum at about 180 GeV, should be visible. In order to have a handle on the bin migration the purity should be above 70% if possible<sup>1</sup>. The purity is defined as the fraction of events that is generated in one bin and reconstructed in the same bin. These criteria are the ones that were used by the ATLAS publication of the  $ZZ$  on-shell measurement [62] and therefore the same binning is chosen here.

Examples of the purity and the fiducial correction in the final binning are shown for  $m_{4\ell}$  and  $m_{j,j}$  of the two hardest jets in Figure 8.1. Further purities and fiducial corrections of other observables can be found in Appendix E.1. The fiducial correction is the fraction of reconstructed events that also pass the fiducial selection. It can be seen that the purity for the four lepton mass is above 70% and the fiducial correction above 98% except for the first bin which has a very sharp raising edge due to the on-shell cut on the dilepton pairs. This leads to a larger possibility of bin migration. The purity for jet sensitive observables such as  $m_{j,j}$  is much lower which is caused by a large fraction of jets from pileup effects. This is also the reason for a smaller fiducial correction. Also a worse energy resolution as well as a larger uncertainty on the energy scale

<sup>1</sup>If a high purity would mean to lose a significant amount of information on the shape, the criteria is not applied.

compared to leptons causes smaller purities and fiducial corrections. In general it can be seen that the purity is higher when bins gets wider.

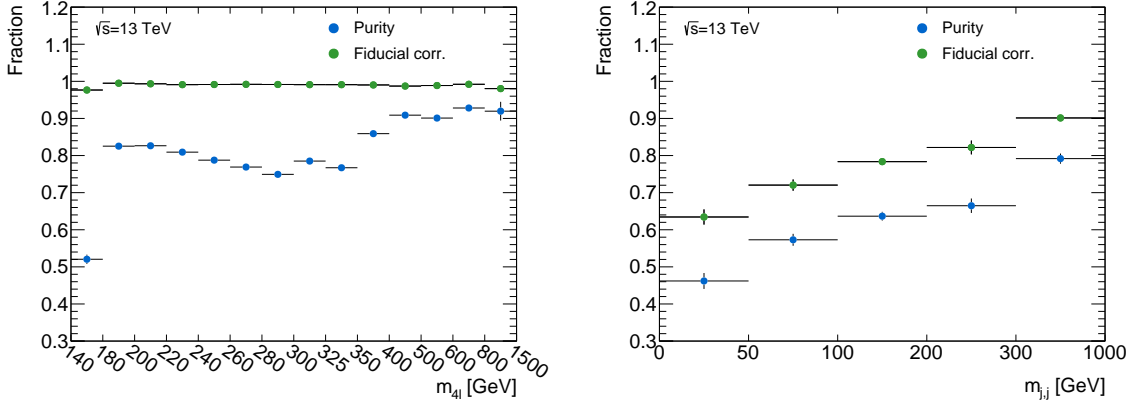


FIGURE 8.1: Fraction of events generated in one bin and reconstructed in the same bin (purity) for  $m_{4l}$  and  $m_{j,j}$  of the two hardest jets. The fiducial corrections show the fractions of events that pass the selection on detector level and the fiducial selection. The bins are not equidistant but for better visualization shown in an equidistant way. Only statistical uncertainties are shown.

## 8.2.4 Unfolding input

The efficiency and a measure of the bin migration are also needed to build the response matrix. The efficiency is defined as the ratio of signal events generated in the fiducial volume and the events in the fiducial volume that are reconstructed. It is constructed in a way that the numerator is a subset of the denominator. In this analysis all input for the unfolding is estimated using the POWHEG sample for the  $q\bar{q} \rightarrow ZZ$  process and not the SHERPA sample. In Figure 8.2 the efficiency as function of  $m_{4l}$ ,  $|y_{4l}|$  and  $m_{j,j}$  of the two leading jets is shown. The efficiencies for the other kinematic variables can be found in Appendix E.1. It can be seen that the efficiency for jet inclusive variables is rather flat at about 60% which is mostly driven by the lepton reconstruction and identification efficiencies as already explained in Section 6.6. The decrease in  $|y_{4l}|$  for higher rapidities is mainly caused by two effects. At high rapidities the leptons mostly have larger  $|\eta|$  and are therefore measured in the endcaps of the electromagnetic calorimeter. In the endcaps more material is between the beam axis and the calorimeter and therefore identification is more difficult. Secondly, there is an extrapolation for electrons since a cut is applied at  $|\eta| = 2.47$  on detector level but at  $|\eta| = 2.7$  at generator level which is an acceptance effect but included here in the efficiency correction. The efficiency in the first  $m_{4l}$  bin is much higher compared to the other bins which is correlated to the low purity in that bin. This means that a small amount of events might migrate from the second bin at detector level to the first one, leading to an increased efficiency and a lower purity. The decreasing behavior of the efficiency for higher jet multiplicities is caused by a reconstruction efficiency of a jet smaller than 100% which then enters multiplicative to the efficiency in the number of additional jets. Also the efficiency is decreasing for higher  $m_{j,j}$  and  $|\Delta y_{j,j}|$  which is caused by an increased suppression of pileup jets with higher jet  $p_T$  as shown in [125]. Thus the numerator of the efficiency is smaller due to less jets (from pileup) where the denominator stays the same.



In order to measure the bin migration between all bins of a variable a bin migration matrix is

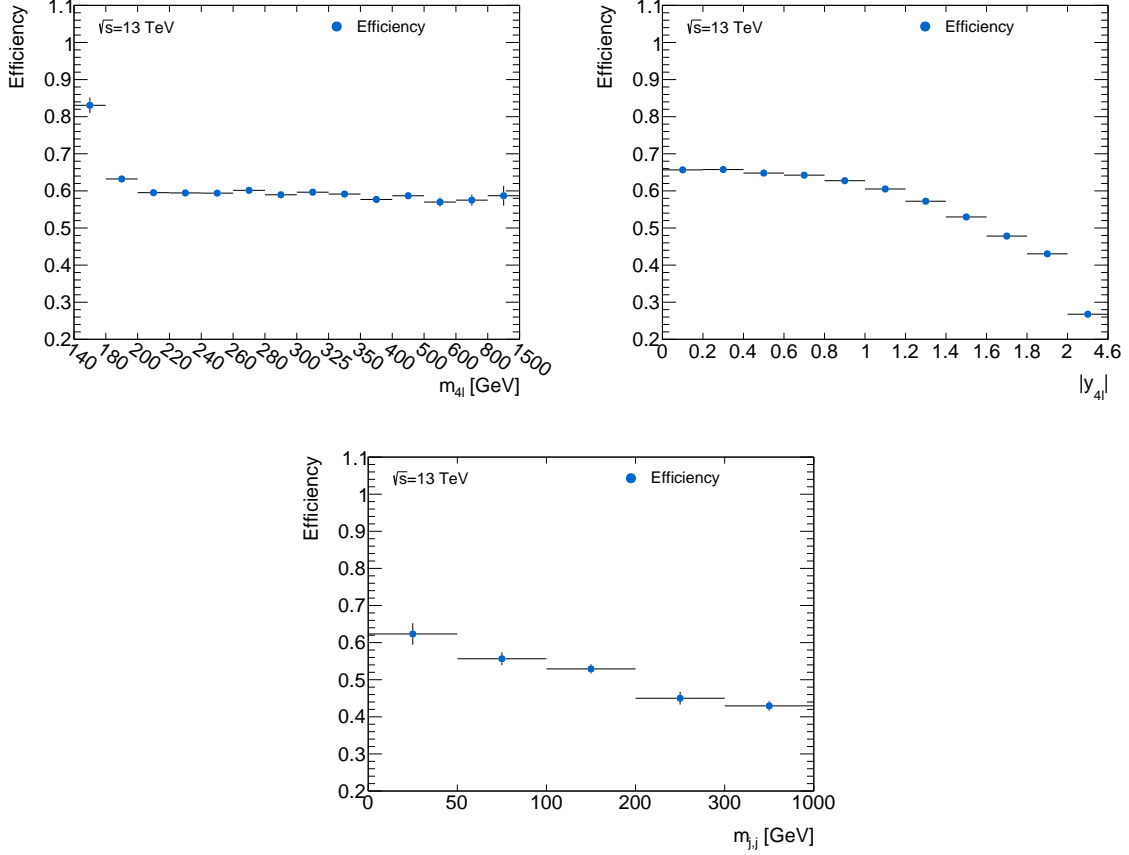


FIGURE 8.2: Efficiency correction as function of  $m_{4l}$ ,  $|y_{4l}|$  and  $m_{j,j}$  of the two hardest jets. The bins are not equidistant but for better visualization shown in an equidistant way. Only statistical uncertainties are shown.

build. Figure 8.3 shows bin migration matrices for the four lepton mass and  $m_{j,j}$ , the matrices for the others variables are given in Appendix E.1. Events passing the selection on detector level and the fiducial selection are filled into the matrix. On the x-axis values at detector level and on the y-axis the values at generator level are shown. The entries are normalized to the total number of reconstructed events in one bin of the reconstructed value. The diagonal elements correspond to the purity that was shown before. It can be seen that the migration matrix for  $m_{4l}$  is not diagonal especially in the low mass regime. Migration from a bin with higher mass on generator level to the next bin with lower mass on detector level is more dominant than the other way around. A reason for bin migration is the finite detector resolutions for measuring the energy and angular properties of particles. The energy resolution is not symmetric, especially for electrons. The resolution distribution tends to be skewed to lower values due to radiation losses in the detector [116] (e.g. *Bremsstrahlung*). The resolution of variables that are strongly correlated with the energy of the leptons inherit this behavior. For the four lepton mass this effect is even amplified since four leptons are included and therefore show a migration from high energetic bins into low energetic ones. Whereas the  $p_T$  of the four lepton system is not so much affected from this lepton resolution effect since it is not strongly correlated to the energy of the leptons but more on the momentum of the recoil particle which has a more symmetric energy

resolution. For a symmetric resolution the migration probability from one bin at generator level to neighboring bins on detector level is the same. For a falling distribution this results in, relatively speaking, more events migrating from bins with more entries to bins with less entries. Variables correlated to angular properties of particles do not show much migration since they depend primarily on the spatial resolution of the detector. Furthermore it can be seen that migrations over more than one bin are very small except of  $m_{j,j}$  where it is 7% in one bin.

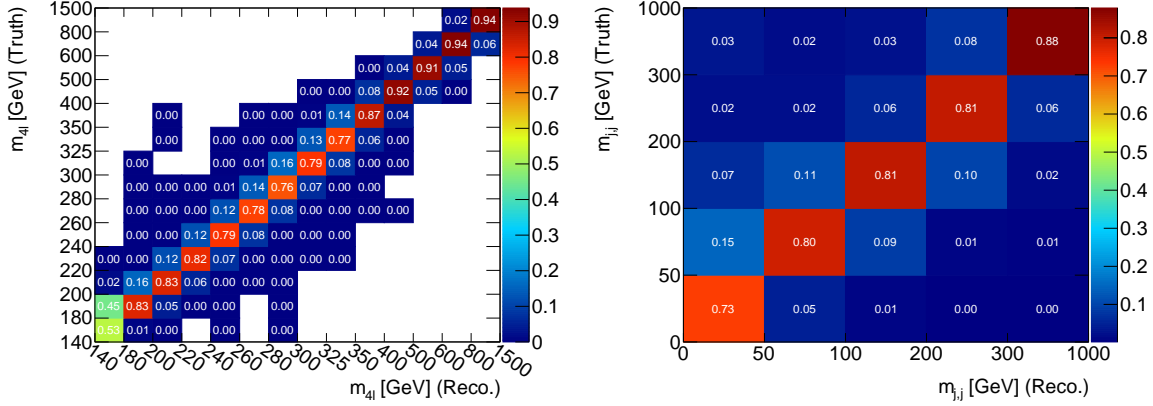


FIGURE 8.3: Bin migration matrices for  $m_{4l}$  and  $m_{j,j}$  of the two hardest jets. The y-axis corresponds to the value of the variable on generator level, the x-axis on detector level. The bins are not equidistant but for better visualization shown in an equidistant way. The entries are normalized to the number of reconstructed events in one bin integrated over the truth variable.

## 8.2.5 Monte Carlo based closure check

A way to test if the unfolding setup is working, is a so-called Monte Carlo closure check. The distribution of the MC simulation at detector level is used instead of data and the unfolded result is compared to the distribution on generator level. If everything is implemented in the right way this should lead to exactly the same distributions. For this closure the sum of all Signal MC samples is used which includes  $q\bar{q}$  induced processes from POWHEG and  $gg$  induced and EW  $ZZjj$  processes from SHERPA. Figure 8.4 shows the closure for the example of  $m_{4l}$  and  $m_{j,j}$ . The other distributions can be found in Appendix E.2. All distributions show full closure.

## 8.2.6 Systematic and statistical uncertainties

The sources of different systematic uncertainties were discussed in Section 7.3. They are propagated to the differential cross sections by redoing the unfolding with varied response matrix (see Section 8.2).

The relative systematic uncertainties after unfolding of the different jet inclusive variables, are shown in Figure 8.5. It can be seen that the theory uncertainties are in most bins below 1% since the theory uncertainties influence the variables at detector level as well as on generator level and therefore compensate to some extent during the unfolding procedure. Experimental uncertainties and their size were already explained in Section 7.3 and have about the same impact on the

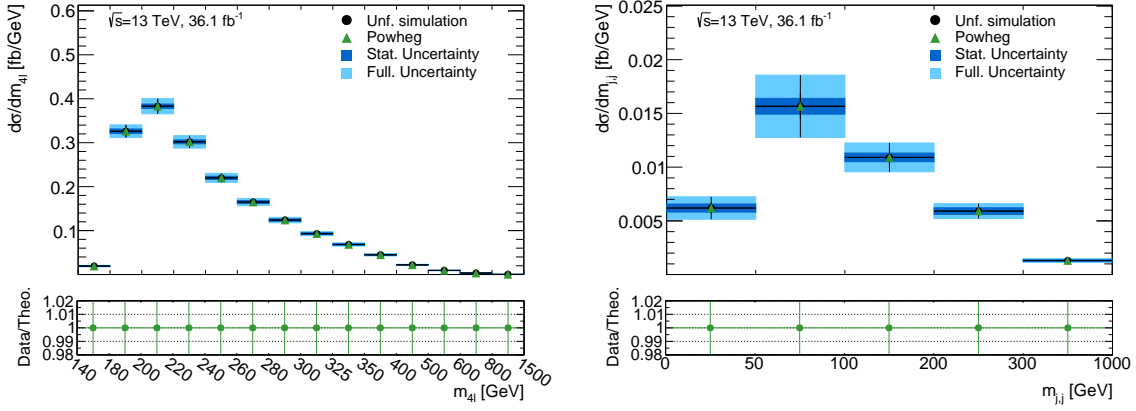


FIGURE 8.4: Monte Carlo closure check for  $m_{4l}$  and  $m_{j,j}$  of the two hardest jets. Instead of data the distribution of the signal MC samples on detector level is used for unfolding and compared to the distribution on generator level. The lower panel shows the ratio of the unfolded distribution and the one on generator level. The bins are not equidistant but for better visualization shown in an equidistant way.

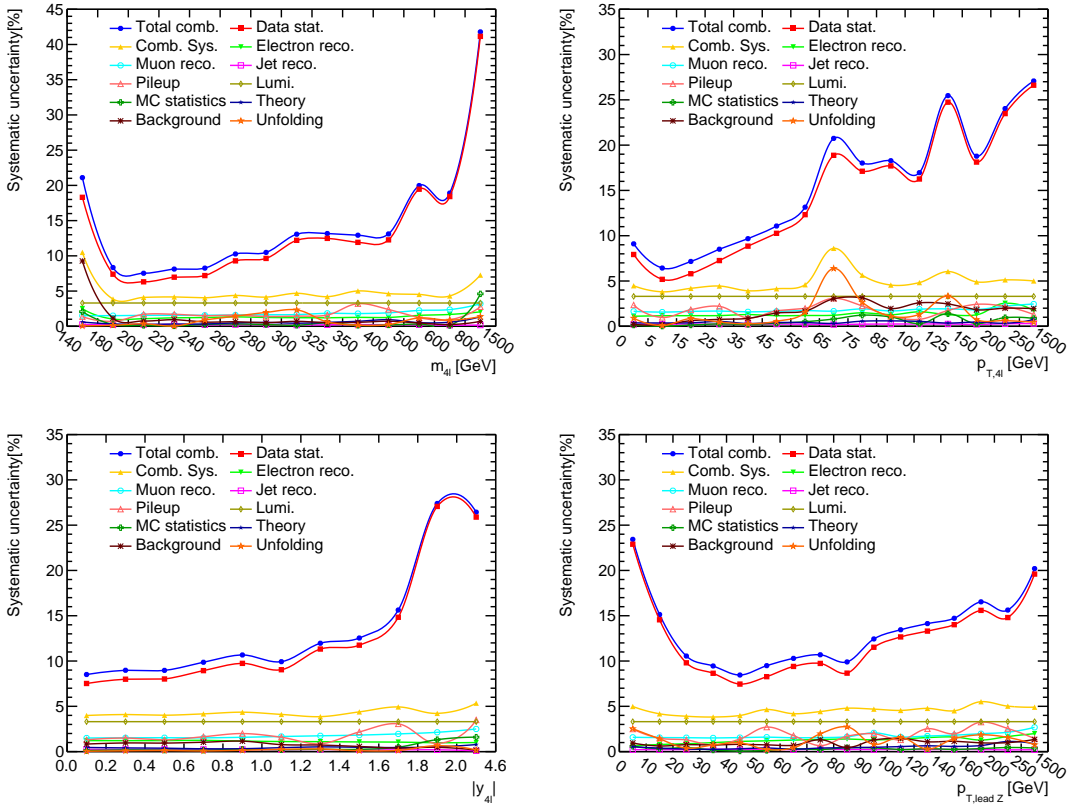


FIGURE 8.5: Relative uncertainties of the differential cross sections for jet inclusive variables. The bins are not equidistant but for better visualization shown in an equidistant way.

unfolded result. The unfolding uncertainty due to different numbers of iterations is in most bins a minor systematic uncertainty but can be large if the agreement between data and prediction is poor. This shows that after two iterations the bias due to the prior is still large in those bins and is decreased after further iterations. In order to have a conservative estimate of this

behavior the two iteration variation is included in the uncertainty. The statistical uncertainty from data is by far the largest uncertainty which reflects the perspective of future analysis with more data. The correlations of uncertainties between bins is shown in Appendix E.4.

The relative uncertainty for different sources of jet exclusive observables is shown in Figure 8.6. It can be seen that the jet scale and resolution (summarized as jet reconstruction) get dominant at high jet multiplicities. Also here the unfolding uncertainty is large in bins with bad agreement between data and prediction due to a larger prior dependence for the variation with only two iterations. The correlations of uncertainties between bins is shown in Appendix E.4.

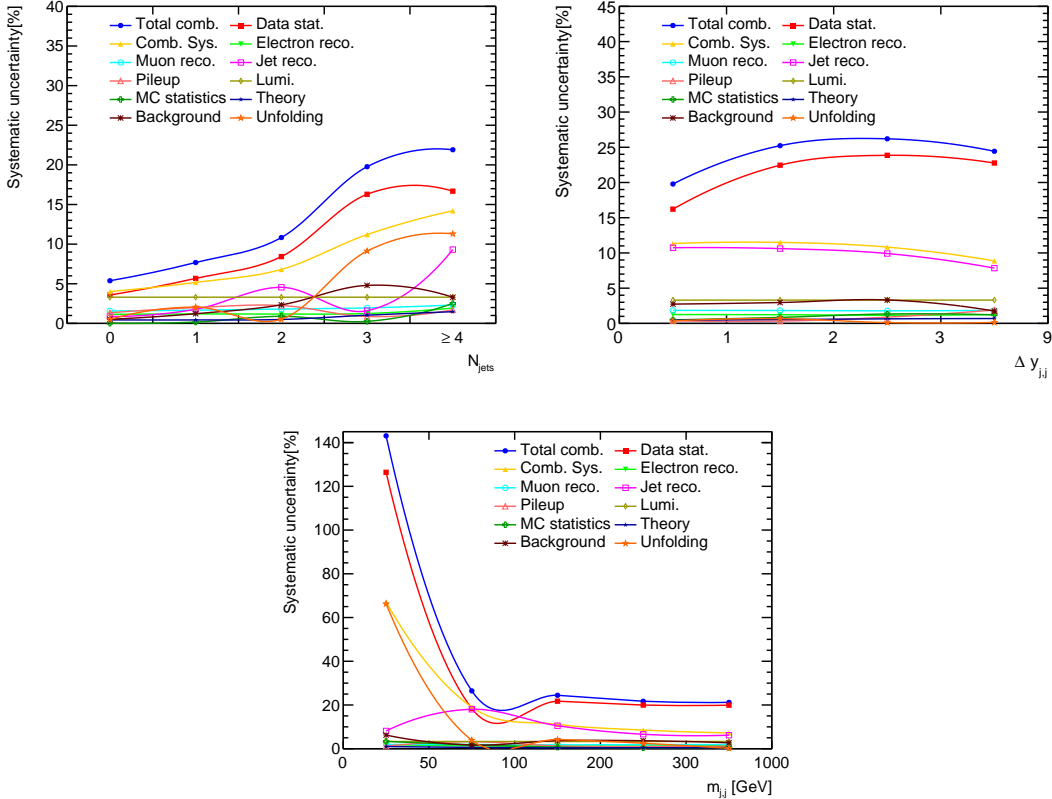


FIGURE 8.6: Relative uncertainties of differential cross sections for jet exclusive variables. The bins are not equidistant but for better visualization shown in an equidistant way.

## 8.2.7 Results

**Jet inclusive observables** The final unfolded distributions are shown in Figure 8.7 for jet inclusive variables together with two theory predictions. One prediction is built using POWHEG for the  $q\bar{q}$  initiated process, the other one using SHERPA. It can be seen that for  $m_{4l}$  and  $p_{T,4l}$  the agreement between data and the simulations is good within the uncertainties. There is one bin at  $600 \text{ GeV} < 800 \text{ GeV}$  in  $m_{4l}$  which has an excess of data with a local significance of about  $2.2 \sigma$ . This significance is based on a calculation done with data before unfolding and simulation on detector level similar to the procedure described in Section 7.4. This is not done with the unfolded data since it is easier to treat the uncertainty of data before unfolding with a simple Poisson approach. The local significance gets smaller when including the fact that many

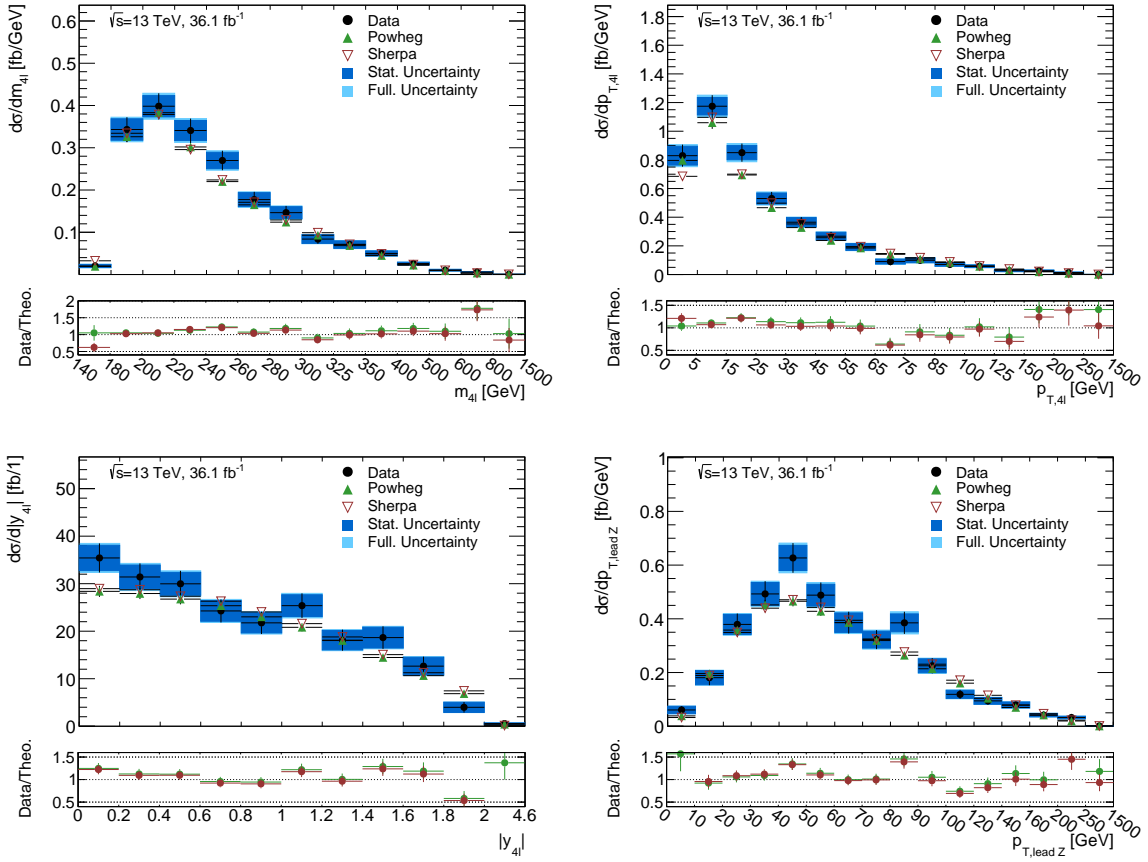


FIGURE 8.7: Differential cross section for jet inclusive variables. The black points represent the unfolded data with all statistical and systematic uncertainties. The lower panel shows the ratio of the unfolded distribution and two theory predictions. One is done with POWHEG (including higher order QCD and EW corrections) for the  $q\bar{q}$  initiated processes, the other one with SHERPA. Both include the  $gg$  and EW  $ZZjj$  from SHERPA. The bins are not equidistant but for better visualization shown in an equidistant way. The theory prediction with POWHEG for the  $q\bar{q}$  initiated process includes systematic theory uncertainties (PDF, QCD scale, HO corrections) whereas the SHERPA prediction includes only statistical uncertainties.

observables with many bins are unfolded which is called the "look elsewhere effect" [178] and therefore the difference is expected to be a statistical fluctuation. Also the ATLAS analysis that searches for resonant structures in the  $m_{4l}$  spectrum [173] observes this excess. This analysis also includes the case where one  $Z$  bosons decays to neutrinos where no excess is visible which supports the argument of a statistical fluctuation.

The  $p_{T,4l}$  distribution is described well by both theory predictions within in the uncertainties. One bin between 65 GeV and 75 GeV has a difference between data and theory of about 40%. The measured cross section in that bin is also below the cross section of the next bin which contradicts the expected decreasing behavior of the cross section for higher  $p_{T,4l}$ . Given the large number of bins it is expected that this disagreement is a statistical fluctuation of data. The absolute four lepton rapidity shows a small tendency of disagreement between data and theory expectation towards low  $|y_{4l}|$ . This might hold information to improve the PDF of the proton but given the large statistical uncertainties per bin it is not possible to quantify if an improvement is possible. The prediction using POWHEG for the  $q\bar{q}$  initiated part includes

---

also the PDF uncertainty, see Section 7.3.4 for more information, which reaches up to 3% for low  $|y_{4l}|$ , decreasing to 2% in the last  $|y_{4l}|$  bin. The  $p_T$  of the leading  $Z$  boson shows good agreement between theory prediction and unfolded data except of two bins, one at 45 GeV and one at 85 GeV which have a local significance of  $2.3 \sigma$  and  $2.0 \sigma$ , respectively. Physics due to anomalous triple gauge couplings would show up in the high  $p_T$  range. Therefore and due to a lowering of the significance because of the "look elsewhere effect" the differences are expected to be caused by statistical fluctuations.

The results that are published within the ATLAS collaboration [62] are within uncertainties the same as presented here. There are some differences which are dominantly caused by using POWHEG for the determination of the response matrix instead of SHERPA<sup>2</sup>. Larger differences are visible when comparing the relative size of the theory uncertainty which is much larger in the ATLAS publication. The theory uncertainty there also includes the difference between unfolding done with SHERPA and POWHEG which is not included here.

**Jet exclusive observables** Differential cross sections of jet exclusive observables are shown in Figure 8.8. Again data is compared to a prediction that uses POWHEG for the  $q\bar{q}$  initiated process or SHERPA. The jet multiplicity shows reasonable agreement for events with up to two jets. For events with three additional jets SHERPA does not agree with data and for events with four or more POWHEG fails to describe data. This is the case since both generators include only two parton radiation in the matrix element and therefore higher jet multiplicities are based only on the parton shower modeling. In the two leading jet distributions  $m_{j,j}$  and  $\Delta y_{j,j}$  an offset of about 40% between the two generators can be observed that is also visible in the  $N_{jet} = 2$  bin. Nevertheless, the shape of both predictions agrees well within the uncertainties except for the first  $m_{j,j}$  bin where both predictions fail to describe the data. These observables are important when looking at the EW  $Zjj$  production, which tends to higher  $m_{j,j}$  and  $\Delta y_{j,j}$  values but due to the large uncertainties the sensitivity to such processes is low. Also the selection is not optimized for the electroweak process.

The comparison with the ATLAS publication [62] shows for the jet exclusive variables some differences due to using POWHEG for unfolding instead of SHERPA.

### 8.3 Fiducial and total cross section

This section describes the determination of the integrated fiducial cross sections and the extrapolation to a total cross section for on-shell  $ZZ$  production. It starts with an explanation of the method followed by a presentation of the efficiency corrections per channel which is needed for the fiducial cross section and afterwards the extrapolation to a larger phase space. The resulting cross sections are then compared to results from analyses using data from ATLAS and other experiments.

---

<sup>2</sup>The choice to use POWHEG for this analysis presented here was made, since SHERPA has much more events which reduces the processing time significantly. This makes it impossible to use the same technical infrastructure which is used with the POWHEG setup.

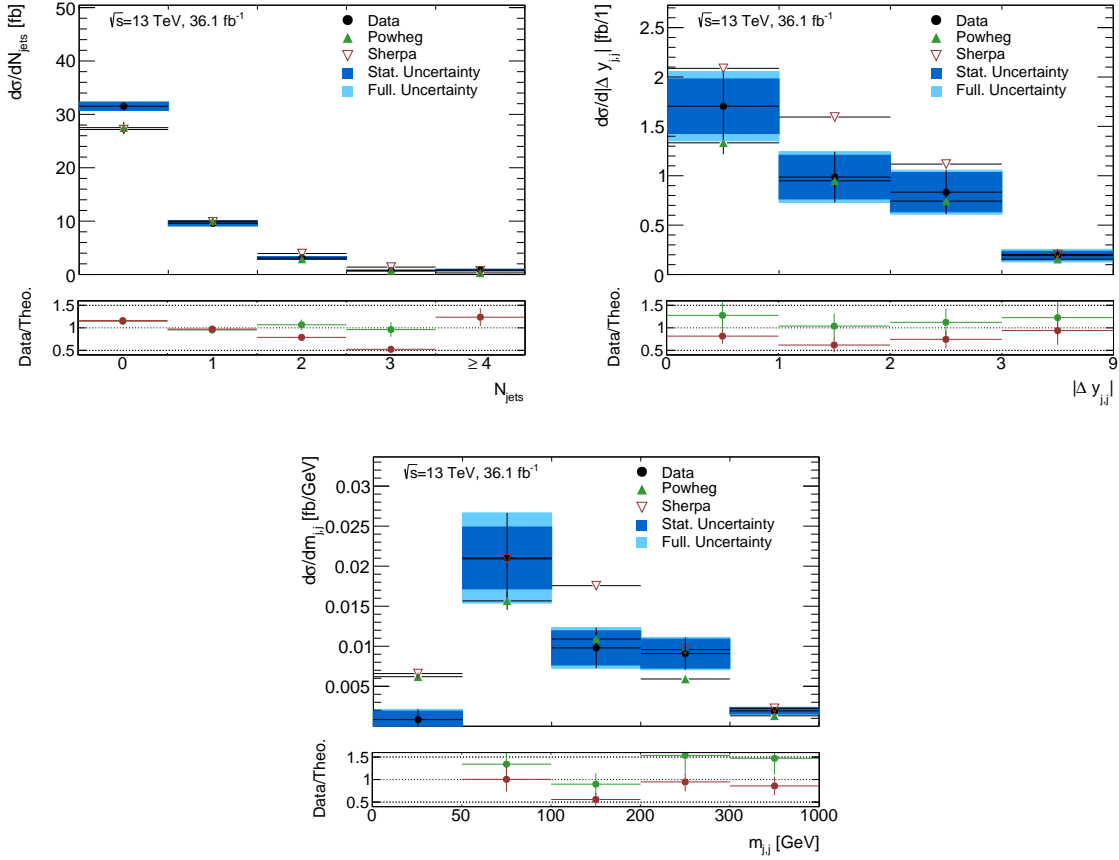


FIGURE 8.8: Differential cross section for jet inclusive variables. The black points represent the unfolded data with all statistical and systematic uncertainties. The lower panel shows the ratio of the unfolded distribution and two theory predictions. One is done with POWHEG (including higher order QCD and EW corrections) for the  $q\bar{q}$  initiated processes, the other one with SHERPA. Both include the  $gg$  and EW  $ZZjj$  from SHERPA. The bins are not equidistant but for better visualization shown in an equidistant way. The theory prediction with POWHEG for the  $q\bar{q}$  initiated process includes systematic theory uncertainties (PDF, QCD scale, HO corrections) whereas the SHERPA prediction includes only statistical uncertainties.

### 8.3.1 Method

The central relation between the selected number of events and a cross section in a given fiducial phase space ( $\sigma_{\text{fid}}^i$ ) is given by:

$$\sigma_{\text{fid}}^i = \frac{N_{\text{data}}^i - N_{\text{bkg}}^i}{L C_{ZZ}^i},$$

where  $N_{\text{data}}^i$  indicates the selected data events in channel  $i$ ,  $N_{\text{bkg}}^i$  the background events in that channel,  $C_{ZZ}^i$  the efficiency correction that takes into account detector inefficiencies<sup>3</sup> and  $L$  the integrated luminosity. The number of selected data and background events were already presented in detail before and summarized in Section 7.4. Also the efficiency corrections were introduced before in Section 6.6. In order to extract the cross section the approach is similar to the case of the unfolding, but having only one bin and therefore no migration and thus

<sup>3</sup>The factor also includes corrections from events that pass the selection on detector level but not the fiducial selection which are typically very small (< 1%).

no regularization is needed. Statistical uncertainties of the data are estimated by generating 2000 sets of random pseudodata following a Poisson distribution with a mean at the number of events in each bin. The unfolding is repeated for each of the pseudo datasets and the root mean square (RMS) of the results is taken as data statistical uncertainty. Systematic uncertainties are propagated by using varied  $C_{ZZ}^i$  or  $N_{bkg}$ .

The result of the combined channel is estimated by using the input numbers of the combined channel.

### 8.3.2 Efficiency correction ( $C_{ZZ}$ )

The efficiency correction is needed to correct detector effects. The values are calculated using the POWHEG sample for the  $q\bar{q}$  initiated processes and where already shown in Section 6.6. It has to be taken into account that some selected, reconstructed events do not pass the fiducial selection due to energy smearing effects which is at maximum 1%.  $C_{ZZ}$  is then the quotient of efficiency divided by the fiducial correction.

The different experimental and theoretical uncertainties on  $C_{ZZ}$  are shown in Table 8.2. They are calculated as described in Section 7.3. The lepton efficiency and resolution uncertainty is dominating with up to 3% in the muon channel. The theory uncertainty is below 1% due to the fact that numerator and denominator are both varied. The fact that the theory uncertainty is not the same for  $4e$  and  $2e2\mu$  channel is caused by a larger extrapolation from detector level selection to the fiducial selection for electrons compared to muons. This extrapolation introduces additional theory dependencies and thus a larger impact from variations due to theoretical variations like PDFs variations. Overall the systematic uncertainty is in the order 3%.

The final  $C_{ZZ}$  is  $0.490\pm 0.014$  in the  $4e$  channel,  $0.600\pm 0.015$  in the mixed channel,  $0.719\pm 0.025$  in the  $4\mu$  channel and  $0.603\pm 0.015$  in the combined channel.

Systematic	$4e$	$2e2\mu$	$4\mu$	combined
Electron reco.	2.6 %	1.3 %	–	1.2 %
Muon reco.	– %	1.5 %	3.0 %	1.6 %
Pileup modeling	1.1 %	1.6 %	1.8 %	1.6 %
MC statistics	0.21 %	0.1 %	0.1 %	0.1 %
Theory	0.55 %	0.43 %	0.23 %	0.4 %
Combined	2.8 %	2.6 %	3.5 %	2.6 %

TABLE 8.2: Summary of the systematic uncertainties on  $C_{ZZ}$ .

### 8.3.3 Extrapolation to full on-shell phase space

It is possible to extrapolate the integrated combined fiducial cross section to a phase space independent of kinematic cuts and decay channel. Therefore an acceptance correction ( $A_{ZZ}$ ) has to be applied and also the branching fraction ( $BR$ ) has to be taken into account. The



extrapolated integrated cross section is therefore given by:

$$\sigma_{tot} = \frac{N_{data} - N_{bkg.}}{L C_{ZZ} A_{ZZ} \times 4 \times BR^2}.$$

The factor of four accounts for the different flavor combinations and the branching fraction enters with the power of two due to two decaying  $Z$  bosons. The combined factor of  $C_{ZZ} \times A_{ZZ}$  is calculated with POWHEG and is found to be  $0.349 \pm 0.009$  which corresponds to an acceptance of about 57%. The relative uncertainties of the combined factor are like the one for  $C_{ZZ}$  with the exception of the theory uncertainty, which is doubled to 0.8%. This reflects the dependence on the theory predictions once the phase space is beyond the detector volume. In order to check this dependency it is useful to also use other generators for calculating the extrapolation. In the official ATLAS analysis [62] MCFM was used to calculate the extrapolation and was found to be 0.57 which matches the number used here and therefore no further systematic uncertainty is applied. The branching fraction is 3.3658% [31] neglecting the uncertainty which is below 0.1% and therefore not relevant given the relative size of the uncertainties of other parameters.

### 8.3.4 Results

**Integrated fiducial cross sections** The uncertainties of the different parameters of Equation 8.3.1 are shown in Table 8.3. It can be seen that in the different channels the statistical uncertainty is larger than the systematic uncertainty except for the combined channel, where the combined systematic uncertainty (including the luminosity uncertainty) is dominating.

Systematic	$4e$	$2e2\mu$	$4\mu$	combined
$C_{ZZ}$	2.8 %	2.6 %	3.5 %	2.6 %
Background	0.9 %	0.8 %	1.7 %	0.9 %
Lumi.	3.2 %	3.2 %	3.2 %	3.2 %
Combined Sys.	4.2 %	4.0 %	4.6 %	4.0 %
Data stat.	6.4 %	4.7 %	5.9 %	3.2 %
Total combined	7.7 %	6.2 %	7.7 %	5.2 %

TABLE 8.3: Summary of the systematic uncertainties on the integrated fiducial cross section per channel.

The resulting fiducial cross sections are shown in Table 8.4 together with the result of the ATLAS publication [62]. The results of the official ATLAS analysis are slightly higher in the  $4e$  and mixed channel and slightly lower in the  $4\mu$  channel. A reason for these small differences is a more sophisticated likelihood based fit method, used for the ATLAS publication, to extract the cross sections, which is a better way to treat systematic uncertainties in a correlated and uncorrelated way. Nevertheless the results agree well within the uncertainty.

The theory prediction, also shown in the table, is based on a NNLO calculation from MATRIX where the  $gg$  initiated part is scaled by a  $k$ -factor of 1.67. The  $q\bar{q}$  initiated process is scaled by 0.95 to account for HO EW corrections and the EW  $ZZjj$  production is added using the SHERPA prediction. The ratio of the measured and predicted cross section is shown in Figure 8.9. It can be seen that agreement is found in all channels except the electron channel. The difference there is about  $2.5 \sigma$  and reflects the disagreement that was already seen when comparing observed

events with predictions on detector level, which was discussed in Section 7.4.1.

	Channel	Measurement [fb]	Prediction [fb]
This analysis	4e	$13.8 \pm 1.1$ [ $\pm 0.9$ (stat.) $\pm 0.4$ (sys.) 0.5 (lumi.)]	$10.9^{+0.5}_{-0.4}$
	2e2 $\mu$	$21.0 \pm 1.3$ [ $\pm 1.0$ (stat.) $\pm 0.6$ (sys.) 0.7 (lumi.)]	$21.2^{+0.9}_{-0.8}$
	4 $\mu$	$11.3 \pm 0.8$ [ $\pm 0.7$ (stat.) $\pm 0.4$ (sys.) 0.4 (lumi.)]	$10.9^{+0.5}_{-0.4}$
	Combined	$46.2 \pm 2.3$ [ $\pm 1.5$ (stat.) $\pm 1.2$ (sys.) 1.5 (lumi.)]	$42.9^{+1.9}_{-1.5}$
ATLAS [62]	4e	$13.7^{+1.1}_{-1.0}$ [ $\pm 0.9$ (stat.) $\pm 0.4$ (sys.) $^{+0.5}_{-0.4}$ (lumi.)]	
	2e2 $\mu$	$20.9^{+1.4}_{-1.3}$ [ $\pm 1.0$ (stat.) $\pm 0.6$ (sys.) $^{+0.7}_{-0.6}$ (lumi.)]	
	4 $\mu$	$11.5^{+0.9}_{-0.9}$ [ $\pm 0.7$ (stat.) $\pm 0.4$ (sys.) $\pm 0.4$ (lumi.)]	
	Combined	$46.2^{+2.5}_{-2.3}$ [ $\pm 1.5$ (stat.) $^{+1.2}_{-1.1}$ (sys.) $^{+1.6}_{-1.4}$ (lumi.)]	

TABLE 8.4: The top four rows show the resulting measured and predicted integrated fiducial cross section of this analysis. The bottom rows show the published ATLAS result [62]. The prediction is based on a NNLO calculation from MATRIX where the  $gg$  initiated part is scaled by a k-factor of 1.67. The  $q\bar{q}$  initiated process is scaled by 0.95 to account for HO EW corrections and the EW  $ZZjj$  production is added using the SHERPA prediction. The prediction includes QCD scale uncertainties.

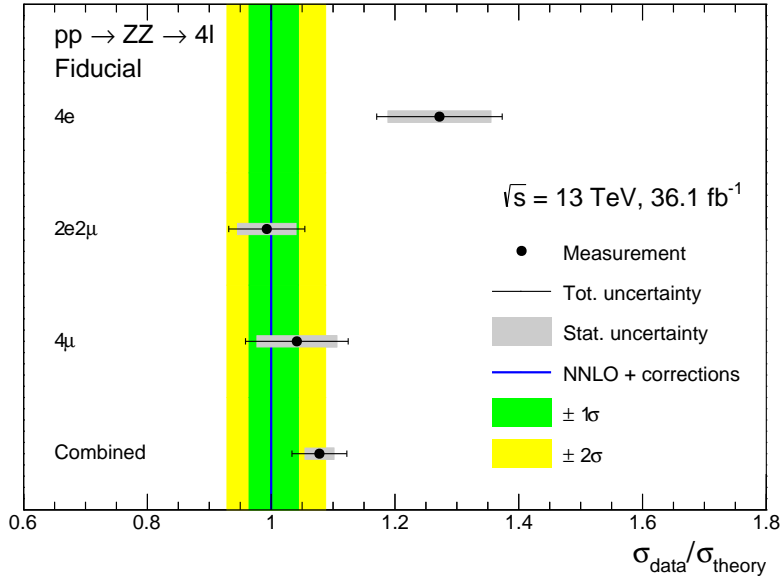


FIGURE 8.9: Comparison of measured integrated fiducial cross sections to a SM prediction. The prediction is based on a NNLO calculation from MATRIX where the  $gg$  initiated part is scaled by a k-factor of 1.67. The  $q\bar{q}$  initiated process is scaled by 0.95 to account for HO EW corrections and the EW  $ZZjj$  production is added using the SHERPA prediction. The prediction includes QCD scale uncertainties.

The integrated fiducial cross section is based on kinematic cuts that mimic the selection criteria which are at least partially dependent on the experimental apparatus where the data is collected. Therefore a comparison of the fiducial cross sections with other experiments is difficult. The CMS collaboration also published a measurement of the fiducial cross section [179]

but uses different lepton  $p_T$  thresholds and a different mass window. It is therefore better to compare extrapolated cross sections which are independent of the fiducial selection. However the measurement of the integrated fiducial cross sections at 13 TeV has been measured before by the ATLAS experiment using only data from 2015 [154]. The kinematic criteria in the fiducial volume were more stringent but also showed good agreement with a NNLO prediction of MATRIX. More details about the differences of the measurement with data from 2015 to the analysis using the full dataset can be found in Appendix E.5.

**Extrapolated cross section** The resulting total  $ZZ$  on-shell cross section is shown in Table 8.5 together with the result of the published ATLAS analysis and a result of the CMS collaboration and the result of the previous ATLAS measurement using only 2015 data. Also shown in this table is a prediction using MATRIX with applied k-factor on the  $gg$ -initiated process as already described before. First it can be seen that the results of this analysis agree with the one published by ATLAS. Also the cross section when using only 2015 data is in agreement with this measurement. There the impact of more data can be seen by a reduced statistical uncertainty of more than a factor of three. The result of the CMS collaboration is done in a mass window of  $60 < m_{\ell\ell} < 120$  GeV. For a proper comparison the result using data from ATLAS has to be multiplied by a factor of 1.014. This factor extrapolates from the ATLAS mass window to the CMS mass windows and was calculated by the official ATLAS group [62] using the mixed channel from the MATRIX prediction. After applying this, the ATLAS result is increased to  $17.5 \pm 1.0$  pb and still agrees with the CMS results.

Furthermore it is shown in Figure 8.10, how the results behave compared to results at different center of mass energies. The theory prediction of MATRIX does not have a k-factor applied on the  $gg$ -initiated part since this is not available for all center of mass energies.

The uncertainties of the result show that the systematic uncertainties and the statistical uncertainties are in the same order. For future measurements with more data it is necessary to get a better understanding of the experimental uncertainties.

Dataset	Measurement [pb]	Prediction
This analysis 2015+16	$17.3 \pm 0.9[\pm 0.6(\text{stat.})\pm 0.4(\text{syst.})\pm 0.6(\text{lumi.})]$	$16.9^{+0.6}_{-0.5}$ pb
ATLAS 2015+16[62]	$17.3 \pm 0.9[\pm 0.6(\text{stat.})\pm 0.5(\text{syst.})\pm 0.6(\text{lumi.})]$	
ATLAS 2015[154]	$16.7^{+2.6}_{-2.3} \quad [^{+2.2}_{-2.0}(\text{stat.})^{+0.9}_{-0.7}(\text{syst.})^{+0.9}_{-0.7}(\text{lumi.})]$	
CMS 2015+16[179]	$17.2 \pm 1.0[\pm 0.5(\text{stat.})\pm 0.8(\text{syst.})\pm 0.4(\text{lumi.})]$	

TABLE 8.5: Extrapolated cross section compared to other measurements. The prediction is based on MATRIX with a k-factor on the  $gg$ -initiated process of 1.67.

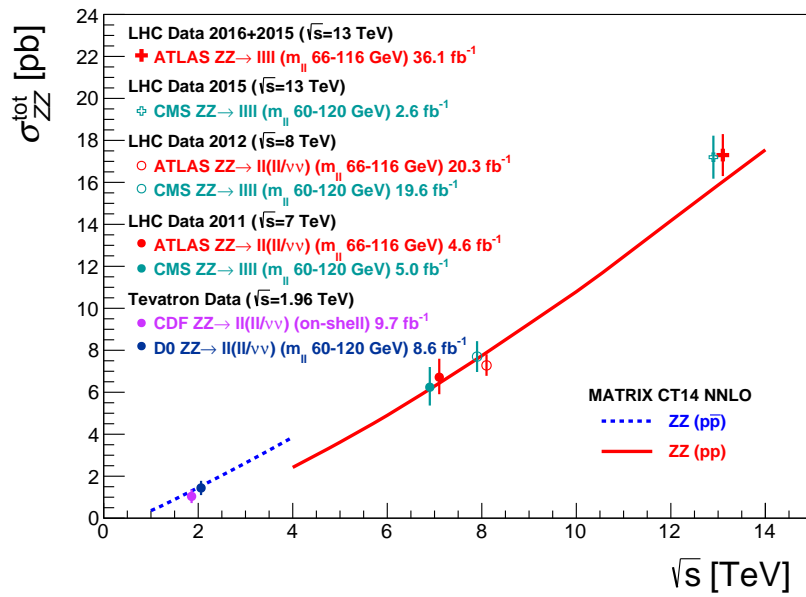


FIGURE 8.10: Extrapolated cross section compared to other measurements at different center of mass energies by ATLAS, CMS, CDF, and D0 [179–184], and to pure NNLO predictions from MATRIX (with no additional higher-order corrections applied). The total uncertainties of the measurements are shown as bars. Some data points are shifted horizontally to improve readability.

## Chapter 9

# Limits on anomalous neutral triple gauge couplings

This chapter describes how data can be used to search for effects from anomalous triple gauge couplings (aTGCs). The first section is about the parameterization of the cross section for processes with anomalous couplings to get theoretical predictions. When searching for physics beyond the SM it is important to look at observables in a way that gives the highest sensitivity to anomalous coupling effects, like the choice of a kinematic variable or the optimization of the binning, which is explained in Section 9.2. The statistical method for a limit setting procedure is described in Section 9.3 and followed by a section where the actual limits are presented in an one and two dimensional way. These are then compared to results from other experiments and analyses.

### 9.1 Signal parameterization

In order to search for effects from aTGCs, it is necessary to obtain theoretical predictions for the differential cross section as a function of the aTGC parameters. While it is in principle possible to generate MC samples for a range of aTGC parameter values, doing this in reality is unfeasible. The generation of full event simulations (i.e. including detector simulation) is computationally demanding. An alternative solution, which is discussed in detail in [185], is summarized here. The aTGC parameters appear linearly in the vertex function of Equation 2.41 (and hence likewise in the matrix element) and therefore will appear bilinearly in expressions for the cross section for processes involving a single aTGC vertex. The cross section for any process involving an aTGC vertex can be expressed as a function of the couplings as

$$\begin{aligned} d\sigma(f_{40}^\gamma, f_{40}^Z, f_{50}^\gamma, f_{50}^Z) &= F_{00} + f_{40}^\gamma F_{01} + f_{40}^Z F_{02} + f_{50}^\gamma F_{03} + f_{50}^Z F_{04} \\ &+ (f_{40}^\gamma)^2 F_{11} + f_{40}^\gamma f_{40}^Z F_{12} + f_{40}^\gamma f_{50}^\gamma F_{13} + f_{40}^\gamma f_{50}^Z F_{14} \\ &+ (f_{40}^Z)^2 F_{22} + f_{40}^Z f_{50}^\gamma F_{23} + f_{40}^Z f_{50}^Z F_{24} \\ &+ (f_{50}^\gamma)^2 F_{33} + f_{50}^\gamma f_{50}^Z F_{34} \\ &+ (f_{50}^Z)^2 F_{44}, \end{aligned} \tag{9.1}$$

where the  $F_{ij}$  are 15 coefficients that depend on the center of mass energy and kinematic properties of the process (e.g. the outgoing particle momenta). In particular, the  $F_{00}$  coefficient corresponds to the Standard Model cross section for the given process. The aTGC parameters,  $f_{40}^\gamma, f_{40}^Z, f_{50}^\gamma, f_{50}^Z$ , are the bare couplings (low-energy limit values of Equation 2.42). With Equation 9.1 it would in principle be possible to generate samples at any given aTGC configuration. In order to test a large range of configurations this would result in the need of having to generate numerous samples. To avoid this, all 15 coefficients  $F_{ij}$  are determined using the Baur, Hans and Ohnemus (BHO) [186] cross section calculator. This makes it possible to reweight a sample of events generated at a particular aTGC parameter space point  $\vec{f}_{\text{ref}} = \{f_{4\text{ref}}^\gamma, f_{4\text{ref}}^Z, f_{5\text{ref}}^\gamma, f_{5\text{ref}}^Z\}$  to any other parameter space point,  $\vec{f}$ , by applying the event-specific weight:

$$w(\vec{f}, \vec{f}_{\text{ref}}) = \frac{d\sigma(f_{40}^\gamma, f_{40}^Z, f_{50}^\gamma, f_{50}^Z)}{d\sigma(f_{4\text{ref}}^\gamma, f_{4\text{ref}}^Z, f_{5\text{ref}}^\gamma, f_{5\text{ref}}^Z)} \equiv \frac{d\sigma}{d\sigma_{\text{ref}}}. \quad (9.2)$$

The  $ZZ$  production cross section within a defined phase space is given in terms of the aTGC parameters by

$$\sigma_f^{\text{sel}} = \sigma_{\text{ref}} \frac{\sum w(\vec{f}, \vec{f}_{\text{ref}})}{N_{\text{ref}}}, \quad (9.3)$$

where  $\sigma_{\text{ref}}$  is the cross section of a chosen reference aTGC sample,  $N_{\text{ref}}$  is the number of MC events in the reference sample, and the selected events are those within the defined phase space. The cross section parametrization is now developed into a model for the expected number of events in each bin of a kinematic variable as a function of the aTGC parameters. The number of  $ZZ \rightarrow 4\ell$  events in the signal region in terms of the aTGC parameters is given by Equation 9.3 multiplied by the integrated luminosity,  $L$ :

$$N_{ZZ}(\vec{f}) = L\sigma_f^{\text{sel}} = L\sigma_{\text{ref}} \frac{\sum w(\vec{f}, \vec{f}_{\text{ref}})}{N_{\text{ref}}}, \quad (9.4)$$

and the summation over events in the reference sample that pass the selection cuts. By defining normalized coefficients as

$$N_{ij} \equiv \frac{L\sigma_{\text{ref}}}{N_{\text{ref}}} \frac{\sum F_{ij}}{d\sigma_{\text{ref}}}, \quad (9.5)$$

Equation 9.4 can be fully expanded (using Equations 9.1 and 9.2) as

$$\begin{aligned} N_{ZZ}(\vec{f}) &= N_{\text{SMZZ}} + f_{40}^\gamma N_{01} + f_{40}^Z N_{02} + f_{50}^\gamma N_{03} + f_{50}^Z N_{04} \\ &+ (f_{40}^\gamma)^2 N_{11} + f_{40}^\gamma f_{40}^Z N_{12} + f_{40}^\gamma f_{50}^\gamma N_{13} + f_{40}^\gamma f_{50}^Z N_{14} \\ &+ (f_{40}^Z)^2 N_{22} + f_{40}^Z f_{50}^\gamma N_{23} + f_{40}^Z f_{50}^Z N_{24} \\ &+ (f_{50}^\gamma)^2 N_{33} + f_{50}^\gamma f_{50}^Z N_{34} \\ &+ (f_{50}^Z)^2 N_{44}. \end{aligned} \quad (9.6)$$

In the above expression,  $N_{\text{SMZZ}}$  is the full Standard Model predicted yield using POWHEG for the  $q\bar{q}$  induced process and SHERPA for the  $gg$  induced and the electroweak  $ZZjj$  production.

### 9.1.1 Validation of the signal generator

In order to test the reweighting and parametrization from the BHO algorithm, distributions from a sample generated by SHERPA with a fixed set of aTGC parameters are compared to distributions using the reweighting procedure. Two technical implementations of reweighting are tested. The first one directly uses the weights from Equation 9.2 during the processing of a reference sample as an event weight which is used when filling a histogram with a kinematic variable. The other implementation uses the 15  $F_{ij}$  parameters as weights for 15 different histograms of the kinematic variable. Afterwards, the fifteen different histograms are added to one, using a different set of aTGC parameters by taking Equation 9.6 into account. The result is shown in Figure 9.1 for the  $p_T$  of the leading  $Z$  boson<sup>1</sup>. The shape differs largely from the Standard Model only expectation which is explained more in section 9.2.1, here only the validation of the reweighting procedure is discussed. The labels aTGC 0-2 refer to different, arbitrary (high) aTGC parameter configurations which are:

- aTGC 0:  $f_4^\gamma = 0.1, f_5^\gamma = 0.0, f_4^Z = 0.0, f_5^Z = 0.0,$
- aTGC 1:  $f_4^\gamma = 0.1, f_5^\gamma = 0.0, f_4^Z = 0.0, f_5^Z = 0.1,$
- aTGC 2:  $f_4^\gamma = 0.1, f_5^\gamma = 0.1, f_4^Z = 0.1, f_5^Z = 0.1.$

It can be seen that the reweighted histogram is compatible with the one generated at a specific aTGC configuration. The histogram using the 15 parameter description of Equation 9.6 is hidden behind the blue histogram. This shows that the generators of the samples use the same cross section calculation as the BHO method.

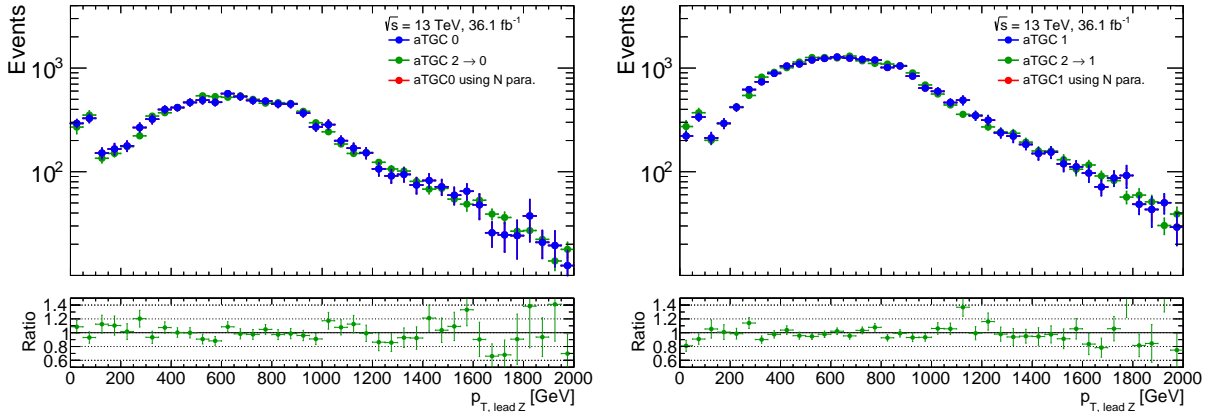


FIGURE 9.1: Test of the reweighting procedure using the  $p_T$  of the leading  $Z$  boson. The blue histogram shows a generated sample with SHERPA. The green histogram shows the histogram when reweighting a reference sample to the same aTGC parameter configuration as the blue histogram. The red histogram is obtained using the parametrization from 9.6 which is hidden behind the blue one.

<sup>1</sup>Also other distributions have been checked and showed good agreement within the statistical uncertainties.

## 9.2 Input for the limit setting

### 9.2.1 Choice of kinematic variable

It is clear from Equation 2.41 that the influence of the aTGC parameter is higher for larger momenta of the outgoing  $Z$  bosons. Therefore it is expected that most sensitivity for effects of aTGCs are in the higher energy regime of observables related to the momenta of the outgoing  $Z$  bosons. This behavior is demonstrated in Figure 9.2 where the Standard Model expectation is compared to distributions where aTGCs are switched on. One of the anomalous coupling is set to the upper value of the exclusion limits that were estimated by an analysis from ATLAS at 8 TeV [187]. The other couplings are set to zero. It can be seen that most of the aTGC contribution is in higher energy regimes which is at about 800 GeV in  $m_{4l}$  and 600 GeV for  $p_{T, \text{lead } Z}$ . Also the opening angle of the leptons from the decay of the  $Z$  boson with higher momentum shows some sensitivity in central regions, because this variable is correlated with the  $p_T$  of the boson. The absolute rapidity difference,  $|\Delta Y_{Z,Z}|$ , of the two  $Z$  bosons also has sensitivity above absolute values of 3.2. Judging from the number of expected SM and SM+aTGC events in

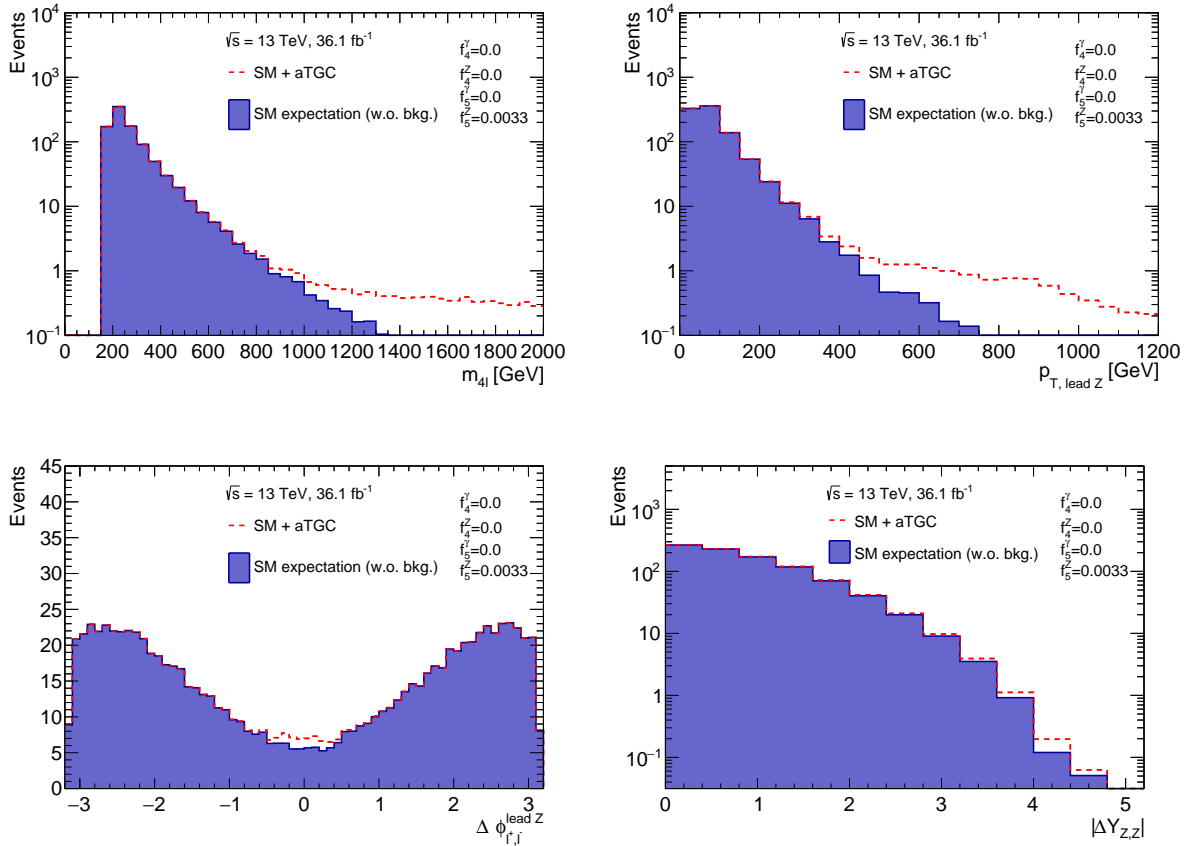


FIGURE 9.2: Comparison of Standard Model distributions with distributions including aTGCs. The Standard Model expectation is shown without background due to its small size and only statistical uncertainties are shown due to the finite size of the simulation. The aTGC configuration is shown as labels in each plot. The distributions are normalized to an integrated luminosity of  $36.1 \text{ fb}^{-1}$ .



sensitive regions, the choice of  $m_{4l}$ ,  $p_{T,leadZ}$  or  $\Delta\phi_{l^+l^-}^{leadZ}$  looks most promising.

When comparing data to expectation and searching for differences due to new physics, it is necessary to use as precise predictions as possible. Since higher order QCD and EW corrections can have large effects on the shape and the normalization of the expectation it is important to use predictions at the highest available order. For the  $q\bar{q}$  induced process from POWHEG this is NLO for the QCD part and LO for the electroweak part which is corrected via k-factors to NNLO QCD and NLO EW, as described before in Section 5.1. When looking at different distributions and comparing them to data it is beneficial to have k-factors as function of the variable of interest that are calculated in the same kinematic regions as the selection. One problem in this analysis is, that the EW k-factor is not provided as a function of the four lepton mass in the needed fiducial volume, but instead it is given using a different fiducial phase space. The pairing is done in a lexicographic way (see section 6.5.3). In order to get an idea whether higher order corrections are affected by this difference, the impact on distributions of two different QCD k-factors is tested. One k-factor is obtained in the fiducial volume that is used in this analysis and the other one in a volume with the changes mentioned before. The results can be seen in Figure 9.3, where the four lepton mass and the  $p_{T,leadZ}$  are compared when changing the QCD k-factor. It can be seen that there is an impact on the normalization and the shape. Although the difference might not be so big for the EW k-factor, it is decided to use  $p_{T,leadZ}$  as variable to search for new physics from aTGCs. It is also easier to combine these results with results from analysis that consider one  $Z$  boson decaying into neutrinos. The neutrinos can not be detected, therefore it is not possible to build an invariant four lepton mass.

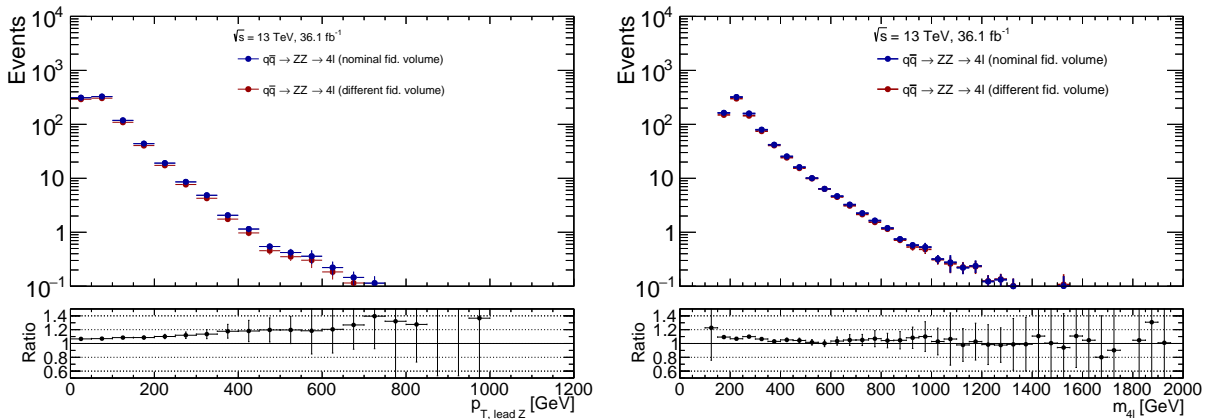


FIGURE 9.3: Comparison of the POWHEG  $q\bar{q} \rightarrow ZZ$  sample using different QCD k-factors. The nominal one uses a k-factor that is calculated in the same kinematic region as the selection. The alternative k-factor uses a different pairing procedure to form the  $Z$  bosons from the leptons. The distributions are normalized to the integrated luminosity of  $36.1 \text{ fb}^{-1}$ .

## 9.2.2 Binning optimization for highest sensitivity

The search for aTGC phenomena and the latter limit setting on the aTGC parameters is done using data and expectation binned in  $p_{T,leadZ}$ . The choice of the bin sizes and borders therefore has an influence on the sensitivity to the effects from aTGCs. This section gives a description how the binning is optimized.

The start point are two histograms with 5 GeV wide bins from 0 GeV to 3000 GeV: The SM only expectation and a histogram where in addition one aTGC parameter is set to the upper exclusion limit from the 8 TeV ATLAS analysis [187]. The following procedure is done to combine the bins, starting with the last one:

- The current bin is combined with the lower one, when the current bin has less than 10 entries.
- The current bin is combined with the lower one, if the significance of the combined bin does not decrease.
- The current bin is combined with the lower one, when the significance is below  $1\sigma$  after the combination.
- If none of the above criteria hold, the bin is kept and the procedure starts again with the next lower bin.

In this procedure the significance per bin is calculated using the procedure described in [172] and in Section 7.4 but instead of data, the distribution with aTGC is taken. The total combined systematic uncertainty per bin is also taken into account. After applying this scheme the resulting  $p_{T,lead Z}$  has four bins: [0 GeV, 295 GeV, 415 GeV, 555 GeV, 3000 GeV], which are also visible in Figure 9.4. The last bin also contains contributions from entries at higher momenta.

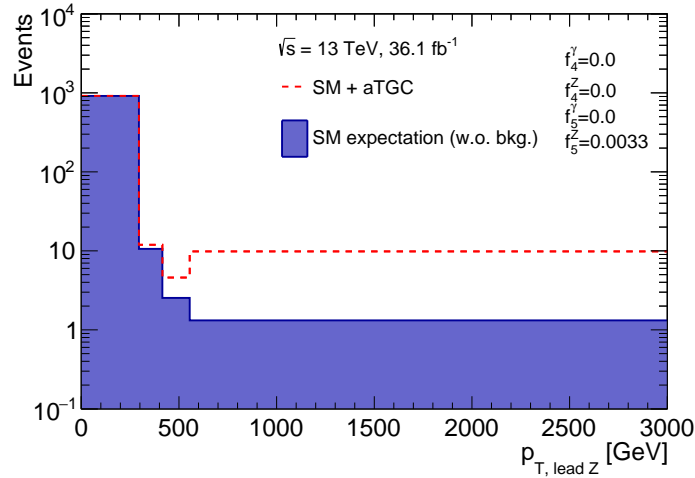


FIGURE 9.4: Comparison of the Standard Model  $p_{T,lead Z}$  distribution with a distribution allowing for aTGCs after binning optimization for highest sensitivity to aTGC effects. The Standard Model expectation is build without background due to its small size. The aTGC configuration is shown as label. The distribution is normalized to the integrated luminosity of  $36.1\text{ fb}^{-1}$ .

### 9.2.3 Comparison of data with expectation

It was already shown in Section 7.4 that overall no significant deviation between data and Standard Model expectation is present. The impact of aTGCs is predominantly in tails of

distributions. The left side of Figure 9.5 shows the  $p_{T,lead Z}$  distribution in a fine binning and on the right side in the optimized binning. The  $q\bar{q}$  initiated process is taken from POWHEG with applied QCD and EW k-factors binned in  $p_{T,lead Z}$ . In these plots also two distributions with allowed aTGCs are shown, where the parameters are set to the upper exclusion limit of the 8 TeV ATLAS analysis. It can be seen that no significant differences between SM and data are visible, especially not in the high momenta region. Therefore the data will be used to set exclusion limits on aTGCs. The preparing of the input for the limit setting procedure is explained in the following.

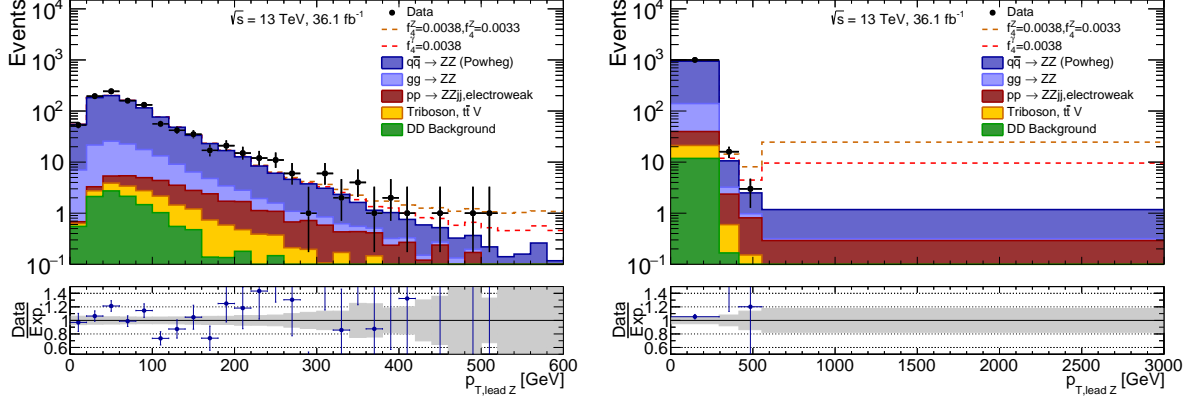


FIGURE 9.5: Data and SM prediction as function of  $p_{T,lead Z}$ . Also shown are the signal+SM expectations with  $f_4^\gamma=0.0038$  and  $f_4^Z=0.0033$ ,  $f_4^\gamma=0.0038$ ,  $f_4^Z=0.0033$ . The left hand side shows a fine binning and the right side the optimized binning. The grey band reflects the total systematic uncertainty.

In Equation 9.6 it was shown how the number of expected events depend on the aTGCs and  $N_{ij}$ . The aTGCs are the parameters of interest, on which exclusion limits are set, the  $N_{ij}$  are yields that are determined by histogramming 14 different weights from the BHO calculation (see Section 9.1). The expected yields of the SM  $ZZ$  production ( $N_{SM,ZZ}$ ), the genuine background ( $N_{genuine}$ ), the fake induced background which is estimated with data driven techniques ( $N_{DD}$ ) and the 14 different  $N_{ij}$  are shown in Table 9.1 for the optimized binning. Total systematic uncertainties for the SM contributions are shown in the table. The uncertainties were already discussed in Section 7.3 but are shown again in Table 9.2 for the different  $p_{T,lead Z}$  bins grouped into different categories. The experimental uncertainties are the relative uncertainties of the SM  $ZZ$  yields without background, which are also applied to the  $N_{ij}$  yields later and used for the limit setting. Since POWHEG and SHERPA treat the parton shower matching differently, a difference in the modeling of the  $p_{T,lead Z}$  might be present. Figure 9.6 shows the  $p_{T,lead Z}$  for both generators when no EW k-factor is applied to the POWHEG prediction. The differences at high  $p_{T,lead Z}$  are covered by statistical uncertainties of the samples and therefore no further systematic uncertainty is applied.

Yield	Bin 1	Bin 2	Bin 3	Bin 4
$N_{01}$	21.98	13.62	6.62	4.27
$N_{02}$	5.37	11.43	4.49	2.69
$N_{03}$	-1.01	1.52	0.33	-0.06
$N_{04}$	-0.57	1.68	0.43	-0.0
$N_{11}$	51877.32	86875.1	133459.47	580303.05
$N_{12}$	52510.64	81573.7	124175.39	518458.24
$N_{13}$	-4.08	-4.17	-1.37	-9.32
$N_{14}$	-1.59	-2.36	-0.22	-2.64
$N_{22}$	82998.82	125461.67	190312.65	781835.62
$N_{23}$	-1.84	-2.37	-0.3	-2.66
$N_{24}$	-5.03	-7.74	-0.33	-6.12
$N_{33}$	47829.9	85048.31	132573.15	581420.0
$N_{34}$	48399.95	79845.39	123187.52	519209.5
$N_{44}$	76493.85	122795.86	188701.65	782815.9
$N_{SM,ZZ}$	$925 \pm 35$	$10.0 \pm 0.7$	$2.34 \pm 0.31$	$1.10 \pm 0.19$
$N_{genuine}$	$9.4 \pm 2.8$	$0.43 \pm 0.13$	$0.15 \pm 0.05$	$0.078 \pm 0.027$
$N_{DD}$	$12 \pm 8$	$0.17 \pm 0.11$	$< 0.01$	$< 0.01$
$N_{obs}$	998	16	3	0
$N_{SMexp.}$	$950 \pm 40$	$10.6 \pm 0.8$	$2.50 \pm 0.32$	$1.18 \pm 0.19$

TABLE 9.1: Expected yields for different parameter of Equation 9.6 for different bins of the transverse momenta of the leading  $Z$ .  $N_{SM,ZZ}$  describes the yields of the Standard Model  $ZZ$  expectation without background and  $N_{SMexp.}$  the sum of  $N_{SM,ZZ}$  and data driven background ( $N_{DD}$ ) and genuine background ( $N_{genuine}$ ). The uncertainties shown are the total systematic uncertainties.

Name	Bin 1	Bin 2	Bin 3	Bin 4
aTGC sample MC stat.	6.8%	9.4%	7.5%	2.3%
SM sample MC stat.	0.4%	3.9%	8.4%	12.7%
Higher order EW corrections	0.9%	4.9%	5.2%	9.3%
Theory (PDF, QCD scale, $gg$ cross section)	3.1%	3.7%	4.7%	5.2%
Electron efficiency	0.88%	1.7%	2.2%	2.6%
Electron energy scale	$< 0.1\%$	1.8%	0.2%	1.1%
Muon efficiency	1.7%	2.9%	3.4%	4.3%
Muon momentum resolution	0.4%	1.2%	5.6%	5.8%
Pileup modeling	1.5%	2.7%	2.8%	3.5%
Luminosity	3.2%	3.2%	3.2%	3.2%

TABLE 9.2: Grouped systematic uncertainties for input bins in %. The theory uncertainty includes PDF and scale uncertainties which is applied to both SM and aTGC part. The experimental uncertainties are applied to the aTGC part and the SM part. The k-factor uncertainty represents the uncertainty of the higher order EW k-factor which is only applied to the SM part.

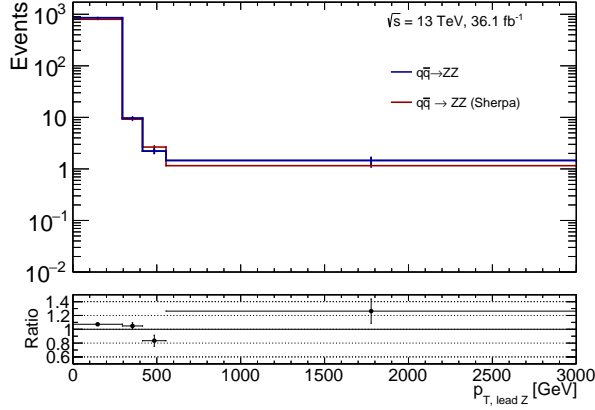


FIGURE 9.6: Comparison between SHERPA and POWHEG to investigate differences in modeling of the  $p_{T, lead Z}$ . The uncertainties only reflect statistical uncertainties due to limited number of generated MC events.

### 9.3 Limit setting procedure

The central question in the context of setting an observed limit is: How much signal contribution, in this case contribution from aTGCs, can be added to the Standard Model expectation to be still consistent with data (or pseudo data based on the SM expectation when extracting expected limits). For a counting experiment the likelihood is given by a Poisson probability distribution ( $P$ ):

$$L(N_{\text{data}}, \vec{f}) = \prod_{i=1}^m P(N_{\text{data}}^i, \mu^i(\vec{f})), \quad (9.7)$$

where

$$\mu^i(\vec{f}) = N_{\text{sig}}^i(\vec{f}) + N_{\text{SMexp}}^i. \quad (9.8)$$

In these equations  $m$  is the number of bins,  $N_{\text{data}}^i$  the data yield in bin  $i$ ,  $N_{\text{SMexp}}^i$  the Standard Model only expectation in bin  $i$  and  $N_{\text{sig}}^i(\vec{f})$  the signal yield in bin  $i$  which is given by Equation 9.6 without the Standard Model part. The expectation as well as the different  $N_{kl}$  parameters of  $N_{\text{sig}}^i(\vec{f})$  also have uncertainties as pointed out in the previous section. These uncertainties are taken into account by introducing nuisance parameters. These parameters allow  $N_{\text{SMexp}}^i$  and  $N_{\text{sig}}^i(\vec{f})$  to be varied by:

$$N_{\text{sig}}^i(\vec{f}, \vec{\beta}) = N_{\text{sig}}^i \cdot \left(1 + \sum_{j=1}^n \beta_j \delta_j^i\right), \quad (9.9)$$

$$N_{\text{SMexp}}^i(\vec{\beta}) = N_{\text{bkg}}^i \cdot \left(1 + \sum_{j=1}^n \beta_j \delta_j^i\right), \quad (9.10)$$

where  $\beta_j$  is one of the  $n$  nuisance parameters and  $\delta_j^i$  the relative uncertainty on the expectation in the  $i$ -th bin which was shown in Table 9.2. The nuisance parameter are constrained to follow a Gaussian shape with mean zero and standard deviation of one, which is multiplied to

---

the likelihood. The full likelihood is therefore:

$$L(N_{data}, \vec{f}, \vec{\beta}) = \prod_{i=1}^m P(N_{data}^i, \mu^i(\vec{f}, \vec{\beta})) \times \exp\left(\sum_{j=1}^n \frac{\beta_j^2}{2}\right) \quad (9.11)$$

In order to get exclusion limits for the aTGCs it is necessary to quantify how well the agreement between data and expectation for a given aTGC configuration is. To do this a likelihood ratio test statistic is chosen, motivated by the procedure from Feldman and Cousins [188], which is given by:

$$q_{obs}(\vec{f}) = -\ln\left(\frac{L(N_{data}, \vec{f}, \hat{\vec{\beta}})}{L(N_{data}, \hat{\vec{f}}, \hat{\vec{\beta}})}\right), \quad (9.12)$$

where  $\hat{\vec{\beta}}$  is the maximum likelihood estimator of  $\vec{\beta}$  which maximizes the numerator of the test statistics  $q(\vec{f})$  at a given value of  $\vec{f}$ . The parameters  $\hat{\vec{f}}$  and  $\hat{\vec{\beta}}$  are the maximum likelihood estimator of  $\vec{f}$  and  $\vec{\beta}$  which maximize the denominator of  $q(\vec{f})$ . Since a maximization is computational more intense than a minimization, the negative logarithm is taken and minimized. This is done using the ROOT [105] implementation of MINUIT [189]. The p-value is a measure of how well data and expectation for a given aTGC agree. It is extracted using a frequentist approach which is summarized in the following. A large number of pseudo observations ( $p_o$ ) is generated for different test values of  $\vec{f}$ . The test statistic for each pseudo observation  $q_{p_o}(\vec{f})$  is computed, and compared with the observed  $q_{obs}(\vec{f})$ . The p-value at each value of  $\vec{f}$  is calculated as the fraction of pseudo observations whose test statistic  $q_{p_o}(\vec{f})$  is smaller than the observed value  $q_{obs}(\vec{f})$ :

$$p(\vec{f}) = \frac{N_{p_o}(q_{p_o}(\vec{f}) < q_{obs}(\vec{f}))}{N_{p_o}} \quad (9.13)$$

The number of pseudo observations is chosen to be 10000 for each tested  $\vec{f}$  configuration. The aTGCs ( $\vec{f}$ ) are now varied, up to a point where the p-value is 0.05 or a confidence level of 95% is reached. Also negative values of  $f_i$  are considered. They also lead to an increased yield due to the dominating quadratic terms in the cross section since SM interference effects are subdominant at the LHC as explained in Section 2.3.2. The limits on the 4 different aTGCs,  $f_i^V$ , are set in two different ways. One way is to fix all but one coupling to zero and set only limits on this coupling. The other way fixes all but two couplings to zero which leads to dependencies of the limits of two couplings of interest and therefore two dimensional exclusion limits. Higher dimensional limits are not calculated due to limited computational resources. Also in the two dimensional case the limit setting would need very much computational power when probing the 2D space randomly. Therefore, the parameters are transformed into polar coordinate like variables, where one variables describes the distance to the origin and the other one the angle ( $\theta$ ) between the pointing vector and the abscissa. The limits are then estimated along rays in the 2D plane with increasing  $\theta$  until one complete turn is reached. The number of rays can be varied but with increasing number of rays also the computing time increases.

Before observed limits on parameters are obtained, it is beneficial to extract expected limits which are completely based on expectation without taking data into account. This makes the testing of the extraction (testing of code and formalism) possible without being biased by the data and also points out differences between data and expectation afterwards. Also expected limits make sensitivity studies possible without being influenced by looking at data. These

expected limits are extracted by generating pseudo experiments using the expectation when  $\vec{f} = 0$  (i.e. Standard Model) instead of the observed number of events. The generation follows a Poisson distribution with mean at the expected number of events. The set of upper and lower bounds on the aTGCs, derived from this procedure form two distributions, one for the upper bound and one for the lower bound. The median of each is used as the expected upper and lower bound, and  $\sigma$  is the standard deviation.

The complete described procedure is implemented within the Frequentist Likelihood based Inferences Tool (FLIT) [190, 191] which is used in this analysis.

## 9.4 One and two dimensional exclusion limits

The expected one dimensional limit is obtained by generating pseudo experiments and using the median of the resulting limits as central expected limit. This is done for the lower and upper end of the limits separately. The resulting distribution of the limits using 2000 pseudo experiments is shown exemplary for  $f_4^\gamma$  in Figure 9.7 together with the median, the error bands and the observed limit. Already here it is visible that the observed limit is better than the expected which is mainly driven by the fact of not observing events in the last bin but expecting about 1.2. The expected and observed limits are shown in Table 9.3. The quoted uncertainty of the expected limit corresponds to the root-mean-square (RMS) of the distributions from the pseudo experiments.

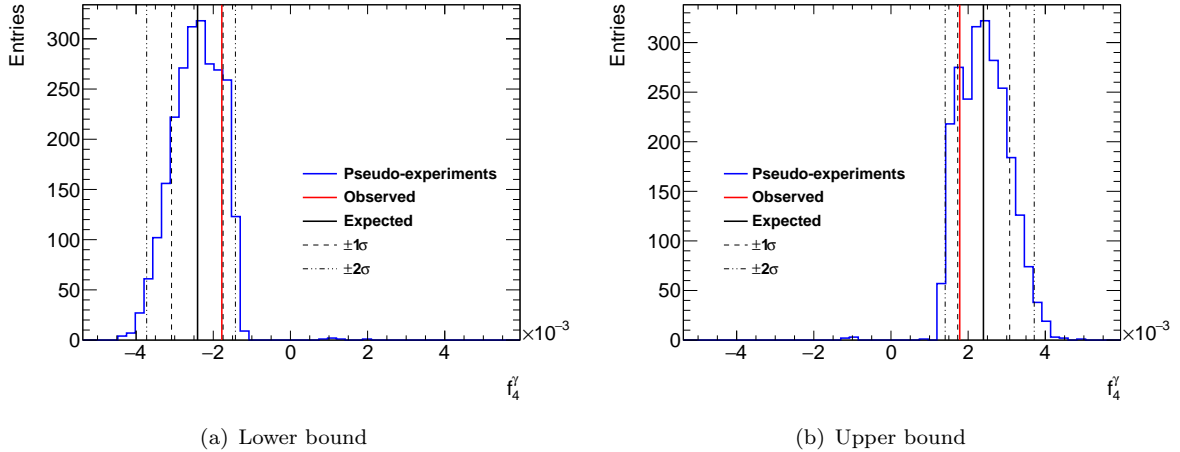


FIGURE 9.7: 95% C.L. limits on  $f_4^\gamma$  using 5000 pseudo experiments. The expected limit is the median of the distribution shown with its 1- and 2 $\sigma$  band marked with dashed lines. Also shown in the observed limit when using data instead of pseudo experiments.

The 2D limits are estimated along rays, as explained before. An example how the observed limits look like along these rays, is shown for the  $f_4^\gamma, f_4^Z$  plane when using 26 rays in Figure 9.8. For the presentation of the 2D results the limits of each ray are interpolated, also the expected limit and the correspondent 1- $\sigma$  and 2- $\sigma$  variations. Figure 9.9 shows the resulting limits for all 2D combinations. The green and yellow band corresponds to 1- $\sigma$  and 2- $\sigma$  variations on the expected limits using 1000 pseudo experiments for each of the 26 rays.

An alternative approach to describe anomalous couplings is an effective field theory approach

Coupling	Expected ( $10^{-3}$ )	Observed ( $10^{-3}$ )
$f_4^\gamma$	$-2.4\pm 0.7, 2.4\pm 0.7$	-1.8 , 1.8
$f_4^Z$	$-2.1\pm 0.6, 2.1\pm 0.6$	-1.5 , 1.5
$f_5^\gamma$	$-2.4\pm 0.7, 2.4\pm 0.7$	-1.8 , 1.8
$f_5^Z$	$-2.0\pm 0.6, 2.1\pm 0.6$	-1.5 , 1.5
EFT parameter	Expected [ $\text{TeV}^{-4}$ ]	Observed [ $\text{TeV}^{-4}$ ]
$C_{\tilde{B}W}/\Lambda^4$	$-8.0\pm 2.3, 8.02\pm 2.3$	-5.9 , 6.0

TABLE 9.3: One dimensional expected and observed 95% C.L. intervals of the aTGCs. Each limit is obtained setting all other aTGCs to zero. The last row shows the limit on an EFT parameter transformed from the limits of  $f_5^\gamma$ .

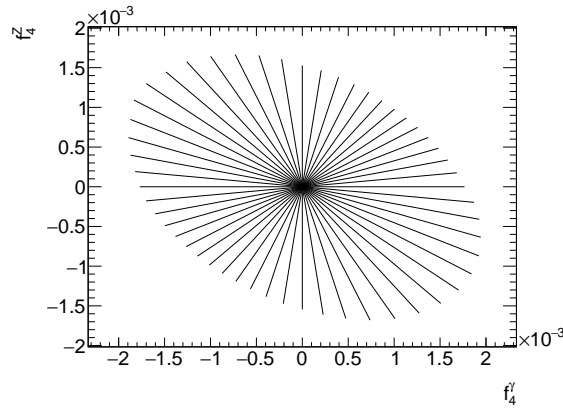


FIGURE 9.8: Observed 2D limits calculated along 26 rays in the  $f_4^\gamma, f_4^Z$  plane.

(EFT) [74] which was already discussed in Section 2.3. The transformation of vertex factor parameters into the EFT parameters needs values for the  $Z$  mass, the Higgs vacuum expectation and the Weinberg angle that are taken from the Particle Data Group (PDG) [31]. The resulting limit on  $C_{\tilde{B}W}$  by transforming the limit of the vertex factor parameter is also shown in Table 9.3. Since only for  $C_{\tilde{B}W}$  and  $f_5^\gamma$  a direct one to one relation is given, it is only possible to make this transformation after the limits have been set for this parameter. In order to get the 1D limits also for the other EFT parameters together with 2D limits the re-parameterization has been done before the limit setting procedure, so that the parameter of interest are then the EFT parameters. The results of the 1D parameters can be found in Table 9.4 and for the 2D limits in Figure 9.10.

These results are also part of the  $\sqrt{s} = 13$  TeV ATLAS publication [62].

Coupling parameter	Expected [ $\text{TeV}^{-4}$ ]	Observed [ $\text{TeV}^{-4}$ ]
$C_{\tilde{B}W}/\Lambda^4$	$-8.1\pm 2.3, 8.1\pm 2.3$	-5.9 , 5.9
$C_{WW}/\Lambda^4$	$-4.0\pm 1.1, 4.0\pm 1.1$	-3.0 , 3.0
$C_{BW}/\Lambda^4$	$-4.4\pm 1.2, 4.4\pm 1.3$	-3.3 , 3.3
$C_{BB}/\Lambda^4$	$-3.7\pm 1.0, 3.7\pm 1.0$	-2.7 , 2.8

TABLE 9.4: One dimensional expected and observed 95% C.L. intervals of the EFT parameters. Each limit is obtained setting all other EFT parameters to zero.



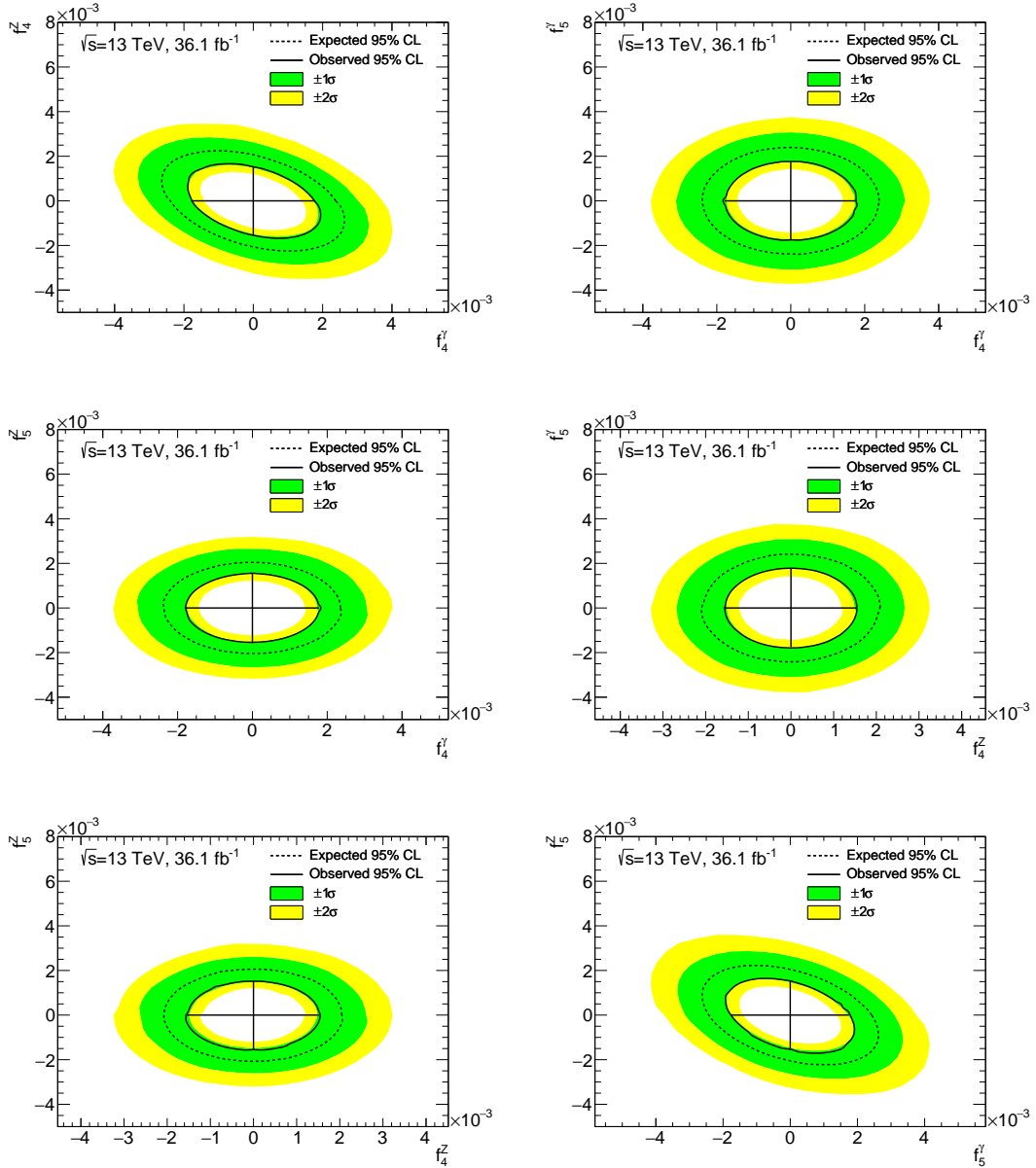


FIGURE 9.9: Observed and expected two dimensional 95% C.L. intervals on aTGC parameters without any form factor. The expected interval corresponds to the mean of 2500 pseudo experiments with the 1- and  $2\sigma$  band shown in green and yellow. The black lines show the observed 1D limits at 95% C.L.

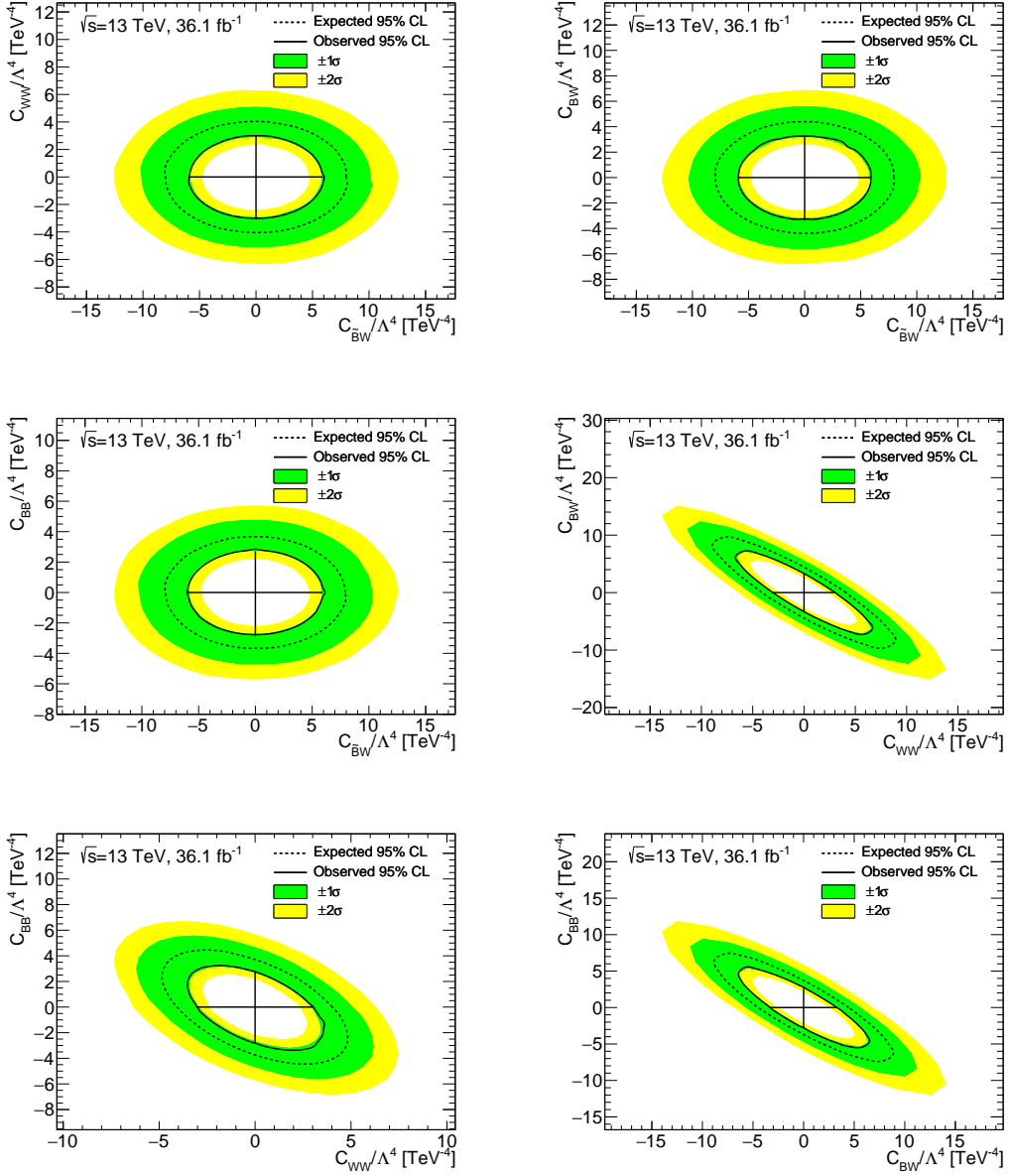


FIGURE 9.10: Observed and expected two dimensional 95% C.L. intervals on EFT paramters. The expected interval corresponds to the mean of 2500 pseudo experiments with the 1- and  $2\sigma$  band shown in green and yellow. The black lines show the observed 1D limits at 95% C.L.

### 9.4.1 Comparison to other results

It is possible to compare the limits to previous results of ATLAS and also to results from different experiments. The search for anomalous neutral triple gauge couplings has been done also with data from previous colliders like the Large Electron Positron collider (LEP) or the proton anti-proton collider Tevatron. A comparison of the observed limits between different experiments is presented in Table 9.5 and in Figure 9.11 for LHC experiments.

When comparing the results of this analysis (shown in the last row of the table) with the LEP

Experiment	$\sqrt{s}$ [TeV]	$\int Ldt$ [fb $^{-1}$ ]	$f_4^\gamma [\times 10^{-3}]$	$f_4^Z [\times 10^{-3}]$	$f_5^\gamma [\times 10^{-3}]$	$f_5^Z [\times 10^{-3}]$
LEP [192]	130-209 GeV	0.7	[-170,190]	[-300,300]	[-320,360]	[-340,380]
DØ [193]	1.96 TeV	1	[-260,260]	[-280,280]	[-300,280]	[-310,290]
ATLAS [194]	8 TeV	20.3	[-3.8,3.8]	[-3.3,3.2]	[-3.8,3.8]	[-3.3,3.3]
CMS [181]	7+8 TeV	5.1+19.6	[-2.9,2.6]	[2.2,2.6]	[-2.6,2.7]	[-2.3,2.3]
CMS [179]	13 TeV	35.9	[-1.2,1.3]	[-1.2,1.0]	[-1.2,1.3]	[-1.0,1.3]
ATLAS [62]	13 TeV	36.1	[-1.8,1.8]	[-1.5,1.5]	[-1.8,1.8]	[-1.5,1.5]

TABLE 9.5: Comparison of observed 95%C.L. limits on aTGC parameter with results from other experiments.

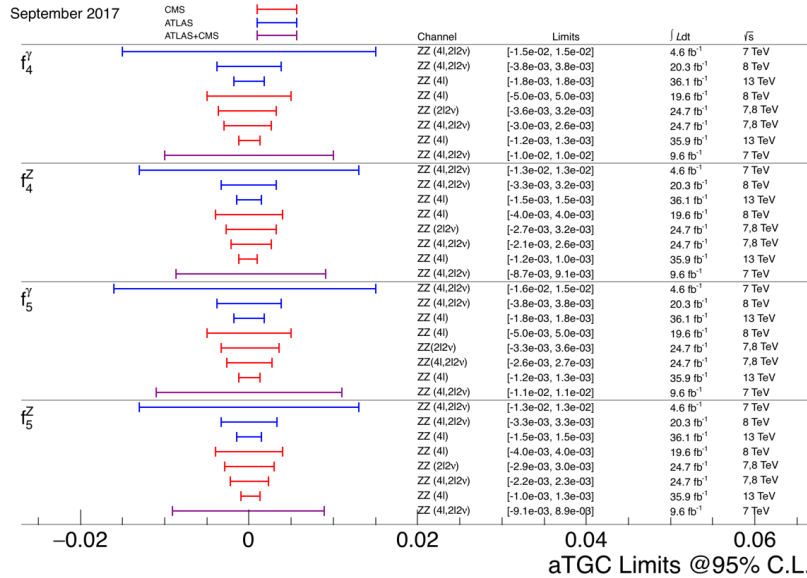


FIGURE 9.11: Comparison of various observed 95%C.L. limits on neutral aTGC parameters from different analyses done at the LHC at different  $\sqrt{s}$ . Figure is taken from [195].

and DØ results an improvement of two orders of magnitude is visible due to the much higher center of mass energy and the resulting possibility to probe higher energy regimens where the aTGC parameter contribute more. Also in comparison with results from ATLAS at  $\sqrt{s} = 8$  TeV, which also include data where one  $Z$  decays to neutrinos, an improvement of about a factor of two is visible.

The improvement with respect to the combined CMS result using data from  $\sqrt{s} = 7$  TeV and 8 TeV that also takes one  $Z \rightarrow \nu\bar{\nu}$  decay into account is better by a factor of about 1.5. When comparing both 13 TeV results, the one from CMS and the one from this analysis, the result of this analysis yields less stringent limits. But the comparison of observed exclusion limits

often is very sensitive to the observed number of events. Statistical fluctuations can therefore lead to more stringent limits. A comparison of the expected limit would be better, but it is not provided by all mentioned analyses in particular not by the 13 TeV CMS analysis. One difference between the CMS analysis and this one is the usage of the  $m_{4l}$  spectrum for the limit setting instead of  $p_{T,leadZ}$ . Therefore the resulting expected limits were checked when using the  $m_{4l}$  distribution<sup>2</sup>, instead of the  $p_{T,leadZ}$ . The resulting limits are more stringent by about  $0.2 \cdot 10^{-3}$  for all couplings. But it should be considered that the EWK k-factor used for the SM expectation is not binned in  $m_{4l}$  and therefore not considered systematic uncertainties might influence this number as it was explained in Section 9.2.1. Furthermore the last bin of the CMS  $m_{4l}$  distribution is empty where about 0.7 events are expected which also shrinks the room for aTGCs when calculating the observed limit. In this analysis the last  $m_{4l}$  bin has 2 observed events which is also the size of the expectation. Additionally the process of how the limits are calculated is different. CMS uses differently generated aTGC samples from SHERPA where one or two couplings are varied and interpolates between those points. Whereas here the parameterization of Equation 9.6 is used including the SM expectation by POWHEG with higher order corrections. The CMS method seems to use the SM part for the samples with aTGCs as it comes out from SHERPA which might not include higher order corrections. Due to this differences it is expected to see differences in the observed 1D limit. For the 2D limit CMS provides also expected 95% C.L. contours. The visual comparison of these contours with the 2D limits of this analysis shows good agreement. This indicates that there might be further differences for the 2D limit setting that might have opposite effects compared to the differences explained before.

There are also other analyses that search for anomalous triple gauge couplings in different processes which include for example charged bosons or photons in the final state. The couplings are different than the one presented in this analysis and therefore a direct comparison makes no sense. It is also possible to search for anomalous quartic gauge couplings when analyzing vector boson scattering processes or triple gauge boson production. In all of these analyses no significant deviation to the SM had been found and limits were put on the anomalous couplings. A summary of these results can be found at [195].

## 9.4.2 Outlook

The LHC will deliver about  $120 \text{ fb}^{-1}$  until end of 2018 and after an upgrade phase an amount of about  $300 \text{ fb}^{-1}$  will be gathered until 2022. After a further upgrade phase of several years, the *High luminosity* (HL) LHC will deliver up to  $3000 \text{ fb}^{-1}$  until 2035. This increased amount of data will increase the sensitivity to aTGCs further. In order to see the impact of more data, the limits are calculated again by scaling the SM and signal predictions to higher luminosities. The resulting limits for  $f_4^Z$  when treating the SM expectation as data (also called *asimov* limits [196]) are shown for four different luminosities in Figure 9.12. The qualitative behavior of the other limits is the same. It can be seen that the limits get more stringent by a factor of  $\approx 2$  for  $300 \text{ fb}^{-1}$  compared to  $36.1 \text{ fb}^{-1}$  but then only a small benefit is gained from the upgrade to  $3000 \text{ fb}^{-1}$ . These numbers are only a very rough estimation and not optimized for highest sensitivity with such high integrated luminosities. For example the binning was kept the same as it was for the

<sup>2</sup>The binning tested is the same as the one CMS uses.

results using  $36.1 \text{ fb}^{-1}$  of data. This has to be reoptimized when more data is available. Also the relative experimental systematic uncertainties are kept the same which will probably decrease when more data is available. One example is the momentum calibrations that can be done up to higher momenta when more data is used. Another fact that limits the benefit of having more data, is the size of theoretical uncertainties. It was already discussed before that in high energy regions the electroweak correction and its uncertainty grows which will play a major role once the statistical uncertainty from data gets lower. In addition the amount of generated events is too low to probe the high energy region good enough. With increasing sensitivity to aTGC also higher order electroweak corrections (fermion loops) from the SM, which were discussed in Section 2.3.2 will play a larger role. The impact of these contributions and the interference with the aTGCs have to be taken into account.

For future analyses it might also be necessary to modify the selection of  $ZZ$  events. For

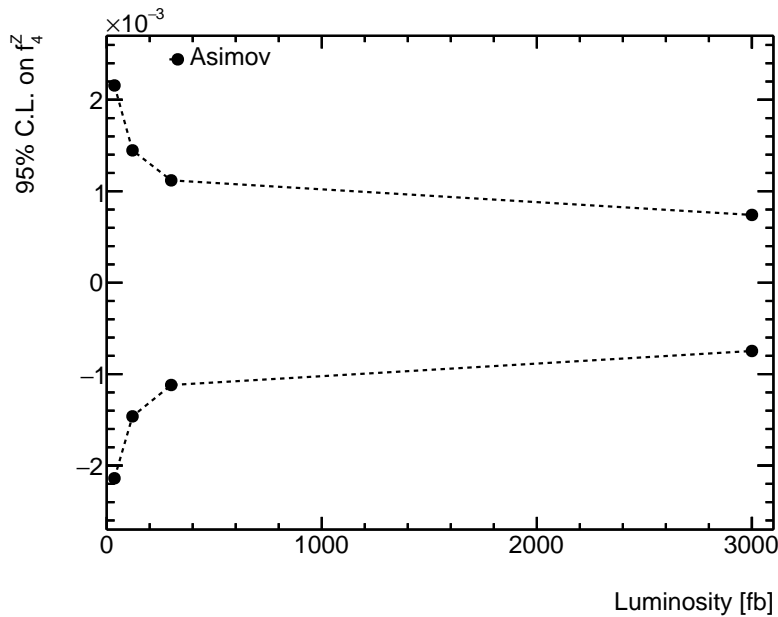


FIGURE 9.12: Expected 95% C.L. limit on  $f_4^Z$  for different luminosities when treating the SM prediction as data (called *asimov* [196]). The lines are a simple connection between the dots.

example the  $\Delta R$  cut, to separate between leptons, limits the range of the  $p_{T,lead Z}$  spectrum since the leptons get more collimated at higher values. This will also challenge the isolation criteria placed on the leptons. It might be beneficial to think of techniques that also take information from other observables into account which have sensitivity to aTGC, like  $m_{4l}$  or  $\Delta\phi_{l^+l^-}^{lead Z}$ . One possibility to do this would be multi-variate methods like *boosted decision trees* or *artificial neural networks*.

Furthermore the search for aTGCs will benefit from higher center of mass energies. The LHC may operate at  $\sqrt{s} = 14 \text{ TeV}$  in 2018 which could be useful, but is only a small increase of the energy. In order to probe much higher  $\sqrt{s}$  new accelerators are necessary. There are plans to build larger hadron colliders, for example the Future Circular Collider (FCC) [197], that can reach  $\sqrt{s}$  of up to 100 TeV. The cross section in invariant mass regions above 800 GeV will increase roughly by a factor of 10 when comparing the cross section of this analysis in the highest mass bin with the cross section from [197]. This means that with the same amount of data the FCC will probably have a much higher sensitivity to aTGCs compared to the LHC.



# Chapter 10

## Conclusion

Studies of diboson processes at high energies are important to probe the electroweak sector and especially the electroweak symmetry breaking of the Standard Model. In addition, diboson processes often build a dominating background for processes involving the Higgs boson. An example of such a process is the decay of a Higgs boson to two  $Z$  bosons. Therefore a precise knowledge of  $ZZ$  production is mandatory to measure properties of the Higgs boson. The leptonic decay of two  $Z$  bosons to electrons or muons is a very clean channel to study  $ZZ$  production. Although the rate is low compared to semi-leptonic decays, they can be fully reconstructed, easily identified and are expected to have low background.

Furthermore  $ZZ$  production can also be used to search for phenomena that can not be explained by the Standard Model. Couplings of three neutral gauge bosons, such as  $\gamma^*ZZ$ , are not allowed in the SM, but it is possible to search for signatures of such anomalous triple gauge couplings. Those signatures lead to enhancements in tails of distributions that are correlated to the energy of the outgoing leptons.

The LHC at CERN, where protons collide at a center of mass energy of 13 TeV, is a good environment to measure  $ZZ$  processes and search for anomalous couplings. In 2015 and 2016 the ATLAS experiment collected a high-quality data set at  $\sqrt{s} = 13$  TeV with an integrated luminosity of  $36.1 \text{ fb}^{-1}$ .

In the presented analysis  $pp \rightarrow ZZ + X \rightarrow \ell^+ \ell^- \ell'^+ \ell'^- + X$  ( $\ell = e, \mu$ ) events are selected with two on-shell  $Z$  boson candidates in a mass range between 66 GeV and 116 GeV. The selected data is compared to predictions that include simulations of  $pp \rightarrow ZZ + X \rightarrow \ell^+ \ell^- \ell'^+ \ell'^- + X$  as well as simulated and data driven background contributions in three different channels. The channel, where both  $Z$  bosons decay to an electron-positron pair, shows a deviation to the expectation of about  $2.7 \sigma$ . The differences are mostly located in regions where the leptons have low momentum, which makes it less probable to be a hint of new physics which is expected to contribute more to high energy regions. Intensive investigations had been done, but no clear cause for this deviation was found. Therefore and because the other channels show good agreement with the expectation, it is assumed that the main reason is a statistical fluctuation.

The selected events per channel have been used to calculate integrated cross sections in the kinematic region of the selection. The cross sections were compared to predictions from calculations done with the program MATRIX at NNLO in QCD perturbation theory which uses NNPDF 3.0 parton distribution functions. Except for the four electron channel the measured

cross sections agree with the predictions within the uncertainties. The cross section had also been extrapolated to the full on-shell  $ZZ$  phase space using simulations. It was measured to:

$$17.3 \pm 0.9[\pm 0.6(\text{stat.}) \pm 0.4(\text{sys.}) \pm 0.6(\text{lumi.})]\text{pb}, \quad (10.1)$$

which is in agreement with the MATRIX prediction of  $16.9_{-0.5}^{+0.6}$  pb. Differential cross sections were determined for several observables and compared to two theory predictions where the  $q\bar{q}$  initiated process is either generated using SHERPA or POWHEG. In general, good agreement was found for all observables besides for variables that take additional jets in the event into account, for example the invariant mass of two jets with highest transverse momentum. But due to limited number of events per bin it is not possible to decide which is better in describing data.

Searches for anomalous triple gauge couplings (aTGCs) were performed using the transverse momentum distribution of the reconstructed  $Z$  bosons that has higher transverse momentum. Two different approaches to describe aTGCs were used. One approach is describing the aTGC vertex with four parameters that are zero in the Standard Model. Since no significant differences between SM expectation and data were found, 95% C.L. limits had been set on these parameters:

$$-0.0018 < f_4^\gamma < 0.0018, \quad -0.0018 < f_5^\gamma < 0.0018, \quad (10.2)$$

$$-0.0015 < f_4^Z < 0.0015, \quad -0.0015 < f_5^Z < 0.0015, \quad (10.3)$$

which are more stringent by a factor of approximately two compared to results from ATLAS at  $\sqrt{s} = 8$  TeV. Another approach is an effective field parameterization of the aTGCs. With this approach most stringent 95% C.L. limits on four coefficients of dimension eight operators could be set:

$$-5.9 \text{ TeV}^{-4} < C_{\tilde{B}W}/\Lambda^4 < 5.9 \text{ TeV}^{-4} \quad (10.4)$$

$$-3.0 \text{ TeV}^{-4} < C_{WW}/\Lambda^4 < 3.0 \text{ TeV}^{-4} \quad (10.5)$$

$$-3.3 \text{ TeV}^{-4} < C_{BW}/\Lambda^4 < 3.3 \text{ TeV}^{-4} \quad (10.6)$$

$$-2.7 \text{ TeV}^{-4} < C_{BB}/\Lambda^4 < 2.8 \text{ TeV}^{-4}. \quad (10.7)$$

The data taking at  $\sqrt{s} = 13$  TeV had continued in 2017 and will go on in 2018 which will amount to an integrated luminosity of approximately  $120 \text{ fb}^{-1}$ . This will lower the statistical uncertainty of the cross section measurement further. For the inclusive cross section this will lead to the domination of experimental systematic uncertainties. In order to decrease these uncertainties further development, especially of the lepton efficiency, will be needed. For differential cross sections the statistical uncertainty is dominant in most bins. Therefore this measurement will greatly benefit from more data. With more data the sensitivity to electroweak production of  $ZZjj$ , through vector boson scattering processes for example, will increase and an experimental observation of this predicted process might be possible. Also the search of aTGCs is mostly limited due to low amount of events in high energy regions. More data will help to improve the limits substantially if no evidence of new physics is found.

When measuring  $ZZ$  production and searching for aTGCs higher center of mass energies are of great interest because it is possible to test the SM at so far unreached energies and probe for new physics. The LHC may operate at  $\sqrt{s} = 14$  TeV in 2018 which could be useful but is only a small increase of the energy. In order to probe much higher  $\sqrt{s}$  new accelerators are



---

necessary. There are plans to build a larger hadron collider, for example the Future Circular Collider (FCC), that can reach a  $\sqrt{s}$  of up to 100 TeV.

There are also plans to build a new linear electron-positron collider. At the International Linear Collider (ILC) electron-positron center of mass energies of about 500 GeV are planned. At electron colliders no PDFs of protons are needed to describe the interaction which removes one source of uncertainty. Furthermore it is possible to probe different energy regimes by varying the center of mass energy. This will make measurements of electroweak processes, like  $ZZ$  and Higgs production, very precise.



# Appendix



# Appendix A

## Detailed information about simulated samples

In this appendix detailed information about Monte Carlo samples is given which are used in this analysis. In Table A.1 information of the  $ZZ$  signal Monte Carlo samples is given together with information of samples that have contributions from anomalous triple gauge couplings. Table A.2 holds detailed information about the Monte Carlo samples that were used to estimate background contributions.

ID	Process	Generators	Events	Filter eff.	Cross section
361603	$q\bar{q} \rightarrow \ell^+\ell^-\ell'^+\ell'^-$	POWHEG + PYTHIA	3920000	1.0	1269.6 fb
363490	$q\bar{q} \rightarrow \ell^+\ell^-\ell'^+\ell'^-$	SHERPA	17825300	1.0	1255.7 fb
361074	$g\bar{g} \rightarrow \ell^+\ell^-\ell'^+\ell'^- (m_{4l} > 100)$	SHERPA	498500	1.0	16.16 fb
361072	$pp \rightarrow \ell^+\ell^-\ell'^+\ell'^-jj$ (EW $ZZjj$ )	SHERPA	60000	1.0	31.5 fb
Signal samples with aTGCs					
363842	$pp \rightarrow \ell^+\ell^-\ell'^+\ell'^-$ (TGC0)	SHERPA	98000	1.0	5.6 pb
363843	$pp \rightarrow \ell^+\ell^-\ell'^+\ell'^-$ (TGC1)	SHERPA	97000	1.0	6.4 pb
363844	$pp \rightarrow \ell^+\ell^-\ell'^+\ell'^-$ (TGC2)	SHERPA	100000	1.0	8.8 pb

TABLE A.1: Summary of  $ZZ$  signal Monte Carlo samples used in this analysis with information of the generated process. The ID corresponds to an iterative sample ID within the ATLAS collaboration. The cross section refers to the total cross section of the generated process after applied generator dependent kinematic cuts.

ID	Process	Generators	Events	Filter eff.	Cross section
Genuine background samples					
361625	$ZZZ \rightarrow 6\ell$	SHERPA	35000	1.0	17.1 ab
361623	$WZZ \rightarrow 5\ell 1\nu$	SHERPA	36108	1.0	217.8 ab
361626	$ZZZ \rightarrow 4\ell 2\nu$	SHERPA	34600	0.23	441.3 ab
361621	$WWZ \rightarrow 4\ell 2\nu$	SHERPA	33992	1.0	1.7 fb
410069	$t\bar{t}Z, Z \rightarrow \ell\ell+0$ partons	MadGraph+PYTHIA	192178	1.0	18.1 fb
410070	$t\bar{t}Z, Z \rightarrow \ell\ell+1$ parton	MadGraph+PYTHIA	206115	1.0	30.6 fb
Background samples for fake studies					
361106	$Z \rightarrow ee$	POWHEG+PYTHIA	19918600	1.0	1.9 nb
361108	$Z \rightarrow \mu\mu$	POWHEG+PYTHIA	19958000	1.0	1.9 nb
361601	$WZ \rightarrow \ell\nu\ell\ell$	POWHEG+PYTHIA	9875000	1.0	4.5 pb
361094	$WZ \rightarrow \ell\ell jj$	SHERPA	4500000	1.0	3.4 pb
361096	$ZZ \rightarrow \ell\ell jj$	SHERPA	4500000	0.14	16.4 pb
361096	$t\bar{t} \rightarrow lX, +$ jets	SHERPA	49386600	0.54	0.70 nb
361500	$Z \rightarrow ee+0$ partons	MadGraph+PYTHIA	6873800	1.0	1.4 nb
361501	$Z \rightarrow ee+1$ parton	MadGraph+PYTHIA	3595000	1.0	0.21 nb
361502	$Z \rightarrow ee+2$ parton	MadGraph+PYTHIA	2542800	1.0	0.067 nb
361503	$Z \rightarrow ee+3$ parton	MadGraph+PYTHIA	634200	1.0	0.019 nb
361504	$Z \rightarrow ee+4$ parton	MadGraph+PYTHIA	222500	1.0	7.3 pb
361505	$Z \rightarrow \mu\mu+0$ partons	MadGraph+PYTHIA	6880400	1.0	1.4 nb
361506	$Z \rightarrow \mu\mu+1$ parton	MadGraph+PYTHIA	3597000	1.0	0.21 nb
361507	$Z \rightarrow \mu\mu+2$ parton	MadGraph+PYTHIA	2542600	1.0	0.067 nb
361508	$Z \rightarrow \mu\mu+3$ parton	MadGraph+PYTHIA	633200	1.0	0.019 nb
361509	$Z \rightarrow \mu\mu+4$ parton	MadGraph+PYTHIA	220500	1.0	7.3 pb

TABLE A.2: Summary of  $ZZ$  background Monte Carlo samples used in this analysis. The SHERPA samples are generated with CT10 PDF [58] and the MadGraph+PYTHIA samples with NNPDF23LO PDF [57]. The ID corresponds to an iterative sample ID within the ATLAS collaboration. The cross section refers to the total cross section of the generated process after applied generator dependent kinematic cuts.

# Appendix B

## Signal efficiencies

In this appendix event selection efficiencies are shown using different  $ZZ$  signal simulations. Table B.1 shows the signal efficiency using POWHEG for  $q\bar{q} \rightarrow ZZ \rightarrow \ell^+\ell^-\ell'^+\ell'^-$ . Table B.2 shows the signal efficiency using SHERPA for  $gg \rightarrow ZZ \rightarrow \ell^+\ell^-\ell'^+\ell'^-$ . Table B.3 shows the signal efficiency using SHERPA for the electroweak production of  $q\bar{q} \rightarrow ZZjj \rightarrow \ell^+\ell^-\ell'^+\ell'^-jj$ . A selection is applied on generator level (before detector simulation) that corresponds to the selection applied on data.

Selection step	Event efficiency			
Trigger	$99.449 \pm 0.020$			
Vertex	$100 \pm 0$			
Jet Cleaning	$99.9879 \pm 0.0029$			
$\geq 2$ selected leptons	$99.912 \pm 0.008$			
$\geq 3$ selected leptons	$98.892 \pm 0.028$			
$\geq 4$ selected leptons	$87.97 \pm 0.09$			
Contains SFOC pairs	$94.65 \pm 0.06$			
Electron Quality	$99.981 \pm 0.004$			
Hierarchical $p_T$ cut	$99.933 \pm 0.008$			
Muon Quality	$99.940 \pm 0.007$			
	4e	$2e2\mu$	$4\mu$	combined
$\Delta R$	$99.909 \pm 0.019$	$99.547 \pm 0.029$	$99.993 \pm 0.005$	$99.755 \pm 0.015$
Quarkonia Veto	$99.788 \pm 0.029$	$99.944 \pm 0.010$	$99.971 \pm 0.010$	$99.915 \pm 0.009$
Electron ID	$77.17 \pm 0.27$	$88.25 \pm 0.14$	$100 \pm 0$	$88.904 \pm 0.100$
Impact Parameter	$99.30 \pm 0.06$	$98.91 \pm 0.05$	$98.76 \pm 0.06$	$98.944 \pm 0.033$
Isolation	$92.93 \pm 0.19$	$92.78 \pm 0.12$	$90.97 \pm 0.17$	$92.25 \pm 0.09$
On-shell	$99.24 \pm 0.07$	$99.12 \pm 0.05$	$98.50 \pm 0.07$	$98.958 \pm 0.035$
overall	$48.26 \pm 0.26$	$59.43 \pm 0.19$	$71.26 \pm 0.24$	$59.60 \pm 0.13$

TABLE B.1: Event selection efficiency for the  $q\bar{q} \rightarrow ZZ \rightarrow 4\ell$  contribution using the POWHEG MC sample. The efficiencies are given with respect to the previous selection step, except for the first row which is in relation to all events in the fiducial region and the last row which shows the combined efficiency of all selection steps. Only statistical uncertainties are shown.

Selection step	Event efficiency			
Trigger	99.435 ± 0.020			
Vertex	100 ± 0			
Jet Cleaning	99.982 ± 0.004			
≥ 2 selected leptons	99.957 ± 0.006			
≥ 3 selected leptons	99.295 ± 0.023			
≥ 4 selected leptons	89.80 ± 0.08			
Contains SFOC pairs	95.31 ± 0.06			
Electron Quality	99.974 ± 0.005			
Hierarchical $p_T$ cut	99.914 ± 0.009			
Muon Quality	99.931 ± 0.008			
	4e	2e2 $\mu$	4 $\mu$	combined
$\Delta R$	99.935 ± 0.021	99.688 ± 0.032	99.993 ± 0.006	99.827 ± 0.013
Quarkonia Veto	99.886 ± 0.028	99.979 ± 0.008	100 ± 0	99.963 ± 0.006
Electron ID	78.83 ± 0.34	89.25 ± 0.18	100 ± 0	89.74 ± 0.09
Impact Parameter	99.45 ± 0.07	98.99 ± 0.06	98.63 ± 0.09	98.974 ± 0.033
Isolation	93.23 ± 0.24	91.57 ± 0.17	90.92 ± 0.22	91.71 ± 0.09
On-shell	99.27 ± 0.08	99.46 ± 0.05	99.53 ± 0.06	99.444 ± 0.025
overall	52.12 ± 0.35	61.75 ± 0.24	72.52 ± 0.31	62.11 ± 0.13

TABLE B.2: Event selection efficiency for the  $gg \rightarrow ZZ \rightarrow 4\ell$  contribution using the SHERPA MC sample. The efficiencies are given with respect to the previous selection step, except for the first row which is in relation to all events in the fiducial region and the last row which shows the combined efficiency of all selection steps. Only statistical uncertainties are shown.



Selection step	Event efficiency			
Trigger	$99.49 \pm 0.09$			
Vertex	$100 \pm 0$			
Jet Cleaning	$99.84 \pm 0.05$			
$\geq 2$ selected leptons	$100 \pm 0$			
$\geq 3$ selected leptons	$99.87 \pm 0.05$			
$\geq 4$ selected leptons	$97.81 \pm 0.19$			
Contains SFOC pairs	$93.87 \pm 0.32$			
Electron Quality	$99.956 \pm 0.029$			
Hierarchical $p_T$ cut	$99.91 \pm 0.04$			
Muon Quality	$100 \pm 0$			
	4e	2e2 $\mu$	4 $\mu$	combined
$\Delta R$	$100 \pm 0$	$99.01 \pm 0.21$	$100 \pm 0$	$99.52 \pm 0.10$
Quarkonia Veto	$100 \pm 0$	$100 \pm 0$	$100 \pm 0$	$100 \pm 0$
Electron ID	$55.0 \pm 1.4$	$76.5 \pm 0.9$	$100 \pm 0$	$76.5 \pm 0.6$
Impact Parameter	$99.69 \pm 0.21$	$99.25 \pm 0.21$	$99.25 \pm 0.25$	$99.34 \pm 0.13$
Isolation	$93.6 \pm 0.9$	$89.6 \pm 0.7$	$85.4 \pm 1.0$	$89.0 \pm 0.5$
On-shell	$99.72 \pm 0.21$	$99.33 \pm 0.21$	$97.9 \pm 0.5$	$98.98 \pm 0.18$
overall	$45.6 \pm 1.3$	$55.9 \pm 0.9$	$64.4 \pm 1.2$	$55.6 \pm 0.7$

TABLE B.3: Event selection efficiency for the electroweak  $q\bar{q} \rightarrow ZZjj \rightarrow 4ljj$  contribution using the SHERPA MC sample. The efficiencies are given with respect to the previous selection step, except for the first row which is in relation to all events in the fiducial region and the last row which shows the combined efficiency of all selection steps. Only statistical uncertainties are shown.



# Appendix C

## Event display

In this appendix an further event display is shown in Figure C.1. The energy depositions of the electrons in the calorimeter are shown in green. The tracks are shown in blue for the electrons and in red for the muons.

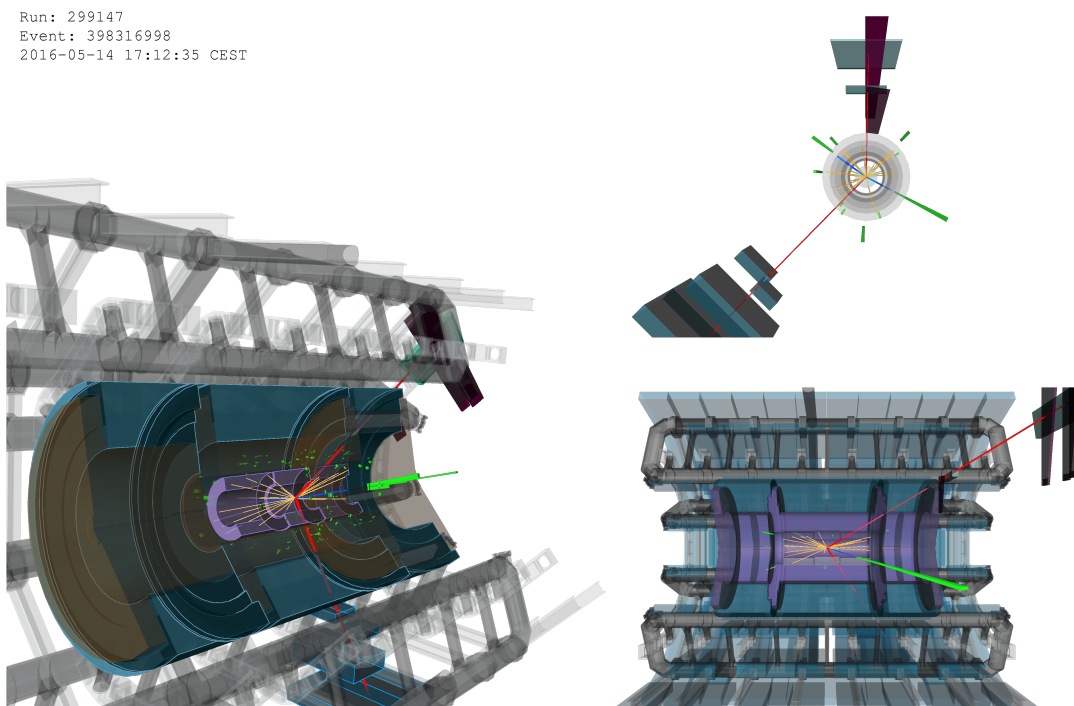


FIGURE C.1: Event display of an event recorded in 2016. The top right panel shows the  $r - \phi$  plane and the bottom right panel the  $z - \eta$  plane. The energy depositions of the electrons in the calorimeter are visualized in green. The tracks of the electrons are shown in blue and the one of the muons in red. Inner detector tracks with a transverse momentum larger than 2.5 GeV are shown in yellow. The four lepton system has an invariant mass of 209 GeV, a transverse momentum of 31 GeV, and a rapidity of 0.8. The first  $Z$  boson candidate is reconstructed from two oppositely charged electrons ( $p_T = 67$  GeV,  $\eta = 1.23$  and  $p_T = 12$  GeV,  $\eta = -1.03$ ), has a mass of 96 GeV and a transverse momentum of 55 GeV. The other candidate has a mass of 91 GeV, a transverse momentum of 40 GeV and is reconstructed from two oppositely charged muons ( $p_T = 36$  GeV,  $\eta = 1.29$  and  $p_T = 56$  GeV,  $\eta = 0.45$ ).



# Appendix D

## Background

### D.1 Data driven background

#### D.1.1 Real lepton correction model uncertainty

The contribution of real leptons that is subtracted in Equation 7.4 can also be influenced from uncertainties due to differences between the efficiency in data and simulation. For the leptons that pass the cuts this is corrected by using scale factors (see Chapter 5.4.1), but for the leptons that fail the cuts the correction is not done by default. This scale factor for leptons failing a cut is given by:

$$SF_{fail} = \frac{1 - eff_{data}}{1 - eff_{MC}} \Leftrightarrow SF_{fail} = \frac{1 - eff_{MC} * SF_{pass}}{1 - eff_{MC}}, \quad (D.1)$$

where  $eff_{data}$  is the cut efficiency of real leptons in data,  $eff_{MC}$  the cut efficiency in simulation and  $SF_{pass}$  the scale factor for leptons that pass the cut which is provided by the corresponding ATLAS performance group. So the only needed quantity is  $eff_{MC}$ , which is calculated by the ratio:

$$eff_{MC,cut} = \frac{\#leptons \text{ pass the cut}}{\#leptons \text{ before applying the cut}}. \quad (D.2)$$

Here, only leptons are used that are coming from the hard processes by using the MCTruth-Classifier. The resulting efficiencies together with the  $SF_{fail}$  are shown in Table D.1.

Selection cut	Simulation efficiency	Scale factor for leptons failing cut
Electron identification	95.93%	0.97
Electron isolation	98.32%	$\approx 1$
Muon isolation	97.98%	$\approx 1$
Muon $d_0$ -significance	99.62%	-

TABLE D.1: Selection efficiency for different selection criteria that are inverted for the background determination. Also shown is the resulting scale factor for leptons failing the cuts for inversion. Since the efficiency is done with simulation, the statistical uncertainty is very small and therefore not shown. Systematic effects are not investigated. The scale factor for leptons passing the  $d_0$  significance is not known and therefore the scale factor where the leptons fail the cut can not be estimated.

---

It can be seen that only for the identification of electrons the scale factor is different from one, while the others are very close to one. In order to see the impact on the final background estimate this scale factor is applied to  $N^{\ell\ell j}$  events, where the real lepton correction is largest in the following way (shown for the electron case):

$$N_{MC, failID}^{\ell\ell j} * SF_{failID} + N_{MC, failIso}^{\ell\ell j} * SF_{failIso}. \quad (D.3)$$

The result for the  $4e$  case is 2.22, which is about 50% higher compared to the correction quoted in Table 7.5. This estimate is very rough, for example it does not include any kinematic dependence but given the small size of the background it is expected to be sufficient enough. The 50 % variation is applied to all other channels as a conservative approach.

# Appendix E

## Cross section

### E.1 Unfolding input parameter

This appendix shows further input that is needed for unfolding. The fiducial phase space correction together with the purity for jet inclusive variables is shown in Figure E.2 and for jet exclusive variables in Figure E.1. The efficiency correction for jet inclusive variables is shown in Figure E.3 and for jet exclusive variables in Figure E.4. The migration of bins due to detector energy resolution effects is shown in Figure E.5 for jet inclusive variables and in Figure E.6 for jet exclusive variables.

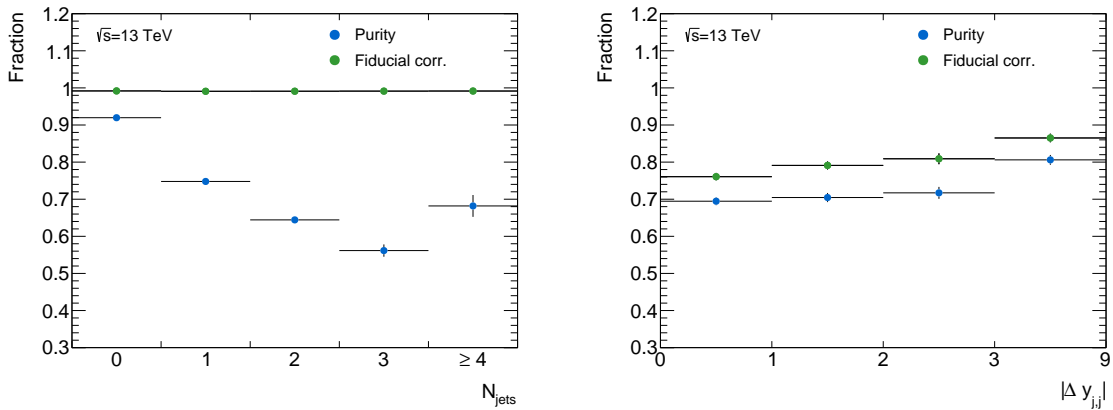


FIGURE E.1: Shown in green is the fraction of events generated in one bin and reconstructed in the same bin. In blue the fraction of events that are reconstructed in a bin but not selected in the same bin after the fiducial phase space selection. Only jet exclusive variables are shown. The bins are not equidistant but for better visualization shown in an equidistant way. Only statistical uncertainties are shown.

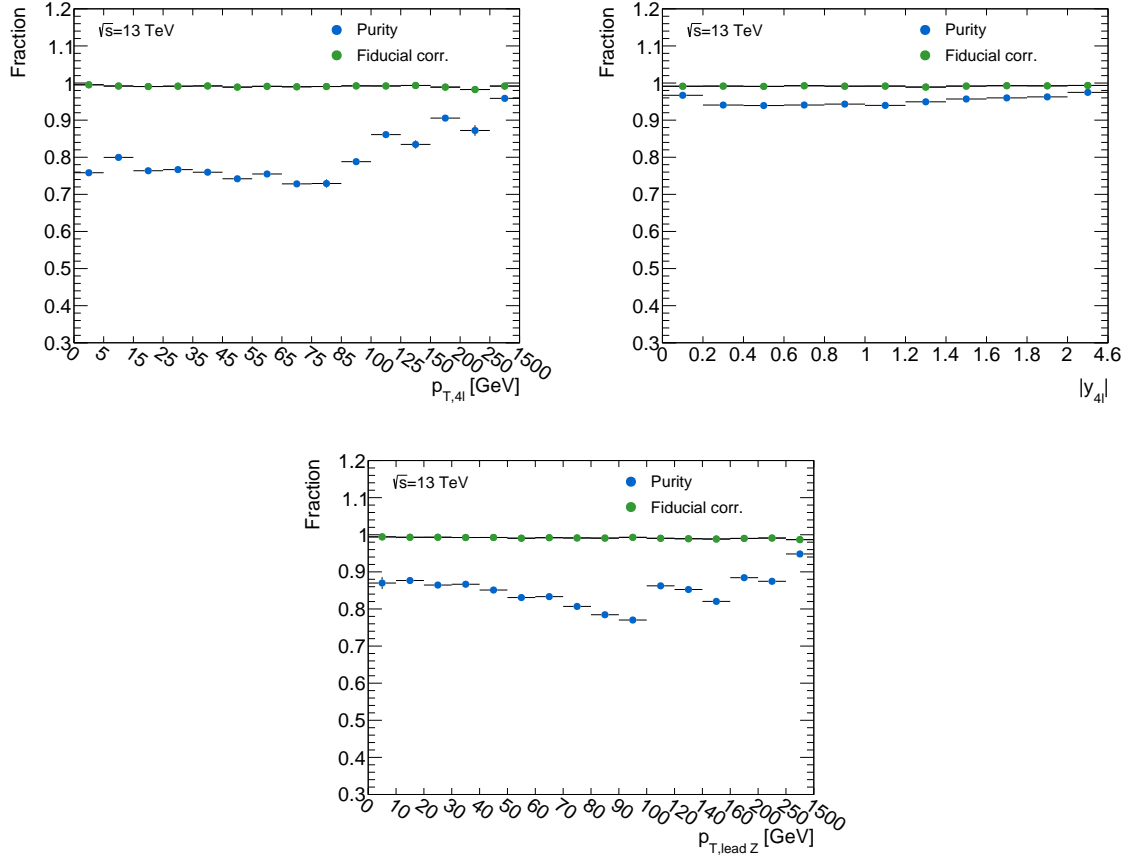


FIGURE E.2: Shown in green is the fraction of events generated in one bin and reconstructed in the same bin. In blue the fraction of events that are reconstructed in a bin but not selected in the same bin after the fiducial phase space selection. Only jet inclusive variables are shown. The bins are not equidistant but for better visualization shown in an equidistant way. Only statistical uncertainties are shown.

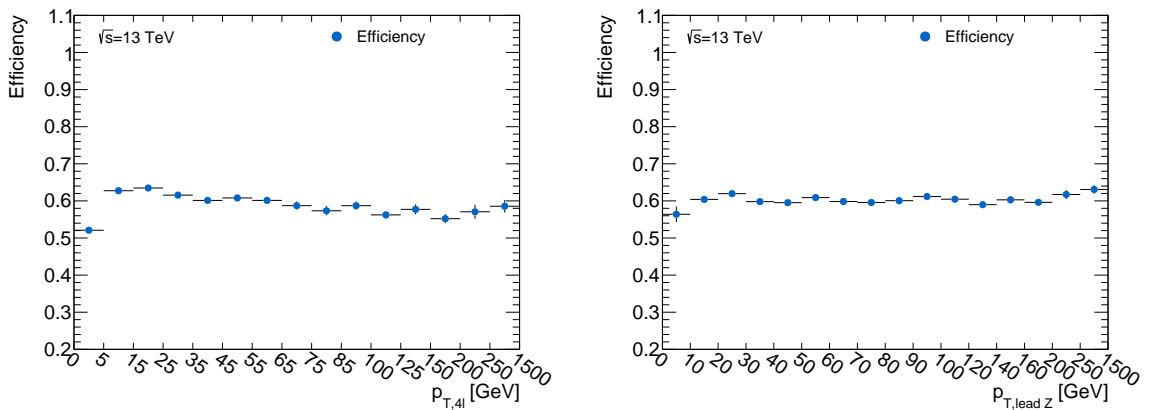


FIGURE E.3: Efficiency correction as function of different jet inclusive variables. The bins are not equidistant but for better visualization shown in an equidistant way. Only statistical uncertainties are shown.



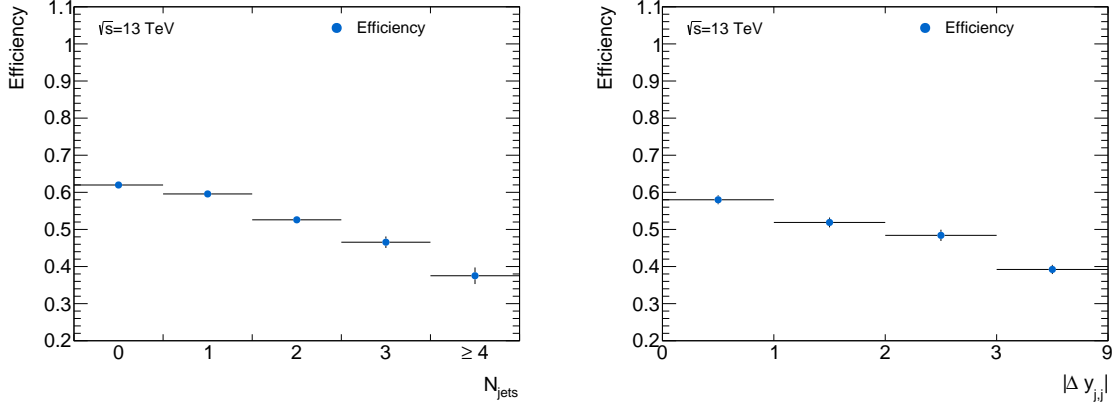


FIGURE E.4: Efficiency correction as function of different jet exclusive variables. The bins are not equidistant but for better visualization shown in an equidistant way. Only statistical uncertainties are shown.

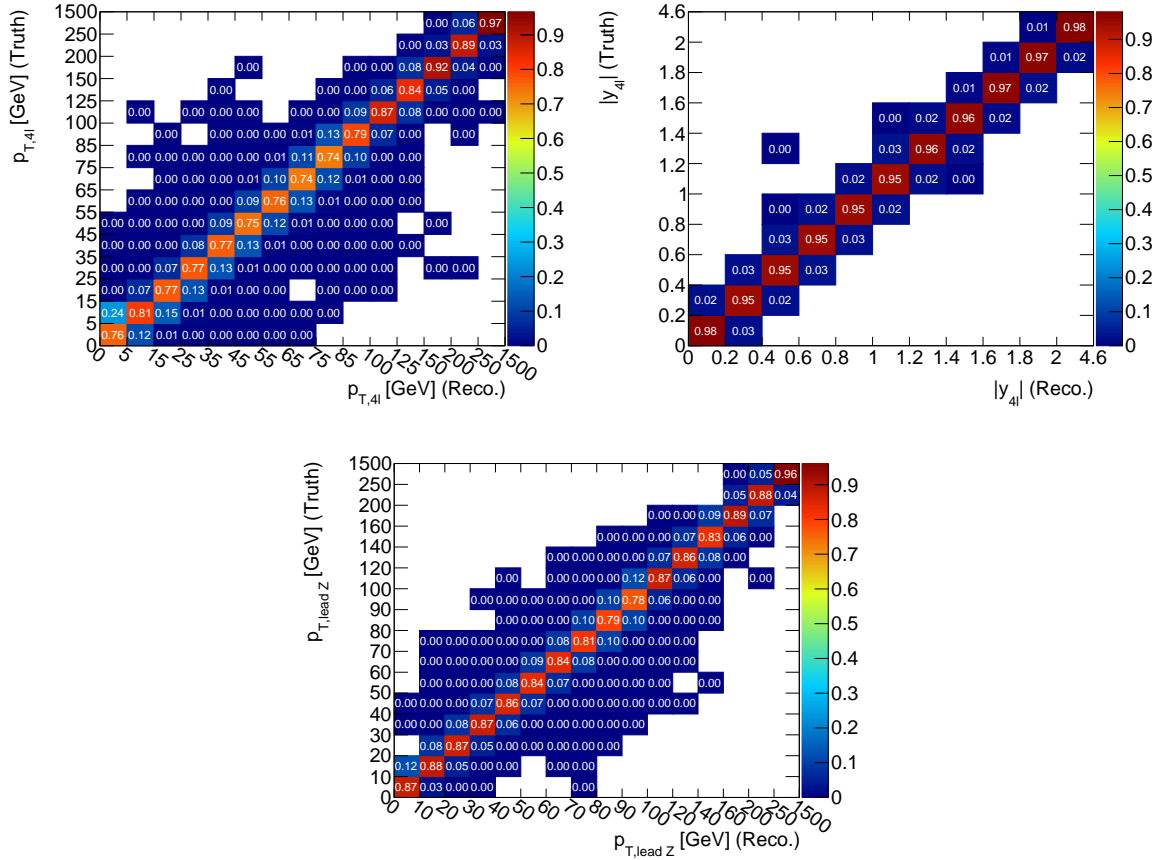


FIGURE E.5: Bin migration matrices for different jet inclusive variables. The y-axis corresponds to the value of the variable on generator level, the x-axis on detector level. The bins are not equidistant but for better visualization shown in an equidistant way. The entries are normalized to the number of reconstructed events in one bin integrated over the truth variable.

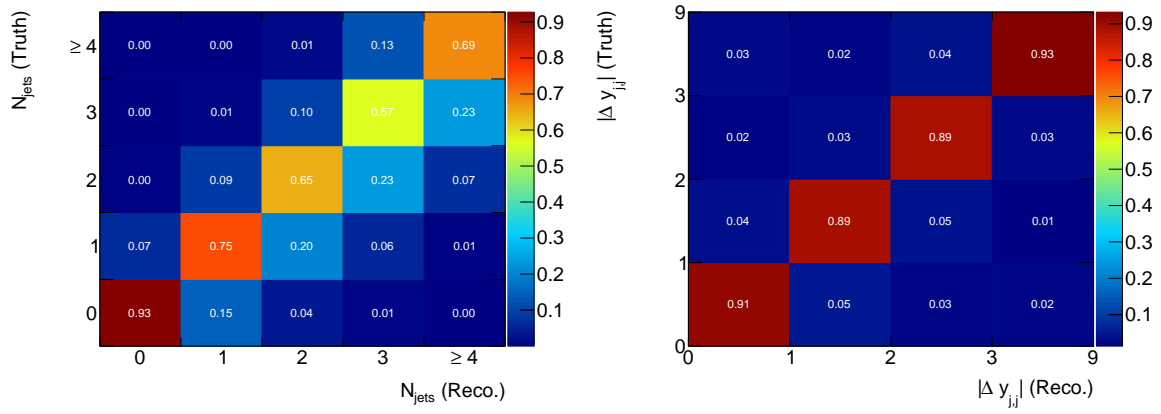


FIGURE E.6: Bin migration matrices for different jet exclusive variables. The y-axis correspond to the value of the variable on generator level, the x-axis on detector level. The bins are not equidistant but for better visualization shown in an equidistant way. The entries are normalized to the number of reconstructed events in one bin integrated over the truth variable.

## E.2 Monte Carlo based closure check

In this appendix further MC based closure checks are shown. The unfolding is done using simulations where the  $q\bar{q}$  initiated process is produced with POWHEG instead of data. The resulting distributions in comparison with corresponding generator distributions is shown in Figure E.7 for jet inclusive variables and in Figure E.8 for jet exclusive variables. Full closure is visible for all distributions.

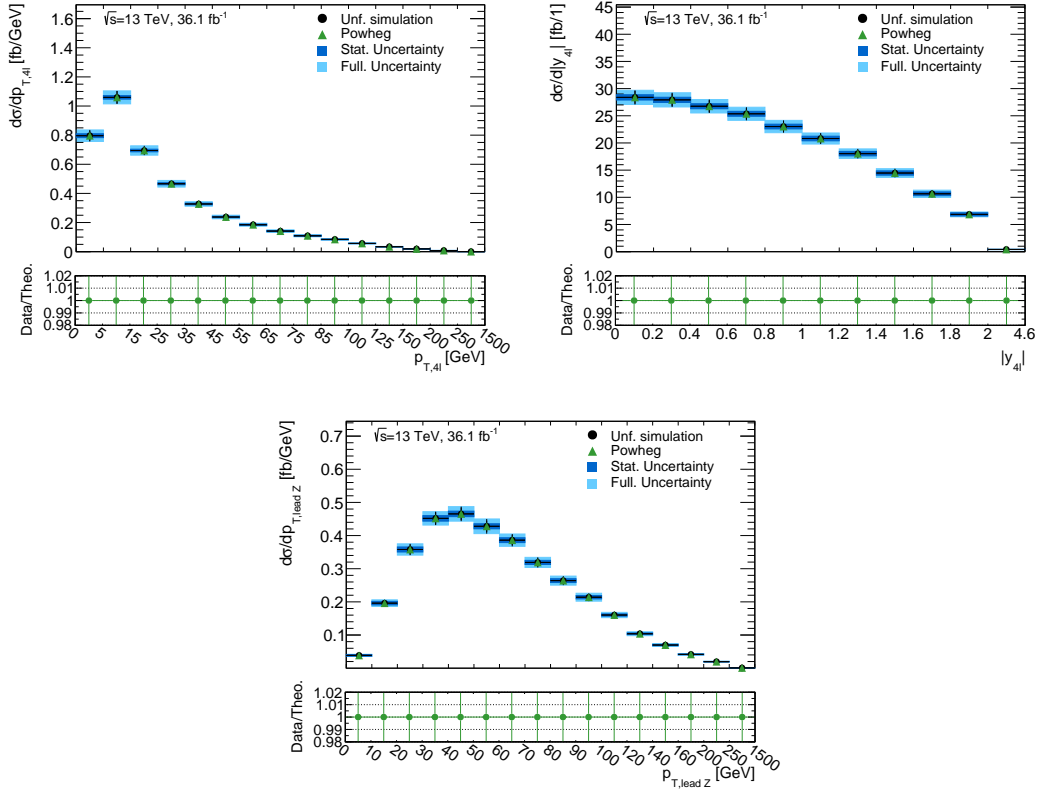


FIGURE E.7: Monte Carlo based closure check for different jet inclusive variables. Instead of data distributions the signal MC samples on detector level are used for unfolding and compared to the distribution on generator level. The lower panel shows the ratio of the unfolded distribution and the one on generator level.

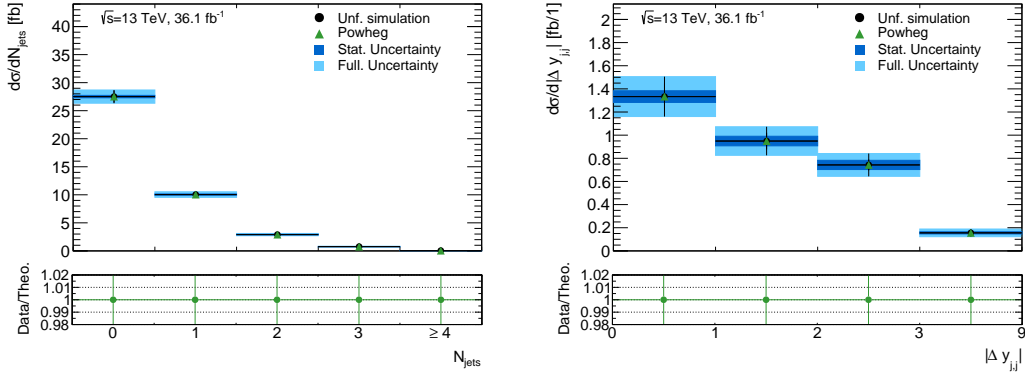


FIGURE E.8: Monte Carlo based closure check for different jet exclusive variables. Instead of data distributions the signal MC samples on detector level are used for unfolding and compared to the distribution on generator level. The lower panel shows the ratio of the unfolded distribution and the one on generator level.

### E.3 Differential cross section tables

This appendix shows the differential cross section for all seven observables in a tabular way. In Table E.1 the cross sections with combined statistical and systematical uncertainty are shown for jet exclusive observables. The resulting cross sections with uncertainties for jet inclusive variables are shown in Table E.2.

$ \Delta y_{j,j} $	$d\sigma/d \Delta y_{j,j} $ [fb/1]	$m_{j,j}$ [GeV]	$d\sigma/dm_{j,j}$ [fb/GeV]	$N_{jets}$	$d\sigma/dN_{jets}$ [fb]
0-1	$1.33 \pm 0.18$	0-50	$0.0061 \pm 0.0011$	0	$27.5 \pm 1.2$
1-2	$0.95 \pm 0.13$	50-100	$0.016 \pm 0.0030$	1	$10.04 \pm 0.51$
2-3	$0.743 \pm 0.098$	100-200	$0.011 \pm 0.0013$	2	$2.90 \pm 0.22$
3-9	$0.156 \pm 0.040$	200-300	$0.00591 \pm 0.00072$	3	$0.757 \pm 0.077$
		300-1000	$0.00136 \pm 0.00020$	$\geq 4$	$0.299 \pm 0.016$

TABLE E.1: Differential cross sections for jet exclusive variables. The uncertainties contain statistical and systematic uncertainties.

$p_{T,lead Z}$ [GeV]	$d\sigma/dp_{T,lead Z}$ [fb/GeV]	$ y_{4l} $	$d\sigma/d y_{4l} $ [fb/1]	$m_{4l}$ [GeV]	$d\sigma/dm_{4l}$ [fb/GeV]	$p_{T,4l}$ [GeV]	$d\sigma/dp_{T,4l}$ [fb/GeV]
0-10	$0.0385 \pm 0.0033$	0-0.2	$35.4 \pm 3.1$	140-180	$0.0202 \pm 0.0042$	0-5	$0.837 \pm 0.076$
10-20	$0.196 \pm 0.010$	0.2-0.4	$31.4 \pm 2.9$	180-200	$0.343 \pm 0.029$	5-15	$1.176 \pm 0.077$
20-30	$0.358 \pm 0.0179$	0.4-0.6	$29.9 \pm 2.7$	200-220	$0.400 \pm 0.031$	15-25	$0.843 \pm 0.062$
30-40	$0.451 \pm 0.0201$	0.6-0.8	$24.3 \pm 2.4$	220-240	$0.341 \pm 0.028$	25-35	$0.533 \pm 0.046$
40-50	$0.465 \pm 0.022$	0.8-1	$21.8 \pm 2.3$	240-260	$0.267 \pm 0.023$	35-45	$0.366 \pm 0.036$
50-60	$0.428 \pm 0.022$	1-1.2	$25.3 \pm 2.6$	260-280	$0.180 \pm 0.018$	45-55	$0.266 \pm 0.030$
60-70	$0.386 \pm 0.019$	1.2-1.4	$18.2 \pm 2.2$	280-300	$0.144 \pm 0.016$	55-65	$0.189 \pm 0.026$
70-80	$0.319 \pm 0.015$	1.4-1.6	$18.6 \pm 2.4$	300-325	$0.086 \pm 0.011$	65-75	$0.096 \pm 0.018$
80-90	$0.264 \pm 0.014$	1.6-1.8	$12.6 \pm 2.0$	325-350	$0.0703 \pm 0.0096$	75-85	$0.097 \pm 0.018$
90-100	$0.214 \pm 0.012$	1.8-2	$4.0 \pm 1.1$	350-400	$0.0499 \pm 0.0065$	85-100	$0.071 \pm 0.013$
100-120	$0.1603 \pm 0.0080$	2-4.6	$0.56 \pm 0.15$	400-500	$0.0259 \pm 0.0034$	100-125	$0.0570 \pm 0.0099$
120-140	$0.1039 \pm 0.0059$			500-600	$0.0104 \pm 0.0021$	125-150	$0.0276 \pm 0.0069$
140-160	$0.0698 \pm 0.0042$			600-800	$0.0058 \pm 0.0011$	150-200	$0.0264 \pm 0.0050$
160-200	$0.0416 \pm 0.0027$			800-1500	$0.00039 \pm 0.00016$	200-250	$0.0139 \pm 0.0034$
200-250	$0.0195 \pm 0.0014$					250-1500	$0.00053 \pm 0.00014$
250-1500	$0.000783 \pm 0.00058$						

TABLE E.2: Differential cross section for jet inclusive variables. The uncertainties contain statistical and systematic uncertainties.

## E.4 Systematic bin correlations

It is important to know the correlations of the uncertainties between bins of the unfolded differential cross section. The relative uncertainty correlation of the fiducial unfolded cross section for jet inclusive variables is shown in Figure E.9 and for jet exclusive variables in Figure E.10. Comparing the correlations to the official ATLAS publication [62] much larger off-diagonal correlations are visible, which is caused by applying a more stringent grouping of systematic uncertainties before unfolding. This combination is done in a fully correlated way and therefore the overall bin to bin correlation is increased.

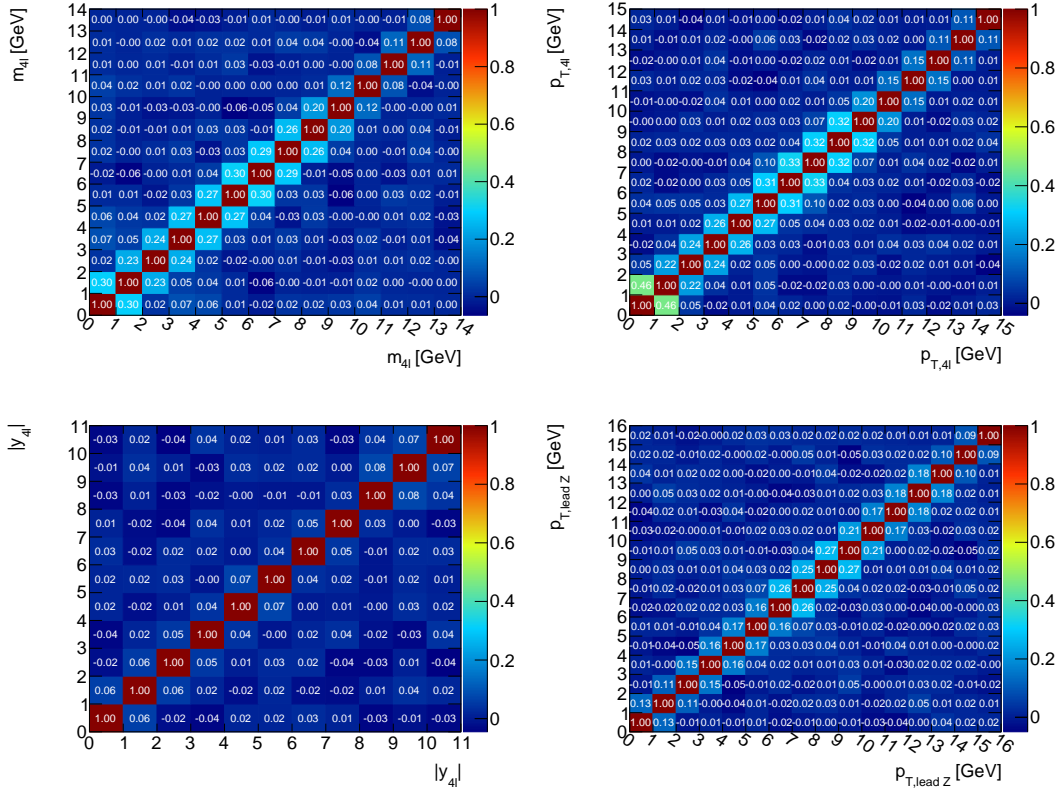


FIGURE E.9: Relative uncertainty correlation of the fiducial unfolded cross section for different jet inclusive variables including statistical uncertainties of data and systematic uncertainties from background and signal predictions. The bins are consecutively numbered but have the same sizes as the main unfolded result.

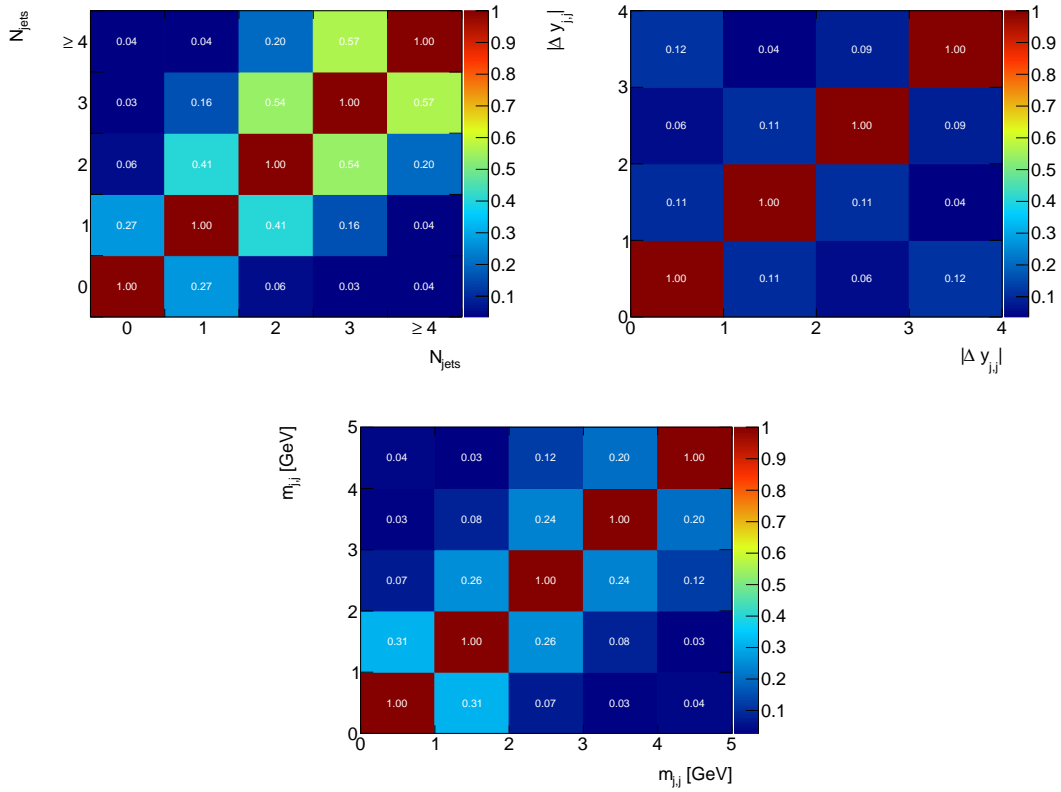


FIGURE E.10: Relative uncertainty correlation of the fiducial unfolded cross section for different jet exclusive variables including statistical uncertainties of data and systematic uncertainties from background and signal predictions. The bins are consecutively numbered but have the same sizes as the main unfolded result.

## E.5 Differences between cross section measurements with 2015 and full 2015+2016 data

The integrated fiducial and extrapolated cross section was also measured by using 2015 data only [154]. Many techniques that are presented in this thesis were used for this very early 13 TeV publication, especially the data driven background determination. The reason to first do a measurement with the relatively small data set of 2015 was to see quickly if the predicted cross sections at 13 TeV agree with data, since this center of mass energy was never reached before. The main mentality of this very early 13 TeV analysis was therefore to keep things simple and robust and have a fast result of the measured cross section. Then afterwards a more sophisticated analysis was done, measuring larger phase spaces and using more advanced techniques. This is the reason why the fiducial volume and the data selection of the early 2015 analysis is not the same as the one which uses the complete data from 2015+2016. More details of the differences are shown in Table E.3. One of the main differences is the higher  $p_T$  cut on the leptons. It is at 20 GeV on all leptons for the early analysis and  $p_T > 20$  GeV, 15 GeV, 10 GeV, 5 GeV on the  $p_T$  ordered leptons for the later analysis. The main reason for using 20 GeV was that only for this  $p_T$  threshold the lepton energy calibration and efficiency corrections could be provided in the timescale of the publication. A simpler way of the  $\Delta R$  in the early analysis also reduces the acceptance but does not make it necessary to distinguish between channels at that point. Furthermore the early analysis only measured integrated, inclusive cross sections and therefore no jet selection was applied. There are further differences in the data selection aiming for reducing background contributions but since the background is very low and only the resulting cross sections are compared, this is not described in further detail.

Type	Full 2015+16 analysis	Early 2015 analysis
Leptons	Prompt	
	Dressed with prompt photons within $\Delta R = 0.1$ (added to closest prompt lepton)	
	$p_T > 5$ GeV	$p_T > 20$ GeV
	$ \eta  < 2.7$	
Quadruplets	Two same-flavor opposite-charge lepton pairs	
	Hierarchical $p_T$ cut: $p_T > 20$ GeV, 15 GeV, 10 GeV	–
Events	Only quadruplet minimizing $ m_{\ell\ell,a} - m_Z  +  m_{\ell\ell,b} - m_Z $ is considered	
	$m_{\ell\ell} > 5$ GeV	–
	$\Delta R > 0.1$ (0.2) between same-flavor (different-flavor) leptons	$\Delta R > 0.2$ for all leptons
	Dileptons minimizing $ m_{\ell\ell,a} - m_Z  +  m_{\ell\ell,b} - m_Z $ are taken as $Z$ boson candidates	
	$Z$ boson candidates have invariant masses within $66 \text{ GeV} < m_{\ell\ell} < 116 \text{ GeV}$	

TABLE E.3: Differences in the fiducial phase space definitions of the early 2015 analysis and the analysis using the full 2015+16 dataset. When requirements are not applied it is marked with “–”.



# Bibliography

- [1] K. Freeman, *Ancilla to the Pre-Socratic Philosophers: A Complete Translation of the Fragments in Diels Fragmente Der Vorsokratiker*, Forgotten Books, 1948, ISBN: 9781606802564.
- [2] *A Dictionary of Physics*, Oxford University Press, 2009, ISBN: 9780199233991.
- [3] J. J. Thomson, *Cathode rays*, *Phil. Mag.* **44** (1897) p. 293.
- [4] E. Rutherford,  
*The scattering of alpha and beta particles by matter and the structure of the atom*,  
*Phil. Mag.* **21** (1911) p. 669.
- [5] A. H. Compton, *A Quantum Theory of the Scattering of X-rays by Light Elements*,  
*Phys. Rev.* **21** (5 1923) p. 483.
- [6] J. Chadwick, *Possible Existence of a Neutron*, *Nature* **129** (1932) p. 312.
- [7] S. H. Neddermeyer and C. D. Anderson, *Note on the Nature of Cosmic-Ray Particles*,  
*Phys. Rev.* **51** (10 1937) p. 884.
- [8] M. Gell-Mann, *A Schematic Model of Baryons and Mesons*,  
*Phys. Lett.* **8** (1964) p. 214.
- [9] G. Zweig,  
'An SU(3) model for strong interaction symmetry and its breaking. Version 2',  
*Developments in the quark theory of hadrons. Vol. 1. 1964-1978*,  
ed. by D. Lichtenberg and S. P. Rosen, 1964 p. 22,  
URL: <http://inspirehep.net/record/4674/files/cern-th-412.pdf>.
- [10] M. Breidenbach et al.,  
*Observed Behavior of Highly Inelastic electron-Proton Scattering*,  
*Phys. Rev. Lett.* **23** (1969) p. 935.
- [11] C. Berger et al.,  
*Evidence for Gluon Bremsstrahlung in  $e^+ e^-$  Annihilations at High-Energies*,  
*Phys. Lett.* **B86** (1979) p. 418.
- [12] W. Bartel et al., *Observation of Planar Three Jet Events in  $e^+ e^-$  Annihilation and Evidence for Gluon Bremsstrahlung*, *Phys. Lett.* **B91** (1980) p. 142.
- [13] R. Brandelik et al., *Evidence for Planar Events in  $e^+ e^-$  Annihilation at High-Energies*,  
*Phys. Lett.* **B86** (1979) p. 243.
- [14] D. P. Barber et al., *Discovery of Three Jet Events and a Test of Quantum Chromodynamics at PETRA Energies*, *Phys. Rev. Lett.* **43** (1979) p. 830.

- [15] G. Arnison et al., *Experimental Observation of Isolated Large Transverse Energy Electrons with Associated Missing Energy at  $\sqrt{s}=540$  GeV*, *Phys. Lett.* **122B** (1983) p. 103.
- [16] M. Banner et al., *Observation of Single Isolated Electrons of High Transverse Momentum in Events with Missing Transverse Energy at the CERN anti-p p Collider*, *Phys. Lett.* **B122** (1983) p. 476.
- [17] G. Arnison et al., *Experimental Observation of Lepton Pairs of Invariant Mass Around 95-GeV/c<sup>2</sup> at the CERN SPS Collider*, *Phys. Lett.* **B126** (1983) p. 398.
- [18] P. Bagnaia et al., *Evidence for  $Z^0 \rightarrow e^+e^-$  at the CERN anti-p p Collider*, *Phys. Lett.* **B129** (1983) p. 130.
- [19] ATLAS Collaboration, *Observation of a new particle in the search for the Standard Model Higgs boson with the ATLAS detector at the LHC*, *Phys.Lett.* **B716** (2012) p. 1, arXiv: [1207.7214](https://arxiv.org/abs/1207.7214) [[hep-ex](#)].
- [20] S. Chatrchyan et al., *Observation of a new boson at a mass of 125 GeV with the CMS experiment at the LHC*, *Phys.Lett.* **B716** (2012) p. 30, arXiv: [1207.7235](https://arxiv.org/abs/1207.7235) [[hep-ex](#)].
- [21] G. Hinshaw et al., *Five-Year Wilkinson Microwave Anisotropy Probe (WMAP) Observations: Data Processing, Sky Maps, and Basic Results*, *Astrophys. J. Suppl.* **180** (2009) p. 225, arXiv: [0803.0732](https://arxiv.org/abs/0803.0732) [[astro-ph](#)].
- [22] M. Becker and S. Tapprogge, *Search for a heavy gauge boson in the decay channel  $W' \rightarrow e\nu$  with the ATLAS experiment*, Presented 09 Sep 2013, MA thesis, URL: <https://cds.cern.ch/record/1646406>.
- [23] A. Zannoni, *On the Quantization of the Monoatomic Ideal Gas*, (1999), arXiv: [cond-mat/9912229](https://arxiv.org/abs/cond-mat/9912229).
- [24] P. A. M. Dirac, *On the Theory of Quantum Mechanics*, *Proceedings of the Royal Society of London A: Mathematical, Physical and Engineering Sciences* **112** (1926) p. 661.
- [25] Bose, *Plancks Gesetz und Lichtquantenhypothese*, *Zeitschrift für Physik* **26** (1924) p. 178.
- [26] F. Halzen and A. Martin, *Quarks and leptons: an introductory course in modern particle physics*, Wiley, 1984.
- [27] J. Maxwell, *A Treatise on Electricity and Magnetism*, A Treatise on Electricity and Magnetism Bd. 1, Clarendon Press, 1873.
- [28] E. Fermi, *Versuch einer Theorie der  $\beta$ -Strahlen. I*, *Zeitschrift für Physik* **88** (1934) p. 161.
- [29] H. Fritzsch, M. Gell-Mann and H. Leutwyler, *Advantages of the color octet gluon picture*, *Physics Letters B* **47** (1973) p. 365 .
- [30] M. Fukugita, M. Tanimoto and T. Yanagida, *Atmospheric neutrino oscillation and a phenomenological lepton mass matrix*, *Phys.Rev.* **D57** (1998) p. 4429, arXiv: [hep-ph/9709388](https://arxiv.org/abs/hep-ph/9709388) [[hep-ph](#)].
- [31] C. P. et al., *Review of Particle Physics*, *Chin. Phys.* **C40** (2016) p. 100001.

- [32] R. Aaij et al., *Observation of the resonant character of the  $Z(4430)^-$  state*, *Phys. Rev. Lett.* **112** (2014) p. 222002, arXiv: 1404.1903 [hep-ex].
- [33] M. Ablikim et al., *Observation of a Charged Charmoniumlike Structure in  $e^+e^- \rightarrow \pi^+\pi^- J/\psi$  at  $\sqrt{s}=4.26$  GeV*, *Phys. Rev. Lett.* **110** (2013) p. 252001, arXiv: 1303.5949 [hep-ex].
- [34] R. Aaij et al., *Observation of  $J/\psi p$  Resonances Consistent with Pentaquark States in  $\Lambda_b^0 \rightarrow J/\psi K^- p$  Decays*, *Phys. Rev. Lett.* **115** (2015) p. 072001, arXiv: 1507.03414 [hep-ex].
- [35] M. E. Peskin and D. V. Schroeder, *An Introduction To Quantum Field Theory*, Addison-Wesley Publishing Company, 1995, ISBN: 9780201503975.
- [36] E. Noether, *Invariante Variationsprobleme*, ger, Nachrichten von der Gesellschaft der Wissenschaften zu Göttingen, Mathematisch-Physikalische Klasse (1918) p. 235, URL: <http://eudml.org/doc/59024>.
- [37] R. P. Feynman, *The Theory of Positrons*, *Phys. Rev.* **76** (1949).
- [38] Orear, J. and Fermi, E., *Nuclear Physics: A Course Given by Enrico Fermi at the University of Chicago*, University of Chicago Press (1950).
- [39] D. Griffiths, *Introduction to Elementary Particles*, Wiley, 2008, ISBN: 9783527406012.
- [40] A. Pich, *Quantum chromodynamics*, (1995), arXiv: hep-ph/9505231 [hep-ph].
- [41] S. Weinberg, *A Model of Leptons*, *Phys.Rev.Lett.* **19** (1967) p. 1264.
- [42] C. Berger, *Elementarteilchenphysik*, Springer-Verlag Berlin Heidelberg, 2006, ISBN: 9783540335948.
- [43] W. Hollik, *Electroweak theory*, *J.Phys.Conf.Ser.* **53** (2006) p. 7.
- [44] J. H. Christenson, J. W. Cronin, V. L. Fitch and R. Turlay, *Evidence for the  $2\pi$  Decay of the  $K_2^0$  Meson*, *Phys. Rev. Lett.* **13** (4 1964) p. 138, URL: <https://link.aps.org/doi/10.1103/PhysRevLett.13.138>.
- [45] P. W. Higgs, *Broken symmetries, massless particles and gauge fields*, *Phys.Lett.* **12** (1964) p. 132.
- [46] ATLAS and CMS Collaboration, *Combined Measurement of the Higgs Boson Mass in  $pp$  Collisions at  $\sqrt{s} = 7$  and 8 TeV with the ATLAS and CMS Experiments*, *Phys. Rev. Lett.* **114** (2015) p. 191803, arXiv: 1503.07589 [hep-ex].
- [47] M. Woods, ‘Review of weak mixing angle results at SLC and LEP’, *High-energy physics. Proceedings, International Europhysics Conference, HEP '95, Brussels, Belgium, July 27-August 2, 1995*, 1995 p. 31.
- [48] H. Yukawa, *Quantum Theory of Non-Local Fields. Part I. Free Fields*, *Phys. Rev.* **77** (2 1950) p. 219.
- [49] J. M. Campbell, J. Huston and W. Stirling, *Hard Interactions of Quarks and Gluons: A Primer for LHC Physics*, *Rept.Prog.Phys.* **70** (2007) p. 89, arXiv: hep-ph/0611148 [hep-ph].
- [50] S. Drell and T.-M. Yan, *Partons and their Applications at High-Energies*, *Annals Phys.* **66** (1971) p. 578.

- [51] M. L. Mangano, *Introduction to QCD*, (1999),  
URL: <https://cds.cern.ch/record/454171>.
- [52] G. Altarelli and G. Parisi, *Asymptotic Freedom in Parton Language*,  
*Nucl.Phys.* **B126** (1977) p. 298.
- [53] A. Vogt, S. Moch and J. Vermaseren,  
*The Three-loop splitting functions in QCD: The Singlet case*,  
*Nucl.Phys.* **B691** (2004) p. 129, arXiv: [hep-ph/0404111](https://arxiv.org/abs/hep-ph/0404111) [[hep-ph](#)].
- [54] C. Adloff et al., *Measurement of neutral and charged current cross-sections in positron proton collisions at large momentum transfer*, *Eur.Phys.J.* **C13** (2000) p. 609,  
arXiv: [hep-ex/9908059](https://arxiv.org/abs/hep-ex/9908059) [[hep-ex](#)].
- [55] S. Chekanov et al., *Measurement of the neutral current cross-section and  $F(2)$  structure function for deep inelastic  $e + p$  scattering at HERA*, *Eur.Phys.J.* **C21** (2001) p. 443,  
arXiv: [hep-ex/0105090](https://arxiv.org/abs/hep-ex/0105090) [[hep-ex](#)].
- [56] H. L. Lai et al., *Improved parton distributions from global analysis of recent deep inelastic scattering and inclusive jet data*, *Phys. Rev.* **D55** (1997) p. 1280,  
arXiv: [hep-ph/9606399](https://arxiv.org/abs/hep-ph/9606399) [[hep-ph](#)].
- [57] R. D. Ball et al., *Parton distributions for the LHC Run II*, *JHEP* **04** (2015) p. 040,  
arXiv: [1410.8849](https://arxiv.org/abs/1410.8849) [[hep-ph](#)].
- [58] H.-L. Lai, M. Guzzi, J. Huston, Z. Li, P. M. Nadolsky et al.,  
*New parton distributions for collider physics*, *Phys.Rev.* **D82** (2010) p. 074024,  
arXiv: [1007.2241](https://arxiv.org/abs/1007.2241) [[hep-ph](#)].
- [59] S. Forte and G. Watt,  
*Progress in the Determination of the Partonic Structure of the Proton*, (2013),  
arXiv: [1301.6754](https://arxiv.org/abs/1301.6754) [[hep-ph](#)].
- [60] J. Pumplin, D. Stump, R. Brock, D. Casey, J. Huston et al.,  
*Uncertainties of predictions from parton distribution functions. 2. The Hessian method*,  
*Phys.Rev.* **D65** (2001) p. 014013, arXiv: [hep-ph/0101032](https://arxiv.org/abs/hep-ph/0101032) [[hep-ph](#)].
- [61] W. Stirling, *private communication*.
- [62] ATLAS Collaboration,  *$ZZ \rightarrow \ell^+ \ell^- \ell'^+ \ell'^-$  cross-section measurements and search for anomalous triple gauge couplings in 13 TeV pp collisions with the ATLAS detector*, (2017), arXiv: [1709.07703](https://arxiv.org/abs/1709.07703) [[hep-ex](#)].
- [63] T. Gleisberg, S. Höche, F. Krauss, M. Schönherr, S. Schumann et al.,  
*Event generation with SHERPA 1.1*, *JHEP* **02** (2009) p. 007,  
arXiv: [0811.4622](https://arxiv.org/abs/0811.4622) [[hep-ph](#)].
- [64] S. Hoeche, F. Krauss, M. Schonherr and F. Siegert,  
*QCD matrix elements + parton showers: The NLO case*, *JHEP* **04** (2013) p. 027,  
arXiv: [1207.5030](https://arxiv.org/abs/1207.5030) [[hep-ph](#)].
- [65] D. Hanneke, S. F. Hoogerheide and G. Gabrielse, *Cavity Control of a Single-Electron Quantum Cyclotron: Measuring the Electron Magnetic Moment*,  
*Phys. Rev.* **A83** (2011) p. 052122, arXiv: [1009.4831](https://arxiv.org/abs/1009.4831) [[physics.atom-ph](#)].

- [66] T. Aoyama, M. Hayakawa, T. Kinoshita and M. Nio, *Tenth-Order QED Contribution to the Electron  $g-2$  and an Improved Value of the Fine Structure Constant*, *Phys. Rev. Lett.* **109** (2012) p. 111807, arXiv: [1205.5368 \[hep-ph\]](#).
- [67] V. C. Rubin and W. K. Ford Jr., *Rotation of the Andromeda Nebula from a Spectroscopic Survey of Emission Regions*, *Astrophys. J.* **159** (1970) p. 379.
- [68] D. Clowe et al., *A direct empirical proof of the existence of dark matter*, *Astrophys. J.* **648** (2006) p. L109, arXiv: [astro-ph/0608407 \[astro-ph\]](#).
- [69] B. D. Sherwin et al., *Evidence for Dark Energy from the Cosmic Microwave Background Alone Using the Atacama Cosmology Telescope Lensing Measurements*, *Phys. Rev. Lett.* **107** (2 2011) p. 021302.
- [70] C. Arina, M. E. C. Catalan, S. Kraml, S. Kulkarni and U. Laa, *Constraints on sneutrino dark matter from LHC Run 1*, *JHEP* **05** (2015) p. 142, arXiv: [1503.02960 \[hep-ph\]](#).
- [71] K. Hagiwara, R. Peccei, D. Zeppenfeld and K. Hikasa, *Probing the weak boson sector in  $e^+e^- \rightarrow W^+W^-$* , *Nuclear Physics B* **282** (1987) p. 253 .
- [72] U. Baur and E. L. Berger, *Probing the weak-boson sector in  $Z\gamma$  production at hadron colliders*, *Phys. Rev. D* **47** (11 1993) p. 4889, arXiv: [hep-ph/9412300](#).
- [73] U. Baur and D. L. Rainwater, *Probing neutral gauge boson selfinteractions in  $ZZ$  production at hadron colliders*, *Phys. Rev.* **D62** (2000) p. 113011, arXiv: [hep-ph/0008063 \[hep-ph\]](#).
- [74] C. Degrande et al., *Effective field theory: a modern approach to anomalous couplings*, *Annals Phys.* **335** (2013) p. 21, arXiv: [1205.4231 \[hep-ph\]](#).
- [75] C. Degrande, *A basis of dimension-eight operators for anomalous neutral triple gauge boson interactions*, *JHEP* **02** (2014) p. 101, arXiv: [1308.6323 \[hep-ph\]](#).
- [76] L. Evans and P. Bryant, *LHC Machine*, *JINST* **3** (2008) S08001.
- [77] P. Gessinger-Befurt and S. Tapprogge, *Search for new heavy charged gauge bosons with the ATLAS detector*, Presented 15 May 2017, MA thesis, 2017, URL: <https://cds.cern.ch/record/2276657>.
- [78] Papotti, Giulia, [https://indico.cern.ch/event/448109/contributions/1942059/attachments/1216261/1793941/2015overview\\_paper.pdf](https://indico.cern.ch/event/448109/contributions/1942059/attachments/1216261/1793941/2015overview_paper.pdf).
- [79] Nisbet, David, [https://indico.cern.ch/event/580313/contributions/2359285/attachments/1396590/2135891/Operation\\_in\\_2016\\_v1\\_1.pdf](https://indico.cern.ch/event/580313/contributions/2359285/attachments/1396590/2135891/Operation_in_2016_v1_1.pdf).
- [80] ATLAS Collaboration, *The ATLAS Experiment at the CERN Large Hadron Collider*, *JINST* **3** (2008) S08003.
- [81] S. Chatrchyan et al., *The CMS experiment at the CERN LHC*, *JINST* **3** (2008) S08004.
- [82] A. A. Alves Jr. et al., *The LHCb Detector at the LHC*, *JINST* **3** (2008) S08005.

- [83] G. Anelli et al., *The TOTEM experiment at the CERN Large Hadron Collider*, **JINST** **3** (2008) S08007.
- [84] O. Adriani et al., *The LHCf detector at the CERN Large Hadron Collider*, **JINST** **3** (2008) S08006.
- [85] J. Pinfold et al., *Technical Design Report of the MoEDAL Experiment*, tech. rep. CERN-LHCC-2009-006. MoEDAL-TDR-001, 2009, URL: <https://cds.cern.ch/record/1181486>.
- [86] S Haywood, L Rossi, R Nickerson and A Romaniouk, *ATLAS inner detector: Technical Design Report, 2*, tech. rep., 1997, URL: <https://cds.cern.ch/record/331064>.
- [87] K. Potamianos, ‘The upgraded Pixel detector and the commissioning of the Inner Detector tracking of the ATLAS experiment for Run-2 at the Large Hadron Collider’, *Proceedings, 2015 European Physical Society Conference on High Energy Physics (EPS-HEP 2015): Vienna, Austria, July 22-29, 2015*, 2015 p. 261, arXiv: [1608.07850](https://arxiv.org/abs/1608.07850) [[physics.ins-det](https://arxiv.org/abs/1608.07850)].
- [88] N. Vermes and G Hallewel, *ATLAS pixel detector: Technical Design Report*, tech. rep., 1998, URL: <https://cds.cern.ch/record/381263>.
- [89] M Capeans et al., *ATLAS Insertable B-Layer Technical Design Report*, tech. rep. CERN-LHCC-2010-013. ATLAS-TDR-19, CERN, 2010, URL: <https://cds.cern.ch/record/1291633>.
- [90] N. Nikiforou, ‘Performance of the ATLAS Liquid Argon Calorimeter after three years of LHC operation and plans for a future upgrade’, *Proceedings, 3rd International Conference on Advancements in Nuclear Instrumentation Measurement Methods and their Applications (ANIMMA 2013): Marseille, France, June 23-27, 2013*, 2013, arXiv: [1306.6756](https://arxiv.org/abs/1306.6756) [[physics.ins-det](https://arxiv.org/abs/1306.6756)].
- [91] ATLAS Collaboration, *ATLAS liquid-argon calorimeter: Technical Design Report*, tech. rep., 1996, URL: <https://cds.cern.ch/record/331061>.
- [92] ATLAS Collaboration, *Electron and photon energy calibration with the ATLAS detector using LHC Run 1 data*, **Eur. Phys. J.** **C74** (2014) p. 3071, arXiv: [1407.5063](https://arxiv.org/abs/1407.5063) [[hep-ex](https://arxiv.org/abs/1407.5063)].
- [93] ATLAS Collaboration, *ATLAS tile calorimeter: Technical Design Report*, tech. rep., 1996, URL: <https://cds.cern.ch/record/331062>.
- [94] A. Artamonov et al., *The ATLAS forward calorimeters*, **JINST** **3** (2008) P02010.
- [95] ATLAS Collaboration, *ATLAS muon spectrometer: Technical Design Report*, tech. rep., distribution, 1997, URL: <https://cds.cern.ch/record/331068>.
- [96] ATLAS Collaboration, *ATLAS magnet system: Technical Design Report, 1*, tech. rep., 1997, URL: <https://cds.cern.ch/record/338080>.
- [97] J. P. Badiou, J Beltramelli, J. M. Maze and J Belorgey, *ATLAS barrel toroid: Technical Design Report*, tech. rep., 1997, URL: <https://cds.cern.ch/record/331065>.
- [98] ATLAS Collaboration, *ATLAS end-cap toroids: Technical Design Report*, tech. rep., 1997, URL: <https://cds.cern.ch/record/331066>.



- [99] ATLAS Collaboration, *Performance of the ATLAS Trigger System in 2015*, *Eur. Phys. J.* **C77** (2017) p. 317, arXiv: [1611.09661 \[hep-ex\]](#).
- [100] R. Achenbach et al., *The ATLAS level-1 calorimeter trigger*, *JINST* **3** (2008) P03001.
- [101] M. Shochet et al., *Fast TracKer (FTK) Technical Design Report*, tech. rep., 2013, URL: <http://cds.cern.ch/record/1552953>.
- [102] G. Lehmann Miotto et al., *Configuration and control of the ATLAS trigger and data acquisition*, *Nucl. Instrum. Meth.* **A623** (2010) p. 549.
- [103] R. Jones, *ATLAS computing and the GRID*, *Nucl.Instrum.Meth.* **A502** (2003) p. 372.
- [104] C. Eck et al., *LHC computing Grid: Technical Design Report. Version 1.06 (20 Jun 2005)*, Technical Design Report LCG, CERN, 2005.
- [105] R. Brun and F. Rademakers, *ROOT: An object oriented data analysis framework*, *Nucl.Instrum.Meth.* **A389** (1997) p. 81.
- [106] High Performance Computing Group, University of Mainz, <https://hpc.uni-mainz.de>.
- [107] ATLAS Collaboration, *Improved luminosity determination in pp collisions at  $\sqrt{s} = 7$  TeV using the ATLAS detector at the LHC*, *Eur. Phys. J.* **C73** (2013) p. 2518, arXiv: [1302.4393 \[hep-ex\]](#).
- [108] P. Jenni, M. Nordberg, M. Nessi and K. Jon-And, *ATLAS Forward Detectors for Measurement of Elastic Scattering and Luminosity*, (2008).
- [109] V. Balagura, *Notes on van der Meer Scan for Absolute Luminosity Measurement*, *Nucl.Instrum.Meth.* **A654** (2011) p. 634, arXiv: [1103.1129 \[physics.ins-det\]](#).
- [110] T Cornelissen et al., *Concepts, Design and Implementation of the ATLAS New Tracking (NEWT)*, tech. rep., CERN, 2007, URL: <https://cds.cern.ch/record/1020106>.
- [111] R. Fruhwirth, *Application of Kalman filtering to track and vertex fitting*, *Nucl.Instrum.Meth.* **A262** (1987) p. 444.
- [112] ATLAS Collaboration, *Performance of the ATLAS Track Reconstruction Algorithms in Dense Environments in LHC Run 2*, *Eur. Phys. J.* **C77** (2017) p. 673, arXiv: [1704.07983 \[hep-ex\]](#).
- [113] ATLAS Collaboration, *Vertex Reconstruction Performance of the ATLAS Detector at  $\sqrt{s} = 13$  TeV*, ATL-PHYS-PUB-2015-026, URL: <https://cds.cern.ch/record/2037717>.
- [114] W Lampl et al., *Calorimeter Clustering Algorithms: Description and Performance*, ATL-LARG-PUB-2008-002, URL: <https://cds.cern.ch/record/1099735>.
- [115] ATLAS Collaboration, *Improved electron reconstruction in ATLAS using the Gaussian Sum Filter-based model for bremsstrahlung*, ATLAS-CONF-2012-047, URL: <https://cds.cern.ch/record/1449796>.

- [116] ATLAS Collaboration, *Electron and photon energy calibration with the ATLAS detector using data collected in 2015 at  $\sqrt{s} = 13$  TeV*, ATL-PHYS-PUB-2016-015, URL: <http://cds.cern.ch/record/2203514>.
- [117] ATLAS Collaboration, *Electron efficiency measurements with the ATLAS detector using the 2015 LHC proton-proton collision data*, ATLAS-CONF-2016-024, URL: <https://cds.cern.ch/record/2157687>.
- [118] ATLAS Collaboration, *Muon reconstruction performance of the ATLAS detector in proton-proton collision data at  $\sqrt{s} = 13$  TeV*, *Eur. Phys. J.* **C76** (2016) p. 292, arXiv: [1603.05598](https://arxiv.org/abs/1603.05598) [[hep-ex](#)].
- [119] J. Illingworth and J. Kittler, *A survey of the hough transform*, *Computer Vision, Graphics, and Image Processing* **44** (1988) p. 87 , URL: <http://www.sciencedirect.com/science/article/pii/S0734189X88800331>.
- [120] ATLAS Collaboration, *Jet energy measurement and its systematic uncertainty in proton-proton collisions at  $\sqrt{s} = 7$  TeV with the ATLAS detector*, *Eur. Phys. J.* **C75** (2015) p. 17, arXiv: [1406.0076](https://arxiv.org/abs/1406.0076) [[hep-ex](#)].
- [121] ATLAS Collaboration, *Topological cell clustering in the ATLAS calorimeters and its performance in LHC Run 1*, (2016), arXiv: [1603.02934](https://arxiv.org/abs/1603.02934) [[hep-ex](#)].
- [122] M. Cacciari, G. P. Salam and G. Soyez, *The Anti- $k(t)$  jet clustering algorithm*, *JHEP* **04** (2008) p. 063, arXiv: [0802.1189](https://arxiv.org/abs/0802.1189) [[hep-ph](#)].
- [123] ATLAS Collaboration, *Jet Calibration and Systematic Uncertainties for Jets Reconstructed in the ATLAS Detector at  $\sqrt{s} = 13$  TeV*, ATL-PHYS-PUB-2015-015, URL: <https://cds.cern.ch/record/2037613>.
- [124] ATLAS Collaboration, *Tagging and suppression of pileup jets with the ATLAS detector*, ATLAS-CONF-2014-018, URL: <https://cds.cern.ch/record/1700870>.
- [125] ATLAS Collaboration, *Forward Jet Vertex Tagging: A new technique for the identification and rejection of forward pileup jets*, ATL-PHYS-PUB-2015-034, URL: <https://cds.cern.ch/record/2042098>.
- [126] ATLAS Collaboration, *Expected performance of missing transverse momentum reconstruction for the ATLAS detector at  $\sqrt{s} = 13$  TeV*, ATL-PHYS-PUB-2015-023 (2015), <https://cds.cern.ch/record/2037700>.
- [127] ATLAS Collaboration, *Performance of missing transverse momentum reconstruction for the ATLAS detector in the first proton-proton collisions at  $\sqrt{s} = 13$  TeV*, ATL-PHYS-PUB-2015-027 (2015), <https://cds.cern.ch/record/2037904>.
- [128] M. Grazzini, S. Kallweit and D. Rathlev, *ZZ production at the LHC: fiducial cross sections and distributions in NNLO QCD*, *Phys. Lett.* **B750** (2015) p. 407, arXiv: [1507.06257](https://arxiv.org/abs/1507.06257) [[hep-ph](#)].
- [129] P. Nason and G. Zanderighi,  *$W^+W^-$ ,  $WZ$  and  $ZZ$  production in the POWHEG-BOX-V2*, *Eur. Phys. J. C* **74** (2014) p. 2702, arXiv: [1311.1365](https://arxiv.org/abs/1311.1365) [[hep-ph](#)].
- [130] S. Frixione, P. Nason and C. Oleari, *Matching NLO QCD computations with parton shower simulations: the POWHEG method*, *JHEP* **11** (2007) p. 070, arXiv: [0709.2092](https://arxiv.org/abs/0709.2092) [[hep-ph](#)].



- [131] S. Alioli, P. Nason, C. Oleari and E. Re, *A general framework for implementing NLO calculations in shower Monte Carlo programs: the POWHEG BOX*, **JHEP** **06** (2010) p. 043, arXiv: 1002.2581 [hep-ph].
- [132] F. Caola, K. Melnikov, R. Röntsch and L. Tancredi, *QCD corrections to ZZ production in gluon fusion at the LHC*, **Phys. Rev.** **D92** (2015) p. 094028, arXiv: 1509.06734 [hep-ph].
- [133] B. Biedermann, A. Denner, S. Dittmaier, L. Hofer and B. Jäger, *Next-to-leading-order electroweak corrections to the production of four charged leptons at the LHC*, **JHEP** **01** (2017) p. 033, arXiv: 1611.05338 [hep-ph].
- [134] B. Biedermann, A. Denner, S. Dittmaier, L. Hofer and B. Jäger, *Electroweak corrections to  $pp \rightarrow \mu^+ \mu^- e^+ e^- + X$  at the LHC: a Higgs background study*, **Phys. Rev. Lett.** **116** (2016) p. 161803, arXiv: 1601.07787 [hep-ph].
- [135] *Monte Carlo event generator*, [https://scienode.org/img/img\\_2014/sherpa\\_sim\\_0.jpeg](https://scienode.org/img/img_2014/sherpa_sim_0.jpeg), Accessed: 2017-11-23.
- [136] J. C. Collins, *Sudakov form-factors*, **Adv. Ser. Direct. High Energy Phys.** **5** (1989) p. 573, arXiv: hep-ph/0312336 [hep-ph].
- [137] B. Andersson, G. Gustafson, G. Ingelman and T. Sjostrand, *Parton Fragmentation and String Dynamics*, **Phys. Rept.** **97** (1983) p. 31.
- [138] B. Andersson, *The Lund model*, **Camb. Monogr. Part. Phys. Nucl. Phys. Cosmol.** **7** (1997) p. 1.
- [139] G. C. Fox and S. Wolfram, *A Model for Parton Showers in QCD*, **Nucl. Phys.** **B168** (1980) p. 285.
- [140] M. Dobbs and J. B. Hansen, *The HepMC C++ Monte Carlo event record for High Energy Physics*, **Comput. Phys. Commun.** **134** (2001) p. 41.
- [141] S. Agostinelli et al., *GEANT4: A Simulation toolkit*, **Nucl.Instrum.Meth.** **A506** (2003) p. 250.
- [142] J. L. Henning, *SPEC CPU2000: measuring CPU performance in the New Millennium*, **Computer** **33** (2000) p. 28.
- [143] ATLAS Collaboration, *The ATLAS Simulation Infrastructure*, **Eur.Phys.J.** **C70** (2010) p. 823, arXiv: 1005.4568 [physics.ins-det].
- [144] T. Sjostrand, S. Mrenna and P. Z. Skands, *PYTHIA 6.4 Physics and Manual*, **JHEP** **05** (2006) p. 026, arXiv: hep-ph/0603175 [hep-ph].
- [145] T. Sjöstrand, S. Mrenna, and P. Z. Skands, *A Brief Introduction to PYTHIA 8.1*, **Comput. Phys. Commun.** **178** (2008) p. 852, arXiv: 0710.3820 [hep-ph].
- [146] J. Alwall et al., *A Standard format for Les Houches event files*, **Comput. Phys. Commun.** **176** (2007) p. 300, arXiv: hep-ph/0609017 [hep-ph].
- [147] J. Alwall, M. Herquet, F. Maltoni, O. Mattelaer and T. Stelzer, *MadGraph 5: going beyond*, **JHEP** **06** (2011) p. 128, arXiv: 1106.0522 [hep-ph].

- [148] Physics Analysis Tools, ‘Pileup Reweighting’, <https://twiki.cern.ch/twiki/bin/viewauth/~AtlasProtected/ExtendedPileupReweighting>.
- [149] ATLAS Collaboration, *Measurement of inclusive and differential cross sections in the  $H \rightarrow ZZ^* \rightarrow 4\ell$  decay channel in  $pp$  collisions at  $\sqrt{s} = 13$  TeV with the ATLAS detector*, **JHEP** **10** (2017) p. 132, arXiv: 1708.02810 [hep-ex].
- [150] ATLAS Luminosity Working Group, <https://twiki.cern.ch/twiki/bin/view/~AtlasPublic/LuminosityPublicResults>.
- [151] M. Cacciari and G. P. Salam, *Pileup subtraction using jet areas*, **Phys. Lett.** **B659** (2008) p. 119, arXiv: 0707.1378 [hep-ph].
- [152] ATLAS Collaboration, *Selection of jets produced in 13TeV proton-proton collisions with the ATLAS detector*, ATLAS-CONF-2015-029, URL: <https://cds.cern.ch/record/2037702>.
- [153] A. Ruiz-Martinez, F. Monticelli, J. Hoya and S. D. Jones, *Electron and photon trigger efficiency plots using the full 2016 dataset*, ATL-COM-DAQ-2017-015, URL: <https://cds.cern.ch/record/2254973>.
- [154] ATLAS Collaboration, *Measurement of the ZZ Production Cross Section in pp Collisions at  $\sqrt{s} = 13$  TeV with the ATLAS Detector*, **Phys. Rev. Lett.** **116** (2016) p. 101801, arXiv: 1512.05314 [hep-ex].
- [155] T. Sjöstrand and M. van Zijl, *A multiple-interaction model for the event structure in hadron collisions*, **Phys. Rev. D** **36** (7 1987) p. 2019, URL: <https://link.aps.org/doi/10.1103/PhysRevD.36.2019>.
- [156] A. Collaboration, *Measurement of hard double-parton interactions in  $W(\rightarrow l\nu) + 2$  jet events at  $\sqrt{s}=7$  TeV with the ATLAS detector*, **New J. Phys.** **15** (2013) p. 033038, arXiv: 1301.6872 [hep-ex].
- [157] UA2 Collaboration, J. Alitti et al., *A study of multi-jet events at the CERN pp collider and a search for double parton scattering*, **Phys. Lett. B** **268** (1991) p. 145.
- [158] CDF Collaboration, F. Abe et al., *Study of four jet events and evidence for double parton interactions in  $p\bar{p}$  collisions at  $\sqrt{s} = 1.8$  TeV*, **Phys. Rev. D** **47** (1993) p. 4857.
- [159] CDF Collaboration, F. Abe et al., *Double parton scattering in  $p\bar{p}$  collisions at  $\sqrt{s} = 1.8$  TeV*, **Phys. Rev. D** **56** (1997) p. 3811.
- [160] D0 Collaboration, V. M. Abazov et al., *Double parton interactions in  $\gamma + 3$  jet events in  $p\bar{p}$  collisions  $\sqrt{s} = 1.96$  TeV*, **Phys. Rev. D** **81** (2010) p. 052012.
- [161] ATLAS Collaboration, *Study of hard double-parton scattering in four-jet events in pp collisions at  $\sqrt{s} = 7$  TeV with the ATLAS experiment*, **JHEP** **11** (2016) p. 110, arXiv: 1608.01857 [hep-ex].
- [162] LHCb Collaboration, R. Aaij et. al, *Observation of double charm production involving open charm in pp collisions at  $\sqrt{s} = 7$  TeV*, **JHEP** **06** (2012) p. 141, addendum: **JHEP** **03** (2014) 108, arXiv: 1205.0975 [hep-ex].

- [163] CMS Collaboration, *Study of double parton scattering using  $W + 2$ -jet events in proton-proton collisions at  $\sqrt{s} = 7$  TeV*, **JHEP** **03** (2014) p. 032, arXiv: [1312.5729 \[hep-ex\]](#).
- [164] D0 Collaboration, V. M. Abazov et al., *Double parton interactions in  $\gamma + 3$  jet and  $\gamma + b/c$  jet+2 jet events in  $p\bar{p}$  collisions at  $\sqrt{s} = 1.96$  TeV*, **Phys. Rev. D** **89** (2014) p. 072006, arXiv: [1402.1550 \[hep-ex\]](#).
- [165] ATLAS Collaboration, *Measurement of  $W$  and  $Z$  Boson Production Cross Sections in  $pp$  Collisions at  $\sqrt{s} = 13$  TeV in the ATLAS Detector*, ATL-CONF-2015-039, URL: <http://cdsweb.cern.ch/record/2045487>.
- [166] T. Binoth, G. Ossola, C. G. Papadopoulos and R. Pittau, *NLO QCD corrections to tri-boson production*, **JHEP** **06** (2008) p. 082, arXiv: [0804.0350 \[hep-ph\]](#).
- [167] S. Chatrchyan et al., *Measurement of associated production of vector bosons and top quark-antiquark pairs at  $\sqrt{s} = 7$  TeV*, **Phys. Rev. Lett.** **110** (2013) p. 172002, arXiv: [1303.3239 \[hep-ex\]](#).
- [168] ATLAS Collaboration, *Jet energy scale measurements and their systematic uncertainties in proton-proton collisions at  $\sqrt{s} = 13$  TeV with the ATLAS detector*, (2017), arXiv: [1703.09665 \[hep-ex\]](#).
- [169] ATLAS Collaboration, *Luminosity determination in  $pp$  collisions at  $\sqrt{s} = 8$  TeV using the ATLAS detector at the LHC*, **Eur. Phys. J. C** **76** (2016) p. 653, arXiv: [1608.03953 \[hep-ex\]](#).
- [170] L. A. Harland-Lang, A. D. Martin, P. Motylinski and R. S. Thorne, *Parton distributions in the LHC era: MMHT 2014 PDFs*, **Eur. Phys. J. C** **75** (2015) p. 204, arXiv: [1412.3989 \[hep-ph\]](#).
- [171] S. Gieseke, T. Kasprzik and J. H. Kühn, *Vector-boson pair production and electroweak corrections in HERWIG++*, **Eur. Phys. J. C** **74** (2014) p. 2988, arXiv: [1401.3964 \[hep-ph\]](#).
- [172] G. Choudalakis and D. Casadei, *Plotting the differences between data and expectation*, **European Physical Journal Plus** **127**, 25 (2012) p. 25, arXiv: [1111.2062 \[physics.data-an\]](#).
- [173] ATLAS Collaboration, *Search for heavy  $ZZ$  resonances in the  $\ell^+\ell^-\ell^+\ell^-$  and  $\ell^+\ell^-\nu\bar{\nu}$  final states using proton proton collisions at  $\sqrt{s} = 13$  TeV with the ATLAS detector*, (2017), arXiv: [1712.06386 \[hep-ex\]](#).
- [174] ATLAS Collaboration, *Proposal for particle-level object and observable definitions for use in physics measurements at the LHC*, ATL-PHYS-PUB-2015-013, 2015, URL: <https://cds.cern.ch/record/2022743>.
- [175] M. Cacciari, G. P. Salam and G. Soyez, *The anti- $k_t$  jet clustering algorithm*, **JHEP** **04** (2008) p. 063, arXiv: [0802.1189 \[hep-ex\]](#).
- [176] G. D'Agostini, *A multidimensional unfolding method based on Bayes' theorem*, **Nuclear Instruments and Methods in Physics Research Section A: Accelerators, Spectrometers, Detectors and Associated Equipment** **362** (1995) p. 487 .

- [177] T. Adye, ‘Unfolding algorithms and tests using RooUnfold’, *Proceedings, PHYSTAT 2011 Workshop on Statistical Issues Related to Discovery Claims in Search Experiments and Unfolding, CERN, Geneva, Switzerland 17-20 January 2011*, CERN, CERN, 2011 p. 313, arXiv: [1105.1160 \[physics.data-an\]](#).
- [178] L. Lyons, *Open statistical issues in particle physics*, (2008), arXiv: [0811.1663 \[stat.AP\]](#).
- [179] CMS Collaboration, *Measurements of the  $pp \rightarrow ZZ$  production cross section and the  $Z \rightarrow 4\ell$  branching fraction, and constraints on anomalous triple gauge couplings at  $\sqrt{s} = 13$  TeV*, (2017), arXiv: [1709.08601 \[hep-ex\]](#).
- [180] ATLAS Collaboration, *Measurement of  $ZZ$  production in  $pp$  collisions at  $\sqrt{s} = 7$  TeV and limits on anomalous  $ZZZ$  and  $ZZ\gamma$  couplings with the ATLAS detector*, *JHEP* **03** (2013) p. 128, arXiv: [1211.6096 \[hep-ex\]](#).
- [181] CMS Collaboration, *Measurements of the  $Z Z$  production cross sections in the  $2l2\nu$  channel in proton–proton collisions at  $\sqrt{s} = 7$  and 8 TeV and combined constraints on triple gauge couplings*, *Eur. Phys. J.* **C75** (2015) p. 511, arXiv: [1503.05467 \[hep-ex\]](#).
- [182] S. Chatrchyan et al., *Measurement of the  $ZZ$  production cross section and search for anomalous couplings in  $2\ell 2\ell'$  final states in  $pp$  collisions at  $\sqrt{s} = 7$  TeV*, *JHEP* **01** (2013) p. 063, arXiv: [1211.4890 \[hep-ex\]](#).
- [183] CDF Collaboration, T. Aaltonen et al., *Measurement of the  $ZZ$  production cross section using the full CDF II data set*, *Phys. Rev. D* **89** (2014) p. 112001, arXiv: [1403.2300 \[hep-ex\]](#).
- [184] D0 Collaboration, V. M. Abazov et al., *A measurement of the  $WZ$  and  $ZZ$  production cross sections using leptonic final states in  $8.6 \text{ fb}^{-1}$  of  $p\bar{p}$  collisions*, *Phys. Rev. D* **85** (2012) p. 112005, arXiv: [1201.5652 \[hep-ex\]](#).
- [185] G. Bella, *Weighting Di-Boson Monte Carlo Events in Hadron Colliders*, (2008), arXiv: [0803.3307 \[hep-ph\]](#).
- [186] U. Baur, T. Han and J. Ohnemus, *QCD corrections and anomalous couplings in  $Z\gamma$  production at hadron colliders*, *Phys. Rev. D* **57** (1998) p. 2823, arXiv: [hep-ph/9710416](#).
- [187] ATLAS Collaboration, *Measurement of the  $ZZ$  production cross section in proton–proton collisions at  $\sqrt{s} = 8$  TeV using the  $ZZ \rightarrow \ell^- \ell^+ \ell'^- \ell'^+$  and  $ZZ \rightarrow \ell^- \ell^+ \nu\bar{\nu}$  decay channels with the ATLAS detector*, *JHEP* **01** (2017) p. 099, arXiv: [1610.07585 \[hep-ex\]](#).
- [188] G. J. Feldman and R. D. Cousins, *A Unified approach to the classical statistical analysis of small signals*, *Phys. Rev.* **D57** (1998) p. 3873, arXiv: [physics/9711021 \[physics.data-an\]](#).
- [189] F. James, *MINUIT - Function Minimization and Error Analysis.*, CERN Program Library entry D506, Geneva. 1998.
- [190] J.-F. L. et al., *FLIT Package*, 2013, URL: <https://laportej.web.cern.ch/laportej/refman.pdf>.

- [191] J.-F. Laporte, *private communication*.
- [192] J. Alcaraz et al., *A Combination of preliminary electroweak measurements and constraints on the standard model*, (2006), arXiv: [hep-ex/0612034](#) [[hep-ex](#)].
- [193] V. M. Abazov et al., *Search for ZZ and Z $\gamma^*$  production in p $\bar{p}$  collisions at  $\sqrt{s} = 1.96$  TeV and limits on anomalous ZZZ and ZZ $\gamma^*$  couplings*, *Phys. Rev. Lett.* **100** (2008) p. 131801, arXiv: [0712.0599](#) [[hep-ex](#)].
- [194] ATLAS Collaboration, *Measurement of the ZZ production cross section in proton-proton collisions at  $\sqrt{s} = 8$  TeV using the ZZ  $\rightarrow \ell^-\ell^+\ell'^-\ell'^+$  and ZZ  $\rightarrow \ell^-\ell^+\nu\bar{\nu}$  channels with the ATLAS detector*, *JHEP* **01** (2017) p. 099, arXiv: [1610.07585](#) [[hep-ex](#)].
- [195] *Limits on anomalous triple and quartic gauge couplings*, <https://twiki.cern.ch/twiki/bin/view/CMSPublic/PhysicsResultsSMPaTGC>, Accessed: 2017-11-23.
- [196] G. Cowan, K. Cranmer, E. Gross and O. Vitells, *Asymptotic formulae for likelihood-based tests of new physics*, *Eur. Phys. J.* **C71** (2011) p. 1554, [Erratum: *Eur. Phys. J.*C73,2501(2013)], arXiv: [1007.1727](#) [[physics.data-an](#)].
- [197] M. Mangano, *Physics at the FCC-hh, a 100 TeV pp collider*, CERN Yellow Reports: Monographs, CERN, 2017, URL: <https://cds.cern.ch/record/2270978>.



## *Danksagung*

Personenbezogene Daten sind aus Datenschutzgründen aus der elektronischen Version gelöscht.





# Lebenslauf

## Kontaktdaten

Name Maurice Becker  
Adresse Bonifaziusplatz 4a, 55118 Mainz  
E-Mail mauriceb@students.uni-mainz.de

## Persönliche Angaben

Geburtsdatum 31.05.1989  
Geburtsort Frankfurt am Main  
Nationalität Deutsch  
Familienstand ledig

## Schulbildung

1995-1999 Grundschule Bingen am Rhein  
1999-2008 Stefan-George-Gymnasium Bingen am Rhein  
März 2008 Allgemeine Hochschulreife

## Akademische Laufbahn

09/2008-10/2011 Bachelor of Science in Physik, Johannes Gutenberg-Universität Mainz,  
Gesamtnote: gut (2,2)  
10/2011-09/2013 Master of Science in Physik, Johannes Gutenberg-Universität Mainz,  
Gesamtnote: sehr gut (1,1)  
seit Jan. 2014 Promotion in Physik, Johannes Gutenberg-Universität Mainz